The University of Nottingham

UNITED KINGDOM · CHINA · MALAYSIA

Development of Lagrangian Soot Tracking Method for the Study of Soot Morphology in Diesel Spray Combustion

Jiun Cai Ong, M.Eng (Hons)

Thesis Submitted to the University of Nottingham Malaysia Campus for the Degree of Doctor of Philosophy

December 2016

ABSTRACT

The weakness of a conventional Eulerian soot model in capturing primary soot size and its inability to access individual soot information led to the development of a Lagrangian soot tracking (LST) model as reported in this thesis. The LST model aimed to access the history of individual soot particles and capture the soot concentration and primary soot size distribution in high pressure spray flames, under diesel-like conditions. The model was validated in a constant volume spray combustion chamber by comparing the predicted soot volume fraction (SVF), mean primary soot diameter and primary soot size distribution to the experimental data of *n*-heptane and *n*-dodecane spray combustion. The inception, surface growth and oxidation models were adopted and modified from the multistep Moss-Brookes (MB) soot model, which was used in this study as the representative of Eulerian soot model. Parametric studies were carried out to investigate the influence of soot surface ageing and oxidation rates on the overall soot formation. Following the parametric study, the developed LST model which incorporated surface ageing effect and higher oxidation rates was implemented to investigate the effect of ambient oxygen and density on soot morphology in *n*-heptane spray flame.

The LST model was shown to have better primary soot size prediction capability while still maintaining comparable performance in predicting SVF with respect to its Eulerian counterpart. The SVF distributions predicted by the LST model qualitatively correspond to the experimental results despite the peak soot location being predicted further downstream by 30 mm. The primary soot size distribution predicted by the LST model had the same order as the measured primary soot size distribution despite predicting larger soot size. The presence of surface ageing factor had a significant effect on the primary soot size distribution whereas only a slight effect on the SVF profile. A maximum soot size reduction of 48% was obtained when incorporating surface ageing effect. The consideration of surface ageing effect led to smaller primary soot size predicted and better agreement with the measured primary soot size distribution.

The peak and mean primary soot sizes increased with increasing ambient density, from 14.8 kg/m^3 to 30 kg/m^3, at the core of spray jet. Meanwhile, the decrease in oxygen level from 21% to 12% at an ambient density of 14.8 kg/m^3 caused a non-monotonic effect on the primary soot sizes at the core of spray jet. Trivial differences were predicted when oxygen level decreased from 21% to 15%. However, a significantly smaller primary soot sizes were predicted when oxygen level decreased further to 12%. In addition to net growth rates, soot cloud span and soot age were also found to play an important role in evolution of primary soot size. An increase in ambient oxygen and density resulted in a more upstream first-soot location. The effect of ambient density on soot age was not significant, whereas a lower oxygen level resulted in a longer soot age. A maximum soot age of 0.50 ms was obtained for both 21% and 15% O_2 cases at both density levels. As oxygen level decreased to 12%, the maximum soot age increased to 0.58 ms due to lower combustion temperature.

Overall, the LST model was shown to perform better in predicting primary soot size and can access information of individual soot particles which are both shortcomings of the Eulerian method. In addition, the LST model was also demonstrated to be able to predict soot age. Apart from playing a role in determining primary soot size, soot age can also serve as a useful parameter to answer various fundamental questions, such as when and where soot particles grow to a certain size, and help in the understanding of fundamental soot processes. Optimisation of the model and extension of its capability to capture soot aggregate structure, size and fractal dimension will be of interest in the future.

TABLE OF CONTENTS

ABBREVIATIONS

1-D	One-dimensional
2-D	Two-dimensional
A_1	Benzene
A_2	Naphthalene
A_3	Phenanthrene
A_4	Pyrene
AAC	Aerodynamic aerosol classifier
A_i	Aromatic molecule with *i* rings
$A_{i\text{-}}$	Radical of aromatic molecule with *i* rings
amu	Atomic mass unit
APM	Aerosol particle mass analyser
ASO	After soot onset
ASOI	After start of injection
C_2H_2	Acetylene
CO	Carbon monoxide
CO_2	Carbon dioxide
CERC	Combustion Engine Research Center

CFD	Computational fluid dynamics
CFL	Courant-Friedrichs-Lewy
CPC	Condensation particle counter
CPMA	Centrifugal particle-mass analyser
DRW	Discrete random walk
DSM	Discrete sectional method
ECN	Engine combustion network
EURO	European Union
FANS	Favre-Averaged Navier-Stokes
FTD	Fischer-Tropsch diesel
H	Hydrogen atom
H_2	Hydrogen
H_2O	Water
HACA	H-Abstraction-Carbon-Addition
HCCI	Homogeneous charge compression ignition
HNS	Hiroyasu-Nagle and Strickland
HRR	Heat release rate
HR-TEM	High-resolution transmission electron microscopy

ID	Ignition delay timing
ISAT	In-situ adaptive tabulation
KMD	Kinetic molecular dynamics
LES	Large eddy simulation
LHS	Left-hand side
LII	Laser-induced incandescence
LLNL	Lawrence Livermore National Laboratory
LOL	Lift-off length
LPL	Liquid penetration length
LST	Lagrangian soot tracking
MB	Moss-Brookes
MOM	Method of moments
NDS	Nottingham Diesel Surrogate
NO_2	Nitrogen dioxide
NSC	Nagle and Strickland-Constable
O_2	Oxygen
ODE	Ordinary differential equation
OH	Hydroxyl radical

PAH	Polycyclic aromatic hydrocarbon
PSR	Perfectly stirred reactor
PSDF	Particle size distribution function
PSIC	Particle source in cell method
RANS	Reynolds-Averaged Navier-Stokes
RD	Reitz-Diwakar
RHS	Right-hand side
SEM	Scanning electron microscopy
SMPS	Scanning mobility particle sizer
SVF	Soot volume fraction
TEM	Transmission electron microscopy
TIRE-LII	Time-resolved laser-induced incandescence
TCI	Turbulence-chemistry interaction
VPL	Vapour penetration length

NOMENCLATURE

Variables

$[X_i]$	Molar concentration of species i (kmol/m^3)
$\Delta h_{f,j}^0$	Enthalpy of formation of species j at standard temperature and pressure (J/ kg)
Δt	Computational time-step (s)
Δx	Mesh size (mm)
$a_{n=1,2,\ldots,5,j}$	Coefficients of the j-th species to fit 4-th order NASA polynomials (Unit varies)
A_{ox}, A_f	Model constants for Hiroyasu's soot model (Unit varies)
$A_{i=1,2\ldots5}$	Constants for Fairweather's soot model (Unit varies)
A_p	Particle residence time (ms)
b_{nuc}^*	Normalized radical nuclei concentration (No. of particles × 10^{-15}/kg)
$c_{p,j}$	Specific heat capacity of species j (J /kg K)
C_p	Heat capacity at constant pressure of mixture (J /kg K)
$C_{1\epsilon}, C_2, C_3, C_\mu$	Model constants for standard $k-\epsilon$ turbulent model (Unit varies)
C_D	Drag coefficient (-)
$C_{D,sphere}$	Drag coefficient of perfect sphere (-)
C_F, C_b, C_k, C_d	Constants for droplet distortion (Unit varies)
$C_{b1}, C_{b2}, C_{s,}\ T_{strp}$	Model constants for Reitz-Diwakar spray model (Unit varies)
C_{inc}	Model constant for soot incipient rate (s^{-1})
C_{sg}	Surface growth rate scaling factor (kg m/kmol s)

C_{OH}	Model constant for soot oxidation due to *OH* (kg m/kmol $K^{0.5}$ s)
C_{O_2}	Model constant for soot oxidation due to O_2 (kg m/kmol $K^{0.5}$ s)
d_p	Diameter of Lagrangian soot particle (m)
d_{soot}	Soot diameter (m)
D	Mass diffusivity (m^2/s)
D_d	Liquid droplet diameter (m)
$D_{d,stable}$	Stable liquid droplet diameter (m)
E	Activation energy (kJ/kmol)
E_f	Activation energy for soot formation in Hiroyasu's model (kJ/kmol)
E_O	Activation energy for soot oxidation in Hiroyasu's model (kJ/kmol)
$\mathbf{g}$	Gravitational acceleration (m/s^2)
h	Specific enthalpy (J/ kg)
h_c	Chemical enthalpy (J/ kg)
h_{fuel}	Enthalpy of combustion of fuel (J/ kg)
h_j	Specific enthalpy of species j (J/ kg)
h_o	Total enthalpy (J/ kg)
h_s	Sensible enthalpy (J/ kg)
$\mathbf{I}$	Identity matrix (-)
k	Turbulent kinetic energy (m^2/s^2)
k_j	Reaction rate constant of an Arrhenius equation for reaction j (Unit varies)
K_f	Formation coefficient (s^{-1})

K_{ox}	Oxidation coefficient (s^{-1})
l	Turbulence length scale (m)
L	Diffusive flux (mole/ m s)
m	Mass (kg)
m_d	Liquid droplet mass (kg)
m_p	Mass of Lagrangian soot particle (kg)
M_i	Mass concentration of soot formed/destroy due to inception for Fairweather's soot model (kg/m^3)
M_g	Mass concentration of soot formed/destroy due to growth for Fairweather's soot model (kg/m^3)
M_{ox}	Mass concentration of soot formed/destroy due to oxidation for Fairweather's soot model (kg/m^3)
M_{soot}	Soot mass concentration (kg/m^3)
MW	Molar mass (kg/kmol)
MW_P	Molar mass of an incipient soot particle (kg/kmol)
MW_j	Molar weight of species j (kg/kmol)
MW_c	Molar weight of carbon (kg/kmol)
N_A	Avogadro constant (1/mol)
N_i	Soot number density from inception for Fairweather's soot model (No. of particles/m^3)
N_{agg}	Soot number density from agglomeration for Fairweather's soot model (No. of particles/m^3)
N_s	Number of species (-)
N_r	Number of reaction (-)
N_d	Number of droplets represented by the parcel tracked (-)

N_{soot}	Soot number density (No. of particles/m^3)
$\mathbf{p}_d$	Particle droplet force (N)
P	Gas Pressure (Pa)
P_0	Operating pressure (Pa)
P_u	Partial pressure of unburned fuel (Pa)
P^0	Standard pressure (Pa)
P_k	Production term for standard $k-\epsilon$ turbulent model (Pa/s)
$\dot{\mathbf{q}}$	Heat flux due to of heat conduction and enthalpy diffusion (J /s m^2)
$\dot{\mathbf{q}}_{\mathbf{source}}$	Heat from other sources (J /s m^3)
$\dot{q}_{reaction}$	Heat of reaction (J /s m^3)
r_d	Liquid droplet radius (m)
R	Universal gas constant (Unit varies)
$\dot{\mathbf{R}}\mathbf{R}$	Reaction rate (mol /s m^3)
S_p	Cross-sectional area of particle (m^2)
S_{soot}	Specific soot surface area (No. of soot particles/m)
S_ρ	Spray source term for continuity equation (kg/m^3 s)
$S_{\rho Y}$	Spray source term for species transport equation ((kg/m^3 s)
$S_{\rho u}$	Spray source term for momentum equation (kg/ m^2 s^2)
$S_{\rho h}$	Spray source term for energy equation (J/m^3 s)
t	Time (s)
t_{inj}	Injection duration (s)
t_{soot}	Time of formation for the primary soot particle (s)

T	Gas temperature (K)
T_u	Local temperature (K)
T_{ref}	Standard temperature (K)
T_{inc}	Activation temperature of soot inception (K)
T_{sg}	Activation temperature of surface growth (K)
T_{O_2}	Activation temperature of soot oxidation due to O_2 (K)
$\mathbf{u}$	Velocity vector (m/s)
$\mathbf{u}_d$	Liquid droplet velocity (m/s)
U_{rms}	Mean swirl velocity (m/s)
$\mathbf{v}_f$	Final velocity (m/s)
$\mathbf{v}_i$	Initial velocity (m/s)
$\mathbf{v_p}$	Velocity of Lagrangian soot particle (m/s)
V	Volume (m^3)
$\mathbf{x}$	Position vector (m)
X	Molar fraction (-)
y_d	Droplet distortion (-)
Y	Mass fraction (-)
Y_f	Local mass fractions of fuel (-)
Y_{soot}	Local mass fraction of soot (-)

Greek symbols

α	Surface ageing factor (-)
ϵ	Turbulent dissipation rate (m^2/s^3)
ζ	Gaussian random number (-)
η_{coll}	Collision efficiency parameter (-)
θ	Critical age (ms)
κ	Chemical reaction rate multiplier (-)
λ	Thermal conductivity (J/m K s)
μ	Coefficient of viscosity (Pa s)
μ_g	Coefficient of viscosity of surrounding gas (Pa s)
ρ	Density (kg/m^3)
ρ_d	Liquid droplet density (kg/m^3)
ρ_g	Density of surrounding gas (kg/m^3)
ρ_p	Density of Lagrangian soot particle (kg/m^3)
ρ_{soot}	Soot density (kg/m^3)
σ_d	Surface tension coefficient of the liquid droplet (N/m)
τ	Time interval (s)
τ_b	Breakup time (s)
$\boldsymbol{\tau_s}$	Stress tensor (kg/s^2)
$\boldsymbol{\tau_s^R}$	Reynolds-stress tensor (kg/s^2)
ϕ, φ	Flow variable (-)
$\overline{\phi}$	Mean flow variable based on Reynolds-averaging (-)
ϕ'	Fluctuating flow variable on Reynolds-averaging (-)

$\widetilde{\phi}$	Mean flow variable based on Favre-averaging (-)
ϕ"	Fluctuating flow variable on Favre-averaging (-)
$\omega_{ox,i}$	Oxidation rate of individual soot particles (kg/s m^3)
$\omega_{sg,i}$	Surface growth rate of individual soot particles (kg/s m^3)
$\omega_{sg,poly}$	Surface growth rate based on poly-dispersed assumption (kg/s m^3)
$\dot{\omega}_{NSC}$	NSC soot mass oxidation rate per unit surface area (kg/s m^2)

Superscript

f	Forward reaction
r	Reverse reaction

Subscript

d	Liquid droplet
g	Surrounding gas
p	Lagrangian particle

Dimensionless number

Le	Lewis number
Pr	Prandlt number
Re	Reynolds number
Sc	Schmidt number
We	Weber number

LIST OF FIGURES

LIST OF TABLES

ACKNOWLEDGEMENTS

Over the last four years, my journey to this Ph.D. in University of Nottingham, Malaysia Campus as a graduate student has been a memorable experience. I would like to take this opportunity to acknowledge a few individuals for all the help and support they provided over this period.

First, I would like to express my gratitude to my advisors, Professor Ng Hoon Kiat and Dr. Ho Jee Hou, for their encouragement, support and guidance that helped me overcome the research roadblocks while working towards my Ph.D. I would also like to express my sincere thanks to Dr. Pang Kar Mun for his invaluable suggestions and comments throughout my doctoral work. I would also like to acknowledge the help and support I received from my fellow colleagues and friends.

Last but not least, I deeply appreciate the support I received from my parents in fulfilling my dream. It is their love, guidance and unrelenting support that helped me grow stronger in difficult times.

CHAPTER 1
INTRODUCTION

1.1 Background

Soot particles have been a major concern for the car industry as they not only exhibit adverse health and environmental effects, but also affect engine performance. Numerous experimental observations [1,2] suggest that combustion-generated soot particles have a fractal-like aggregate structure with a typical size between 1 nanometer (nm) and a few microns in diameter. Soot particles of such size once emitted into the atmosphere and inhaled by humans are able to cause respiratory disease and organ damage [3,4]. Moreover, combustion-generated organic compounds such as polycyclic aromatic hydrocarbons (PAHs) which are present on the soot surface can cause additional damage to the respiratory system.

From the environmental perspective, soot emission can significantly degrade air quality such as reducing visibility [5,6]. Newly emitted soot particles in the atmosphere can act as nuclei for cloud formation, causing secondary environmental issues such as changing the rain pattern [5,6]. Soot emission is also closely related to global warming as soot is a strong absorber of solar energy and is found to be the second most important contributor after CO_2 [7]. It also poses threats to global and regional climate [8,9] when released into the atmosphere.

It has been shown that, of the soot produced within the engine, only 29% reaches the atmosphere through the exhaust pipe [10], with the remainder being deposited into lubricant layer on the cylinder walls and piston crown [11,12]. This soot-laden lubricant will eventually end up in the oil sump and contaminate the oil reservoir [13]. The contaminated lubricant oil can lead to an increased in oil viscosity and oil thickening [14] which consequently results in an ineffective filtration of lubricant oil as oil filters are clogged. This eventually causes starvation of lubricant at engine component interface [15,16], higher wear rate of engine parts, and ultimately engine failure.

1.1.1 Legislation of Soot Emission for Soot Mass, Size and Numbers

These concerns about public health and environment led the European Union to adapt its norms for cars emissions. Initially, the EURO norms (European emission standards) limit the mass of soot emitted by Diesel powered cars with lower and lower values from the EURO1 in 1992 to the EURO4 in 2005. As more and more studies showed that particle number and size play a more important role in affecting public health [17], a particle number emission limit has been proposed [18,19] in the legislation implementation draft of Euro 5/6 in addition to requiring lower mass of soot emitted.

Driven by the increasingly stringent legislations for pollutant emissions, diesel engines with more complex engine configurations including in-cylinder strategies and aftertreatment devices are being developed to achieve better reduction of gaseous and particulate emissions. Since emission related processes lie at the end of the chain of combustion events, physical understanding of all affecting phenomena is essential in order to identify the most promising concepts for pollutant abatement.

1.1.2 Understanding the Soot Formation Process

Soot formation is the conversion of hydrocarbon fuel molecules into a carbonaceous agglomerate containing millions of carbon atoms. It is a transition of gas-phase species to solid particles by going through different physical and chemical processes which are complicated and have yet to be fully understood. It is generally agreed that the soot formation process involves six identified processes, namely pyrolysis, nucleation, coalescence, surface growth, agglomeration, and oxidation. A sequence depicting the first five of these processes of the soot formation process are pictured schematically in Figure 1-1, while oxidation, which converts hydrocarbons to CO, CO_2 and H_2O, can occur at any point along the process.

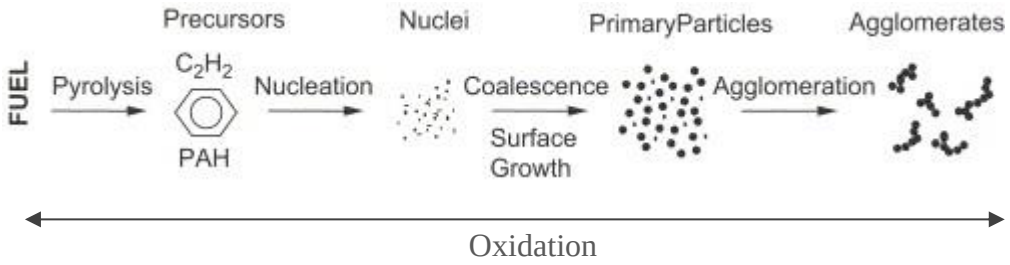

Figure 1- 1: Schematic diagram of the steps in the soot formation process from gas phase to solid agglomerated particles [20]**.**

Studies and investigations of the correlations of operating conditions with combustion and emission characteristics are constantly being pursued to improve our understanding of soot formation processes. Optically accessible test rigs and engines in conjunction with the emergence of cycle-resolved measurement techniques and high-speed imaging in recent years have significantly improved the understanding of underlying soot processes during combustion. The use of ex-situ diagnostics on exhaust soot has been used to investigate soot nanostructures and size by studying the soot particles itself, thus compensating for the drawback of optical imaging techniques that can only provide an overview of the soot phenomena. The advent of direct in-flame soot sampling technique has made it possible to study in-flame soot as opposed to conventional exhaust soot [21–24]. Even with probing or imaging capabilities, intrusive or non-intrusive, the experiments on internal combustion engines can only provide information which is not temporally and spatially complete. Some experimental measurements are even complicated to set up and fairly costly. Hence, an alternative to investigate the soot formation processes during combustion is via computational method, which is more feasible and cost-effective.

1.1.3 Modelling of Soot Processes

Computational Fluid Dynamics (CFD) has become an important tool for supporting experimental investigations in engine research. This is due to its ability to overcome some of the limitations in experimental techniques and can provide reasonable prediction of the actual combustion process and the interactions of species inside the combustion chamber. The development of modelling capabilities on soot

formation based on fundamental chemistry and physics accounting for soot nanostructure and size distribution is thus an indispensable tool to gain such understanding.

The results of most modelling studies have been focused on the soot mass and concentration inside the combustion chamber [25,26]. It is mentioned earlier that the health and environmental effects of soot depend not only on the total amount of soot formed as indicated by soot volume fraction but also on the soot particle nanostructure and size distribution. Therefore, knowledge of soot particle nanostructure and size distribution would benefit us in finding effective ways to eliminate unburned carbon and to better understand the roles of individual chemical and physical processes in soot formation. As such, the interest in soot research has recently expanded from studying soot volume fraction to investigating soot particle nanostructure and size distribution. Soot modelling studies that capture particle size distribution function (PSDF) have been reported in [27–32].

Recently, the size of primary soot particles is of main interest as they make up the whole soot aggregate structure. The understanding of its formation can lead to a better insight into the formation of soot aggregates and the overall soot formation processes. Modelling methods such as Method of Moments (MOM) [29,33] and discrete sectional method (DSM) [34–36] have been an indispensable tool in the study of the size and number density of primary soot size. Despite being commonly used in flame application, they can only provide the mean primary soot size and have no access to individual soot information. An alternative method is the Monte-Carlo stochastic approach [30,31,37] which poses the capability to access individual soot particle information and has the potential to provide a detailed PSDF, including primary soot size distribution, number density of primary soot size, aggregate size, etc. Yet, this approach has limited application due to its relatively high computational cost [28]. Thus, it is imperative to develop a method which can provide more soot information and be computationally feasible in diesel spray application.

Despite extensive study on soot formation and oxidation processes experimentally or numerically, whether the soot particles present in the diesel spray flame is dominant by young soot or mature soot remains unknown. The parameter, "soot age", is used to measure the age of the soot particles formed and is defined as the duration from its formation to the time it is fully oxidised. This parameter has emerged to be an important parameter in the study of surface ageing [31,38,39] in laboratory flame configuration. However, there has been no study linking "soot age" with soot formed in diesel spray flame. Therefore, it is of great interest to be able to gain insight into its effect on primary soot particles.

1.2 Objectives of Thesis

In view of the current state of knowledge, the present work aims to address issues related to soot dynamic modelling, along with its applications in multi-dimensional CFD simulations concerning diesel spray combustion.

i. *Develop a simpler and easily integrated soot model to predict the soot morphology and soot concentration while having access to individual soot information.*

Soot modelling of particle size distribution are either too computationally expensive or only provide limited soot information. Set against this background, a soot model is developed based on an Eulerian soot model from literature which can adequately capture the soot formation phenomena. The developed soot model involves treating soot particles formed as Lagrangian particles and tracks them. Utilising the Lagrangian technique to treat soot particles allows the accessibility and storage of more soot information, thus overcoming the shortcomings of the Eulerian soot model. As the Lagrangian soot model is adopted from the Eulerian model, it is expected to possess the combined benefits of both soot models in terms of soot concentration and soot sizing prediction capabilities.

ii. Compare the soot predictive capabilities of the developed Lagrangian soot model with that of Eulerian soot model.

The aim of this phase of work is to verify that the predictive capabilities of the Lagrangian soot model are on par with its Eulerian counterpart. A successful verification of its capabilities would imply that the Lagrangian soot model performs equally well as its Eulerian counterpart in addition to having its own Lagrangian capabilities.

Here, their performances are compared in both *n*-heptane and *n*-dodecane spray combustion, under diesel engine-like conditions. As soot models are strongly dependent on the species concentrations predicted in the simulation, a suitable chemical mechanism should be chosen. A reduced chemistry mechanism is chosen for each *n*-heptane and *n*-dodecane fuel with consideration of their balance in accuracy and computational cost. The ignition delay (ID) and lift-off lengths (LOL) are first validated against measured results to ensure the accuracy of the reduced mechanisms selected. The developed Lagrangian and Eulerian soot model are then integrated with the reduced chemical mechanism to predict the soot concentration and mean primary soot size distribution.

iii. Validate the prediction of individual primary soot size by the developed Lagrangian soot model.

This phase of work aims to investigate the accuracy and capability of the Lagrangian model in predicting individual primary soot size. The validation of the Lagrangian model would demonstrate its potential to be an alternative modelling method to predict primary soot size in diesel spray application.

This numerical study is carried out only for reacting *n*-dodecane spray combustion in constant volume combustion chamber. Average soot diameter distribution only provides spatial information of the overall soot but not the detailed primary soot size distribution inside the soot cloud. Therefore, the individual soot information (size and position) are extracted to obtain a primary soot size distribution and

compare it with experimentally measured primary soot size distribution from literature. The soot information is extracted from the Lagrangian soot particles that are along the spray axis.

iv. *Study the effect of ambient oxygen content and ambient density on the primary soot size distribution using the developed Lagrangian soot model.*

Optical diagnostics carried out in reacting spray combustion experiments can only resolve the equivalent soot size of the soot particles formed, but not the primary soot size. Only with transmission electron microscopy (TEM) can the primary soot particle size be resolve accurately. A recent experiment via TEM had been carried out and the effect of ambient oxygen on primary soot size distribution was obtained [40]. However, no clear explanation about the observed results was provided. Hence, this phase of work serves to explain the phenomenon in [40] and extend the current knowledge to include the effect of ambient density on primary soot size distribution.

The developed Lagrangian soot model is implemented to study the effect of oxygen content and ambient density on the primary soot size evolution. This investigation is carried out for reacting *n*-heptane spray flame in constant volume chamber. The oxygen content is varied from 12% - 21%, while the ambient density is varied from 14.8 - 30.0 kg/m^3.

1.3 Outline of the Thesis

The chapters of the thesis are organised as follows. Background information on soot characteristics and formation pathway, and a literature review of experimental soot studies and soot modelling are provided in Chapter 2.

Accordingly, the theoretical backgrounds and corresponding governing equations for various numerical models including the flow model, spray models and soot model used in the thesis are described in Chapter 3.

In Chapter 4, the formulation of Lagrangian soot model is explained in detail for the nucleation of Lagrangian soot particles and its size change via surface growth and oxidation processes. The assumptions made in this work are also comprehensively explained here.

In Chapter 5, the case setup is briefly introduced which includes the boundary conditions, initial conditions and operating conditions. Numerical model validations are carried out to ensure that the spray modelling and combustion characteristics are captured correctly before proceeding into soot modelling in later chapters. The validation of numerical results is done by comparing them with experimental data from Engine Combustion Network (ECN).

In the following Chapter 6, the performance of the Lagrangian soot model is benchmarked against the Eulerian mass-based soot model by comparing their numerical results for SVF, mean primary soot size distribution and primary soot size distribution function. Their results are also compared against experimental data to gauge their accuracy.

A sensitivity study of Lagrangian soot model is carried out in Chapter 7 where the impact of surface ageing effect on the performance of the Lagrangian soot model is investigated. Besides surface ageing effect, the effect of oxidation factor is also included to investigate their effect on the prediction of SVF and primary soot size distribution.

In Chapter 8, the well-validated Lagrangian soot model is then implemented to study the effect of ambient oxygen content (21%, 15% and 12%) and ambient density (14.8 kg/m^3 and 30.0 kg/m^3) on the primary soot size evolution from the start of soot formation in a constant volume diesel spray combustion. Their effects on primary soot size are investigated from by considering the inter-relationship between soot age, soot cloud span and net growth rates.

Lastly, the overall appraisals of the research work reported in this project are summarised in Chapter 9 where key conclusions are highlighted and some recommendations for future work are presented.

CHAPTER 2
LITERATURE REVIEW

2.1 Background

This chapter explores some background information necessary to fully understand the present work and its associated goals. Current understanding of soot and its formation/oxidation processes are explained in Section 2.2 and 2.3. A brief introduction on the experimental soot studies is given in Section 2.4. Subsequently, different approaches that are generally employed to model and predict soot emissions are listed and discussed in Section 2.5 and 2.6. Next, a summary of numerical studies regarding soot in diesel spray flame is compiled and presented in Section 2.7.

2.2 Soot Characteristics and Structure

Soot particles are formed during high temperature pyrolysis or rich combustion of hydrocarbon fuels. Unlike other common pollutants such as NO_x or CO, which are emitted in gaseous phase, soot is emitted as a solid. There are a few review papers that have done a comprehensive discussion on the structure and composition of soot, for example [41,42]. Soot is found to be in the form of a necklace-like agglomerates which has a size of around 100 μm. Within these agglomerates are smaller, basic particles that are spherical or nearly spherical [43], which often have a diameter of 15-50 nm [44]. The spherules are called “primary soot particles” [43] while clusters of primary soot particles are defined as “secondary particles”. Young soot particles are first formed before evolving into spherical primary soot particles, also known as mature soot. At early stages, young soot particles are not spherical but in an elliptic shape [45]. They can contain equal number of hydrogen atoms as carbon atoms and high concentrations of PAH residuals. As young soot particles mature, they undergo structural reorganisation and dehydrogenation and/or graphitisation processes [46]. This lead to a decrease in its hydrogen content to 0.1 or even less [46]. The primary soot particles evolve to be spherical due to the

simultaneous presence of both soot aggregation and surface growth, which will be introduced in later section. Mitchell et al. [47] demonstrated, using Monte-Carlo simulation, that aggregation with sufficiently small spherical particles in the presence of surface growth can lead to a spherical shape. Figure 2-1 shows the structure of the soot particles when they collide and fuse together. The overlapping region is indicated by "A" in Figure 2-2. This phenomenon is explained by Mitchell et al. to be caused by the rearrangement of crystallite structure to accommodate the energy released upon collision [47].

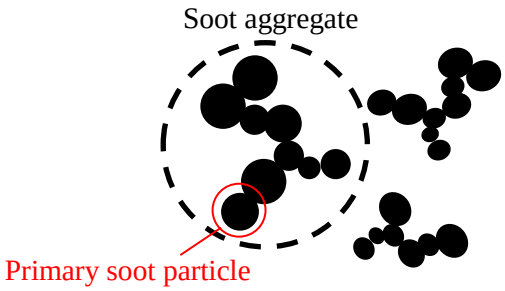

Figure 2- 1: Soot aggregates made up of primary soot particles.

By using X-ray diffractions, soot can be subdivided into three substructures, platelet, crystallite and particle as shown in Figure 2-3 [48]. Platelets are actually carbon atoms of primary soot particles that are packed into hexagonal face-centered arrays. By arranging several layers, typically two to five layers, of platelets together, crystallite is formed [48]. The crystallites are arranged in a turbostratic fashion, with their planes nearly parallel to the particle surface. The surface wrinkles on the soot particles are caused by the dislocation of five- and seven-member rings [41].

Under a high-resolution transmission electron microscopy (HR-TEM), the primary soot particle possesses two distinct parts: an outer shell and an inner core [49,50]. The outer shell refers to the platelets mentioned earlier. As for the inner core, it contains fine particles with spherical nucleus. The outer shell is more stable than the inner core as the former one is composed of graphitic crystallites while the latter's structure is thermodynamically instable. The outer shell and inner core coincides with the nanoparticles, Type I and Type II, as suggested by Baquet et al. [49] and supported by Grotheer et al. [51]. Type I particles, found by D' Alessio et

al. [52], are fairly unstable which is similar to the properties of the inner core structure of the primary soot particles. On the other hand, Type II particles, detected by Dobbins and co-works [53] are found to be in a more organised manner or stacks which correspond quite well with the soot structure presented in Figure 2-2. The outer shell can be referred to as "fringes" [54]. Soot formed under high pressure and temperature exhibits more ordered fringes, while soot formed under low pressure and temperature tends to show amorphous nanostructure with disordered fringes. The amorphous soot with disordered, short and curvature fringes and wide lattice fringe separation are more easily oxidised [55].

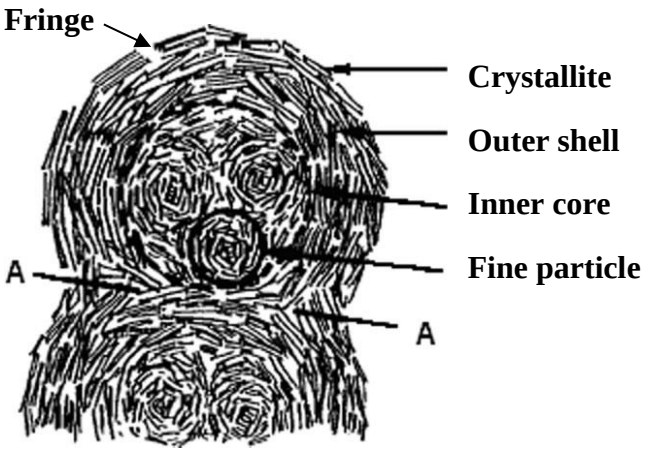

Figure 2- 2: Microstructure of soot particle when coagulated [50]**.**

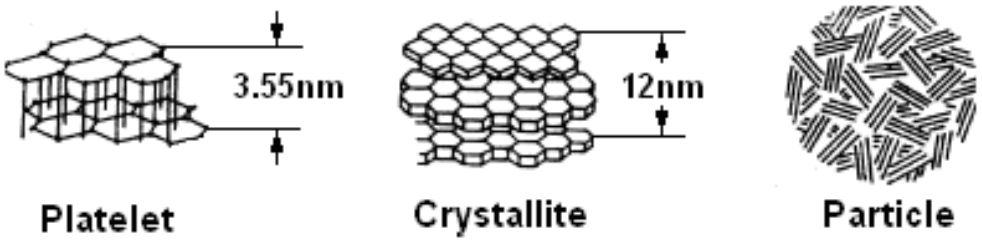

Figure 2- 3: Substructure of soot particles [48]**.**

2.3 Soot Formation and Oxidation Processes

The fundamentals of soot formation and oxidation are briefly reviewed here while a more comprehensive review can be found in [56–58]. This section serves to provide a basic background related to the physical and chemical processes involved in the soot formation and oxidation processes during diesel spray combustion.

Formation of soot, in short, is the conversion of a hydrocarbon fuel molecule into a carbonaceous agglomerate containing millions of carbon atoms. It is a transition from gas phase to solid phase via different physical and chemical processes. The formation of soot is a complex process which still lacks clear understanding of how soot particles and their precursors are formed despite the broad and extensive studies published in the literature [48,57,59,60]. However, there have been a few agreements which are summarised here [60,61]:

i) Formation of soot precursors.
ii) Nucleation of heavy molecules from small molecules to form soot.
iii) Surface growth of soot particles via adsorption of gas phase molecules.
iv) Coagulation via particle-particle collisions.
v) Oxidation of soot particles.

It is important to highlight that oxidation of soot takes place in parallel throughout the whole soot formation process. Therefore, the "net soot formation" is described as the combination of soot formation and oxidation. The five steps in soot formation as mentioned above are briefly discussed in the following sub-sections.

2.3.1 Precursors of Soot Formation

PAHs are important species that act as main building blocks for the transition of gaseous phase to solid phase [57,62,63]. The pyrolysis of fuel gives rise to various so-called "precursor species" that provide the input for PAH species. Several precursor species have been identified. Among them, the most important species are benzene (A_1) and acetylene (C_2H_2) [59,61]. Benzene is crucial to the soot nucleation process as it plays a crucial role in the formation of higher molecular weight PAH. Violi et al. [45] showed that benzene was consumed completely before

the end of oxidation zone which implied that benzene contributes to the start of soot formation. The benzene formation rate was found to positively correlate to the soot formation rate in methane non-premixed flame experiment performed by McEnally et al. [64]. Similar reports from other sources also show that benzene formation is the rate-limiting soot formation step [65,66].

The formation of aromatic ring is followed by its growth into PAH. Acetylene is also an important soot precursor as PAHs grow to form larger PAHs from benzene or other smaller PAHs through the addition of acetylene [59,61]. Frenklach and Wang [67,68] proposed a mechanism known as "H-Abstraction-Carbon-Addition" (HACA), which implies a repetitive reaction of two principal steps: (i) abstraction of a hydrogen atom from the reacting hydrocarbon by gaseous hydrogen atom,

$$A_i + H \leftrightarrow A_{i-} + H_2 \tag{2-1}$$

followed by (ii) addition of a gaseous acetylene molecule to the radical site formed,

$$A_{i-} + C_2H_2 \rightarrow products \tag{2-2}$$

Here A_i is an aromatic molecule with i rings, and A_{i-} is its radical. The key feature of this mechanism is the reversibility of the reaction 2-1. The reverse reaction can be one of the following:

$$A_{i-} + H_2 \leftrightarrow A_i + H \tag{2-3}$$

or

$$A_{i-} + H \leftrightarrow A_i. \tag{2-4}$$

The contribution of reaction 2-3 increases with pressure and molecular size as compared to reaction 2-4. The acetylene addition step (reaction 2-2) determines the total rate of molecular growth. It has been found that this mechanism of PAH growth is the most thermodynamically stable pathway. By repetitive re-activation through hydrogen atom, the PAH molecules grow by acetylene addition and hop from one island of stability to another [69]. Acetylene is not the only species that

can be responsible for the growth of aromatic rings. Several other species are also found to contribute to growth, such as methyl, propargyl, cyclopentadienyl radicals. A good summary of these mechanisms can be found in [69].

It is noteworthy to mention that aromatic oxidation, primarily by O_2 and OH, also occurs in parallel to aromatic growth. However, the PAH oxidation mechanism is still not completely understood. The effect of oxidation at this small-molecular level is two-sided [70]. Oxidation of aromatics removes carbon mass from further growth at earlier stages which precede the PAH formation. However, if added in relatively small quantities in high-temperature pyrolytic environment, oxygen molecules are found to promote the formation of soot by building various radicals, specifically H atoms. This phenomenon is observed in different experimental studies in shock tubes [71], computational analysis [72], and in diffusion flames [73].

2.3.2 Soot Nucleation Process

A general consensus that soot nucleation occurs due to the combination of PAHs that transition to the solid phase [57,62,63]. The transition of gas-phase PAH species to solid particles is probably the least understood part of the soot formation process. Experimental observations of this phenomenon are difficult due to the relatively small diameters of PAH molecules [61]. The molecular mass of nascent soot is approximately 2000 atomic mass unit (amu) [57] with an effective diameter of about 1.5 nm [61]. It is commonly believed that nucleation starts at lower amu around 300-700 [74].

Particle inception can be considered to be a process of physical condensation or a process of chemical (reactive) condensation. The physical condensation suggests that when the supersaturation of macro-molecular precursors generated by gas-phase reactions becomes sufficiently high, the partial pressure of precursors forces the macromolecules to condense physically into liquid-phase soot [75,76]. The homogeneous condensation can be approximated by classical nucleation theory, which gives the number of critical nuclei per unit volume [76,77]. On the other hand, the chemical (reactive) condensation considers the process of continuous

reactions of macro-molecular precursors as the driving mechanism of homogeneous soot particle inception.

Frenklach and Wang [68] studied the reactive coagulation of stable PAH. The coagulation process was assumed to be in free molecular regime and irreversible. When PAH monomers reach a certain size, they begin to stick to one another during collisions and form PAH dimers. These dimers collide with PAH molecules forming trimers, or with other dimers forming tetramers, and so on. Consequently, these PAH clusters slowly change into solid particles as their size increases. Another suggestion is by Howard [78] and D'Anna et al. [79] who emphasised the role of PAH activation by hydrogen abstraction. The active sites formed on the PAH provide a chemical basis for reactive coagulation of PAH with one another or with small radicals. Another model in which chemical specificity of the reactive coagulation process was proposed by D'Anna et al [79]. In the model, the radical-molecule reaction between gas-phase PAH have conjugated double bonds. In these reactions, resonantly stabilised radical intermediates are formed that continue the addition sequence, forming higher mass species.

Besides PAH model hypothesis, polyacetylene or polyynes is a key gaseous precursors to the formation of soot according to the "polyyne model" proposed by Krestinin [80–82]. The model assumes that every radical capable of forming polyyne complexes becomes a center of polymerisation. Following a polyyne molecule and radical or two polyyne molecules react to form the polyyne complex [83]. The polyyne model is applied for soot formation simulation during pyrolysis of C_2H_2 [81]. The model is later extended and applied in soot formation modelling during pyrolysis of different hydrocarbons in reactive flow experiments [81,83].

2.3.3 Soot Particle Surface Growth Process

Surface growth is the process of adding mass to the surface of a nucleated soot particle. The greater part of soot (>95 %) is formed by surface growth rather than soot inception [84]. There is no clear distinction between the end of nucleation and the beginning of surface growth and the two processes are said to be concurrent. After transitioned from PAH molecules into solid soot particles, they can continue

to grow in size due to heterogeneous chemical reactions with gaseous species on the surface of the soot particle. During surface growth, the hot reactive surface of the soot particle readily accepts gas-phase hydrocarbons. This leads to an increase in soot mass, while the number of particles remains constant. Surface growth continues as the particles move away from the primary reaction zone into cooler and less reactive regions, even where hydrocarbon concentrations are below the soot inception limit [57]. It is generally agreed upon that acetylene plays a major role in contributing to soot surface growth, as demonstrated in [62,69,85]. Frenklach et al. [62,67,69] suggested that surface growth via acetylene follows the HACA reaction sequence, where C-H bonds on the surface of soot particles can react with gaseous species. The reactions contained in HACA are analogous to PAH gas phase reactions.

Besides acetylene, PAHs have also been proposed to contribute to surface growth in soot particles, in a mechanism known as PAH condensation [62,86]. Similar to the forming of nascent soot particles from the collision of PAH molecules, PAH molecules can also collide with existing soot particles and condense on the surface. Macadam et al. [86] showed that in acetylene-lean conditions, surface growth via PAH condensation was especially important. However, in acetylene-rich conditions, surface growth via acetylene was dominant.

It was previously stated that surface growth of the soot particles is a heterogeneous process where the surface of the soot particles reacts with the gaseous species when exposed to high temperatures. The reactivity of the soot surface depends on the number of active sites which are available to react with gaseous species [39,69]. It was experimentally observed that the reactivity of surface sites was dependent on particle size [69,87], particle age [57,69,88–90] and temperature [88,91,92]. The reduction of surface reactivity is known as “surface ageing”. Surface ageing can be explained by the HACA mechanism as a reduction in the availability of active sites on the soot particle, a decrease in *H* atom concentration, and/or an arrival at an equilibrium state for *H* atoms in the mixture. The decrease in active sites reduces the kinetic driving force of HACA mechanism while the decrease in *H* atom reduces the surface reactivity of soot particle. This also explains the higher surface growth

rates for small particles than larger particles due to more reactive radical sites [87]. This change in surface reactivity needs to be accounted for in numerical studies. The various forms of "surface ageing" implemented in numerical studies from the literature can be seen in [38,39].

2.3.4 Soot Particle Coagulation and Agglomeration Process

The coagulation and agglomeration process are physical processes. Coagulation, sometimes called coalescence, is the process where two or more particles collide and combine to form a larger particle. Coalescence usually occurs in the collisions of small and newly formed particles, where the two particles collide and merge into a larger spherical particle due to their liquid-like behaviour [93]. Agglomeration is a process that increases the soot particle size through the collision of two or more soot particles. It commonly occurs in the collisions of larger particles, where they stick to one another and form complex fractal-like aggregate structure. Depending on the circumstances of the collision and the particles involved, some intermediary result can occur, where particles partially merge and form "bridge" or "neck" at the particle-particle interface [1]. Recent kinetic molecular dynamics (KMD) performed by Frenklach and co-workers [94] showed that particle aggregation begins at the onset of nucleation itself. It was also demonstrated that surface growth plays an important role in constructing spherical soot particles. However, the surface reactions need to be fast enough to smoothen the colliding particles stuck on the surface of larger particles. A non-spherical mass-fractal-like structure is observed if the colliding particles are too large or the surface reaction is too slow. It is also noteworthy to mention that not all collisions will result in merging or sticking of particles involved as observed by Kellerer et al. [95]. D'Alessio et al. [96] noted that under certain flame temperature conditions, particles might not stick due to a thermal rebound effect. This observation contradicts earlier belief that all collisions had 100% sticking efficiency. Soot particle agglomeration generally affects the total number of soot particles formed with negligible effect on the total mass of soot formed.

2.3.5 Soot Particle Oxidation Process

Soot particle oxidation is the mechanism by which soot particles is oxidised and converted back into gaseous species. Just like surface growth, oxidation is a heterogeneous process that takes place on the particle surface and occurs throughout the entire course of the soot formation [97,98]. It depletes the carbon mass accumulated in the soot particles through the formation of CO and CO_2 [60,99]. Unlike the surface growth of soot, which occurs in a specific step, oxidation happens all the time during and after soot formation. The main oxidation reactants are OH and O_2 [100–103] where OH and O_2 are the dominant species under fuel-rich and fuel-lean conditions, respectively [103]. Oxidation by other species, such as the oxygen radical O has been investigated [103] and gasification of soot via H_2O and NO_2 has been shown to be possible [104]. Some studies have demonstrated that soot oxidation can lead to fragmentation of aggregates into smaller structures [105,106].

2.4 Experimental Study of Soot Formation and Oxidation Processes

For the research of soot formation and oxidation and their interaction with fluid flow field, advanced optical diagnostics and numerical simulations are necessary. Several methods have been employed to measure the soot distribution quantitatively by different research groups. All the techniques have inherent strengths and potential weaknesses and characteristics that can be exploited for selected applications.

The non-invasive, instantaneous and spatially resolved optical measurement techniques based on laser or other additional light sources are commonly used to observe and investigate the process of soot formation and oxidation. In many studies laser light scattering and light extinction measurements have been used to provide information on soot characteristics, including soot concentration and primary particle diameter size [107–111]. Though with the advantage of relatively low cost and ease of application, these methods suffer from various limitations, such as line-of-sight averaging in extinction measurements and interferences of shadows

and scattered light [112], and sensitivity of the detected signal to molecular absorption and fluorescence [113].

Another technique is the two-colour pyrometry, which is widely employed in soot concentration and temperature measurements [114–119]. Although its results are susceptible to soot concentration gradients along the line of sight [120], it is relatively more effective than most planar or extinction techniques to study downstream soot distribution where the soot opacity is high. In addition, the two-colour method can obtain two-dimensional transient soot concentration and temperature simultaneously for soot processes in spray combustion.

Besides that, laser-induced incandescence (LII) and time-resolved laser-induced incandescence (TIRE-LII) are also powerful tools for the quantitative measurement of soot volume fraction and soot particle size [121–127] with high spatial and temporal resolution. These techniques involve heating particles up to typically around 4000 K with a high-power pulsed laser of several nanoseconds duration followed by cooling down until they reach thermal equilibrium with the combustion environment, and analysing the thermal radiation from the hot particles. These techniques have been applied to study soot processes in internal combustion engines [40,126,128–132]. Another way to quantify the measured soot particle size and number density in an optical diesel engine is by using LII and laser induced scattering (LS) techniques simultaneously. This technique, which was proposed by Pinson [133] and Dec [134,135], was recently used to study the effect of ambient oxygen on soot size [40]. Despite being commonly used in soot studies, it is important to note that the optically measured soot size is basically a relative, qualitative and spatially averaged value. Recent study by Cenker et al. [132] showed that LII signal is bias towards larger particles under high pressure condition. The bias towards large particles can lead to the loss of small particle information. This finding is also supported by [128].

To compensate for the lack of small particle information, TEM analysis of soot particles directly sampled in diesel spray flame has emerged to be a powerful and quantitative technique for soot sizing. Particle samples from flames and hot gases

are gathering via thermophoretic sampling. Such in-flame soot sampling is widely used in an open flame burner [108] to provide essential information of soot precursor carbonisation [136–138], particle oxidation [139,140] and extinction coefficient of soot particles [141]. For sampled particles, TEM and scanning electron microscopy (SEM), have been invaluable for characterising aggregate morphologies and sizes and primary particle sizes, e.g. [57,142–148]. At the same time, the TEM image post processing technique has been advanced for boundary detection of soot aggregates, primary particle selection and fractal dimension calculation [24]. The combine use of direct soot sampling technique with TEM imaging have been implemented in reacting diesel jet, under high-pressure and high-temperature ambient conditions for soot study in a constant volume vessel [23,24,40,149–151] and more recently in a diesel engine [22,152]. Various studies have utilised this technique for the examination of soot along different in-flame axial locations [23,150], fuel comparison among conventional diesel, biodiesel and Fischer-Tropsch Diesel (FTD) [24,151], effect of ambient oxygen levels on soot sizing [40], and nanostructure analysis of primary particles [55]. However, a major limitation of this direct soot sampling and TEM analysis as compared to the highly spontaneous optical techniques explained above is the time resolution. Since the TEM grid is constantly exposed to diesel flame, the sampled soot is considered to be a time-integrated mixture of soot particles throughout the injection and combustion duration.

2.5 Modelling of Soot Formation

A successful modelling of soot requires accurate accounting of both formation and oxidation of soot. Furthermore, it is important that the soot models developed and employed are able to give good predictions of soot information, mainly soot volume fraction (SVF) and soot particle size information. SVF is found to affect the combustion characteristics directly as radiative emission is directly proportional to SVF. Moreover, SVF is a quantity that can be obtained relatively easily from experiments. Therefore, this quantity is important in assessing the accuracy of the soot model. The second assessment for a soot model is to capture the size and number of the soot particles accurately. This also includes resolution of the PSDF.

Models of different sophistication levels have been proposed and applied in many practical systems, and can be generally classified into four categories:

(i) Empirical model – It uses correlations of experimental data to predict trends in soot production [153–157]. They are easily implemented and provide excellent correlations for a given set of operating conditions. Furthermore, they are useful for testing previously established designed experiments under specific conditions. However, empirical models have limited applicability to investigate underlying mechanisms of soot productions.

(ii) Semi-empirical model – It solves rate equations that are calibrated using experimental data [153,156,157]. It reduces computational cost primarily by simplifying the chemistry in soot formation and oxidation.

(iii) Detailed model – It contains full panoply of soot phenomena, from the initial pyrolysis of fuel to the inception of soot particles, surface growth, coagulation and oxidation. However, such comprehensive models impose heavy computational cost.

(iv) Phenomenological soot model – Phenomenological models use sub-models developed to describe the different processes (or phenomena) observed during the combustion process. These sub-models can be empirically developed from observation or by using basic physical and chemical relations.

As soot models from each category have been extensively reviewed by Kennedy [158] and Haynes and Wagner [57], only a few soot models from each category are discussed in the following sections.

2.5.1 Empirical Models

Empirical models are usually based solely on direct correlations between operating conditions and the amount of soot that is emitted. In the case where a flow solver is neglected, the empirical soot model for an engine can be solely a function of combustion input parameters, such as engine load or fuel input. They are easily implemented and have lower computational cost. Due to the nature of correlation, empirical models cannot be applied to applications or operating conditions that are significantly different from the baseline from which the model was developed. They

also fail to give any insight on the specifics of soot formation, such as where/when/why soot is formed in a diesel engine. For these reasons, empirical models may not be practical for predictive purposes where engine geometries and operating parameters may change radically from case to case. Despite having this drawback, empirical models can serve as a useful tool in diagnostics systems where a user can obtain real time information on how heavily their engine is sooting based on parameters such as combustion temperatures.

The empirical soot model proposed by Tesner et al. [156] was one of the first soot model that includes a branched-chain process and soot particle formation. Tesner's model implemented an idea that soot is formed as a result of adsorption of radical nuclei on the precursor surface. Meanwhile, another empirical model is developed by Khan et al. [154] for diesel engine applications. In this model, Khan and co-workers assumed that the diameters of soot particles did not vary with respect to operating speeds or loads. They also assumed that the overall formation rate of soot was only dependent on inception, while neglecting soot growth and oxidation. The formation rate of soot is given as:

$$\frac{dM_{soot}}{dt} = cP_u\chi^n \exp\left(-\frac{E}{RT_u}\right) \tag{2-5}$$

where M_{soot} is the soot mass concentration, c and n are model parameters, E is the activation energy of soot formation set to 1.7 x 10^5 kJ/kmol, P_u is the partial pressure of unburned fuel, χ is the local unburned equivalence ratio, and T_u is the local temperature. As model parameters were adjusted to fit the available experimental data, the model performed reasonably well for the given conditions. However, it is expected to perform poorly if the conditions deviate from the base set of calibrated data. This is also partly due to neglecting many fundamental soot formation/oxidation mechanisms.

Another example of empirical soot model is the model developed by Hiroyasu et al. [159]. Hiroyasu and co-workers assumed that soot mass emissions were solely based on pressure, temperature, fuel concentration, and O_2 concentration. They

omitted intermediary soot formation/oxidation mechanisms. The formation rate of soot mass is defined as:

$$\frac{dM_{soot}}{dt} = K_f M_f - K_{ox} M_s \tag{2-6}$$

where K_f is the formation coefficient, K_{ox} is the oxidation coefficient, M_f is the fuel vapour mass. K_f and K_{ox} are subsequently defined as:

$$K_f = A_f P^{0.5} e^{-E_f/RT} \tag{2-7}$$

$$K_{ox} = X_{O_2} A_{ox} P^{1.8} e^{-E_{ox}/RT} \tag{2-8}$$

where A_f and A_{ox}, are model parameters. E_f and E_O are the activation energies, while X_{O_2} is the oxygen mole fraction.

The Hiroyasu soot model in Equation (2-6) is modified in various studies [157,160] by replacing the Arrhenius global oxidation rate equation in Equation (2-8) with the experimentally based oxidation rate of Nagle and Strickland-Constable (NSC) [161,162]. Based on the oxidation experiments of carbon graphite in an O_2 environment over a range of partial pressures, the oxidation rate is modelled by two mechanisms whose rates depend on the surface chemistry involving more reactive "A" sites and less reactive "B" sites and the conversion of "A" sites to "B" sites. The oxidation coefficient K_{ox}, in Equation 2-8, is replaced by the NSC oxidation rate coefficient

$$K_{ox} = \frac{MW_c}{\rho_{soot} d_{soot}} \dot{\omega}_{NSC} \tag{2-9}$$

where $\dot{\omega}_{NSC}$ is the NSC soot mass oxidation rate per unit surface area. The Hiroyasu's model has been very helpful in providing knowledge on the bulk distribution and transport of the soot in the high-temperature combustion environments of conventional diesel engines [163]. Moreover, this model and its modifications are popularly implemented in multi-dimensional diesel combustion simulations [164]. However, this two-step approach of Hiroyasu's model [159] has

oversimplified the diesel soot formation processes. It contains no dependence on the type, composition or structure of fuel. The oxidation expression considers only oxygen molecules in the model [139]. These oversimplifications have led to the underprediction of soot concentration [163]. Therefore, the Hiroyasu's model is regarded to be very practical and simple, but it needs more parameters to be upgraded for further studies [161,162,165].

2.5.2 Semi-empirical Models

Semi-empirical models represent a middle ground between empirical models and detailed models and provide a compromise between computational costs and the ability to model fundamental soot formation/oxidation behaviour. Semi-empirical models reduce computational costs by simplifying the complex soot phenomena and only considering essential soot formation/oxidation mechanisms.

Fairweather et al. [166] developed a model where nucleation of soot particles was solely based on the precursor species acetylene, allowing the use of reduced chemical mechanism without the need to model PAH formation. The model developed by Fairweather and co-workers represents a popular two-equation approach to soot modelling – where one equation is used to compute SVF and another equation for soot number density. These two equations typically resemble the following form:

$$\frac{dM_{soot}}{dt} = A_1 \frac{dM_i}{dt} + A_2 \frac{dM_g}{dt} - A_3 \frac{dM_{ox}}{dt} \tag{2-10}$$

$$\frac{dN_{soot}}{dt} = A_4 \frac{dN_i}{dt} - A_5 \frac{dN_{agg}}{dt} \tag{2-11}$$

M_i, M_g and M_{ox} represent the mass concentration of soot formed/destroyed due to inception, growth, and oxidation, respectively. N_{soot} represents soot number density, while N_i and N_{agg} represent soot number density from inception and agglomeration, respectively. $A_{i=1,2\ldots5}$ represents the specific model constants that are usually calibrated based on the exact mechanisms used to represent the aforementioned soot mechanisms and the application for which the model is used.

This model was applied to a turbulent diffusion natural gas/air flame where chemistry was solved by using a flamelet library. Surface growth was considered to occur via C_2H_2 surface reactions, while oxidation was considered to occur only via O_2. Further simplifications were made by neglecting soot aggregate structure and assuming all soot particles were solid spheres. Finally, it was assumed that surface growth and oxidation rates were linearly related to the surface area of soot particles. Despite these simplifications, the model was able to perform satisfactory. As opposed to empirical model, it can provide some insight to soot formation/oxidation mechanisms and also provide additional soot data, such as soot number density and diameters. The model was later updated by Woolley et al. [167] to include inception via benzene molecules and also an additional oxidation pathway via *OH*.

Another similar semi-empirical, two-equation soot model was developed by Moss et al. [168] where the major difference was in the rate equations used to represent inception, surface growth, oxidation, and agglomeration. Similar to Fairweather et al. [166], Moss and co-workers [168] assumed that surface growth and oxidation were linearly dependent on soot surface area. A flamelet library was again used to solve for combustion chemistry. Unlike the Fairweather et al. [166] model, only *OH* oxidation was considered. The model was able to match experimental data in ethylene laminar diffusion flame [168] and turbulent methane/air jet diffusion flame [169]. However, it is important to note that the parameters of the model in both cases were adjusted to fit the experimental data. The Moss-Brookes soot model [169] was also recently applied to predict soot in an automotive diesel engine simulation conducted by Pang et al. [170]. Pang et al. found that the values for constants in the Moss-Brookes model typically reported in literature could not reproduce satisfactory soot behaviour in the engine. Henceforth, the model constants need to be carefully calibrated to reproduce experimental results.

2.5.3 Detailed Models

On the opposite end of the spectrum is the detailed soot models, which are typically based on fundamental combustion chemistry and make use of aerosol dynamics theory. Detailed models are capable of giving insight into the soot formation process and are also able to provide information on the population size distribution of soot particles. The disadvantage of using detailed soot models is that they tend to be very computationally expensive. Most detailed soot models are limited to simulations with simple geometry (1-D/2-D) and laminar flow conditions.

A commonly cited example of a detailed model is the one developed by Frenklach and Wang [67–69]. It contains the chemical kinetic mechanism that describes everything from the pyrolysis of fuel to the formation of PAHs is an integral component. Further details such as inception via PAH molecules, growth by the HACA mechanism, oxidation, agglomeration, and aggregate structures were also considered in this model. It is important to note that chemical kinetics play a major role in the formation of soot at nearly every phase of soot production (inception, surface growth, and oxidation) [158] and as such, detailed models almost ubiquitously employ some form of a PAH chemical kinetic mechanism. Recent efforts such as those by Dworkin et al. [63] and Chernov et al. [171] have been made in the application of improved PAH chemical mechanisms in detailed soot models.

It should be noted that there are some approaches that saddle between a “detailed model” and a “semi-empirical” model. An example is the work by Lindstedt [172] which employs a detailed chemical mechanism and simplified soot chemistry to model soot formation in ethylene and propane counterflow diffusion flames. Soot nucleation was based on the precursor species of acetylene and benzene, with some focus in the work spent on developing the chemical kinetic mechanism to accurately predict benzene. Oxidation was modelled by considering only O_2 as an oxidative species, using rates developed by Lee et al. [101]. Surface growth via acetylene was considered. Reasonable predictions for both the ethylene and propane flame were obtained in terms of SVF and particle diameters.

2.5.4 Phenomenological Soot Models

As mentioned earlier, soot formation and oxidation are very complex processes to be modelled. The empirical and semi-empirical models simplified the soot formation processes, while the detailed model describes the formation, growth, and oxidation of soot using a detailed chemical reaction mechanism. Motivated by the demand for a soot model which is computationally feasible and accurate to be implemented in diesel engine combustion simulation, Fusco et al. [173] proposed a phenomenological soot model which is able to overcome some limitations of the soot models in diesel engine combustion simulation. A phenomenological model describes the complex process of soot formation and oxidation in terms of several key global steps. The eight-step phenomenological model by Fusco and co-workers [173] accounts for the number of carbon atoms of the major constituent molecules in the fuel and incorporates the physical process of inception, surface growth, coagulation and oxidation. Their model was compared with existing two-step empirical models. Their studies showed the non-applicability of the two-step empirical models for a wide range of operating conditions in diesel engines [173].

Later, Fusco's eight-step phenomenological soot model was modified by Kazakov and Foster [153]. The model included major generic processes involved in soot formation during combustion: formation of soot precursors, soot particle nucleation, coagulation, surface growth, and oxidation. Meanwhile, Liu et al. [174] extended the original Fusco's model [173] to produce a nine-step model as shown in Figure 2-4. The phenomenological soot model covers oxidation of precursor (C_2H_2) and fuel by either O_2 or OH. Moreover, the role of acetylene in inception and surface growth was crucial in Liu's nine-step model [174]. However, it had a fundamental weakness which is unable to express the role of fuel composition and structure whereas each of the acetylene formation rates is reported to be dependent on fuel structure [20].

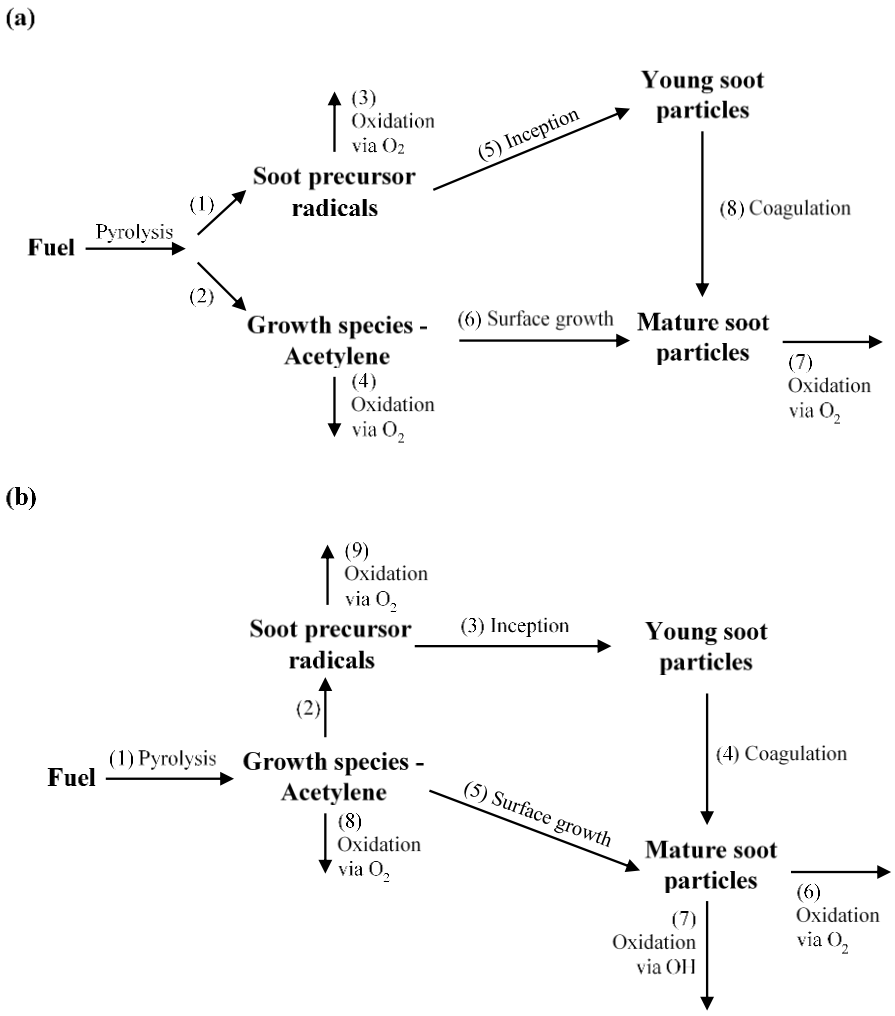

Figure 2- 4: Schematic diagram of soot model processes for (a) Fusco's eight-step [173] **and (b) Liu's nine-step phenomenological soot model** [174]**.**

Another nine-step phenomenological soot model was proposed by Tao et al. [175] based on the original phenomenological model [153,173]. Tao added three major modifications to the original model [153,173]: (1) fuel pyrolysis leads solely to acetylene formation; (2) the soot precursor is formed merely via acetylene (i.e. not directly from fuel); (3) an *OH*-related soot oxidation step is added. The updated nine-step soot model [175] was successfully applied to analyse the soot distribution in a conventional diesel for a benchmark heavy-duty diesel engine.

Jia et al. [176] quantitatively validated and improved the phenomenological soot model by Tao et al. [177] over wide operating conditions of homogeneous charge compression ignition (HCCI) combustion. Later, a six-step phenomenological soot

model with particle dynamics was developed by Pang et al. [178] where the sub-models for soot formation were constructed based on Jia's soot model [176]. The soot formation and oxidation process are divided into several steps including soot precursor formation via C_2H_2, A_3 (aromatic structure with 3 rings) and A_4 conversion, particle inception from soot precursor, particle surface growth by C_2H_2 and A_1, particle coagulation, particle surface oxidation via O_2 and OH, and precursor oxidation. The new model retains the main feature of the original one [176] but with two major modifications as follows:

1. PAHs (A_3, A_4) are used as precursor species.

2. Particle surface growth by A_1 is added in the new soot model.

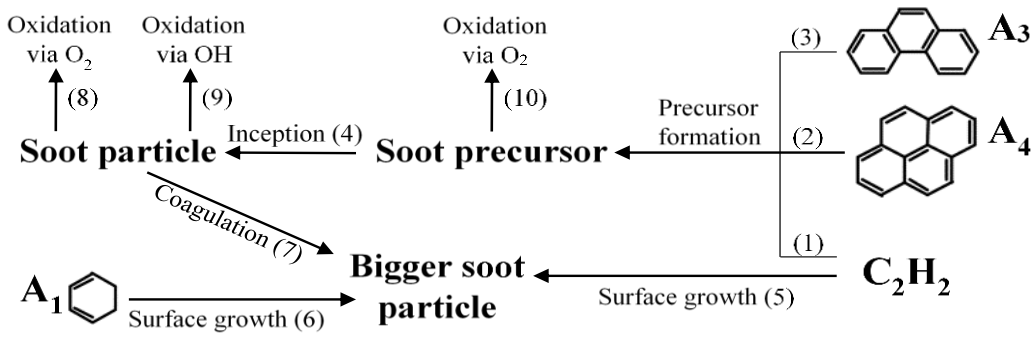

Figure 2- 5: Schematic diagram of soot model processes for Pang's phenomenological soot model [178]**.**

2.5.4 Particle Size Distribution and Soot Aerosol Dynamics

One of the challenges of soot modelling, besides handling the complex soot chemistry, is how to track the size and aggregate structure of every soot particle that is formed. The approach to soot modelling can be said to be split into two parts: the interaction between soot particles and the gas phase species (i.e. soot kinetics detailed in the above sections) and the interaction between soot particles (i.e. soot aerosol dynamics) [179].

The simplest way to calculate soot particle size is by direct implementation of semi-empirical, two equation soot model without tracking the soot particle distribution [166]. With this method, all the soot particles are assumed to be spherical with

identical diameter within a control volume (i.e. mono-dispersed spherical particle). The predicted soot particle size distribution via the semi-empirical soot model is estimated on a cell-by-cell basis where the characteristic diameter of the particles $d_{soot,j}$ in the computational cell j, is computed based on the associated soot mass concentration, M_{soot} and soot particle number density, N_{soot} using,

$$d_{soot,j} = \left(\frac{6M_{soot,j}}{\pi \rho_{soot} N_{soot,j}} \right)^{1/3} \quad (2\text{-}12)$$

where ρ_{soot} is the soot density. Although this approach is computational effective, the mono-disperse assumption can lead to inaccuracy in predicting available soot surface area for soot kinetic calculation. This eventually leads to inaccurate soot sizing prediction [180].

There are currently a few methods that are more promising at modelling the soot particle dynamics. One approach is by using MOM [29], in which the evolution equations for moments of the population distribution are solved instead of explicitly solving the population distribution [181]. A moment can be thought of as a measure of varying aspects in a distribution depending on the order of the moment. This implies that the knowledge of all moments from 0 to ∞ can fully describe the distribution function itself [29]. However, using an infinity of moments is practically impossible. Hence, it has been noted that 3-6 moments are generally sufficient for an accurate soot calculation [179]. Its computational efficiency enables it to be applicable in complex problems such as soot formation in diesel spray [33,182–184] and diesel engine conditions [185].

Another approach which is easy to implement and provides detail particle size distribution is DSM [34–36]. In this method, the population of soot particles is discretised into discrete sections or “bins” and the evolution equations are solved for each of these bins. A good accuracy is achieved when an adequate number of sections is used to represent the particle size distribution. However, it is computationally expensive as the shape of soot particles is described by more than one size property [186]. The implementation of this method in diesel spray flame studies can be seen in [187–189].

Alternatively, the stochastic approach, in which the population of particles is determined by using a stochastic algorithm such as the Monte-Carlo method is also applied for soot dynamics study. The Monte-Carlo stochastic approach [30,31,37] tracks a statistically significant number of soot particles individually and has the potential to provide a detailed representation of PSDF. The process contributing to formation and oxidation of soot particles are treated in a probabilistic manner. It has the following benefits compared to other methods which solves population balance equations: (1) known to converge to exact solution of the population balance equation [190], (2) whole size distribution is resolved, and (3) an expansion of more detailed physical models is straightforward. The method has been used to predict PSDF including data on particle age which allows the numerical study of correlation between some soot modelling parameter and soot aging [31,38,39]. This approach also permit the modelling of molecular structures of soot precursors or particles [191,192]. It has also been implemented in diesel spray flame applications [193–195]. However, due to the nature of the model, it is computationally expensive and is often limited to post-processing of data than being fully integrated with the flow solver [28,196,197].

MOM and DSM have been implemented to study the evolution of primary soot size. However, both MOM and DSM can only provide the mean information of the primary soot size distribution with the latter approach being able to give more information, including number of primary soot size per aggregate. Furthermore, both MOM and DSM do not provide information about the history of soot particles. On other hand, Monte-Carlo stochastic method is able to overcome their shortcomings by providing detailed information on primary soot size and access to the history of soot particles. Despite having higher capabilities, its relatively higher computational cost limits its applicability. In line to address this challenges, an alternative method that can give good prediction of primary soot size while being computationally feasible is desired. A summary of the advantages and disadvantages of soot models is presented in Table 2-1. Examples of numerical studies on diesel combustion application are also listed in Table 2-1.

Table 2- 1: Advantages and shortcomings of models on predicting soot particle size.

	MOM	DSM	Stochastic
Advantages	- Computationally feasible	- No assumption needed for PSDF	- Accurate in predicting PSDF
Disadvantages	- Assumed PSDF	- High computational cost if more sections are used - Commonly for laboratory flame study	- No feedback to flow-field - Computationally expensive - Commonly for laboratory flame study
Accessible soot information	- Mean primary soot size distribution	- Mean primary soot size distribution - Number of primary soot particles per aggregate	- Primary soot size distribution - Number density of primary soot size - Number density of aggregate size - Soot history
Example cases	[33,182–185]	[187–189]	[193–195]

2.6 Soot Particle Tracking

Monitoring the history of individual soot particles is nonetheless essential. Such information is expected to provide a better understanding of the formation, growth, and oxidation of soot particles since the morphology of soot is shown to be dependent on fuel type or composition [151,198–200] and operating conditions [40,201–206]. The soot distribution observed in the flame are due to the cumulative effect of all the individual soot particles interacting with one another and their surrounding environment (e.g. ambient conditions and gas-phase compositions) within the flame. Despite being able to provide good prediction of PSDF, both MOM and DSM do not provide information about the history of soot particles. On the other hand, the Monte-Carlo stochastic approach is able to provide a detailed representation of PSDF and also track the history of particles. However, it is computationally expensive and has limited applicability in complex simulation.

Alternatively, a simpler way to analyse the history and access individual information of soot particles is by employing the Lagrangian soot tracking (LST) method, which treats soot particles as fictitious Lagrangian particles and tracks them individually.

LST has been used to investigate soot transport [207–214] in various combustion applications and non-combustion applications. Katta et al. [209] performed a computational study of an ethylene-air inverse diffusion flame and found that soot particles closely follow the gas flow. In their study, fictitious soot particles of 20 nm were released into the domain along the 1200 K contour line with the assumption that soot inception occurs at 1200 K. A similar study was carried by Fuentes et al. [210] who tracked the history of soot particles, with a size of 50 nm, from nucleation to oxidation along their simulated trajectories in non-bouyant laminar diffusion flame. It is worth mentioning that both works by Katta et al. [209] and Fuentes et al. [210] did not include surface growth and oxidation effect on their fictitious soot particles. Later on, Katta and co-workers improved their soot tracking model to consider the effect of soot oxidation by introducing a soot burnout model, which will delete the ficitious soot particles when the particles enter temperature regions above 1300 K [215] or 1400 K [214]. Despite having incorporated a soot oxidation model, the tracking of constant size particles only allows the investigation of the history of soot particles and the migration of soot particles inside the flame as soot surface growth effect is still neglected. A recent study has been carried out by Mahmood et al. [207,208] who developed a LST model using tri-linear interpolation technique to predict the soot particle trajectories and also soot particle size evolution along the path in diesel engine application. Soot trajectories were traced from selected starting points in the engine cylinder based on soot concentration distribution from CFD simulation. A fourth-order Runge-Kutta and an interpolation technique were applied based on the obtained particle velocity vector data through a MATLAB routine to track the soot pathlines inside the engine cylinder. The soot evolution due surface growth and oxidation were associated with the use of Hiroyasu's soot formation model and Nagle and Strickland-Constable (NSC) soot oxidation model. However, the Hiroyasu's soot formation model is not

comprehensive to govern the size change of soot particles as it is empirically developed to only govern the formation of soot but not specifically for soot surface growth. Therefore, there is a need to implement a more comprehensive soot model with different sub-models for each important soot formation process. Furthermore, it is important to note that the soot particles were tracked from starting locations based on the soot mass concentration but not the soot inception mass concentration. This makes it difficult to differentiate the movement between newly formed soot and old mature soot. Thus, it is more desirable to trace the soot particles from its point of inception till its oxidation to distinctively investigate their movements and interactions with the surrounding. Besides combustion applications, Lagrangian particle tracking has also been used in other applications, such as tracking soot particles in diesel particulate filters [211,212] and predicting aerosol deposition in curved pipes [213].

2.7 Chemical Kinetics and Constant Volume Diesel Spray Combustion

2.7.1 *n*-Heptane and *n*-Dodecane Kinetics

The prediction capability of a soot model highly depends on the fuel chemistry mechanism. Among all the single-component surrogate diesel fuels, much of the development has been centered on *n*-heptane. The cetane number of *n*-heptane is approximately 55, which is close to typical European and Japanese diesel fuels [216]. The primary benefit of using *n*-heptane as a diesel surrogate is that the detailed kinetics for *n*-heptane oxidation for low, intermediate and high temperatures have been explored widely [217]. Reduced kinetic models with a relatively small number of species and reactions are available, which make *n*-heptane a relatively easy choice for CFD computations. A comprehensive review of simulation activities using a variety of established reduced mechanisms are presented in [218,219]. Lately, much of the research effort on surrogate diesel fuel has been directed to the development of chemical kinetics of *n*-dodecane. Its carbon number (12) is in the typical diesel range (10–22) compared to *n*-heptane, and its cetane number is close to those of diesel and *n*-heptane. Carbon content is an important parameter that determines the properties of the fuel. Therefore, *n*-dodecane may be more suitable as a diesel surrogate fuel. Finally, the reasonable

size of the molecule simplifies modelling complexity when compared to even larger long chain alkanes, such as $C_{14}H_{30}$ and $C_{16}H_{34}$. A summary of reactive *n*-dodecane spray numerical cases are presented in [219].

2.7.2 Engine Combustion Network

To bridge the gap in modelling between the canonical laboratory-scale flames and practical diesel engines, a reliable experimental database is required for well-characterised turbulent spray flames under diesel-engine-like conditions. However, practical engine configurations are too complicated for this purpose, in addition to complex fuel injector designs and complicated geometric shapes. The experimental rig in Sandia National Laboratory, by the ECN, is able to resolve this issue. The experimental configuration is a constant volume cubical combustion chamber that can reach the desired thermo-chemical conditions representative of diesel combustion, without incorporating the geometric complexities of a real piston engine.

ECN is an open forum for international collaboration between experimental and modelling groups. The ECN provides experimental measurements for turbulent spray flames at high pressure, diesel-engine-like conditions. The database includes data for non-reacting and reacting sprays, operating under diesel-engine-like conditions. Soot measurements are also provided for different fuel compositions, such as *n*-heptane and *n*-dodecane fuel. The valuable experimental data in ECN serves to validate the chemistry mechanism and soot model in numerical studies. A summary of soot-related numerical simulations using *n*-heptane and *n*-dodecane fuel in diesel spray flame study are presented in Table 2-2 and Table 2-3, respectively.

Table 2- 2: Summary of soot modelling studies using *n*-heptane fuel.

Authors	Chemical mechanism type (Species / Reactions) [Ref.]	Soot model [Ref.]	Soot precursor	Key findings
Bolla M. et al. [230,231]	Reduced *n*-heptane (22 / 18) [223]	Semi-empirical [220]	C_2H_2	Omitting TCI leads to higher oxidation rates and affects quasi-steady soot distribution.
d'Errico G. et al. [232]	Reduced *n*-heptane (32 / 70) [224]	Semi-empirical [168]	C_2H_2	The results of PSR + ISAT agreed with experimental results.
Fu X. et al. [225]	Reduced *n*-heptane (207 / 4094) [225]	Empirical [157]	C_2H_2	1-heptane flame had higher formation of PAH and soot emission than n-heptane flame.
Jia M. et al. [176]	Reduced *n*-heptane (29 / 52) [224]	Phenomenological [176]	C_2H_2	Validated and improved a phenomenological soot model developed by Tao et al. [177]
Pang K.M. et al. [233]	Reduced *n*-heptane + PAH (86 / 311) [226]	Semi-empirical [220]	A_4	An optimised soot model was proposed which could capture accurate quasi-steady soot distribution under varying oxygen (10%-21%) and density (14.8 & 30.0 kg/m^3).
Pang K.M. et al. [234]	Reduced *n*-heptane (68 / 283) [226]	Semi-empirical [220]	C_2H_2, A_1, A_4	Soot precursor and particle distribution prediction was found to be improved with the use of A4 as soot precursor.
Som S. et al. [235]	Reduced *n*-heptane (68 / 283) [227]	Empirical [100,157]	C_2H_2	The instantaneous structure was better captured by the LES model than the RANS model.
Sukumaran et al. [221]	Reduced *n*-heptane + PAH (68 / 145) [224]	Semi-empirical [221]	A_4	A multistep soot model was derived and coupled with a detailed PAH mechanism to simulate soot formation and oxidation processes in diesel sprays.
Vishwanathan G. et al. [228]	Reduced *n*-heptane + PAH (56 / 108) [228]	Empirical [100,157]	C_2H_2, A_1, A_2, A_3, A_4	The use of A_3 as soot precursor had good possibility for better soot location predictions.
Wang H. et al. [229]	Reduced *n*-heptane + PAH + Toluene (71 / 360) [229]	Phenomenological [222]	A_4	A reduced mechanism was developed to model emissions for both nonoxygenated and oxygenated hydrocarbon fuels. It was shown that soot emission can be greatly reduced by addition of n-butanol.

TCI: Turbulence-chemistry Interaction; PSR: Perfectly stirred reactor; ISAT: In-situ adaptive tabulation; LES: Large Eddy Simulation; RANS: Reynolds-averaged Navier-Stokes; C_2H_2: Acetylene; A_1: Benzene; A_2: Naphthalene; A_3: Phenanthrene; A_4: Pyrene

Table 2- 3: Summary of soot modelling studies using *n*-dodecane fuel.

Authors	Chemical mechanism type (Species / Reactions) [Ref.]	Soot model [Ref.]	Soot precursor	Key findings
Gong C. et al. [239]	Reduced *n*-dodecane (103 / 370) [237]	Empirical [236]	C_2H_2	LES n-dodecane spray combustion was studied. Ambient temperature was shown to be able to both increase and decrease soot emission.
Pandurangi S. et al. [240]	Reduced *n*-dodecane (106 / 420) [237]	Semi-empirical [220]	C_2H_2	Soot onset in n-dodecane sprays was investigated both experimentally and numerically. Soot onset occurred at a lower local temperature for lower ambient O_2, but was reversed for variations in ambient temperature.
Pei Y. et al. [241]	Reduced *n*-dodecane (103 / 370) [237]	Empirical [157]	C_2H_2	An n-dodecane spray flame was simulated using a dynamic structure LES model + detailed chemistry. The highest realisation of 14 was required to achieve 99% similarity for temperature, soot and OH mass fraction. More realizations are needed for the magnitude-similarity index for the similar level of similarity as the structure-similarity index.
Wang H. et al. [238]	Reduced *n*-dodecane + PAH (100 / 432) [238]	Phenomenological [222]	A_4	A reduced n-dodecane-PAH mechanism is presented for modelling combustion and soot formation processes of n-dodecane spray flame.

LES: Large Eddy Simulation; C_2H_2: Acetylene; A_4: Pyrene

2.8 Concluding Remarks

Based on the literature review on soot formation and oxidation processes, it is shown that the soot processes are complex phenomena that still lack complete understanding. With increasing interest in modelling soot particle size, it is vital that the soot models developed and employed can provide good predictions of both soot concentration and particle size distribution. Besides having good predictions in SVF and soot sizing, the history of individual soot particles is expected to be an essential information which may provide a better understanding of the formation, growth, and oxidation of soot particles. Furthermore, the available modelling approaches are either too computationally expensive or can only provide limited soot information. Set against this background, an alternative modelling approach is desired which can store and access the soot particle history while having good prediction of SVF and soot sizing distributions.

CHAPTER 3
GOVERNING EQUATIONS

3.1 Background

Fluid dynamic systems such as liquid sprays are described by the Navier-Stokes equations, which include conservation laws of mass, energy and momentum in continuous flows. The Navier-Stokes equations must be coupled with a set of models to describe small-scale processes within the gas and disperse phases. This chapter gives a brief overview on the fundamentals of fluid dynamics and related numerical models. Besides this introduction, this chapter is further divided into five other sections. The Navier-Stokes equations for simulating reacting compressible turbulent fluid flow are introduced in Section 3.2. This is followed by the introduction of the concepts of Reynolds- and Favre-averaging and their differences. The governing equations for reacting turbulent compressible fluids obtained after applying the Favre-averaging to Navier-Stokes equations are presented. In the Section 3.4 the governing equations for liquid spray including the chemical species transport, spray breakup model and drag model for the liquid spray droplets are stated. The bridging between reacting turbulent fluid flow equations and liquid spray equations are presented in Section 3.5. Subsequently, Section 3.6 describes the Eulerian soot model implemented in this work to study the soot formation and oxidation. Lastly, the key numerical models used in this work are summarised.

3.2 Modelling of Reacting Compressible Turbulent Fluid Flow

3.2.1 Continuity Equation

The continuity equation governs the conservation of mass, which means the rate of change of mass in an arbitrary control volume must be equal to the total mass flow over the control boundaries. The continuity equation is given by [242]

$$\frac{\partial \rho}{\partial t} + \nabla \cdot (\rho \mathbf{u}) = 0 \tag{3-1}$$

where ρ denotes the fluid density and $\mathbf{u}$ is the velocity vector field. On the left-hand side (LHS) of Equation 3-1, the first term describes the rate of increase of the mass per control volume, and the second term represents the rate of mass flux passing in-out of the control surface per unit volume [242].

3.2.2 Momentum Equation

To completely describe the velocity vector field, momentum conservation must be enforced by a set of momentum equations, one for each velocity components. The momentum equation governs the conservation of linear and angular momentum. According to the Newton's second law, the rate of change of momentum on a fluid parcel equals to the sum of forces acting on that parcel. The conservation of momentum [242] is given by

$$\frac{\partial (\rho \mathbf{u})}{\partial t} + \nabla \cdot (\rho \mathbf{u}\mathbf{u}) = \rho \mathbf{g} - \nabla P + \nabla \cdot \boldsymbol{\tau}_{\mathbf{s}} \tag{3-2}$$

In Equation 3-2, P denotes the pressure, $\mathbf{g}$ represents the body force and $\boldsymbol{\tau}_{\mathbf{s}}$ denotes the stress tensor, which is given as:

$$\boldsymbol{\tau}_{\boldsymbol{s}} = -\frac{2}{3}\mu(\nabla \cdot \mathbf{u})\mathbf{I} + \mu[\nabla \mathbf{u} + (\nabla \mathbf{u})^T] \tag{3-3}$$

where μ represents the coefficient of viscosity and $\mathbf{I}$ is an identity matrix. The LHS of Equation 3-2 is a time derivative term plus a convective term. The first term on the left describes the rate of change of momentum per unit control volume, while the second term represents the rate of momentum lost through the surface of the control volume. As for the right-hand side (RHS) of Equation 3-2, the first term is the body force per unit volume while the second term represents the pressure gradient.

3.2.3 Species Transport Equation

The transport equation of the mass fraction for each species j in a mixture of N species is given as

$$\frac{\partial(\rho Y_j)}{\partial t} + \nabla \cdot (\rho Y_j \mathbf{u}) = \nabla \cdot \mathbf{L}_j + \kappa \dot{\mathbf{RR}}_j \tag{3-4}$$

where $j = 1,2,3,\cdots,N$. The term $\mathbf{L}$ in Equation 3-4 is the diffusive flux of species j which arises due to concentration gradients. The mass fraction of j-th species is given as $Y_j = m_j/m$, while $\dot{\mathbf{RR}}_j$ is denoted as the reaction rate of species j and κ is the chemical reaction rate multiplier.

The molecular transport processes that cause the diffusive fluxes are quite complicated. Since molecular transport is less important than turbulent transport in turbulent combustion, the most elementary diffusive flux is assumed which is the binary flux approximation [243]

$$\mathbf{L}_j = -\rho D_j \nabla Y_j \tag{3-5}$$

where D_j is the binary diffusion coefficient or mass diffusivity of species j. For simplicity, it is assumed that all mass diffusivities of j-th species D_j are equal to the thermal diffusivity D expressed by

$$D = \lambda/\rho C_p \tag{3-6}$$

In Equation 3-6, λ is the thermal conductivity and C_p is the heat capacity at constant pressure of the mixture. Therefore, the species transport in Equation 3-4 can be simplified to become

$$\frac{\partial(\rho Y_j)}{\partial t} + \nabla \cdot (\rho Y_j \mathbf{u}) = -\nabla \cdot \left(\frac{\mu}{Sc} \nabla Y_j\right) + \kappa \dot{\mathbf{RR}}_j \tag{3-7}$$

where Schmidt number, $Sc = \mu/\rho D$ and is assumed to be unity [244]. This means that the effective species diffusivity is equal to the molecular viscosity. The molecular viscosity μ is calculated based on Sutherland's law [245].

3.2.4 Energy Equation

The heat release during combustion can be represented in different forms for obtaining the governing energy transport equation. The conservation of energy follows the first law of thermodynamics. Applying it to a fluid passing through an infinitesimal fixed control volume, the energy equation in terms of total enthalpy h_o is given as [246,247]

$$\frac{\partial(\rho h_o)}{\partial t} + \nabla \cdot (\rho h_o \mathbf{u}) = -\nabla \cdot \dot{\mathbf{q}} + \frac{\partial P}{\partial t} + \nabla \cdot (\boldsymbol{\tau}_s \cdot \mathbf{u}) + \dot{\mathbf{q}}_{\mathbf{source}} \quad (3\text{-}8)$$

where $\dot{\mathbf{q}}_{\mathbf{source}}$ is a term for the combination of all heat sources such as radiative flux and $\nabla \cdot (\boldsymbol{\tau}_{\mathbf{s}} \cdot \mathbf{u})$ is the irreversible rate of enthalpy due to viscous dissipation. The term $\frac{\partial P}{\partial t}$ is the reversible rate of enthalpy due to compression. The term $\dot{\mathbf{q}}$ is the heat flux due to of heat conduction and enthalpy diffusion:

$$\dot{\mathbf{q}} = -\lambda \nabla T - \sum_{j=1}^{N} h_j \mathbf{L}_j \quad (3\text{-}9)$$

where T is the gas temperature and h_j is the specific enthalpy of species j.

The total enthalpy, h_o can be expressed in terms of sensible enthalpy, h_s and chemical enthalpy, h_c [248] as given to be

$$h_o = h_s + h_c = \int_{T_{ref}}^{T} C_p(T)\, dT + \sum_{j=1}^{N} \Delta h_{f,j}^0 Y_j \quad (3\text{-}10)$$

where $\Delta h_{f,j}^0$ is the enthalpy of formation of species j at standard temperature (T_{ref}) and pressure (P^0). The heat capacity, $C_p(T)$ in Equation 3-10 is the mixture averaged heat capacity, which is expressed as

$$C_p(T) = \sum_{j=1}^{N} c_{p,j}(T) Y_j \quad (3\text{-}11)$$

The temperature dependencies of the pure species specific heat capacities $c_{p,j}$ are fitted by 4-th order NASA polynomials:

$$\frac{c_{p,j}(T) MW_j}{R} = a_{1,j} + a_{2,j} T + a_{3,j} T^2 + a_{4,j} T^3 + a_{5,j} T^4 \quad (3\text{-}12)$$

Here, $a_{n,j}$ are coefficients of the j-th species which has to be given as input. MW_j is the molar weight of species j, while R is the universal gas constant.

By assuming binary flux approximation and neglecting the effects of viscous dissipation and other heat sources such as radiation, the conservation of energy in Equation 3-8 can be simplified and rewritten in terms of sensible enthalpy,

$$\frac{\partial(\rho h_s)}{\partial t} + \nabla \cdot (\rho h_s \mathbf{u}) = \nabla \cdot \left(\frac{\mu}{Pr} \nabla h_s\right) + \frac{\partial P}{\partial t} + \dot{q}_{reaction} + \nabla \cdot \left\{ \left(\frac{\mu}{Sc} - \frac{\mu}{Pr}\right) \left[\sum_{j=1}^{N} \left(h_j \nabla Y_j - \Delta h_{f,j}^0 \nabla Y_j\right) \right] \right\} \quad (3\text{-}13)$$

where the heat of reaction is given by

$$\dot{q}_{reaction} = -\sum_{k=1}^{N} \Delta h_{f,\mathrm{k}}^0 \left(\kappa \dot{\mathbf{R}}\mathbf{R}_j\right) \quad (3\text{-}14)$$

which can be used as a definition for the heat release rate (HRR). In the sensible enthalpy equation, the Prandtl number Pr is defined as

$$Pr = \frac{\mu C_p}{\lambda} \quad (3\text{-}15)$$

The Lewis number for species j is defined as

$$Le_j = \frac{\lambda}{\rho D_j C_p} = \frac{Sc_j}{Pr} \quad (3\text{-}16)$$

Under the assumption of single diffusion coefficient, i.e. $D_j = D$ and constant Lewis number of unity, the sensible enthalpy equation simplifies to

$$\frac{\partial(\rho h_s)}{\partial t} + \nabla \cdot (\rho h_s \mathbf{u}) = \nabla \cdot \left(\frac{\mu}{Pr} \nabla h_s\right) + \frac{\partial P}{\partial t} + \dot{q}_{reaction} \quad (3\text{-}17)$$

To obtain the temperature from the sensible enthalpy, the definition of the sensible enthalpy (Equation 3-17) is solved for T by using the following equations.

$$T = \frac{h_s - Y_f h_{fuel}}{\overline{C_p}} \quad (3\text{-}18)$$

$$\overline{C_p} = \frac{1}{T - T_{ref}} \int_{T_{ref}}^{T} C_p dT \quad (3\text{-}19)$$

where h_{fuel} is the enthalpy of combustion of fuel.

3.3 Favre-Averaging of Navier-Stokes (FANS) Equations

In the last section, the instantaneous governing equations for reacting flows are described. However, since only the mean characteristics of the flow are of interest, the average of instantaneous equations governing reacting flows is computed to deduce the mean flow characteristics. An instantaneous flow variable $\phi(\mathbf{x}, t)$ can be decomposed to a time-averaged part $\phi_a(\mathbf{x}, t)$ and the fluctuation part $\phi_f(\mathbf{x}, t)$,

$$\phi(\mathbf{x}, t) = \phi_a(\mathbf{x}, t) + \phi_f(\mathbf{x}, t) \tag{3-20}$$

There are two ways to track these averaging components. One way of averaging is by using the standard Reynolds averaging method, which is used to derive the Reynolds-Averaged Navier-Stokes (RANS) equations [249]. Another way is the mass-weighted or Favre averaging technique employed with turbulent compressible flows, which leads to the Favre-Averaged Navier-Stokes (FANS) equations [250].

3.3.1 Reynolds Time-Averaging

Reynolds time-averaging is introduced in 1985 by Reynolds to solve the turbulent flows [248]. Let ϕ represents the instantaneous value of any of the flow variables involved (e.g. u, P, h_s, T, ρ, etc.) at time t and position $\mathbf{x}$. It is decomposed into a mean value component $\overline{\phi}(\mathbf{x}, t)$ and a fluctuating component $\phi'(\mathbf{x}, t)$, such that

$$\phi(\mathbf{x}, t) = \overline{\phi}(\mathbf{x}, t) + \phi'(\mathbf{x}, t) \tag{3-21}$$

Considering the turbulent flow as statistically stationary flow, the Reynolds time average of the flow variable $\phi(\mathbf{x}, t)$ over a time interval τ is defined by

$$\overline{\phi}(\mathbf{x}, t) = \frac{1}{\tau}\int_{t}^{t+\tau} \phi(\mathbf{x}, t)\, dt \tag{3-22}$$

Reynolds-averaging satisfies the following properties, for any two instantaneous flow variables ϕ, φ and other independent variables,

$$\begin{gathered}\overline{\bar{\phi}\varphi} = \overline{\phi\varphi}, \\ \overline{\phi'} = 0, \\ \bar{\bar{\phi}} = \bar{\phi}, \\ \overline{\phi + \varphi} = \bar{\phi} + \bar{\varphi}, \\ \overline{\frac{\partial\phi}{\partial t}} = \frac{\partial\bar{\phi}}{\partial t}\end{gathered} \tag{3-23}$$

3.3.2 Favre Time-Averaging

For compressible flows, the density is not constant due to turbulence [251]. It is demonstrated that the presence of density fluctuations give rise to additional terms when Reynolds-averaging is used [251]. The additional terms arise from correlations between velocity and density fluctuations in a reacting flow and have to be modelled. Therefore, a weighted averaging procedure known as Favre-averaging is used in order to reduce the number of terms which required additional modelling.

In Favre-averaging the density-weighted mean flow variables is defined as $\tilde{\phi}(\mathbf{x}, t)$. The instantaneous flow variables, $\phi(\mathbf{x}, t)$ is written as

$$\phi(\mathbf{x}, t) = \tilde{\phi}(\mathbf{x}, t) + \phi''(\mathbf{x}, t) \tag{3-24}$$

In contrast to the Reynolds decomposition, where $\phi'(\mathbf{x}, t)$ represents the turbulent fluctuation term, the quantity $\phi''(\mathbf{x}, t)$ includes the effects of density fluctuations. The Favre time-averaging of the flow variable $\phi(\mathbf{x}, t)$ over a time interval τ is defined as

$$\tilde{\phi}(\mathbf{x}, t) = \frac{\int_t^{t+\tau} \rho(\mathbf{x}, t)\phi(\mathbf{x}, t)\, dt}{\int_t^{t+\tau} \rho(\mathbf{x}, t)\, dt} \tag{3-25}$$

The Favre-averaging and Reynolds-averaging have the following relationship:

$$\begin{gathered}\overline{\phi\varphi} = \overline{\phi\tilde{\varphi}} = \bar{\phi}\tilde{\varphi}, \\ \overline{\phi"} \neq 0, \\ \overline{\rho\phi"} = 0, \\ \tilde{\phi} = \bar{\phi} + \frac{\overline{\rho'\phi'}}{\bar{\rho}}\end{gathered} \tag{3-26}$$

3.3.3 Favre-averaged Navier-Stokes Equation

Using the Favre-averaging method, the averaged Navier-Stokes equations and species transport equation become [244,248]:

$$\frac{\partial\bar{\rho}}{\partial t} + \nabla\cdot(\bar{\rho}\tilde{\mathbf{u}}) = 0 \tag{3-27}$$

$$\frac{\partial(\bar{\rho}\tilde{\mathbf{u}})}{\partial t} + \nabla\cdot(\bar{\rho}\tilde{\mathbf{u}}\tilde{\mathbf{u}}) = \bar{\rho}\mathbf{g} - \nabla\bar{P} + \nabla\cdot\left(\bar{\boldsymbol{\tau}}_s - \bar{\rho}\overline{\mathbf{u}"\mathbf{u}"}\right) \tag{3-28}$$

$$\frac{\partial\left(\bar{\rho}\widetilde{Y_J}\right)}{\partial t} + \nabla\cdot\left(\bar{\rho}\widetilde{Y_J}\tilde{\mathbf{u}}\right) = -\nabla\cdot\left(\mu\nabla\widetilde{Y_J} - \bar{\rho}\overline{Y"\mathbf{u}"}\right) + \kappa\overline{\dot{\mathbf{R}}\mathbf{R}_J} \tag{3-29}$$

$$\frac{\partial\left(\bar{\rho}\widetilde{h_s}\right)}{\partial t} + \nabla\cdot\left(\bar{\rho}\widetilde{h_s}\tilde{\mathbf{u}}\right) = \nabla\cdot\left(\frac{\mu}{Pr}\nabla\widetilde{h_s} - \bar{\rho}\overline{h_s"\mathbf{u}"}\right) + \frac{\partial\bar{P}}{\partial t} + \bar{\dot{q}}_{reaction} \tag{3-30}$$

In Equation 3-29 and 3-30, $\bar{\rho}\overline{Y"\mathbf{u}"}$ and $\bar{\rho}\overline{h_s"\mathbf{u}"}$ are closed using the classical gradient assumption,

$$\bar{\rho}\overline{Y"\mathbf{u}"} = -\frac{\mu_t}{Sc_t}\nabla\widetilde{Y_J} \qquad\qquad \bar{\rho}\overline{h_s"\mathbf{u}"} = -\frac{\mu_t}{Pr_t}\nabla\widetilde{h_s} \tag{3-31}$$

The new variable, Reynolds stress tensor $\bar{\rho}\overline{\mathbf{u}"\mathbf{u}"}$, is defined as

$$-\bar{\rho}\overline{\mathbf{u}"\mathbf{u}"} = -\bar{\rho}\begin{bmatrix}\overline{u_1''u_1''} & \overline{u_1''u_2''} & \overline{u_1''u_3''} \\ \overline{u_2''u_1''} & \overline{u_2''u_2''} & \overline{u_2''u_3''} \\ \overline{u_3''u_1''} & \overline{u_3''u_2''} & \overline{u_3''u_3''}\end{bmatrix} = \boldsymbol{\tau}_s^R \tag{3-32}$$

where the subscripts 1, 2, and 3 denote the three axial directions. By including the turbulent fluctuations and Reynolds stress tensors, there are more unknowns than number of equations to solve them. This is referred to as the closure problem of turbulence [242].

3.3.4 Solving Closure Problem using Standard $k-\epsilon$ Turbulence Model

By the above discussion, the Reynolds or Favre time-averaging of Navier-Stokes equations yield the Reynolds stress tensor. The Reynolds stress tensors are associated with the turbulent motions. To balance the number of unknowns and the number of equations, further assumptions and approximations about the new quantities are needed for the "closure" of the system.

According to Boussinesq's assumptions, the Reynolds stress tensor is assumed to be linearly related to the mean flow straining field as follows

$$\boldsymbol{\tau}_s^R = 2\mu_t \mathbf{G} - \frac{2}{3}\bar{\rho}\tilde{k} \tag{3-33}$$

where the mean strain rate, $\mathbf{G}$ is defined by

$$\mathbf{G} = \frac{1}{2}[\nabla\tilde{\mathbf{u}} + (\nabla\tilde{\mathbf{u}})^T] - \frac{1}{3}(\nabla\cdot\tilde{\mathbf{u}})\mathbf{I} \tag{3-34}$$

Numerous number of approaches have been developed to close the problem of turbulence. The first turbulence model based on k and ϵ was originally presented in [252]. The model is built on the concept of a turbulent eddy viscosity, μ_t, describing the Reynolds stress tensor ($\boldsymbol{\tau}_s^R$). The $k-\epsilon$ is a two equation model that models the eddy viscosity, μ_t, by setting up the transport equations for the turbulent kinetic energy, k, and its dissipation rate, ϵ which are shown below:

$$\frac{\partial(\bar{\rho}\tilde{k})}{\partial t} + \nabla\cdot(\bar{\rho}\tilde{k}\tilde{\mathbf{u}}) = \nabla\cdot\left[\left(\frac{\mu_t}{\mathrm{Pr}_k} + \mu\right)\nabla\tilde{k}\right] - \frac{2}{3}\bar{\rho}\tilde{k}(\nabla\cdot\tilde{\mathbf{u}}) + P_k - \bar{\rho}\tilde{\epsilon} \tag{3-35}$$

$$\frac{\partial(\bar{\rho}\tilde{\epsilon})}{\partial t} + \nabla\cdot(\bar{\rho}\tilde{\epsilon}\tilde{\mathbf{u}}) = \nabla\cdot\left[\left(\frac{\mu_t}{\mathrm{Pr}_\epsilon} + \mu\right)\nabla\tilde{\epsilon}\right] + C_{1\epsilon}P_k\frac{\tilde{\epsilon}}{\tilde{k}} - \left(\frac{2}{3}C_{1\epsilon} + C_3\right)\bar{\rho}\tilde{\epsilon}(\nabla\cdot\tilde{\mathbf{u}}) - C_2\bar{\rho}\frac{\tilde{\epsilon}^2}{\tilde{k}} \tag{3-36}$$

where the turbulent viscosity, μ_t is modelled as:

$$\mu_\mathrm{t} = \bar{\rho}C_\mu\frac{\tilde{k}^2}{\tilde{\epsilon}} \tag{3-37}$$

The production term P_k is defined as $P_k = \mu_\mathrm{t}|S|^2$, where $|S| \equiv \sqrt{2\mathbf{GG}}$. The model constants are given in Table 3-1:

Table 3- 1: Model constants for standard $k-\epsilon$ turbulence model.

Model constant	$C_{1\epsilon}$	C_2	C_3	C_μ	Pr_k	Pr_ϵ
Values	1.44	1.92	-0.33	0.09	1.0	1.3

3.4 Spray Modelling

When injecting fuel into a combustion chamber, a two-phase flow of the spray (liquid) and the surrounding fluid (gas) are created. In contrast to single-phase flow, this requires a coupling between the two phases. There are many ways of coupling the two phases, but taking into account the flow and computational costs, an approach proposed by Nordin [253] is used here. The liquid phase is modelled using a combined stochastic and Lagrangian approach where the droplets are modelled as discrete parcels which are tracked as points in the domain. A parcel is a group of droplets which have the same properties (mass, volume, temperature). As for the gas phase, it is modelled using a normal Eulerian approach. The two phases are coupled by source terms in the transport equations.

3.4.1 Spray Motion Equations

The motion of a Lagrangian particle, which is moving in an Eulerian framework, is governed by one of the most fundamental laws of physics; Newton's second law:

$$\frac{\partial \mathbf{p}_d}{\partial t} = \sum_i \mathbf{F}_i \tag{3-38}$$

The full spray equation often referred to as the BBO equation – from Basset [254], Boussinesq [255] and Oseen [256] – which includes effects of added mass, pressure, Basset force, Magnus effect, Saffman force, and Faxen force. They are all neglected due to high density ratio between the two phases, while the Magnus effect is neglected since the rotation of the droplets is not important. The remaining forces are the drag and gravitational force acting on the droplets.

$$\frac{\partial \mathbf{p}_d}{\partial t} = -\rho_g \frac{\pi {D_d}^2}{8} C_D(\mathbf{u}_d - \mathbf{u})|\mathbf{u}_d - \mathbf{u}| + \rho_d \frac{\pi {D_d}^3}{6}\mathbf{g} \tag{3-39}$$

where D_d is denoted as the liquid droplet diameter and $\mathbf{u}_d$ refers to the droplet velocity. The droplet density and gas density are represented by ρ_d and ρ_g, respectively. The drag coefficient C_D is introduced in Section 3.4.3. This equation can be further simplified by assuming the droplets are spherical and the drag is not affected by changes in mass, thus:

$$\frac{\partial \mathbf{p}_d}{\partial t} = m_d \frac{\partial \mathbf{u}_d}{\partial t} = \rho_d \frac{\pi {D_d}^3}{6} \frac{\partial \mathbf{u}_d}{\partial t} \tag{3-40}$$

The liquid droplet mass is taken to be m_d. By combining Equation 3-39 and 3-40, the resulting equation is:

$$\frac{\partial \mathbf{u}_d}{\partial t} = -\frac{3}{4}\frac{\rho_g}{\rho_d}\frac{1}{D_d} C_D(\mathbf{u}_d - \mathbf{u})|\mathbf{u}_d - \mathbf{u}| + \mathbf{g} \tag{3-41}$$

3.4.2 Breakup Model

The breakup of a liquid jet into droplets is caused by a combination of different mechanisms which are turbulence within the liquid phase, implosion of cavitation bubbles, and external aerodynamic forces acting on the liquid jet. Depending on the injection parameters such as the relative velocity between liquid and gas, the liquid and gas densities and the liquid viscosity and surface tension the contribution of each of the above mechanisms to the spray breakup varies.

Breakup regimes are typically classified in terms of the dimensionless numbers called Weber Number (*We*) which is given by:

$$We = \frac{\rho_g |\mathbf{u} - \mathbf{u}_d|^2 D_d}{2\sigma_d} \tag{3-42}$$

where σ_d is the surface tension coefficient of the liquid droplet. In the current work, the breakup model considered here is the Reitz-Diwakar (RD) model [257]. In this model, two modes of breakup are considered: bag breakup, and stripping breakup. Bag breakup occurs when the pressure distribution around the droplet causes the droplet to expand and eventually disintegrate when the aerodynamic effect overcomes the surface tension. Stripping breakup occurs when liquid is sheared off

the droplet surface. The two breakup regimes are characterised by the Weber number and Reynolds number of the parent droplet. For the high injection pressures that are characteristic of typical diesel engines, the stripping breakup dominates over the bag breakup. In any breakup model, the size of the newly formed droplets from the parent droplets is given by,

$$\frac{dD_d}{dt} = -\frac{D_d - D_{d,stable}}{\tau_b} \tag{3-43}$$

where $D_{d,\text{stable}}$ is the stable liquid droplet diameter and τ_b is the breakup time. The specifications of $D_{d,\text{stable}}$ and τ_b change from one breakup mode to another. If the droplet diameter is larger than the stable droplet diameter, new droplets are formed from the parent droplets.

For the RD breakup model considered for the present work, the criteria for droplet breakup are based on specification of critical Weber numbers for two breakup regimes: bag breakup and stripping breakup.

For bag breakup ($We \geq C_{b1}$), the Weber number has to be larger or equal to C_{b1}, where C_{b1} is an empirical model constant. The stable droplet size needs to satisfy the equality of the above condition. The corresponding characteristic time for breakup is thus given as

$$\tau_b = C_{b2}\sqrt{\frac{\rho_d {D_d}^3}{16\sigma_d}} \tag{3-44}$$

where C_{b2} is a constant.

For stripping breakup $\left(\frac{We}{\sqrt{Re_g}} \geq C_s\right)$, the ratio between Weber number and square root of Reynolds number has to be larger or equal to C_s, where C_s is an empirical constant. The Reynolds number for spray is calculated using

$$Re_g = \frac{\rho_g |\mathbf{u} - \mathbf{u}_d| D_d}{\mu_g} \tag{3-45}$$

where μ_g represent the gas viscosity. The characteristic time scale is given as

$$\tau_b = \frac{T_{strp}}{2}\sqrt{\frac{\rho_d}{\rho_g}}\frac{D_d}{|\mathbf{u}-\mathbf{u}_d|} \tag{3-46}$$

where T_{strp} is an empirical constant.

Table 3- 2: Model constant for RD breakup model.

Constants	Description	Value [257]
C_{b1}	Critical Weber number for bag breakup	6.0
C_{b2}	Time factor for bag breakup	π
C_s	Weber Number for stripping	0.5
T_{strp}	Time factor for stripping	20.0

3.4.3 Drag Model

Prediction of droplet drag is important for accurate spray modelling. Dynamic drag model is used for the simulation. The droplets are assumed to remain in spherical shape throughout the domain, where the drag of a spherical object is determined by

$$C_D = \begin{cases} \frac{24}{Re_g}\left(1+\frac{Re_g^{\frac{2}{3}}}{6}\right) & Re_g < 1000 \\ 0.424 & Re_g > 1000 \end{cases} \tag{3-47}$$

However, as an initially spherical droplet moves through a gas, its shape is distorted significantly when the Weber number is large, approaching to that of a disk in extreme case. The dynamic drag model accounts for variations in the droplet shape to determine the droplet drag coefficient as when a droplet moves through a gas with high speed. The drag coefficient is given by

$$C_D = C_{D,sphere}(1+2.632y_d) \tag{3-48}$$

where the droplet distortion y_d is determined by solving

$$\frac{d^2 y_d}{dt^2} = \frac{C_F}{C_b}\frac{\rho_g}{\rho_d}\frac{|\mathbf{u}-\mathbf{u}_d|^2}{r_d^2} - \frac{C_k \sigma_d}{\rho_d r_d^3} y_d - \frac{C_d \mu_d}{\rho_d r_d^2}\frac{dy_d}{dt} \quad (3\text{-}49)$$

The undisturbed liquid droplet radius is represented by r while μ_d refers to the liquid droplet viscosity. The terms C_F, C_b, C_k and C_d are dimensionless constants where their values are given in Table 3-3.

Table 3- 3: Constants for the droplet distortion equation.

Constants	C_F	C_b	C_k	C_d
Values	1/3	0.5	8	5

3.4.4 Chemistry

After the fuel liquid droplets have undergone breakup and evaporation, the fuel mixes with the surrounding air and forms a combustible mixture. Solving the chemistry numerically means solving a large system of reaction equations. Generally, each elementary reaction can be described as

$$\sum_{i=1}^{N_s} S_{ij}^f [X_i] \rightleftharpoons_{\mathrm{k}_j^r}^{\mathrm{k}_j^f} \sum_{i=1}^{N_s} S_{ij}^r [X_i] \quad (3\text{-}50)$$

where S^f and S^r are the matrices of forward and reverse stoichiometric coefficients, respectively, k_j^f and k_j^r are the corresponding reaction rate constants of reaction j, and $[X_i]$ is the molar concentration of species i in the cell. The matrix of stoichiometric coefficients consists of N_s rows, with the rows corresponding to species. The columns represent reactions, making the matrix $N_s \times N_r$. The reaction rate constant k is itself a function of the Arrhenius constants:

$$\mathrm{k}_j = A_j T^{\beta_j} e^{-\frac{E_{a,j}}{RT}} \quad (3\text{-}51)$$

which need to be specified as part of the mechanism. β_j is defined as the temperature exponent. The rate of formation of species $[X_1]$ from reaction j is written as:

$$\left(\frac{d[X_1]}{dt}\right)_j = S_{1j}^r \left(k_j^f \prod_{i=1}^{N_s} [X_i]^{S_{1j}^f} - k_j^r \prod_{i=1}^{N_s} [X_i]^{S_{1j}^r} \right) \tag{3-52}$$

This equation is formulated for every species included in the chemical mechanism, as well as for every reaction, resulting in an equation system consisting of $N_s \times N_r$ equations. As can be seen from the above equation, it is a system of Ordinary Differential Equations (ODEs), which can be solved coupled using an ODE solver, sequentially using a reference species technique [253], or by an Euler-Implicit method. OpenFOAM has the ability to solve the equations using an ODE solver. Aside from the concentrations, it is also important to find the source term in the species transport equation (Equation 3-29). The source term for species i is:

$$\mathbf{R\dot{R}}_\iota = \frac{MW_i}{\rho} \sum_{j=1}^{N_r} \left(S_{ij}^r - S_{ij}^f\right) \dot{\omega}_j \tag{3-53}$$

$$\dot{\omega}_j = k_j^f \prod_{i=1}^{N_s} [X_i]^{S_{ij}^f} - k_j^r \prod_{i=1}^{N_s} [X_i]^{S_{ij}^r} \tag{3-54}$$

where MW_i is the molar weight for species i.

3.5 Turbulence-Spray Interaction

The disperse phase models introduced earlier describe droplet behaviour with respect to the flow field of the continuous phase. Due to the separation of the Lagrangian disperse phase from the Navier-Stokes equations, phase interaction is uni-directional. This implies that the given models do not consider the response of the flow field to droplet motion and vaporisation. This is captured by setting source terms to the transport equations of mass, energy and momentum, which close the conservation laws across the phases, a method commonly known as particle source in cell method (PSIC) [258].

$$\frac{\partial \bar{\rho}}{\partial t} + \nabla \cdot (\bar{\rho} \widetilde{\mathbf{u}}) = S_\rho \tag{3-55}$$

$$\frac{\partial (\bar{\rho} \widetilde{\mathbf{u}})}{\partial t} + \nabla \cdot (\bar{\rho} \widetilde{\mathbf{u}} \widetilde{\mathbf{u}}) = \bar{\rho} \mathbf{g} - \nabla \bar{P} + \nabla \cdot \left(\bar{\boldsymbol{\tau}}_s - \bar{\rho} \overline{\mathbf{u}'' \mathbf{u}''} \right) + S_{\rho u} \tag{3-56}$$

$$\frac{\partial(\bar{\rho}\widetilde{Y_J})}{\partial t} + \nabla \cdot (\bar{\rho}\widetilde{Y_J}\tilde{\mathbf{u}}) = -\nabla \cdot (\mu \nabla \widetilde{Y_J} - \bar{\rho}\overline{Y''\mathbf{u}''}) + \kappa\overline{\dot{\mathbf{R}}\mathbf{R}_J} + S_{\rho Y} \quad (3\text{-}57)$$

$$\frac{\partial(\bar{\rho}\widetilde{h_s})}{\partial t} + \nabla \cdot (\bar{\rho}\widetilde{h_s}\tilde{\mathbf{u}}) = \nabla \cdot \left(\frac{\mu}{Pr}\nabla\widetilde{h_s} - \bar{\rho}\overline{h_s''\mathbf{u}''}\right) + \frac{\partial \bar{P}}{\partial t} + \bar{\dot{q}}_{reaction} + S_{\rho h} \quad (3\text{-}58)$$

where the source terms for respective conservation equations are given as

$$S_\rho = \frac{N_d}{V\Delta t}[m_{in} - m_{out}] \quad (3\text{-}59)$$

$$S_{\rho u} = \frac{N_d}{V\Delta t}[(m\mathbf{u})_{in} - (m\mathbf{u})_{out}] \quad (3\text{-}60)$$

$$S_{\rho Y} = \frac{N_d}{V\Delta t}[(mY_k)_{in} - (mY_k)_{out}] \quad (3\text{-}61)$$

$$S_{\rho h} = \frac{N_d}{V\Delta t}\left[\left(mc_p\right)_{in} - \left(mc_p\right)_{out}\right] - (m_{in} - m_{out})\Delta h_{vap} \quad (3\text{-}62)$$

For all source terms, N_d is the number of droplets represented by the parcel tracked, V is the volume of the cell passed, and Δt is the computational time-step.

3.6 Soot Model

Different modelling approaches are proposed to study the soot formation and oxidation processes. In this current study, the spray combustion solver is incorporated with a semi-empirical multi-step soot model which is employed from [169] and is known as the Moss-Brookes (MB) soot model. The selected soot model is computed via Eulerian method and able to account for individual soot processes such as soot inception, surface growth, coagulation and oxidation processes. The concentration of soot precursors and surface growth species are first computed based on gas-phase reaction and the information is later imported into the MB soot model to compute the soot mass fraction, Y_{soot} , and normalised radical nuclei concentration, b^*_{nuc} . The two transport equations for Y_{soot} and b^*_{nuc} are expressed below in Equation 3-63 and Equation 3-64.

$$\frac{\partial}{\partial t}(\rho Y_{soot}) + \nabla \cdot (\rho \mathbf{u} Y_{soot}) = \nabla \cdot \left[\frac{\mu_t}{Pr_{soot}}\nabla Y_{soot}\right] + \frac{dM_{soot}}{dt} \quad (3\text{-}63)$$

$$\frac{\partial}{\partial t}(\rho b_{nuc}^{*}) + \nabla \cdot (\rho \mathbf{u} b_{nuc}^{*}) = \nabla \cdot \left(\frac{\mu_t}{Pr_{nuc}} \nabla b_{nuc}^{*}\right) + \frac{1}{N_{norm}} \frac{dN_{soot}}{dt} \qquad (3\text{-}64)$$

The turbulent Prandtl number for soot transport and nuclei transport is represented by Pr_{soot} and Pr_{nuc}, respectively. N_{norm} is a normalisation factor with a value of 10^{15} particles.

The source term for the soot mass fraction, Y_{soot} transport equation in Equation 3-63 computes the production of soot mass and is expressed below:

$$\frac{dM_{soot}}{dt} = \underbrace{k_{inc}[X_{prec}]}_{\omega_{inc}} + \underbrace{k_{sg}[C_2H_2]}_{\omega_{sg}} - \underbrace{k_{OH}\eta_{coll}[OH] - k_{O_2}[O_2]}_{\omega_{ox}} \qquad (3\text{-}65)$$

The first term on the RHS of Equation 3-65 is the soot inception rates, where X_{prec} denotes the molar concentration of the soot precursor. The choice of soot precursor in this study is C_2H_2, hence X_{prec} refers to the molar concentration of acetylene. The second term represents the surface growth rates which governs the mass addition onto the soot surface. In this model, soot particles are assumed to grow primarily by the surface addition of gaseous species C_2H_2 , hence having the molar concentration of C_2H_2 set as the participating surface growth species.

Soot oxidation is a crucial process that occurs on the surface of the particles where carbon is being removed from the soot surface, thus reducing its mass. This process occurs simultaneously with inception and surface growth process. Soot are primarily oxidised by OH and O_2. The oxidation rates due to OH and O_2 are represented by the last two terms on the RHS of Equation 3-65, respectively. The constant η_{coll} denotes the collision efficiency parameter with a value of 0.04 [169] It is noteworthy that the original MB soot model only considers OH radical as the dominant oxidising agent and the surface-specific oxidation rate of soot by the radical may be formulated according to the model proposed by Fenimore and Jones [103]. Additional oxidation due to O_2 is added to the original MB soot model, in addition to the soot oxidation due to the OH radical. The surface-specific oxidation rate by O_2 is based on measurements and a model by Lee et al. [101].

The reaction rate of each sub-process, in Equation 3-65, are calculated using an Arrhenius expression,

$$k_i = C_i T^{b,i} \exp\left(\frac{T_{a,i}}{T}\right) {S_{soot}}^{n,i} \quad (3\text{-}66)$$

where T, C_i and $T_{a,i}$ in Equation 3-66 represents the gas temperature, model constant and activation temperature, respectively. The S_{soot} in Equation 3-66 refers to specific soot surface area. In the formulation of MB soot model, the inception rate is independent of this parameter, while the surface growth rate and oxidation rate are a linear function of this parameter. These sub-models with their respective descriptions and model constant values used in the soot model are summarised in Table 3-4.

Table 3- 4: Model constants for MB soot model.

i	**Description**	***C*** **[units]**	***b***	**Activation temperature,** T_a **[K]**	***n***	**Ref**
inc	Inception	54 [s^{-1}]	0	21000	0	[169]
sg	Surface growth	11700 [kg m $kmol^{-1}$ s^{-1}]	0	12100	1	[169]
OH	Oxidation via OH	105.81 [kg m $kmol^{-1}$ $K^{-0.5}$ s^{-1}]	0.5	0	1	[169]
O_2	Oxidation via O_2	8903.51 [kg m $kmol^{-1}$ $K^{-0.5}$ s^{-1}]	0.5	19778	1	[169]

The source term of the b^*_{nuc} transport equation (Equation 3-64) is the instantaneous production rate of soot particles, which is influenced by the inception and coagulation process. It is computed using Equation 3-67. The first term on the RHS is the product of the Avogadro constant, N_A, and the inception rate, ω_{inc} , as introduced earlier, while the second term is a sink term due to coagulation, ω_{coag}. The latter is described by Equation 3-68 and the model constant value, C_{coag} , is set as 1.0 [169].

$$\frac{dN_{soot}}{dt} = N_A \omega_{inc} - \omega_{coag} \tag{3-67}$$

$$\omega_{coag} = C_{coag} \left(\frac{24RT}{\rho_{soot} N_A}\right)^{1/2} \left(\frac{6M_{soot}}{\pi \rho_{soot}}\right)^{1/6} {N_{soot}}^{11/6} \tag{3-68}$$

The above model with their corresponding default constants are used and validated in soot production prediction in kerosene flames, by modifying only the soot precursor species [168]. Modification on default model constants is accessible for improving the output results. Default values are used for most of the model parameters, except for a few to which modifications are made. The mass of incipient soot particle is set at 1200 kg/kmol corresponding to 100 carbon atoms, whereas the mass density of soot is assumed to be 2000 kg/m^3, as proposed by Hall [259] who further extended the MB model for higher hydrocarbon fuels. The predicted soot particle size distribution is estimated on a cell-by-cell basis based on Equation 2-12.

3.7 Concluding Remarks

In this chapter, the CFD sub-models along with their respective governing equations applied in the numerical study are described. The CFD sub-models applied in the subsequent diesel spray combustion simulations are summarised in Table 3-5.

Table 3- 5: Summary of CFD sub-models employed in the 2-D spray combustion simulation.

Events	CFD Sub-Models
Turbulence model	Standard $k-\epsilon$ model
Breakup model	Reitz-Diwakar
Drag model	Dynamics drag model
Soot model	Moss-Brookes soot model

CHAPTER 4
FORMULATION OF LAGRANGIAN SOOT PARTICLE TRACKING

4.1 Introduction

Several types of soot models are developed to describe the formation and oxidation process of soot and their convective movement in spray flame. There are two methods of modelling particle transport: Eulerian and Lagrangian method. The Eulerian method treats the particle phase as a continuum and develops its conservation equation on a control volume basis, similar to that for a fluid phase. However, the Lagrangian method considers particles as a discrete phase and tracks the pathway of each individual particle [260]. By taking account of the statistics of particle trajectories, the Lagrangian method is able to calculate particle concentration and other phase data as what the Eulerian can produce. In this chapter, the formulation of LST model is explained from Section 4.2 to 4.4. The assumptions in the formulation of LST is discussed and verified in Section 4.5. Finally, some key conclusions are highlighted in Section 4.6.

4.2 Soot Particles as Lagrangian Particles

The MB soot model mentioned in Section 3.6 is computed using Eulerian method. The use of Eulerian method in soot model provides useful information such as the mean diameter, total soot concentration and the overall evolution of the soot cloud. However, more in-depth information such as particle size distribution and individual soot information are not available. Therefore, an alternative method by using Lagrangian method is introduced here which is expected to produce similar computed results as the Eulerian method. Besides, additional information such as soot particle size distribution can also be obtained with this method. As the Lagrangian method is tracking individual particles, information of individual

particles such as diameter, position, velocity and also the age of particles are accessible.

The soot particles in the LST model are tracked via the Lagrangian method, in which the soot particles in the airflow are subjected to inertia and hydrodynamic drag. Due to these external forces experienced in the flow field, the particles can either be accelerated or decelerated. The soot particle velocity change is formulated by

$$m_p \frac{d\mathbf{v_p}}{dt} = -\rho \frac{\pi d_p^2}{8} C_D(\mathbf{v_p} - \mathbf{u})\left|\mathbf{v_p} - \mathbf{u}\right| + \frac{m_p \mathbf{g}(\rho_p - \rho)}{\rho_p} \tag{4-1}$$

The first term on the RHS of Equation 4-1 represents the drag force experienced by the Lagrangian particles. The equation for drag coefficient, C_D is expressed in Equation 4-2 [261]. It is dependent on the particle Reynolds number, Re_p (based on particle diameter, gas density and viscosity) if Re_p is less than 1000. When Re_p is larger than 1000, drag coefficient is set to a constant value of 0.44 [261]. The second term on the RHS of Equation 4-1 represents the gravitational force and buoyancy force, while ρ_p is the density of particle. m_p and $\mathbf{v_p}$ denote the particle mass and velocity, respectively.

$$C_D = \begin{cases} \frac{24}{Re_p}\left(1 + \frac{Re_p^{\frac{2}{3}}}{6}\right) & Re_p < 1000 \\ 0.44 & Re_p > 1000 \end{cases} \tag{4-2}$$

The fluid velocity $\mathbf{u}$ can be decomposed into two components, the mean fluid velocity $\bar{\mathbf{u}}$ and the fluctuating component $\mathbf{u}'$. The trajectories of the particles follow the mean fluid velocity $\bar{\mathbf{u}}$, while the dispersion of particles due to turbulence is influenced by the instantaneous fluctuating velocity $\mathbf{u}'$ [260,262]. In this study, $\mathbf{u}'$ is modelled by applying the discrete random walk model (DRW) [260,262]. It correlates with the flow turbulent kinetic energy k, predicted by the standard $k-\epsilon$ model, and is expressed in Equation 4-3,

$$\mathbf{u}' = \zeta\sqrt{2k/3} \tag{4-3}$$

where ζ is a Gaussian random number [260,262] with zero mean and unit variance.

The LST model in this study considers three main soot phenomena, namely soot inception, surface growth, and oxidation, which are essential to the study of primary soot particles and their subsequent evolution. Here, the coagulation process, which includes the agglomeration into fractal aggregates and coalescent growth [69], is neglected in the LST model. This is because the agglomeration process mainly affects the overall soot number but not the mass addition onto the soot particle surface. Thus, the size of the primary soot particles is more significantly affected by the surface growth process [89,231]. On the other hand, the coalescence growth process is where the collision of small existing particles and newly formed particles leads to larger spherical particles [93]. However, it is observed that not all collisions result in merging or sticking of particles [95,96]. Saffaripour et al. [263] who carried out detailed modelling of soot aggregate formation in laminar co-flow diffusion flames by implementing coalescence sub-models into their model, also suggested that the coalescent growth process may be less significant. Their results showed that the coalescence process is too slow to account for growth of primary particles as it is limited by the rate of particle collisions [263]. In addition, a more recent numerical simulation performed by Mitchell et al. [47] who used the time-dependent Monte-Carlo method to study soot particle growth also showed that the surface growth process is an important factor in affecting the level of particle sphericity. It is shown that coagulation alone is insufficient to construct a spheroidal particle without the presence of surface growth [47]. For these reasons, the proposed LST model considers only the surface growth and neglects the coagulation process. The models for inception (*inc*), surface growth (*sg*) and oxidation (*ox*) are adopted from MB soot model [169] and the associated reaction rates are calculated as below,

$$\omega_{inc} = C_{inc} MW_P \left(\frac{X_{prec} P}{RT}\right) exp\left\{-\frac{T_{inc}}{T}\right\} \tag{4-4}$$

$$\omega_{sg} = C_{sg} \left(\frac{X_{sg} P}{RT}\right) exp\left\{-\frac{T_{sg}}{T}\right\} S_{soot} \tag{4-5}$$

$$\omega_{ox} = C_{OH} \eta_{coll} \left(\frac{X_{OH} P}{RT}\right) \sqrt{T} S_{soot} + C_{O_2} \left(\frac{X_{O_2} P}{RT}\right) exp\left\{-\frac{T_{O_2}}{T}\right\} \sqrt{T} S_{soot} \tag{4-6}$$

Here, X_{prec} and X_{sg} denote the mole fraction of soot precursor and participating surface growth species. The mole fractions for soot oxidants, *OH* and O_2 are represented by X_{OH} and X_{O_2}, respectively. S_{soot} denotes the specific surface area. T, P and R represent the gas temperature, pressure and universal gas constant, respectively. The constant MW_P represents the molar mass of an incipient soot particle which is set to 1200 kg/kmol. The soot model constants, their descriptions and default values are shown in Table 4-1.

4.2.1 Inception of Lagrangian Soot Particles

Different ways for the simulation of Lagrangian soot particle formation inside the computational domain have been proposed. In the studies by Piscaglia and co-workers [211,212], the position and velocity of the soot particles are pre-defined and placed in the computational domain before the start of the simulation. In other studies [207,208], the tracking of soot is carried out from selected starting points depending on the soot concentration. In the current proposed LST model, instead of pre-defining the locations and velocities of the particles, Lagrangian particles are formed when a formation criterion in a computational cell is met. The formation criterion in a particular computational cell is that the total incipient soot mass of that cell has to be larger than the minimum mass of incipient soot, which is 2.0×10^{-24} kg. It is calculated based on the assumption that the minimum diameter of an incipient soot is 1.24 nm [220], with a soot density of 2000 kg/m^3 [220,222].. The single formed Lagrangian particle is assumed to represent the total number of incipient soot particles in that particular computational cell at that instance. It is also assumed that all particles formed in that cell, at that instant, follow the same pathway [209] and size change as the Lagrangian particle.

Table 4- 1: The soot model constants with their respective descriptions and default values [169]**.**

Soot Model Constants	Descriptions	Value [Unit]
C_{inc}	Model constant for soot incipient rate	54 [s^{-1}]
C_{sg}	Surface growth rate scaling factor	11700 [kg m $kmol^{-1}$ s^{-1}]
C_{OH}	Model constant for soot oxidation due to *OH*	105.81 [kg m $kmol^{-1}$ $K^{-0.5}$ s^{-1}]
C_{O_2}	Model constant for soot oxidation due to O_2	8903.51 [kg m $kmol^{-1}$ $K^{-0.5}$ s^{-1}]
T_{inc}	Activation temperature of soot inception	21000 [K]
T_{sg}	Activation temperature of surface growth	12100 [K]
T_{O_2}	Activation temperature of soot oxidation due to O_2	19778 [K]
η_{coll}	Collision efficiency parameter	0.04 [-]

4.2.2 Surface Growth and Oxidation of Lagrangian Soot Particles

The newly formed Lagrangian particles then undergo mass addition and increase in size through the surface growth process which is governed by Equation 4-5. Figure 4-1 shows a computational cell with N number of soot particles with different diameter ranging from d_1 to d_N. The soot diameter calculated using Eulerian method is under the assumption that all the soot inside a computational cell is mono-dispersed. This implies that all particles in a computational cell have equal size as the average diameter of all the particles available in the cell. The average diameter is denoted by d_{avg},which is expressed as follows:

$$d_1 = d_2 = d_3 = \cdots = d_N = d_{avg}\ , where\ d_{avg} = \left[\frac{\sum_{i=1}^{N} {d_i}^3}{N}\right]^{1/3} \quad (4\text{-}7)$$

The rate of mass addition via surface growth is dependent on the specific surface area, S_{soot} of available soot particles in a computational cell. S_{soot} is calculated by

summing up all the available individual soot particles in the computational cell i.e. $S_{soot} = \sum_{i=1}^{N} \pi d_i^2$. As all the soot particles are assumed to have the same size as the average diameter based on the mono-dispersed assumption, the specific surface area is simply the product of total number of soot particles and average soot surface area, $S_{soot} = N\pi d_{avg}^2$.

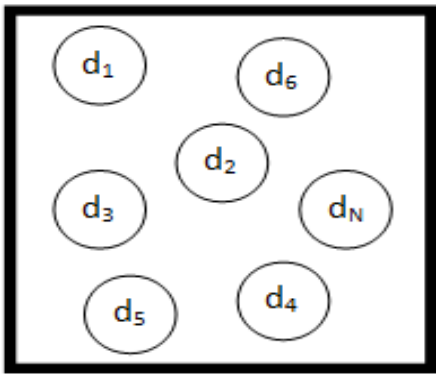

Figure 4- 1: *N* number of soot particles with diameters ranging from d_1 to d_N in a single computational cell.

In the proposed LST model, the poly-dispersed assumption is taken into account. This implies that all the soot particles in a computational cell shown in Figure 4-1 have their own distinct, individual diameters. With the poly-dispersed assumption, Equation 4-5 is modified to consider the surface area of every individual soot particle. The surface growth rate based on poly-dispersed assumption $(\omega_{sg,poly})$ can then be expressed in terms of surface growth rate of individual soot particles $(\omega_{sg,i})$ using Equation 4-8a,

$$\omega_{sg,poly} = C_{sg}\left(\frac{X_{sg}P}{RT}\right) exp\left\{-\frac{T_\gamma}{T}\right\} \sum_{i=1}^{N} \pi d_i^2 \quad (4\text{-}8a)$$

$$= C_{sg}\left(\frac{X_{sg}P}{RT}\right) exp\left\{-\frac{T_\gamma}{T}\right\} [\pi d_1^2 + \pi d_2^2 + \pi d_3^2 + \pi d_4^2 + \cdots + \pi d_N^2] \quad (4\text{-}8b)$$

$$= \omega_{sg,1} + \omega_{sg,2} + \omega_{sg,3} + \omega_{sg,4} + \cdots + \omega_{sg,N} \quad (4\text{-}8c)$$

This implies that the individual soot surface growth model, $\omega_{sg,i}$ is given as,

$$\omega_{sg,i} = C_{sg}\left(\frac{X_{sg}P}{RT}\right) exp\left\{-\frac{T_\gamma}{T}\right\} [\pi d_i^2] = \left.\frac{dm_i}{dt}\right|_{added\ mass,i} \quad (4\text{-}9)$$

which governs the rate of mass addition onto an individual soot particle. Akin to the derivation carried out for the surface growth rate, oxidation model (Equation 4-6) can also be written as:

$$\omega_{ox,i} = C_{OH}\,\eta_{coll}\left(\frac{X_{OH}P}{RT}\right)\sqrt{T}\left[\pi d_i^2\right] + C_{O_2}\left(\frac{X_{O_2}P}{RT}\right)exp\left\{-\frac{T_{O_2}}{T}\right\}\sqrt{T}\left[\pi d_i^2\right] \quad (4\text{-}10a)$$

$$= \left.\frac{dm_i}{dt}\right|_{remove\ mass\ by\ OH,i} + \left.\frac{dm_i}{dt}\right|_{remove\ mass\ by\ O_2,i} \quad (4\text{-}10b)$$

4.2.3 Computation of New Soot Diameter at Each Time-step

The net mass added onto a soot particle is computed from the Lagrangian surface growth and oxidation models, Equation 4-9 and Equation 4-10a, respectively. The net mass is, thus calculated as follows:

$$\left.\frac{dm_i}{dt}\right|_{net\ mass\ added,i} = \omega_{sg,i} - \omega_{ox,i} \quad (4\text{-}11)$$

If the mass added by surface growth is more than the removed mass by oxidation (*OH* and O_2), a positive net mass added is obtained indicating an increase in diameter from initial diameter size. If the mass added by surface growth is less than the removed mass by oxidation, a decrease in diameter from initial diameter is observed. The mass of individual soot, denoted as m_i is given below:

$$m_i = \frac{\pi}{6} d_i^3 \rho_{soot} \quad (4\text{-}12)$$

where ρ_{soot} is the density of soot and d_i is the individual soot diameter. The new soot mass is computed by integrating Equation 4-11 with respect to time, t as shown below:

$$m_{new,i} = m_{old,i} + \int_t^{t+\Delta t}\left(\omega_{sg,i} - \omega_{ox,i}\right) dt \quad (4\text{-}13)$$

The new diameter is then computed using Equation 4-14. Once the Lagrangian soot particles are reduced below a threshold value, they are removed from the computational domain akin to being fully oxidised. The threshold value is set to be the same as the initial incipient soot particle size, which is 1.24 nm.

$$d_{new,i} = \sqrt[3]{\frac{6m_{new,i}}{\pi\rho_{soot}}} \tag{4-14}$$

4.3 Convergence of Soot Diameter Prediction

The new soot diameter computed is found to be dependent on the time-step Δt and the previous soot diameter, $d_{old,i}$ using Equation 4-13 and Equation 4-14. Computing the new soot diameter using the time-step Δt and the previous soot diameter, $d_{old,i}$ is found to be underpredicted as it has not converged to the actual value. To improve the results, the time-step Δt has to be split into smaller segments, between t_{old} and t_{new}, as shown in Figure 4-2. The soot diameter for each segments ($d_1, d_2, d_3, \dots, d_{N-2}, d_{N-1}, d_N$) are computed progressively from t_{old} to t_{new} using Equation 4-15 and Equation 4-16 as shown below:

$$m_{k+1,i} = m_{k,i} + \int_t^{t+\Delta t_k} \left(\omega_{sg,i} - \omega_{ox,i}\right) dt \tag{4-15}$$

$$d_{k+1,i} = \sqrt[3]{\frac{6m_{k+1,i}}{\pi\rho_{soot}}} \tag{4-16}$$

where $\Delta t_k = \frac{\Delta t}{N}$, $k = 0,1,2,3, \dots, N \; and \; N \geq 1$

Equation 4-15 is used to calculate the mass for each segments by utilising the diameter and mass of previous segments. The diameter for each segment is then calculated using Equation 4-16.

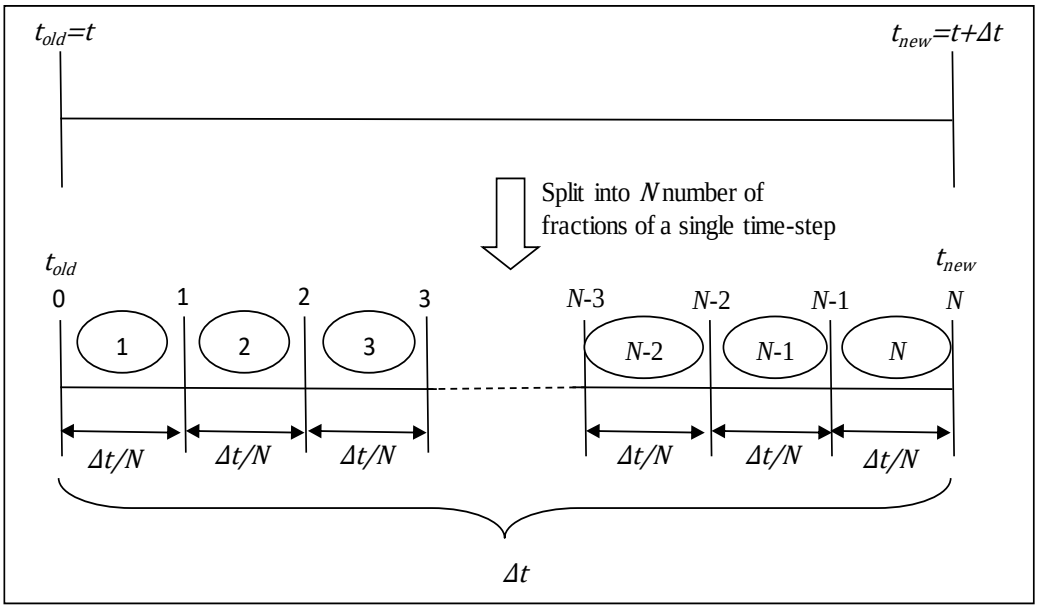

Figure 4- 2: Splitting of a single time-step Δt into *N* segments.

Figure 4-3 shows the calculated soot diameter with respect to the number of time-step segments, *N*. It is observed that as the number of segments *N* increases, the computed new soot diameter d_{new} at $t = t_{new}$ converges. This finding implies that for each time-step, one has to split the time-step into 20 or more segments in order to predict a converged soot diameter at t_{new} . This is however a very tedious task which incurs very high computational cost in order to achieve converged soot diameter prediction for a single time-step and a single Lagrangian particle. The computational time will be even higher as the Lagrangian particles increases, thus making this solution for soot diameter convergence unfeasible.

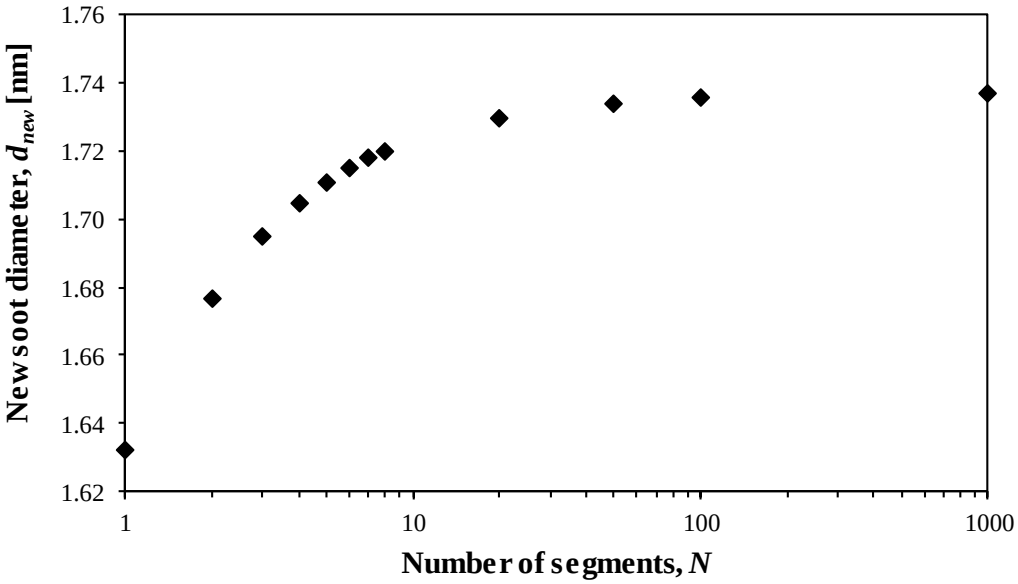

Figure 4- 3: Convergence of new soot diameter based on the number of segments, *N*.

4.3.1 Solving Convergence Soot Diameter Problem

As segmentation of time-step is computationally expensive, another way to overcome this problem is to remove the dependency of Equation 4-9 and Equation 4-10a on soot diameter, d_i. Equation 4-9 can be simplified to become,

$$\omega_{sg,i} = C(X_{sgs}, T, P)[\pi d_i^2] \tag{4-17}$$

where $C(X_{sgs}, T, P) = C_{sg}\left(\frac{X_{sgs}P}{RT}\right) exp\left\{-\frac{T_\gamma}{T}\right\}$. The rate of change of diameter can be derived from the individual soot surface growth model, $\omega_{sg,i}$, by combining Equation 4-17 and mass of individual soot given in Equation 4-12. By differentiating Equation 4-12 with respect to time and equating it to Equation 4-17, the rate of change of soot diameter is formulated as follows and described by Equation 4-20.

$$\frac{d}{dt}\left(\frac{\pi}{6} d_i^3 \rho_{soot}\right) = \frac{dm_i}{dt} \tag{4-18}$$

$$\frac{\pi d_i^2 \rho_{soot}}{2} \frac{d}{dt}(d_i) = C(X_{sg}, T, P)[\pi d_i^2] \tag{4-19}$$

$$\frac{d}{dt}(d_i) = \frac{2C(X_{sg},T,P)}{\rho_{soot}} \tag{4-20}$$

Equation 4-20 implies that the rate of change of soot diameter is only dependent on the temperature, pressure and mole fraction of the computational cell the soot particle is in. Most importantly, the dependence on soot diameter is absent. The rate of change of diameter of Lagrangian particle (by surface growth) can be written in expanded form as:

$$\frac{d}{dt}(d_i)\Big|_{sg} = 2C_{sg}\left(\frac{X_{sg}P}{RT}\right)\frac{1}{\rho_{soot}}exp\left\{-\frac{T_\gamma}{T}\right\} \tag{4-21}$$

The same simplification process is carried out for the oxidation model. The rate of change of diameter of Lagrangian particle (by oxidation via *OH* and O_2), is thus given by,

$$\frac{d}{dt}(d_i)\Big|_{ox\ via\ OH} = 2C_{OH}\eta_{coll}\left(\frac{X_{OH}P}{RT}\right)\frac{\sqrt{T}}{\rho_{soot}} \tag{4-22}$$

$$\frac{d}{dt}(d_i)\Big|_{ox\ via\ O_2} = 2C_{o_2}\left(\frac{X_{O_2}P}{RT}\right)\frac{\sqrt{T}}{\rho_{soot}}exp\left\{-\frac{T_{O_2}}{T}\right\} \tag{4-23}$$

for oxidation via *OH* and O_2. The new soot diameter is therefore calculated using Equation 4-25 which is presented below:

$$\frac{d}{dt}(d_i) = \frac{d}{dt}(d_i)\Big|_{sg} - \frac{d}{dt}(d_i)\Big|_{OX\ via\ OH} - \frac{d}{dt}(d_i)\Big|_{OX\ via\ O_2} \tag{4-24}$$

$$\begin{aligned} d_{new,i} = d_{old,i} + & \int_t^{t+\Delta t}\left(2C_{sg}\left(\frac{X_{sg}P}{RT}\right)\frac{1}{\rho_{soot}}exp\left\{-\frac{T_\gamma}{T}\right\}\right)dt \\ & - \int_t^{t+\Delta t}\left(2C_{OH}\eta_{coll}\left(\frac{X_{OH}P}{RT}\right)\frac{\sqrt{T}}{\rho_{soot}}\right)dt \\ & - \int_t^{t+\Delta t}\left(2C_{O_2}\left(\frac{X_{O_2}P}{RT}\right)\frac{\sqrt{T}}{\rho_{soot}}exp\left\{-\frac{T_{\omega,2}}{T}\right\}\right)dt \end{aligned} \tag{4-25}$$

4.4 Summary of Lagrangian Particle Tracking

The numerical calculation procedure is shown in Figure 4-4(a) for every time-step, while the step-by-step processes for LST modelling is presented in Figure 4-4(b). At the start of the simulation, the velocity, density and pressure are computed for every computational cell according to the continuity and momentum conservation equations. The next stage involves the combustion modelling in which the species concentrations and temperature for every cell are computed. The information from every computational cell is then fed into the LST model to compute the soot formation process rates. The LST model consists of two pathways, one for newly formed Lagrangian particles while another is for those Lagrangian particles that already exist and are evolving inside the computational domain. In the formation of new Lagrangian particles, the inception value of each cell is first computed using Equation 4-4 and compared against the minimum mass of incipient soot. If the inception value at cell i, $\omega_{inc,i}$ exceeds the threshold value, a Lagrangian particle with a diameter of $d_{p,min}$ is formed at cell i, where $d_{p,min}$ is the minimum diameter of incipient soot which is set to 1.24 nm. The existing Lagrangian particles undergo size change depending on Equation 4-21, 4-22 and 4-23, which correspond to the surface growth, *OH* oxidation and O_2 oxidation processes, respectively. Subsequently all the particle diameters are compared against $d_{p,min}$. If the particle diameter is below the minimum soot diameter, the particle is deleted; otherwise, the particle is retained. Next, the new velocity and position of the remaining particles are calculated according to Equation 4-1. Individual particle information such as diameter, position, velocity and onset of formation can be extracted.

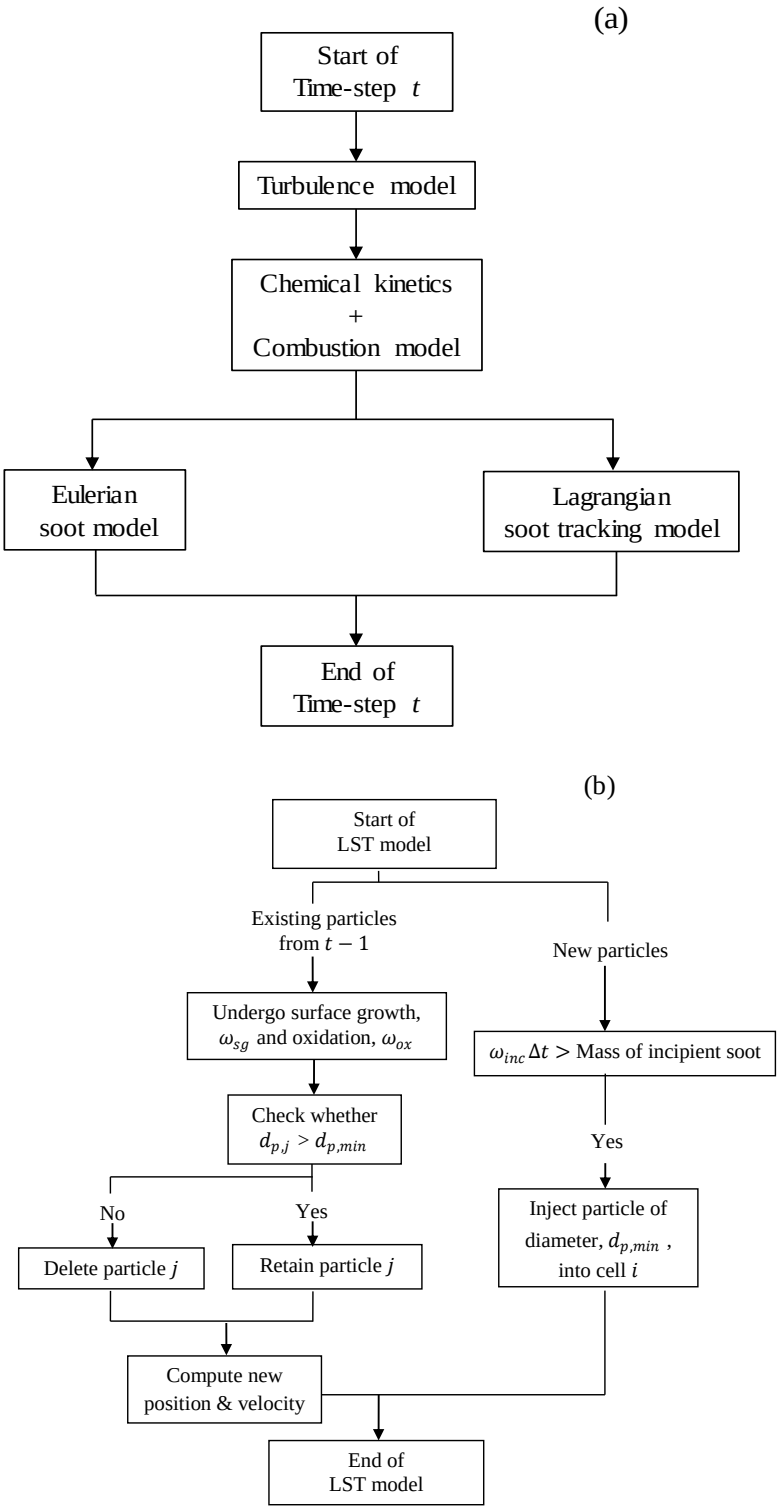

Figure 4- 4: (a) The overall flow chart for each time-step and (b) step-by-step processes in the proposed LST model on computing soot formation.

4.5 Justification of Assumption

In the formulation of LST model, the soot particles have been treated as spherical Lagrangian particles when tracking. This spherical assumption is used to justify the overall assumption that the soot particles follow the in-cylinder bulk gas flow. In addition to assuming spherical soot particles, soot is assumed to be a continuous-phase species. The particle path is dictated by the computed gas state and velocity fields. These fields are computed by taking into account interactions of continuous phase of gas. One-way coupling is assumed when tracking particle paths through these fields. In other words, the particle movement has no effect on the fluid flow field but the fluid flow has an influence on the particle movement.

To justify that soot particles follow the in-cylinder bulk gas flow field, soot particle motion in the cylinder can be described by Equation 4-1 while only considering the drag force for simplification. A soot particle with diameter d_p travels through a continuous gas phase with density ρ_g from a static position or after changing direction at a right angle during a motion to reach velocity $\mathbf{v_p}$ is considered. The soot particle experiences drag force due to its shape and the difference in velocity with the continuous phase. An equation to determine the time taken by a particle to reach the velocity $\mathbf{v_p}$which is also the average spray velocity is obtained in Equation 4-27 from the force balance equation.

$$\mathbf{F_D} = m\mathbf{a} \tag{4-26}$$

$$\frac{1}{2}\rho_g|\mathbf{v_p^2}|C_D S_p = \rho_p V_p \frac{|\mathbf{v}_f - \mathbf{v}_i|}{\Delta t} \tag{4-27}$$

where final velocity, $\mathbf{v}_f = \mathbf{v_p}$ and initial velocity, $\mathbf{v}_i = 0$. The diameter relation is described in Equation 4-28 by rearranging Equation 4-27.

$$d_p = \frac{3}{4}\Delta t|\mathbf{v_p}|C_D\left(\frac{\rho_g}{\rho_p}\right) \tag{4-28}$$

The following assumptions are taken into considerations, where soot density, ρ_p is assumed to be 2000 kg.m^{-3}. The average simulated spray velocity, $|\mathbf{v}|$ is approximately 150 m/s. The drag coefficient, C_D is assumed to be 0.5 (spherical object) for simplicity. The gas density here is taken to be in a range between 14.8 and 22.8 kg/m^3, according to the numerical studies carried out in this work. The maximum size of soot particle that can attain the surrounding fluid flow velocity is obtained by equalizing Δt to the time-step used in this study, which is 2x10^{-7} s and solving Equation 4-28 for diameter, d_p. The maximum diameter of soot particle is calculated to be about 83-128 nm. This means that soot particles with the diameter below 83 nm will reach fluid velocity and follow the fluid flow within the specified time-step. Studies by Katta et al. [209] and Roquemore et al. [215] also found that nanoscale soot particles follow the surrounding gas flow.

In addition to the justification above, further justification is carried out to justify that the time-step used in this study can produce numerical stability when resolving the flow field in continuous carrier gas phase [264]. To show numerical stability is achieved in this study, Courant–Friedrichs–Lewy (CFL) criterion is used. The CFL number requires that the distance travelled by a discrete particle during one time-step is not larger than one spatial increment (an element). Mathematically, for one-dimensional case, the CFL criterion is given by

$$\frac{|\mathbf{v}|\Delta t}{\Delta x} \leq CFL \qquad (4\text{-}29)$$

Where CFL must be between 0 and 1 for numerical stability, where v being the average linear velocity, Δt is the incremental time step and nodal spacing is denoted as Δx. In this study, $|\mathbf{v}|$ = 150 m/s, Δt = 2x10^{-7} s and Δx = 0.5 mm (the smallest nodal spacing in the computational domain) gives a CFL value of 0.06 that satisfies the CFL criterion, hence reinforces the above assumptions.

4.6 Concluding Remarks

In this study, a LST model is developed by treating the soot particles in the combustion chamber as Lagrangian particles. The inception, surface growth and oxidation models are adopted from MB soot model and modified such that the associated reaction rates can be computed using the Lagrangian approach. The soot nuclei are treated as Lagrangian particles when the mass of incipient soot exceeds a designated threshold value. Their trajectories are then computed using the particle momentum equation. The change of soot particle size is dependent on the modified Lagrangian soot surface growth and oxidation models. Moreover, the Lagrangian soot particles are verified to be able to follow the surrounding fluid flow with the mesh size and time-step used in the numerical studies carried out in this work.

CHAPTER 5
CONSTANT VOLUME CASE SETUP AND MODEL CONFIGURATION

5.1 Introduction

Soot formation is an event which lies at the end of the chain of combustion events. This implies that the accuracy of soot modelling is largely dependent on the accurate prediction of combustion characteristics which precede the soot formation event. Combustion characteristics in modern diesel engines are complex and challenging to model. Hence, experimental and computational efforts have been initiated to understand the fundamentals of these advanced combustion systems by studying combustion processes in a constant volume combustion chamber [265]. This chapter discusses the evaluation of CFD models for the combustion modelling in a constant volume combustion chamber. Section 5.2 presents the numerical formulation and setup for the spray combustion modelling in constant volume combustion chamber, under diesel-like conditions. Mesh and time-step independence tests are investigated before carrying out parametric studies on the CFD model constants of spray breakup and turbulence model. Calibration of the model constants are also discussed. Subsequently, the combustion characteristics of different chemical mechanism are assessed and validated in Section 5.5. Lastly, the results obtained in this phase of work are summarised in Section 5.6.

5.2 Numerical Setup for Constant Volume Combustion Chamber

The computational work is performed using the spray combustion solver in an open-source code, OpenFOAM version 2.0.x [266]. Experimental data from two different constant volume combustion vessels are used for the present model validation. The first set of data is the measurements of *n*-heptane spray combustion obtained from the Doshisha combustion vessel. The second measurement is from the Sandia combustion vessel for two different fuels, *n*-heptane and *n*-dodecane. The test case

based on Doshisha setup is henceforth addressed as Doshisha *n*-heptane case. As for the test cases based on Sandia constant volume setup, they are addressed as Sandia *n*-heptane case and Sandia *n*-dodecane case, respectively for brevity. Detailed descriptions of the experimental setup for the Doshisha and Sandia cases can be obtained in [33] and [265], respectively.

Both the constant volume combustion vessels are represented by a cylinder during simulation studies. For computational expediency, the cylindrical chamber is simplified to a 4-degree axisymmetric wedge with a single layer of cells in the *z*-direction. The diameter and height of the cylinder are adjusted such that the total volume of the cylinder is maintained to be the same as the actual combustion chamber. For the Doshisha *n*-heptane case, a radius of 30 mm and height of 120 mm are used. As for both the Sandia cases, the radius and height of the cylinder are set to 54 mm and 138 mm, respectively. A sample mesh is shown in Figure 5-1. The wall boundary conditions include no-slip and no-penetration for velocity components, zero-gradient for scalars and adiabatic or isothermal for the energy variable. The current computations employ a zero heat flux condition. No spray-wall interaction models are required since the liquid spray evaporates before reaching the wall.

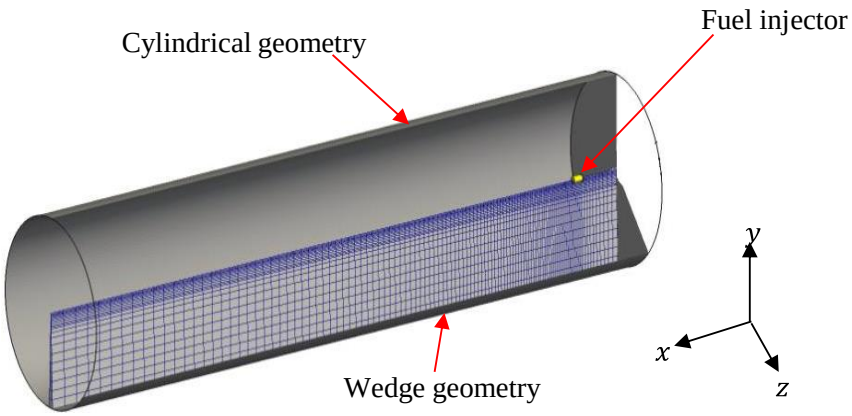

Figure 5- 1: Computational axisymmetric mesh for constant volume chamber.

5.3 Numerical Formulations and Operating Conditions

The non-reacting and reacting spray validations are carried out in Section 5.4 and 5.5, respectively. These validations are carried out to ensure that the fuel-air distribution and combustion characteristics are reasonably simulated and any uncertainties induced by these elements can be minimised prior to studying soot formation events. It is important to note that the validations of non-reacting spray simulations are carried out for the Sandia *n*-heptane and *n*-dodecane test cases, but not for the Doshisha *n*-heptane case. This is due to the lack of experimental data from literature regarding non-reacting conditions for the Doshisha *n*-heptane case.

The reacting Doshisha *n*-heptane case is studied at only a single operating condition, at an ambient temperature of 900 K and ambient density of 16.2 kg/m^3. The non-reacting Sandia *n*-heptane case is studied at an ambient temperature of 1000 K and ambient density of 14.8 kg/m^3 with the absence of oxygen (0% O_2 in ambient gas composition). As for reacting case, there are a total of 7 cases with varying O_2 concentration (from 10-21%) and ambient densities (14.8 and 30 kg/m^3), while having the same initial ambient temperature of 1000 K. For the non-reacting Sandia *n*-dodecane case, the numerical study is carried out at an ambient temperature of 900 K with an ambient density of 22.8 kg/m^3 without the presence of oxygen in the computational domain. The reacting spray case studies for Sandia *n*-dodecane case are carried out at two different oxygen levels, 15% and 21%. Both cases have the same initial ambient temperature of 900 K and ambient density of 22.8 kg/m^3. Details of the operating conditions for the Doshisha and Sandia cases are presented in Table 5-1.

The validation of non-reacting fuel spray against experimental measurements are carried out by comparing the liquid penetration length (LPL), vapour penetration length (VPL), and mixture fraction. Validation of reacting spray case is done by comparing computed ID and LOL against experiment measurements. The definitions for the non-reacting and reacting validation parameters used in this work are given in Table 5-2.

Table 5- 1: Operating conditions for non-reacting and reacting spray case.

Test Case	Ambient temperature [K]	Ambient oxygen level [%]	Ambient density [kg/m^3]	Spray configuration
Sandia *n*-heptane	1000	0	14.8	Non-reacting
Sandia *n*-dodecane	900	0	22.8	
Doshisha *n*-heptane	900	21	16.2	Reacting
Sandia *n*-heptane	1000	21	14.8	
		15		
		12		
		10		
		15	30.0	
		12		
		10		
Sandia *n*-dodecane	900	21	22.8	
		15		

Table 5- 2: Definitions of validation parameters for non-reacting and reacting spray case.

Parameters	Definitions
LPL	Maximum axial location from the injector to the location where 99% of the total liquid mass is found.
VPL	Maximum distance from the nozzle outlet to where the fuel mass fraction (or mixture fraction) is 0.1%.
Mixture fraction	Non-reacting mixture fraction is equal to the fuel mass fraction.
ID	The time of maximum gradient dT/dt in temperature is observed after start of injection (ASOI).
LOL	First axial location of Favre-average *OH* mass fraction reaching 2% of its maximum in the domain.

t_{inj} > 4ms: (long injection)	Time-average of LOL from 3 ms to 6 ms ASOI.
t_{inj} < 4ms: (short injection)	Time-average of LOL from start of ignition to end of injection.

The baseline physical models used are listed in Table 5-3. The standard *k-ϵ* turbulence model is used with initial values *k* and *ϵ* estimated to be 0.735 m^2/s^2 and 3.5 m^2/s^3, respectively. The initial value of *ϵ* and *k* are calculated using Equation 5-1 and 5-2, respectively:

$$\epsilon = C_\mu^{0.75} k^{1.5} / l \quad (5\text{-}1)$$

$$k = 1.5\, U_{rms}^2 \quad (5\text{-}2)$$

where l is the initial turbulence length scale and U_{rms} is the mean swirl velocity which is taken to be 0.7 m/s.

Table 5- 3: Baseline physical models.

Computational time-step [s]	2E-7
Turbulence model	Standard *k-ϵ* model $C_{1\varepsilon}$ = 1.44 (default)
Initial turbulent kinetic energy, *k* [m^2/s^2]	0.735
Initial turbulent dissipation rate, *ε* [m^2/s^3]	3.5
Spray breakup model	Reitz-Diwakar C_s = 10.0 (default)
Injector type	Constant-size blob
Spray angle [°]	12.6
Injection pressure [MPa]	
Doshisha *n*-heptane	70
Sandia *n*-heptane	150
Sandia *n*-dodecane	150
Injector orifice diameter [mm]	
Doshisha *n*-heptane	0.2
Sandia *n*-heptane	0.1
Sandia *n*-dodecane	0.09
Evaporation model	Frossling
Heat transfer model	Ranz-Marshall
Drag model	Dynamic

The spray breakup is described using RD spray model by Reitz [257]. The initial spray angle is set constant at 12.6°. The Frossling and Ranz-Marshall correlations are applied to evaporation and heat transfer model, respectively. A built-in dynamic drag model is used. Droplet collision is neglected due to weak effect between sprays. For both Doshisha *n*-heptane and Sandia *n*-heptane case, the liquid *n*-heptane fuel is injected according to a square-shaped injection profile as seen in Figure 5-2(a). The injection profile implemented for the Sandia *n*-dodecane case studies is shown in Figure 5-2(b).

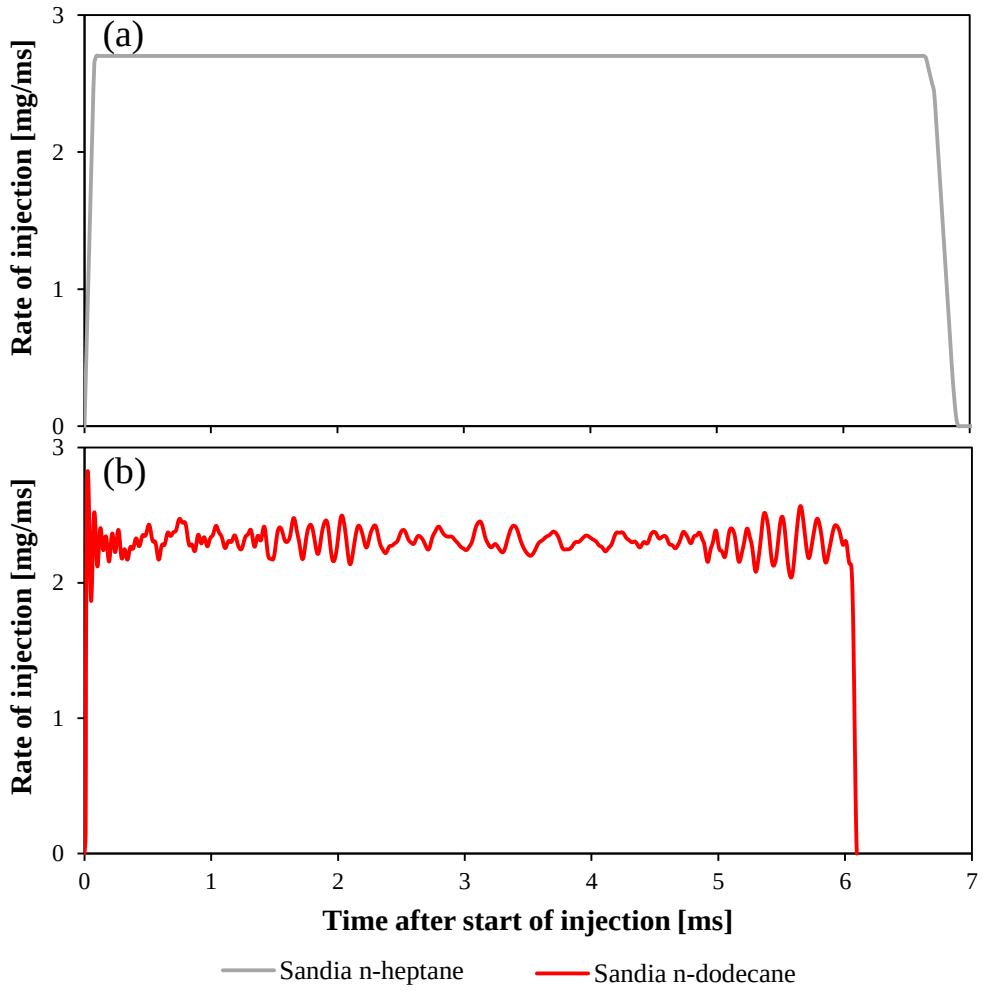

Figure 5- 2: Injection profiles for (a) Sandia *n*-heptane and (b) Sandia *n*-dodecane numerical case studies.

5.4 Non-reacting Sandia Spray Cases

5.4.1 Mesh and Time-step Independence Test

The primary objective of non-reacting case is to establish a set of reference model constants that can then be used for reacting flow, under the assumption that the physical processes that lead to the liquid breakup, evaporation, and turbulent mixing of air and fuel upstream of the lifted-flame remain largely unaffected by the flame at downstream location. Mesh and time-step independence tests are first carried out to decide on a suitable mesh and time-step that ensures grid and time-step convergence. Both independence tests are carried out for Sandia *n*-heptane and *n*-dodecane cases by comparing the computed LPL and VPL. As the Doshisha *n*-heptane case lacks non-reacting experimental data, the independence tests are not performed for it. Instead, the best choice for mesh and time-step decided from the Sandia *n*-heptane independence tests are used in all Doshisha numerical case studies.

The mesh independence test is carried out using three different mesh sizes of 0.25 mm, 0.50 mm and 1.00 mm, which represent fine, semi-fine and coarse mesh, respectively. The time-step test is carried with different time-steps, ranging from 2E-6 to 5E-8 s. The baseline settings in Table 5-1 are used here. As seen in Figure 5-3, the LPL and VPL are shown to increase as the mesh size gets smaller. Both LPL and VPL profiles for the Sandia *n*-dodecane case show that the mesh with 0.50 mm size attained mesh convergence as only a minor change is observed when a smaller size (0.25 mm) is used.

Although the mesh 0.50 mm has attained grid convergence based on the predicted VPL for the Sandia *n*-heptane case, the LPL profile do not exhibit the same convergence. Therefore, to choose the best mesh configuration between the two mesh sizes (0.50 mm and 0.25 mm), other criterias have to be considered:

i) The computational time has to be short.

ii) The standard deviation of computed LPL has to be less than the measured standard deviation of 0.4 mm [265].

The execution time and standard deviation of LPL for both meshes are given in Table 5-4. It shows that the mesh with 0.50 mm size has a shorter runtime relative to the one with 0.25 mm. Despite both meshes having smaller standard deviation as compared to the experimental one, the LPL predicted by the mesh of 0.50 mm size is less fluctuating as seen in Figure 5-4. Therefore, the mesh of 0.50 mm is chosen as the final mesh for the Sandia *n*-heptane case.

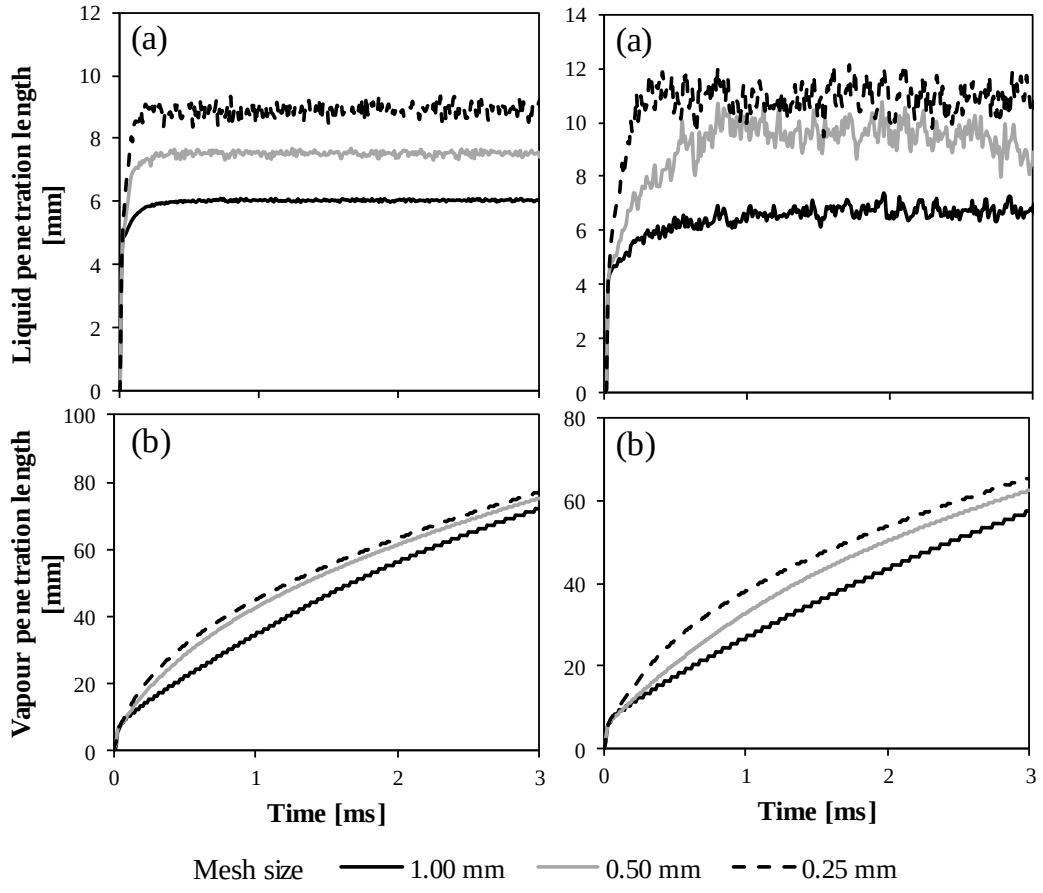

Figure 5- 3: Comparison of the computed (a) LPL and (b) VPL using different mesh sizes for the Sandia *n*-heptane case (left) and Sandia *n*-dodecane case (right).

Table 5- 4: The mean LPL, standard deviation of LPL and execution time (wall-clock time) for Sandia *n*-heptane case with mesh size 0.50 mm and 0.25 mm.

Mesh Size	Mean LPL [mm]	Standard deviation of LPL [mm]	Execution Time [s]
0.50 mm	7.53	0.044	6347
0.25 mm	8.90	0.115	11711
Measured standard deviation for LPL = 0.4 mm			

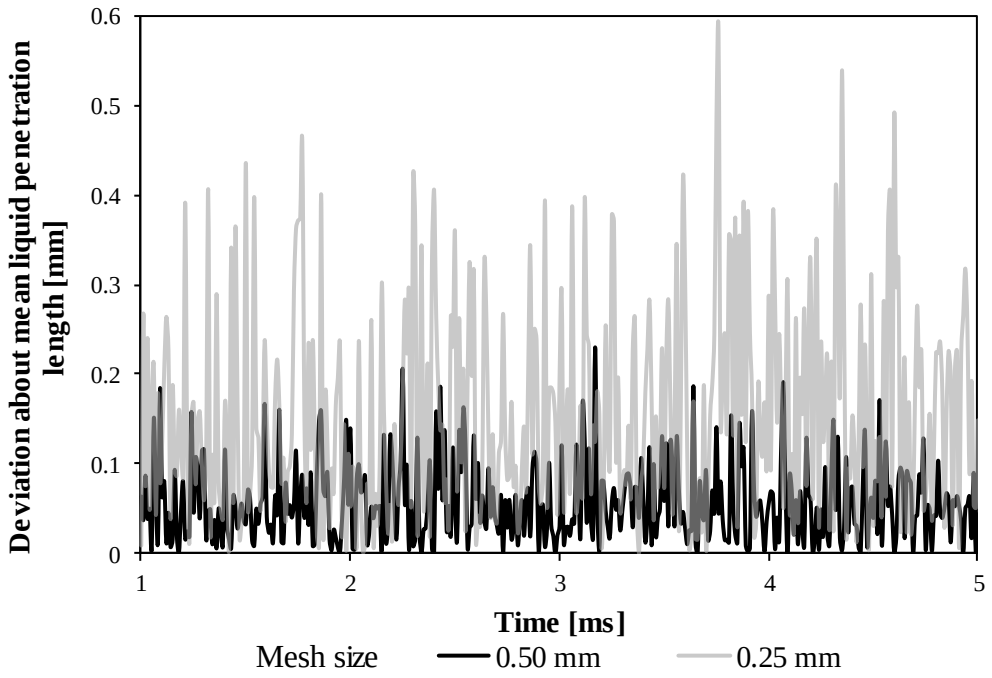

Figure 5- 4: The deviation about computed mean LPL for mesh size of 0.50 mm and 0.25 mm.

After finalising on a suitable mesh size, a time-step test is to be carried out. The LPL and VPL at different time-steps for mesh size 0.50 mm are presented in Figure 5-5 for Sandia *n*-heptane and *n*-dodecane spray case. The predicted VPL profiles for both cases are observed to be less sensitive to the time-step as it decreases slightly from 2E-6 to 5E-8 s. Conversely, the predicted LPLs in both cases are

shown to decrease as the time-step decreases from 2E-6 to 2E-7 s. From Figure 5-5, convergence of time-step for the Sandia *n*-heptane and *n*-dodecane case are attained for the time-step 5E-7 s and 2E-7 s, respectively. However, as lift-off length is found during preliminary studies (not presented in this thesis) to be highly dependent on time-step sizes, the predicted lift-off lengths using the time-step sizes chosen are different than those predicted using smaller time-step sizes. Hence, a smaller time-step sizes of 2E-7 and 1E-7 s are concluded to reach time-step independence for Sandia *n*-heptane and *n*-dodecane case, respectively.

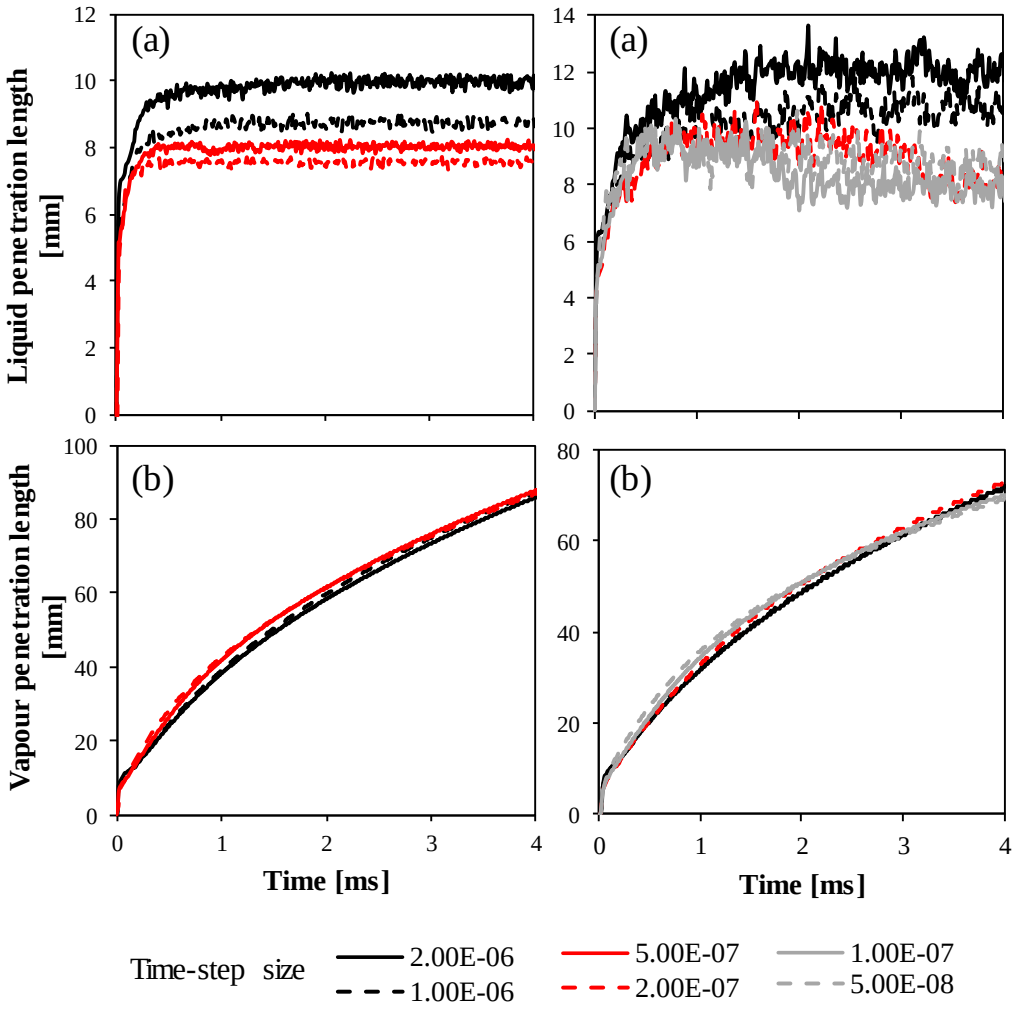

Figure 5- 5: Computed (a) LPL and (b) VPL at different time-steps using mesh size of 0.50 mm for Sandia *n*-heptane case (left) and Sandia *n*-dodecane case (right).

5.4.2 Parametric Study for Spray and Turbulence Model

Next, parametric studies are performed using the non-reacting spray conditions to obtain a set of optimum configurations for the CFD simulations. The test cases for parametric studies are tabulated in Table 5-5. Here, only the results for the Sandia *n*-heptane case are shown as similar trends are captured for the Sandia *n*-dodecane case. The mesh size and time-step used here are 0.50 mm and 2E-7 s, respectively.

Table 5- 5: Parametric study cases for spray and turbulence models.

Models/ Parameters	Test Cases
Type of turbulence model	Standard *k*- ϵ (baseline), RNG *k*- ϵ
Standard *k*- ϵ model	
Model constant, $C_{1\epsilon}$	1.44 (baseline), 1.30, 1.50
RD Model	
Time stripping constant, C_s	10.0 (baseline), 9.0, 11.0

5.4.2.1 Parametric Study: Turbulence Model and Model Constant

Based on Figure 5- 6(a), only a minor difference is observed in the LPL predicted using RNG *k*-ϵ model and standard *k*-ϵ model. Conversely, the RNG *k*-ϵ model predicts higher VPL at the early stage of injection but then slowly converges to the VPL predicted by the standard *k*-ϵ model. Despite converging later on, the standard *k*-ϵ model produces result that better fit with the experimental data (see later in Figure 5-8). Based on the results obtained, standard *k*-ϵ model is chosen and used in all numerical simulations in the present work. In addition, the effect of changing the corresponding model constant $C_{1\epsilon}$ is also studied here and the results are shown in Figure 5-6. In Figure 5-6(b), it is observed that the VPL is highly sensitive to the changes in $C_{1\epsilon}$ value, whereby the length increases with increasing $C_{1\epsilon}$ and vice versa. As for the LPL sensitivity, an increment in $C_{1\epsilon}$ shows insignificant effect on LPL while a decrease in $C_{1\epsilon}$ causes the LPL to decrease.

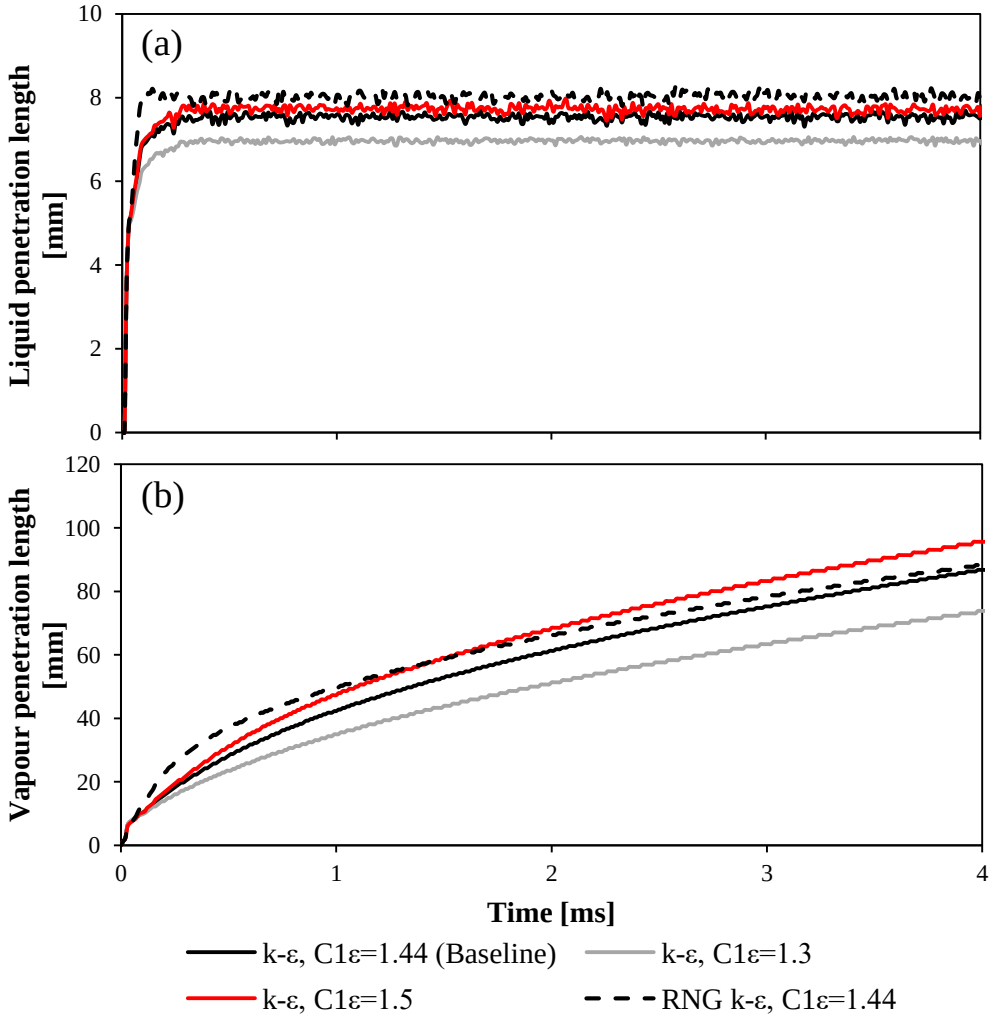

Figure 5- 6: Computed (a) LPL and (b) VPL using different turbulence model and $C_{1\epsilon}$ values of standard *k-ϵ* model for Sandia *n*-heptane case.

5.4.2.2 Parametric Study: Spray Breakup Model Constant

The constant C_s is the time factor constant for stripping breakup whereby liquid is sheared or stripped from the droplet surface. The empirical coefficient C_s is in the range of 2 to 20 [267]. Referring to Figure 5-7, LPL varies with C_s value while VPL is not dependent on C_s value. It is observed that LPL increases as C_s increases and vice versa. The increase in C_s means that the characteristic time scale of the breakup process is increased, consequently reducing the breakup rate, thus leading to the higher LPL observed.

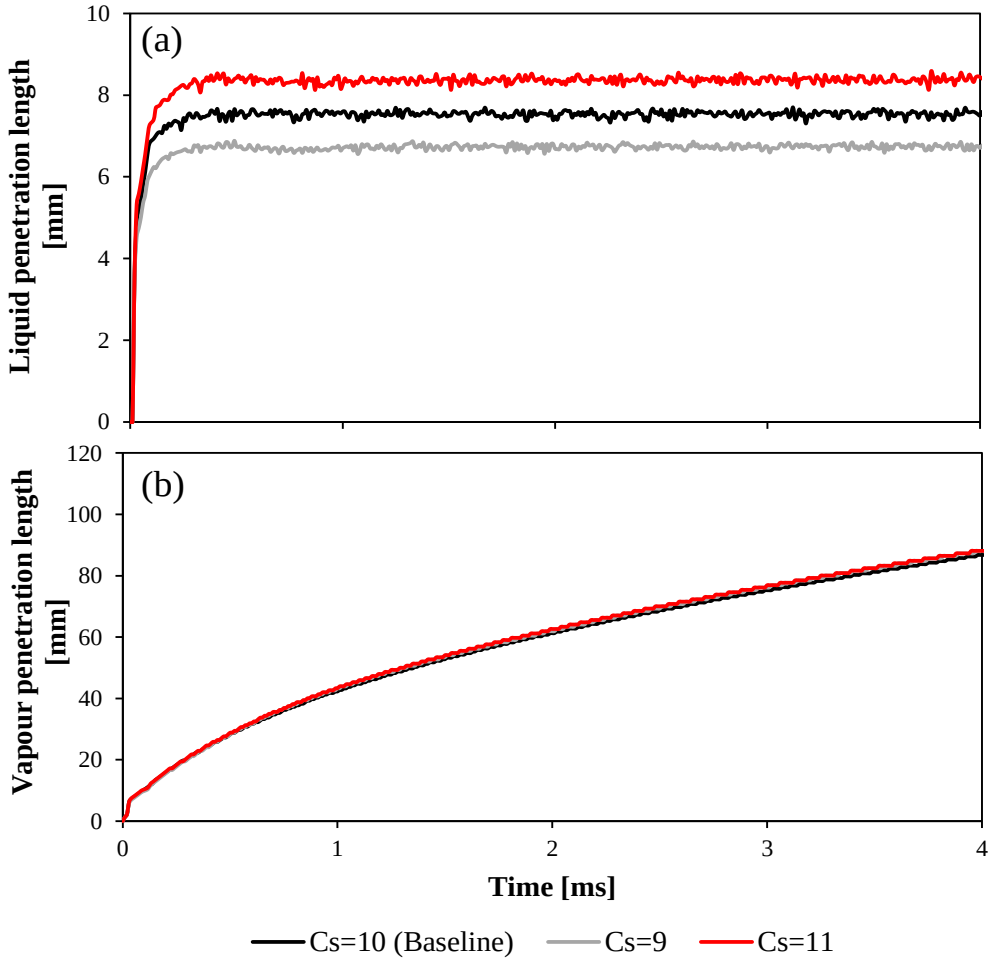

Figure 5- 7: Computed (a) LPL and (b) VPL using different C_s values of RD spray model for Sandia *n*-heptane case.

5.4.2.3 Best-fit Numerical Setup

Through parametric studies conducted in Section 5.4.2, the spray characteristics are found to be sensitive to the turbulence model constant ($C_{1\epsilon}$ in the ϵ equation for the standard *k*-ϵ model) and the time factor for spray stripping (C_s) in RD spray model. The model constants for turbulence ($C_{1\epsilon}$) and spray breakup (C_s) have to be calibrated to match experimental VPL and LPL. The calibrated C_s and $C_{1\epsilon}$ values for Sandia cases are shown in Table 5-6. These calibrated constants are carried over to the reacting numerical studies in Section 5.5 and in later simulations throughtout this thesis. It is noteworthy to mention that the default model constants for $C_{1\epsilon}$ and C_s are implemented for the Doshisha *n*-heptane case studies due to the absence of non-reacting measurement.

Table 5- 6: Best-fit numerical setup for non-reacting and reacting Doshisha and Sandia spray case.

Model/Parameters	Doshisha *n*-heptane	Sandia *n*-heptane	Sandia *n*-dodecane
Mesh size [mm]	0.50	0.50	0.50
Time-step size [s]	2E-7	2E-7	1E-7
Turbulence model	Standard k-ϵ	Standard k-ϵ	Standard k-ϵ
Model constant $C_{1\epsilon}$	1.44	1.53	1.58
Spray breakup model	Reitz-Diwakar	Reitz-Diwakar	Reitz-Diwakar
Model constant C_s	10.0	11.5	10.5

Comparisons between the computed and measured penetration lengths are provided in Figure 5-8(a) and Figure 5-9(a) for Sandia *n*-heptane and *n*-dodecane, respectively using default and calibrated model constants. Overall the tuned model shows excellent agreement with the LPL and VPL measurements for both Sandia cases. The accurate jet penetration lengths shown imply a good prediction of air entrainment.

Computed and measured mean radial mixture fraction profiles for the Sandia cases are next compared. Figure 5-8(b) shows the mean radial mixture fraction profiles for Sandia *n*-heptane case, whereas Figure 5-9(b) shows the mean radial mixture fraction profiles for Sandia *n*-dodecane case. For the Sandia *n*-heptane case, a good agreement of mean mixture fraction profiles are found at 0.49 ms ASOI, x=17 mm, and at 6 ms ASOI, x=20 mm. Although the mean computed mixture fraction profile is slightly underestimated at 6 ms ASOI, x=40 mm, it is still in the acceptable range. As for the *n*-dodecane case, the mixture fraction profiles agrees with the experimental data although the mean mixture fraction profiles at both x=25 mm and 45 mm from the injector are slightly underestimated as compared to the experimental results. Overall the mixture fraction trends are well-captured implying that the air-fuel distributions are reasonably predicted by the model.

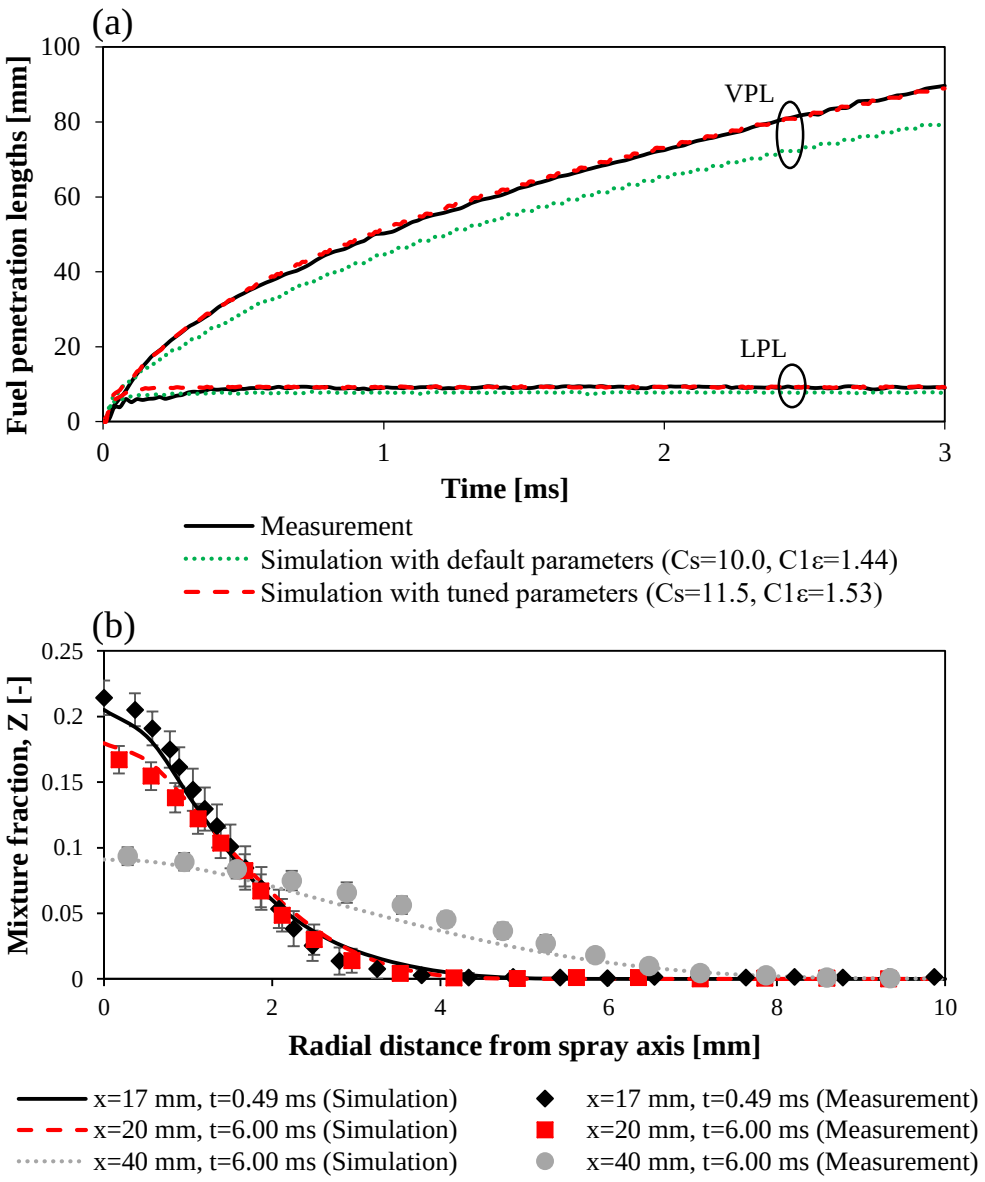

Figure 5- 8: (a) Comparison of LPL and VPL for non-reacting Sandia *n*-heptane spray case. (b) Comparison of simulated and experimental radial mixture fraction for Sandia *n*-heptane spray case.

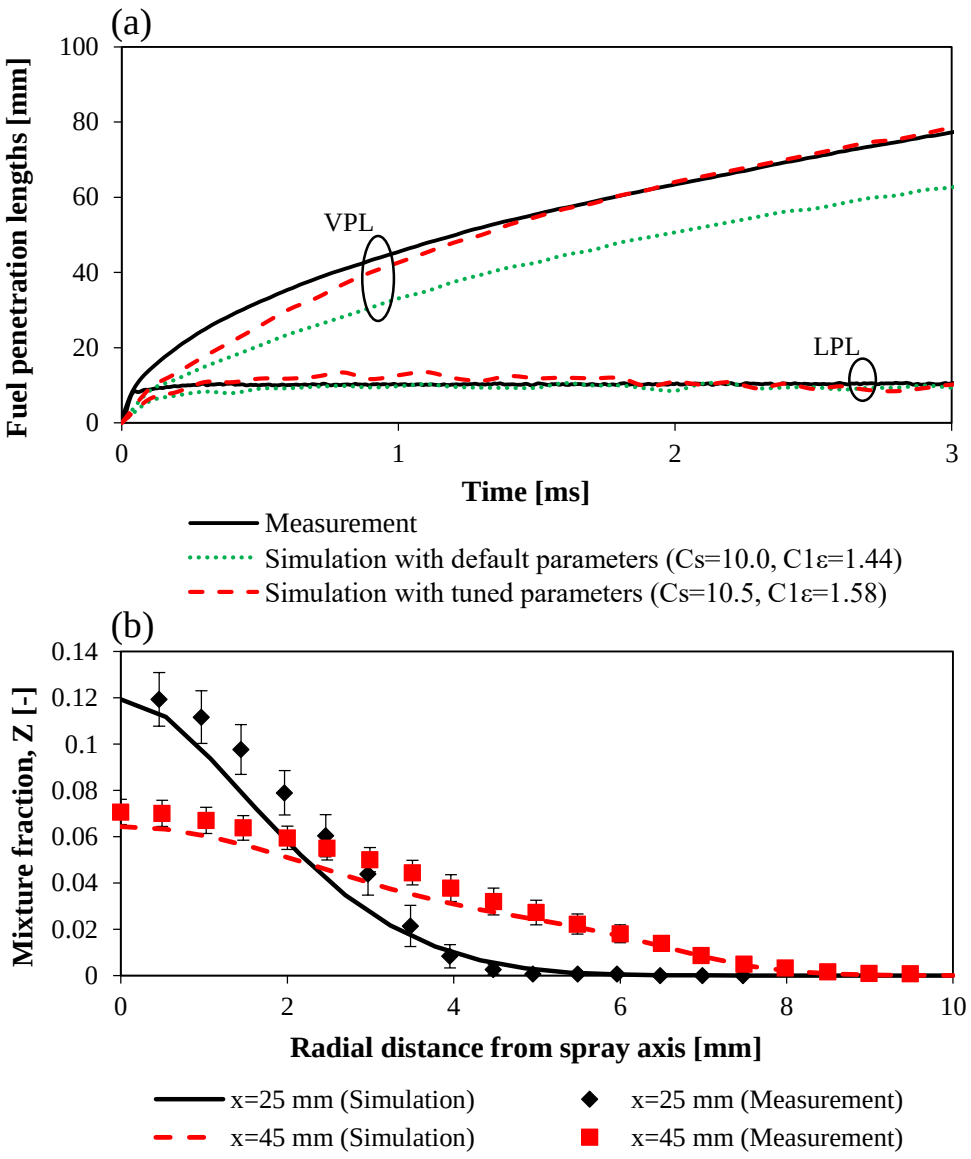

Figure 5- 9: (a) Comparison of LPL and VPL for non-reacting Sandia *n*-dodecane spray case. (b) Comparison of simulated and experimental radial mixture fraction of Sandia *n*-dodecane spray case at *t*=1.5 ms ASOI.

5.5 Reacting Sandia and Doshisha Spray Case

5.5.1 Chemical Mechanism for Sandia *n*-Heptane and *n*-Dodecane Case

In this section, reacting sprays are simulated over a wide range of conditions. The spray and turbulence models and constants are kept the same as the non-reacting spray case. A suitable reduced chemical mechanism has to be chosen to provide a good balance between accuracy and computational cost.

Three *n*-heptane reduced mechanisms [223,226,268], shown in Table 5-7, are examined by comparing their prediction of ID and LOL against experiment measurements. One of the reduced mechanism is the Nottingham Diesel Surrogate (NDS) mechanism, which was developed by Pang et al. [268]. It was built based on the *n*-heptane oxidation model proposed by the Combustion Engine Research Center (CERC) in Chalmers University of Technology. NDS mechanism contains 46 species and 112 reactions that are essential to diesel ignition and combustion. It has been used in several combustion studies [234,268–270]. Another similar sized reduced mechanism is developed by Liu et al. [223], with 44 species and 112 reactions. The mechanism is a skeletal form of a detailed mechanism for *n*-heptane [271]. The validation studies are documented in [223]. This mechanism has been used in various *n*-heptane spray studies [272–276]. The third reduced mechanism examined is the mechanism developed by Lu et al. [226], having 68 species and 283 reactions. This is a skeletal mechanism derived from the Lawrence Livermore National Laboratory (LLNL) detailed mechanism which consists of 561 species. Validation details of the skeletal mechanism with respect to the detailed mechanism can be seen in [226], while its application in diesel spray study can be seen here [218].

For the Sandia *n*-dodecane case, two mechanisms are examined which are also presented in Table 5-7. The first is an *n*-dodecane skeletal mechanism developed by Luo et al. [237]. It comprises 105 species and 420 reactions. The reduction started from the detailed mechanism for *n*-alkanes developed by the LLNL. This mechanism has been applied in various spray combustion simulations [219,237,239,277]. The second mechanism to be examined is a smaller mechanism

[278] which is recently developed by further reducing the skeletal mechanism developed by Luo et al. [237]. It has 54 species and 269 reactions where the kinetics are optimised for spray-flame applications [278]. It has been applied to study soot formation in *n*-dodecane spray flames [279].

Table 5- 7: Summary of the reduced mechanisms for *n*-heptane and *n*-dodecane fuel examined.

Fuel type	Mechanism Name	No. of species	No. of reaction	Reference
n-heptane	NDS-46	46	112	[268]
	LIU-44	44	112	[223]
	LU-68	68	283	[226]
n-dodecane	LUO-105	105	420	[237]
	YAO-54	54	269	[278]

5.5.2 ID and LOL Predictions: Sandian *n*-heptane and Doshisha *n*-heptane

As the Doshisha *n*-heptane case only has a single operating condition, the performance of reduced mechanism in predicting ID and LOL are examined under the Sandia *n*-heptane conditions, where the oxygen contents are varied from 10% to 21% and at ambient density of 14.8 and 30 kg/m^3. The final chosen reduced *n*-heptane mechanism is then used in all subsequent Doshisha numerical studies in this work. The ID and LOL at low density are shown in Figure 5-10, while the high density results are depicted in Figure 5-11. The percentage errors of ID and LOL predictions for low and high densities are shown in Table 5-8. At low density, LIU-44 performs poorly relative to other mechanisms with a maximum relative difference of 78% for both ID and LOL predictions. Both reduced mechanism NDS-46 and LU-68 provide good prediction of ID and LOL with relative differences lower than 24% within oxygen contents of 21% to 12%. However, at the lowest oxygen content of 10%, the predicted ID for NDS-46 has a relative difference of 43%, whereas LU-68 predicts an ID with a higher relative difference of 227%. This observation of overpredicted ID at low O_2 concentration has been reported by Pei et al. [280], Bhattacharjee and co-worker [219] and also Pang et al [234]. Despite

overprediction of ID, both mechanisms perform relatively well in predicting LOL at 10% oxygen content.

At high density, all three mechanisms manage to predict ID which coincide well with the experimental data, while having a maximum relative difference of 18%. The mechanisms also show good prediction of LOL with a maximum 28%, except for LIU-44 which predicts LOL with a higher maximum relative difference of 54%. Based on the performance in predicting ID and LOL, the mechanism NDS-46 is chosen as the best mechanism that is able to capture the ID and LOL with reasonable accuracy, while having cheaper computational cost. This mechanism is used in all subsequent Sandia *n*-heptane and Doshisha *n*-heptane numerical studies in this thesis.

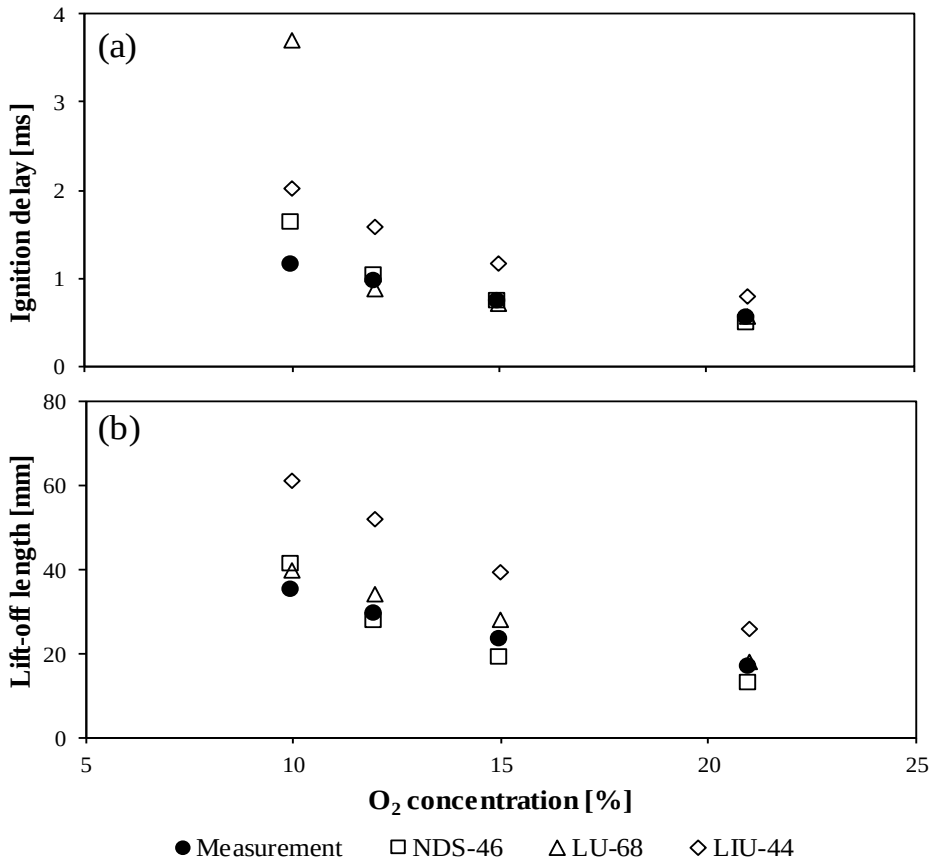

Figure 5- 10: Comparison of simulated ID and LOL for reacting Sandia *n*-heptane spray case at low density and varying oxygen levels with experimental results using various reduced mechanism.

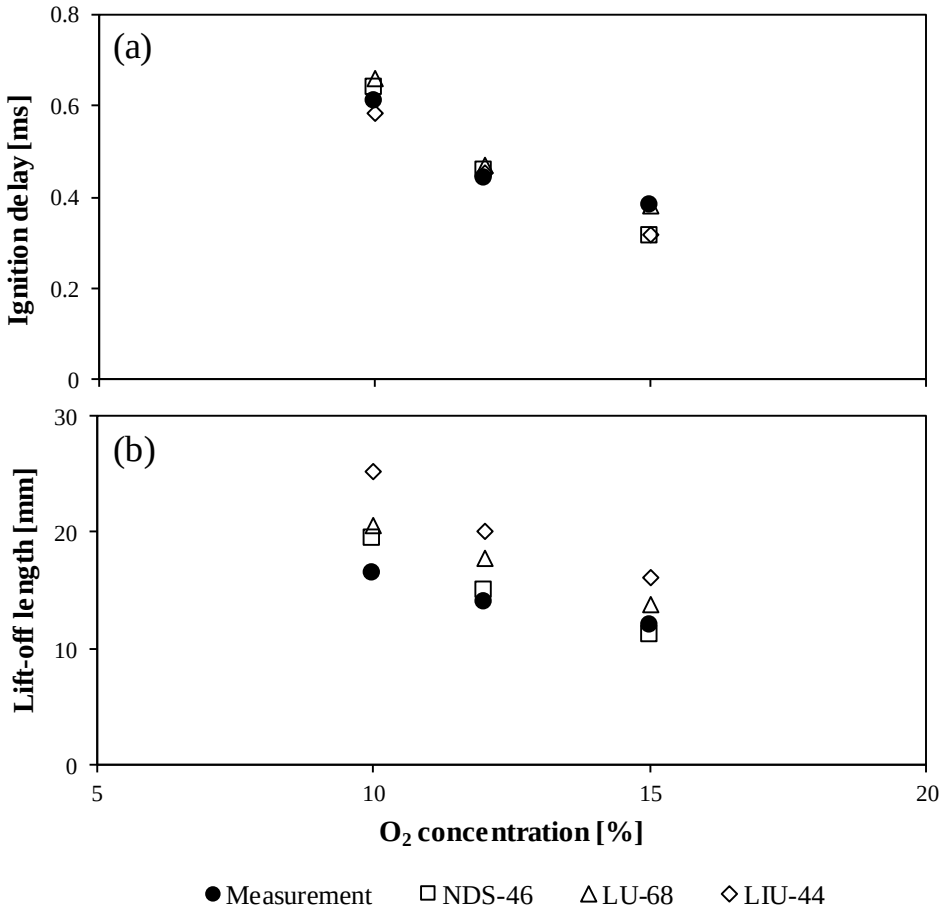

Figure 5- 11: Comparison of simulated ID and LOL for reacting Sandia *n*-heptane spray case at high density and varying oxygen levels with experimental results using various reduced mechanism.

Table 5- 8: Percentage error for ID and LOL for different reduced *n*-heptane mechanism at different ambient densities and oxygen levels.

Ambient density [kg/m^3]	Ambient O_2 level [%]	Percentage error for ID [%]			Percentage error for LOL [%]		
		NDS-46	LIU-44	LU-68	NDS-46	LIU-44	LU-68
14.8	21	11.3	48.9	5.7	23.4	51.8	7.6
	15	0.0	58.2	5.5	19.7	68.3	20.5
	12	7.3	65.2	8.6	5.5	78.0	17.5
	10	43.4	78.8	227.4	17.7	74.3	14.0
30	15	17.5	16.3	0.7	6.7	35.0	16.4
	12	3.8	3.0	6.8	7.6	44.0	27.6
	10	5.0	4.6	7.9	18.5	53.7	25.5

The reacting Doshisha *n*-heptane case is carried out using the NDS-46 mechanism according to the operating condition as shown in Table 5-1. Figure 5-12 shows the computed HRR as compared to experimental data. The premixed combustion peak heat release rate is observed to be very large as compared to the experimental data. Although the peak HRR is overpredicted, the time of peak HRR is predicted to be approximately 0.7 ms ASOI, similar to that of the experimental measurement. The rate-controlled combustion after the premixed combustion is predicted to be higher than the measured data. Despite the overprediction by NDS-46 mechanism, the overall trend of the HRR profile qualitatively coincides with the measure data. The ID is accurately predicted by simulation to be 0.69 ms while experimental ID is around 0.70 ms. However, the LOL is underpredicted where simulated LOL is at 23 mm while experimental LOL is 40 mm. This can be attributed to the difference in LOL definition used in both studies as the experimental LOL definition for the Doshisha *n*-heptane case was not explicitly reported. Despite this, it is shown in Chapter 6 that the predicted soot distribution and position correspond reasonably well with the experimental observation.

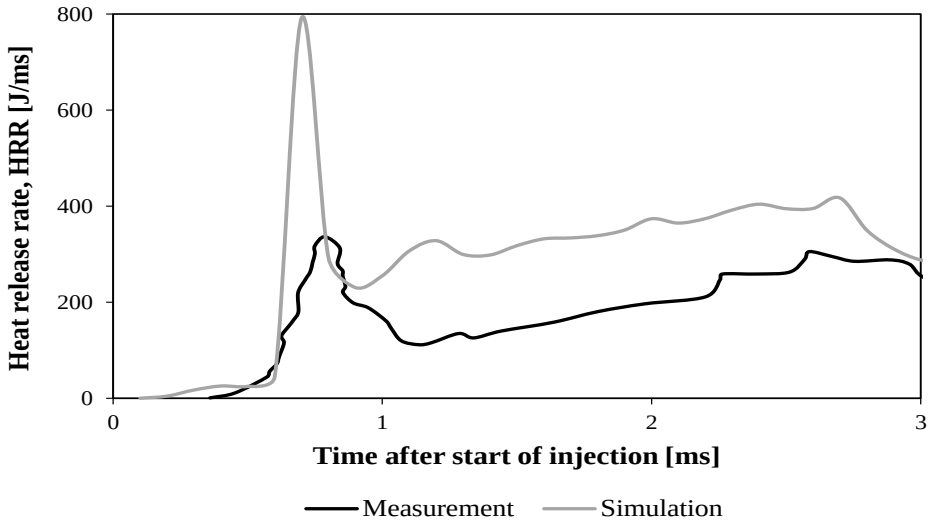

Figure 5- 12: HRR profile for reacting Doshisha *n*-heptane spray case at density 16.2 kg/m^3, temperature of 900 K and ambient O_2 concentration of 21% [33]**.**

5.5.3 ID and LOL Predictions: Sandian *n*-Dodecane

The predicted ID and LOL for both mechanisms are shown in Figure 5-13. The associated percentage errors are presented in Table 5-9. The simulated IDs are overpredicted for both O_2 concentration levels with relative differences of 68%, using LUO-105. Similar overestimations of ID were also reported in [237,277,281] when the same combustion chemistry was used. Despite the overestimated ID, the computed LOLs are reasonable predicted. The computed LOLs for the 15% and 21% O_2 concentration cases have relative differences of 9.6% and of 31.5%, respectively. The predictions for both ID and LOL is relatively better when using the smaller mechanism (YAO-54). The maximum relative difference for the computed IDs using YAO-54 is 25%. The relative differences for the LOL predicted using the smaller mechanism are below 10%. From these findings, YAO-54 mechanism is shown to be superior over the other candidate in predicting the ID and LOL of a reacting spray. However, preliminary soot studies (not presented in this thesis) showed that the mechanism performed poorly in predicting soot distribution. Therefore, LUO-105 mechanism is chosen as the most suitable *n*-dodecane mechanism and is used throughout all Sandia *n*-dodecane numerical studies.

Table 5- 9: Percentage error for ID and LOL for different reduced *n*-dodecane mechanism at different oxygen levels.

Ambient density [kg/m^3]	Ambient O_2 level [%]	Percentage error for ID [%]		Percentage error for LOL [%]	
		LUO-105	YAO-54	LUO-105	YAO-54
22.8	21	66.7	18.4	9.6	1.9
	15	68.3	25.2	31.5	9.8

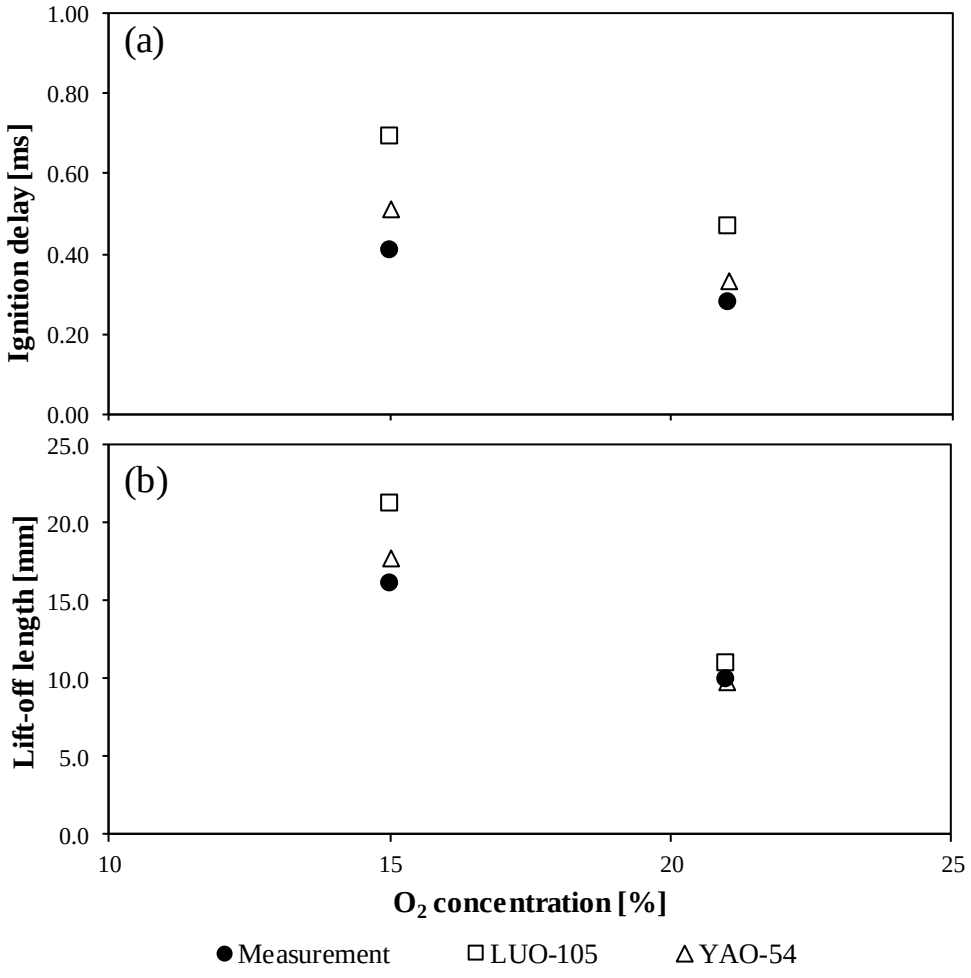

Figure 5- 13: Comparison of simulated ID and LOL for reacting Sandia *n*-dodecane spray case with experimental results using various reduced mechanism at different oxygen levels.

5.6 Concluding Remarks

2-D CFD simulations are performed to study the spray combustion phenomena within a constant volume combustion chamber. LPL and VPL are replicated for non-reacting Sandia *n*-heptane and *n*-dodecane spray cases. The NDS *n*-heptane reduced mechanism (46-species) and the skeletal mechanism (105-species) are chosen to simulate *n*-heptane and *n*-dodecane spray cases, respectively. The predicted ID using NDS mechanism at low density shows a maximum relative difference of 43% at oxygen level of 10%. Otherwise, the relative differences are predicted to be less than 12% at other oxygen levels. At higher ambient density of 30 kg/m^3, the predicted LOL at all oxygen levels are below 24%, with the maximum relative difference at oxygen level of 21%. The implementation of NDS reduced mechanism in Doshisha *n*-heptane case is shown to predict ID and LOL with reasonable accuracy. Despite predicting longer ID at both 21% and 15% oxygen levels, the *n*-dodecane skeletal model is able to capture the LOLs at both oxygen levels with relative differences of less than 32%.

In general, the chosen *n*-heptane and *n*-dodecane mechanisms are able to capture the combustion characteristics at different oxygen levels and ambient densities. These findings provide a good foundation to proceed into numerical studies on soot processes for reacting spray combustion in constant volume combustion chamber.

CHAPTER 6
VALIDATION OF LAGRANGIAN SOOT TRACKING METHOD

6.1 Introduction

Chapter 6 outlines the validation of the LST model which was detailed in Chapter 4. The validation of LST is carried out by comparing the temporal and steady-state SVF predictions with measurement data. The comparative performance between the LST model and Eulerian method are compared and discussed. In addition to validating with SVF, the LST model is also validated by comparing the primary soot size distribution with experimentally measured size distributions. The validation case studies are carried out for Doshisha *n*-heptane, Sandia *n*-heptane and Sandia *n*-dodecane spray case setups. Section 6.2 and 6.3 discuss the validation of the *n*-heptane cases (Doshisha *n*-heptane and Sandia *n*-heptane). The validation of *n*-dodecane case is carried out in Section 6.4 by comparing the SVF distribution and PSDF with experimental measurements. Lastly, the key results are highlighted in Section 6.5.

6.2 Validation in Doshisha *n*-Heptane Case Studies

The validation of LST in Doshisha *n*-heptane case setup is performed based on the operating conditions shown in Table 5-1. The operating conditions for the Doshisha *n*-heptane case are set to be at an ambient oxygen level of 21%, ambient temperature of 900 K and ambient density of 16.2 kg/m^3. In this numerical case study, the SVF and mean diameter distributions are computed using the LST and Eulerian soot model and their performance are compared against one another. The soot prediction results are also compared against the MOM simulation results and the time-resolved LII measurement obtained by Ito et al. [33].

6.2.1 Temporal and Spatial Soot Volume Fraction Evolution

The SVF distributions at 1.0 ms, 1.5 ms and 2.0 ms ASOI are shown in Figure 6-1. The LST model is demonstrated to capture the SVF prediction well when compared with the measured SVF. The transient evolution of SVF predicted by LST model from 1.0 ms to 2.0 ms coincides qualitatively well with the MOM results which show the peak soot forming at the periphery of the jet and then slowly merging at the spray axis as the soot plume propagates downstream. These phenomena are also captured by the Eulerian method although the predicted SVF is shown to merge earlier than the one by LST. By observing the SVF prediction at 1.0 ms ASOI, the Eulerian results show similarity with the ones predicted by MOM where both show that the SVF starts to form away from the axial region. However, at 1.5 ms and 2.0 ms ASOI, the Eulerian SVF starts to merge along the central axis as the soot region moves further downstream.

6.2.2 Soot Particle Size Distribution

Comparisons of simulated and experimental mean primary soot diameter distribution are given in Figure 6-2. The soot diameter distribution observed in the experiment and those computed using MOM by Ito et al. [33] are initially small throughout the soot cloud at 1.0 ms. The soot particles then slowly increase in size, starting from the periphery of the jet as the soot cloud moves downstream. These features are replicated using the LST model. On the contrary, the Eulerian method fails to capture this evolution. At 1.0 ms, the Eulerian result is still comparable with the MOM and LST results. However, at later times, the Eulerian method predicts that the peak soot size to be at the head of the spray jet rather than the periphery of the flame. This implies that the Eulerian method is unable to predict the soot sizing distribution despite showing reasonably well prediction for SVF in Section 6.2.1. This may be attributed to the mono-disperse assumption considered by the Eulerian method. This assumption lead to an inaccurate prediction of soot size as the particle size distribution is lost. As for its Lagrangian counterpart, the poly-disperse assumption is considered where all the Lagrangian particles evolve independently and retain their individual size and position in the combustion domain.

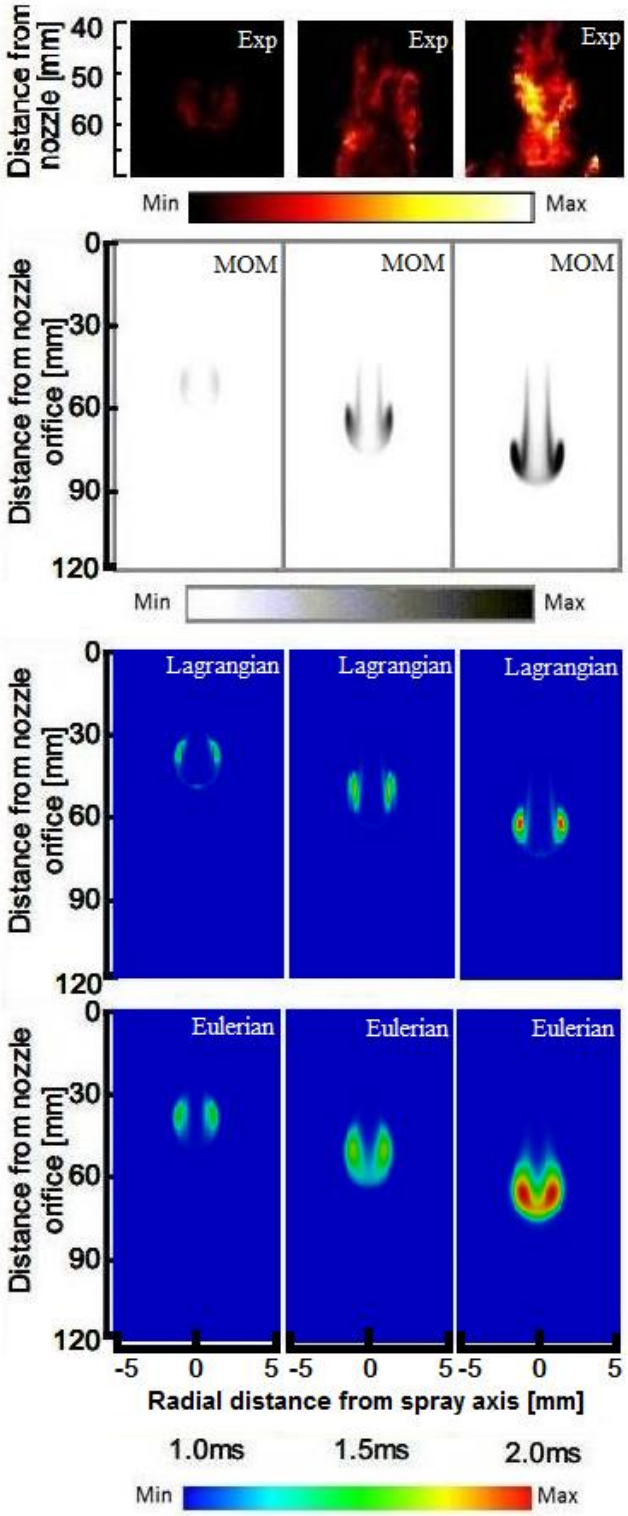

Figure 6- 1: Temporal and spatial SVF distribution compared between experimental [33]**, MOM simulation** [33]**, Eulerian results and LST results at time-steps from 1.0 ms to 2.0 ms for Doshisha *n*-heptane test case.**

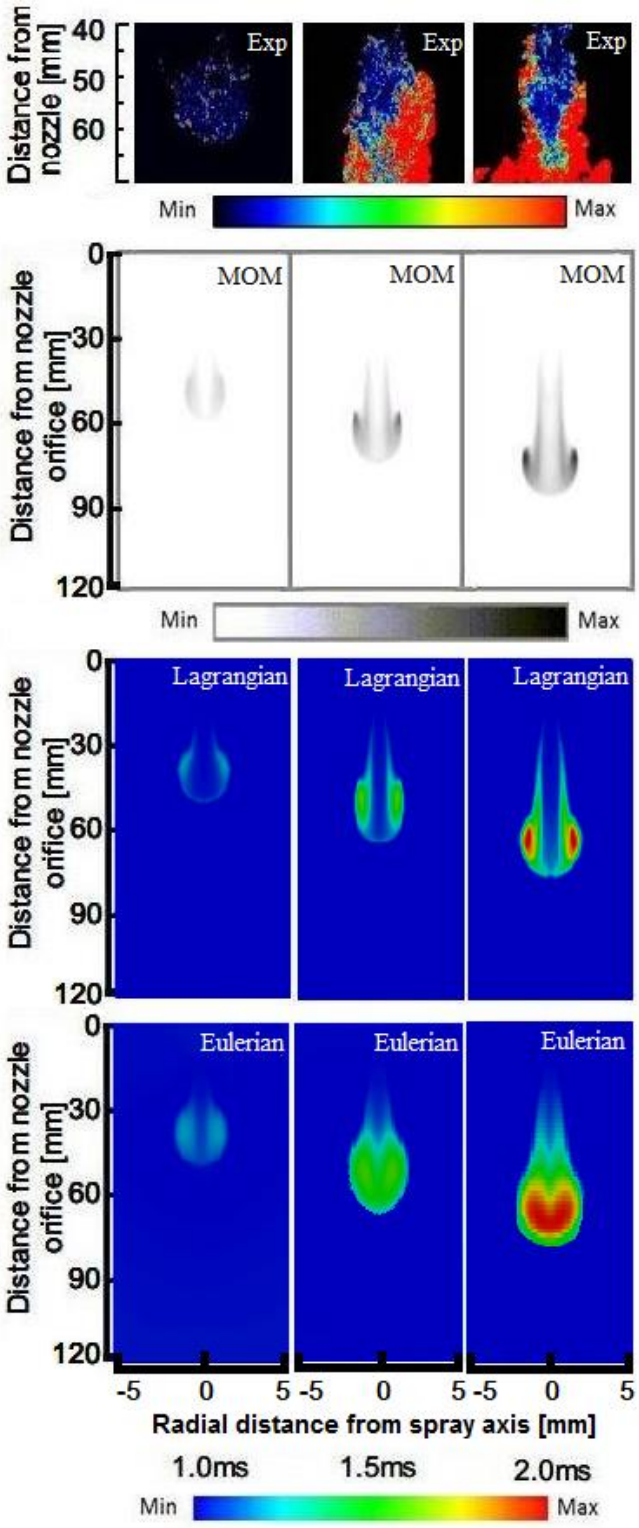

Figure 6- 2: Temporal and spatial mean soot diameter distribution compared between experimental [33]**, MOM simulation** [33]**, Eulerian results and LST results at time-steps from 1.0 ms to 2.0 ms for Doshisha *n*-heptane test case.**

6.3 Validation in Sandia *n*-Heptane Case Studies

The validation of LST in Sandia *n*-heptane case setup is performed based on the operating conditions shown in Table 5-1. The validation is carried out at ambient oxygen levels of 21% to 12%, where the ambient temperature is 1000 K and ambient densities of 14.8 and 30.0 kg/m^3. The validation of LST is not carried out for oxygen level of 10% at both densities as it is shown in Chapter 5 to possess the highest relative differences in ID and LOL among other oxygen levels. In this numerical case study, the SVF computed using the LST and Eulerian method are compared against measured SVF distributions.

6.3.1 Temporal and Spatial Soot Volume Fraction Evolution

Before studying the soot distribution at steady-state, the temporal evolution of soot cloud is studied by comparing the simulated soot distribution by Lagrangian method with the experimental results. Figure 6-3 illustrates the comparisons of simulated and experimental soot cloud evolutions at selected time-steps before reaching the quasi-steady state. Only the result of test case with ambient O_2 levels of 21% at low ambient density is presented as the results at other O_2 levels and higher ambient density follow the same trend. Experimental images are snapshots extracted from the videos provided by ECN [265]. At approximately 1.0 ms ASOI, a noticeable soot cloud is observed in the experimental images, but only a small amount of soot is predicted at the periphery of the jet, as seen in Figure 6-3. The computed and experimental sooty jets further develop towards the downstream, which eventually leads the soot formation event to a quasi-steady state at a region 40 to 80 mm from the injector tip.

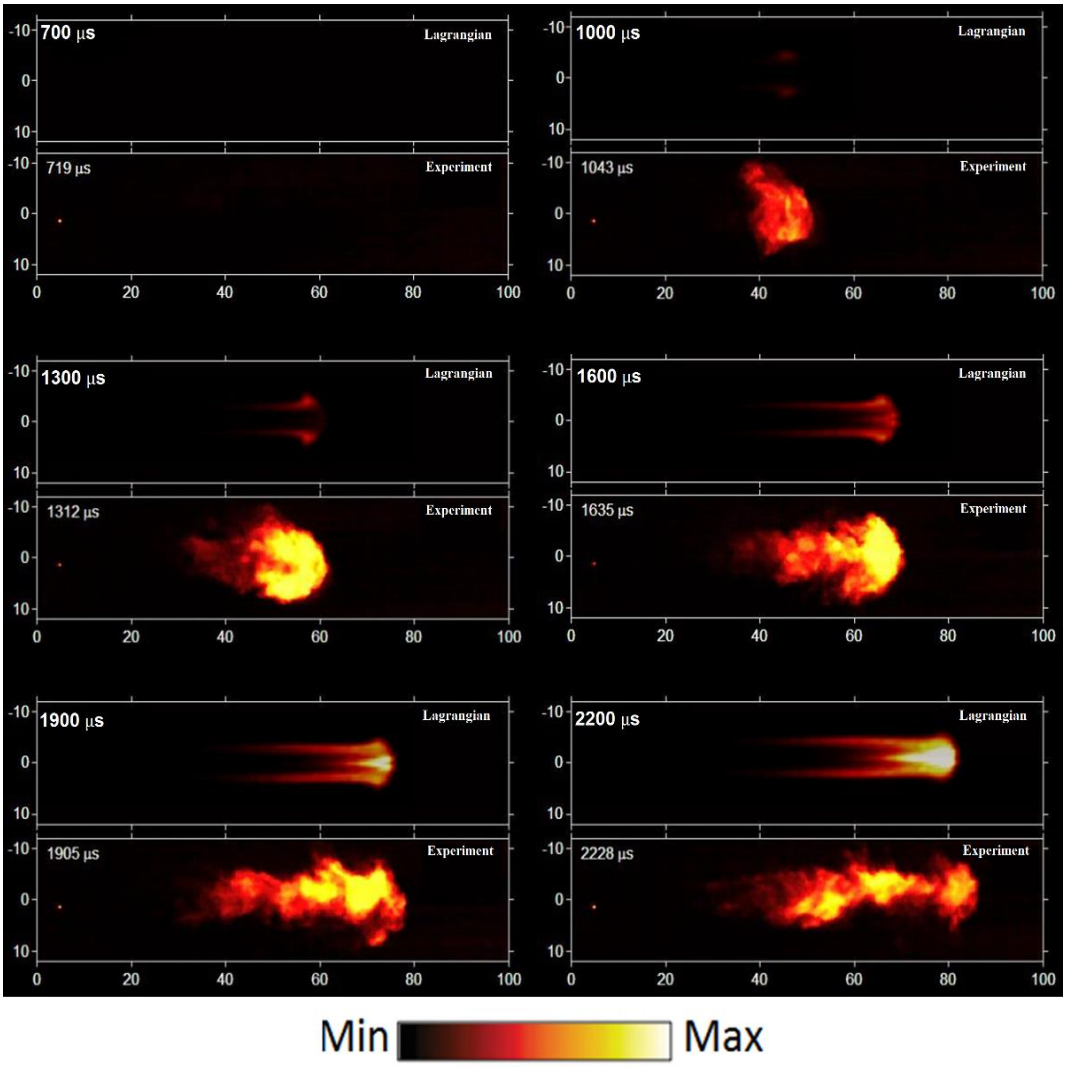

Figure 6- 3: Comparison of simulated SVF distribution and experimental observation [265] **at 21% O_2 level with ambient density of 14.8 kg/m^3 and ambient temperature of 1000 K.**

6.3.2 Steady-state Soot Volume Fraction Distribution

The predicted SVF result using Lagrangian and Eulerian method are compared against measured SVF for different oxygen concentrations and ambient densities. Figure 6-4 and Figure 6-6 shows the comparison of spatial SVF distribution for different oxygen levels at low density (ρ = 14.8 kg/m^3) and high density (ρ = 30.0 kg/m^3) Sandia *n*-heptane cases, respectively. The normalised SVF profiles along spray axis are shown in Figure 6-5 and Figure 6-7 for low density and high density Sandia *n*-heptane case, respectively.

At low density, the spatial predictions of SVF by both the Lagrangian and Eulerian method coincide qualitatively with the experimental SVF at all oxygen levels as shown in Figure 6-4. As the oxygen levels decrease, the steady-state soot cloud is shown experimentally to be further away from the injector. Both the Lagrangian and Eulerian predictions are able to capture this phenomenon. However, the predicted soot clouds by both simulation methods are further downstream relative to the measured soot cloud, where the Lagrangian prediction is the furthest downstream for all oxygen levels. This overprediction in soot cloud location is shown clearly in Figure 6-5 which shows the SVF profile along the spray axis. From Figure 6-5, the peak soot locations predicted by Lagrangian and Eulerian method for all oxygen levels are approximately 30 mm and 20 mm, respectively, downstream from the experimental peak soot location. All these phenomena and observations are also present and captured for the high density cases as seen in Figure 6-6 and Figure 6-7. The observed overprediction of soot cloud location is later found to be due to the absence of surface ageing effect in surface growth model. The consideration of surface ageing effect on SVF profile is investigated in Chapter 7.

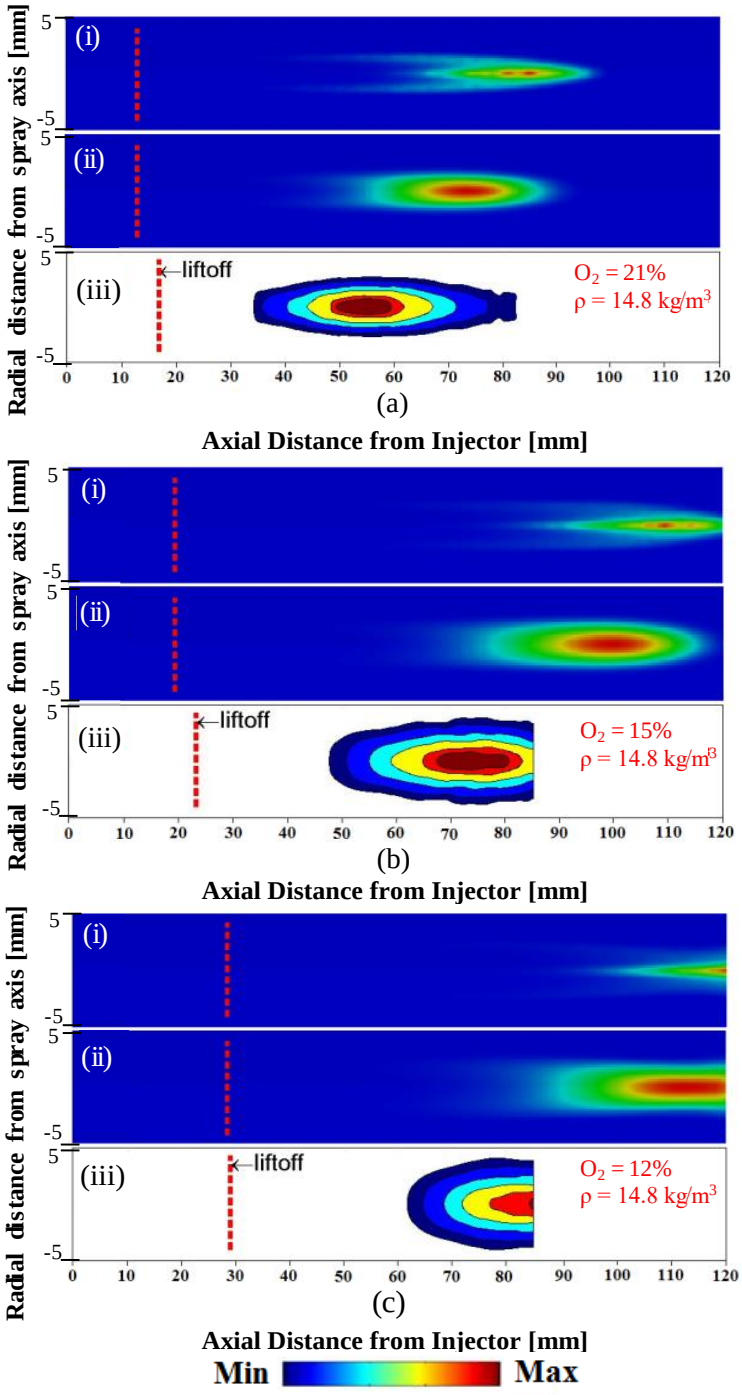

Figure 6- 4: Comparison of steady-state SVF between (i) LST results, (ii) Eulerian results and (iii) experimental results [265] **at different ambient oxygen content, with ambient density of 14.8 kg/m^3 for Sandia *n*-heptane test cases. [Note: The oxygen levels and ambient densities are indicated in red, while the LOL is indicated by the dashed red line]**

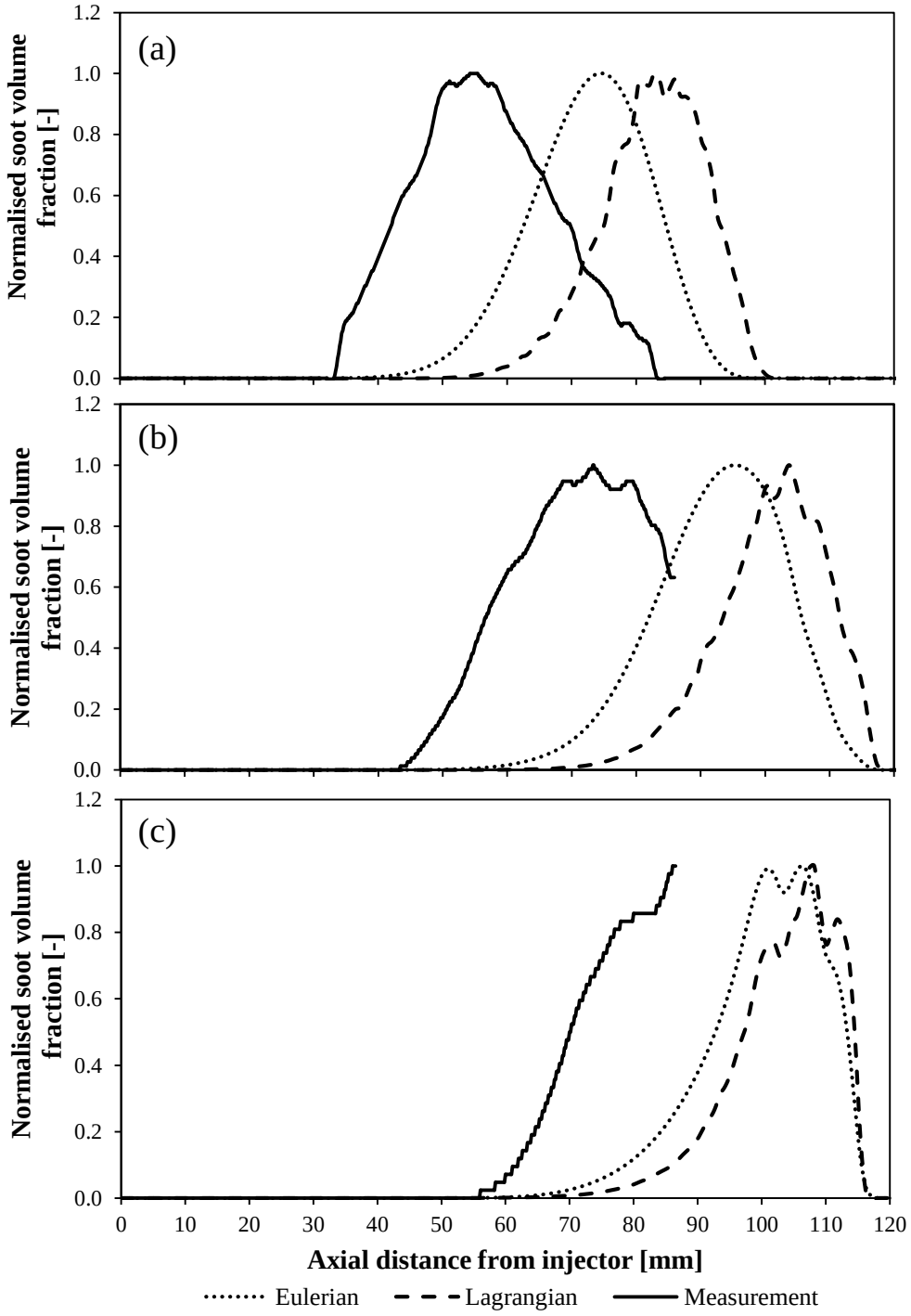

Figure 6- 5: Comparison of normalised SVF along spray axis between (i) LST results, (ii) Eulerian results and (iii) experimental results [265] **at ambient oxygen levels of (a) 21%, (b) 15% and (c) 12%, with ambient density of 14.8 kg/m^3 for Sandia *n*-heptane test cases.**

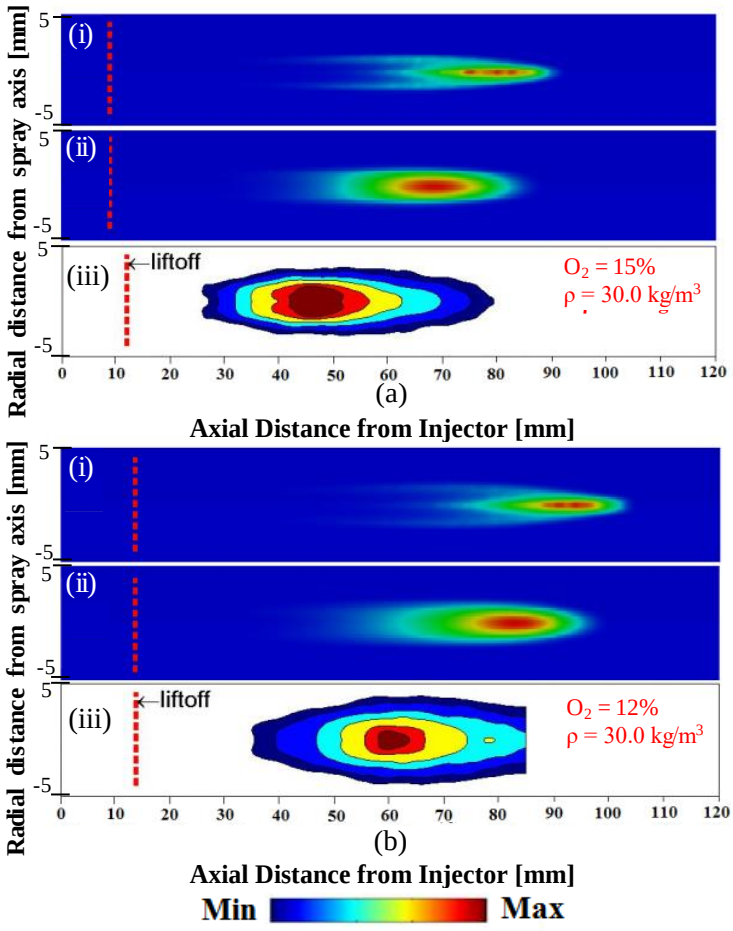

Figure 6- 6: Comparison of steady-state SVF between (i) LST results, (ii) Eulerian results and (iii) experimental results [265] **at different ambient oxygen content, with ambient density of 30.0 kg/m^3 for Sandia *n*-heptane test cases. [Note: The oxygen levels and ambient density are indicated in red, while the LOL is indicated by the dashed red line]**

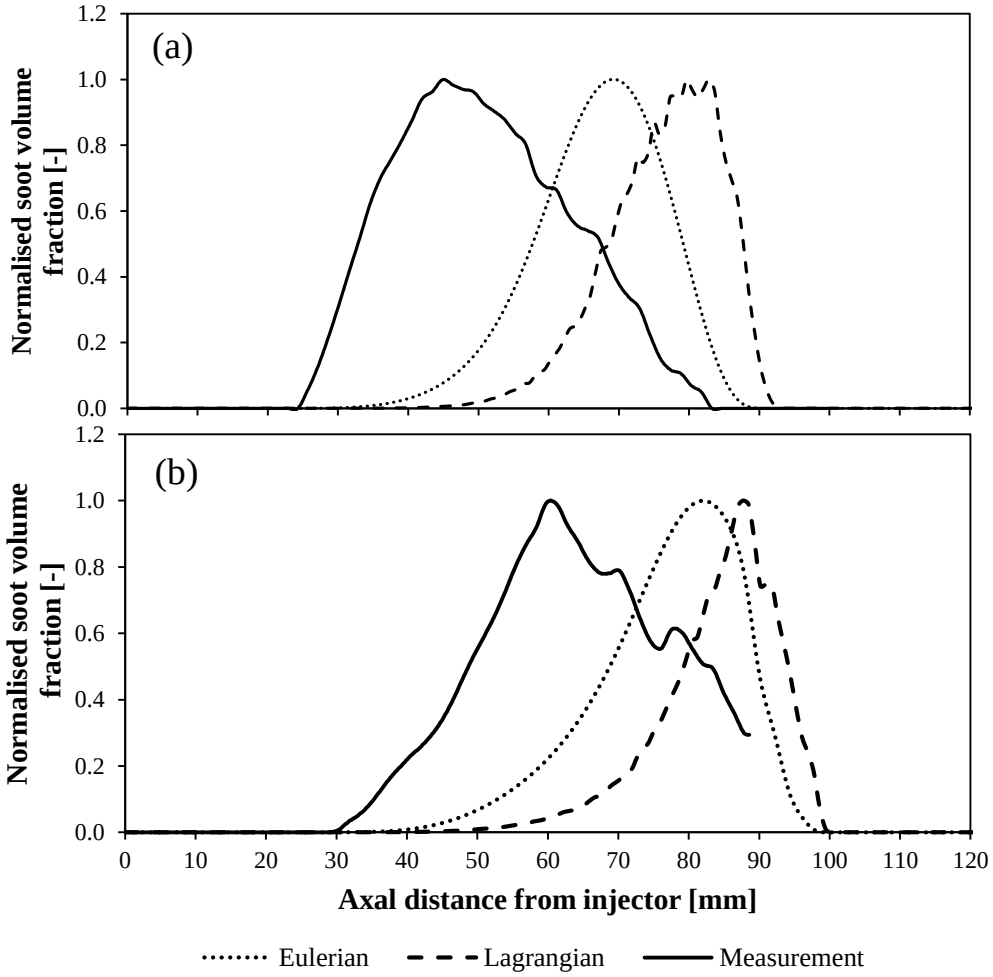

Figure 6- 7: Comparison of normalised SVF along spray axis between (i) LST results, (ii) Eulerian results and (iii) experimental results [265] **at ambient oxygen levels of (a) 15% and (b) 12%, with ambient density of 30.0 kg/m^3 for Sandia *n*-heptane test cases.**

6.4 Validation in Sandia *n*-Dodecane Case Studies

The validation of LST in Sandia *n*-dodecane case setup is performed based on the operating conditions shown in Table 5-1. The validation is carried out at ambient oxygen levels of 21% and 15%, where the ambient temperature is 900 K and ambient density is 22.8 kg/m^3. In this numerical case study, the SVF computed using the LST and Eulerian method are compared against measured SVF distributions. In addition to SVF comparison, the predictions of primary soot size distribution are also compared with measured primary soot size distribution [282] at oxygen levels of 15% and 21%.

6.4.1 Temporal and Spatial Soot Volume Fraction Evolution

Both the LST and Eulerian methods are then applied to simulate the soot formation in the Sandia *n*-dodecane cases. As similar transient SVF is obtained for 15% O_2 level case, only the results for Sandia *n*-dodecane spray at 21% O_2 level is presented here. Figure 6-8 compares that simulated and experimental soot cloud evolutions before reaching the quasi-steady state for the Sandia *n*-dodecane spray case at the ambient O_2 levels of 21%. Experimental images are snapshots extracted from the video provided by ECN [265]. At approximately 0.4 ms ASOI, a noticeable soot cloud is observed in the experimental image but the predicted soot starts to form at the periphery of the jet at approximately 0.6 ms. The delayed in simulated soot onset time can be attributed to the longer ID as predicted in Section 5.5.3. The computed and experimental sooty jets are similarly shown to further develop towards the downstream, which eventually leads the soot formation event to a quasi-steady state downstream.

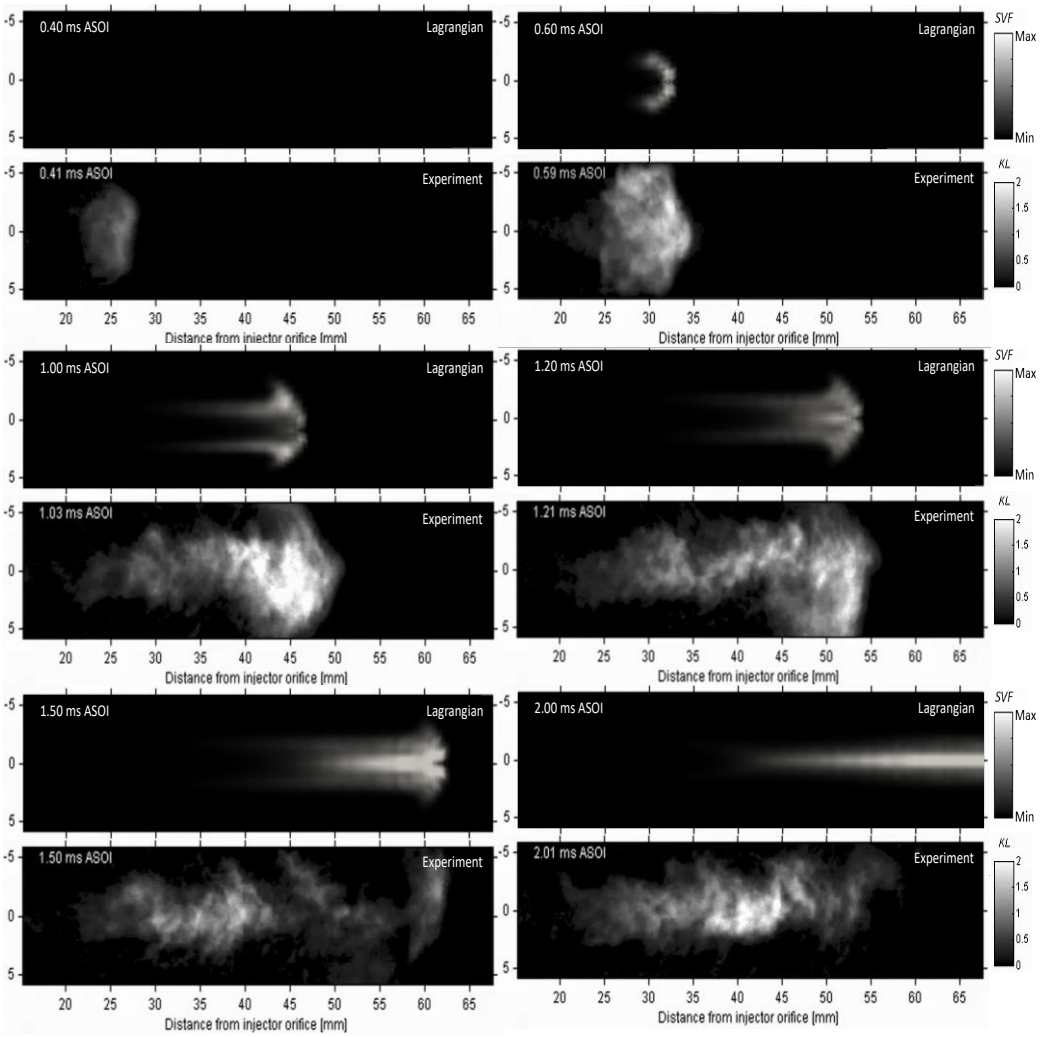

Figure 6- 8: Comparison of simulated transient SVF contours using LST model and experimental observation [265] **for the Sandia *n*-dodecane spray case.**

6.4.2 Steady-state Soot Volume Fraction Distribution

The computed steady-state SVF using LST and Eulerian methods are compared to the experimental measurement for Sandia *n*-dodecane test cases at both O_2 levels of 15% and 21% in Figure 6-9. Both predicted SVF by Eulerian and Lagrangian methods are shown to correspond qualitatively well with experimental SVF despite both overpredicting their steady-state soot cloud position. Peak soot location for experimental, Lagrangian and Eulerian SVF can be clearly seen in Figure 6-10 which shows the normalised SVF profile along spray axis at 21% and 15% oxygen levels. The experimental peak soot location for the 15% O_2 case, shown Figure 6-10(a), is approximately 60 mm from the injector. At higher oxygen content, the

experimental peak is measured to be approximately at 36 mm from the injector as seen in Figure 6-10(b). At both oxygen levels, the predicted Eulerian and LST peak are approximately 20 mm and 30 mm, respectively, further downstream from the experimental peak. This overprediction for Eulerian and Lagrangian peak coincide with the observations in Section 6.3.2.

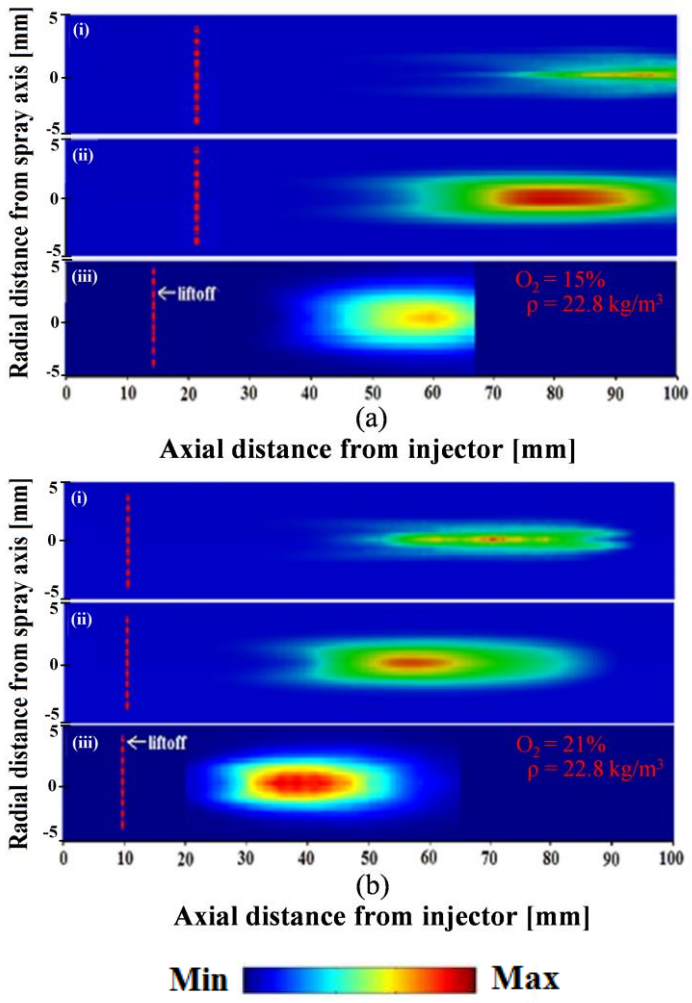

Figure 6- 9: Comparison of steady-state SVF between (i) LST results, (ii) Eulerian results and (iii) experimental results [265] **at different ambient oxygen content for Sandia *n*-dodecane test cases. [Note: The oxygen levels and ambient densities are indicated in red, while the LOL is indicated by the dashed red line.]**

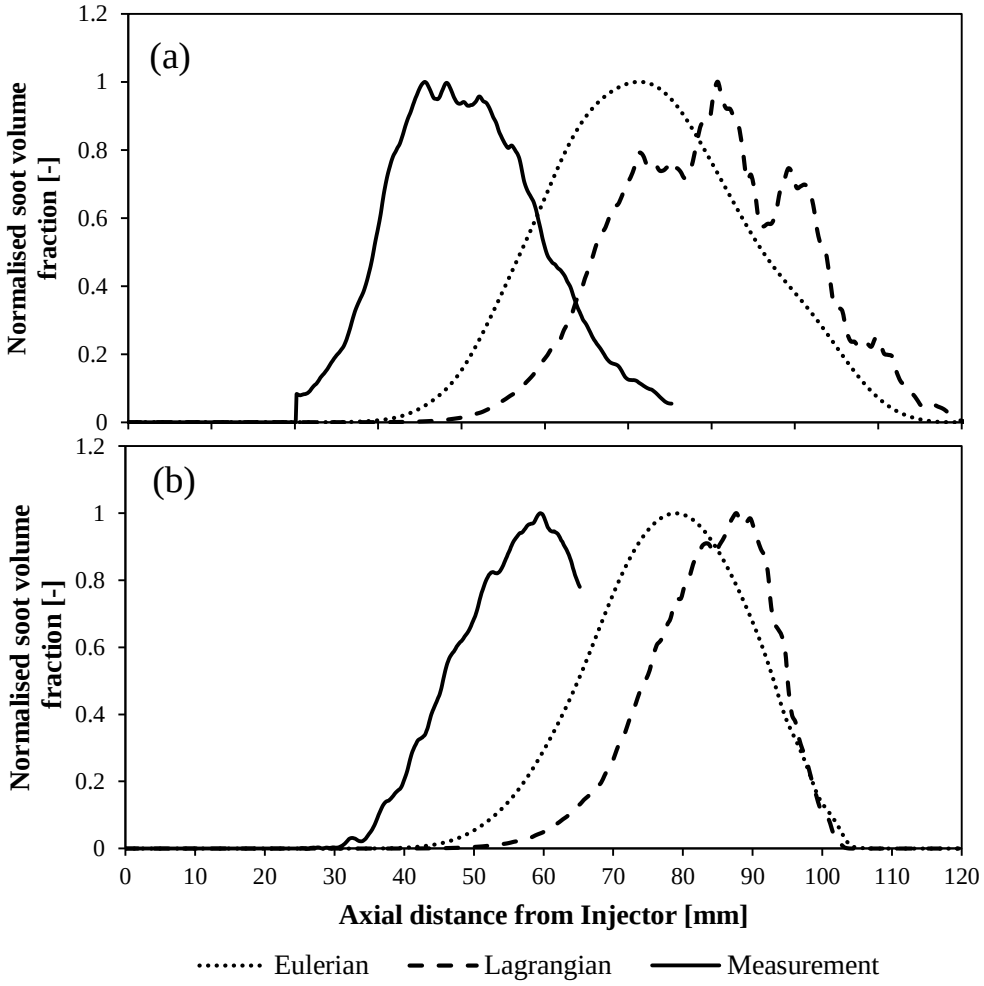

Figure 6- 10: Comparison of normalised SVF along spray axis between (i) LST results, (ii) Eulerian results and (iii) experimental results [265] **at ambient oxygen levels of (a) 21% and (b) 15%, with ambient density of 22.8 kg/m^3 for Sandia *n*-dodecane test cases.**

6.4.3 Soot Particle Size Distribution

Ex-situ soot study was performed by Cenker et al. [282] for *n*-dodecane spray combustion in the same Sandia combustion vessel configuration [265]. The soot was sampled at different locations of the soot cloud by the thermophoretic deposition on a carbon-coated copper grid which was held in place by a steel grid-holder probe. The sampling location was chosen as the position of maximum soot emission along the spray axis. The deposited soot samples were investigated using the HR-TEM in Meiji University. Details of the experimental setup can be found in

[282] while the HR-TEM measurement techniques and primary soot particle definition can be referred to in [283]. In the current simulation study, the Lagrangian particles which are in close proximity to the location of experimental soot sampler are assumed to be collected by the soot sampler and their information are recorded. The Lagrangian particles that are $\pm$1.5 mm axially and $\pm$0.5 mm radially about the sample locations are recorded and the analysis is carried out from the start of ignition to 6.0 ms ASOI.

For the 15% O_2 Sandia *n*-dodecane case, the sampling location is at 60 mm from the injector location which corresponds to the peak soot location of the experimental reacting *n*-dodecane spray. In Figure 6-11, the computed Lagrangian soot size distribution is compared with the experimentally measured soot size distribution at 60 mm from the injector location. It clearly shows that the Lagrangian predicted primary soot size is larger than the measured primary soot diameter size. The maximum measured soot diameter sizes range from 20 to 22 nm, while the LST model predicts a maximum soot diameter size of up to 30 nm.

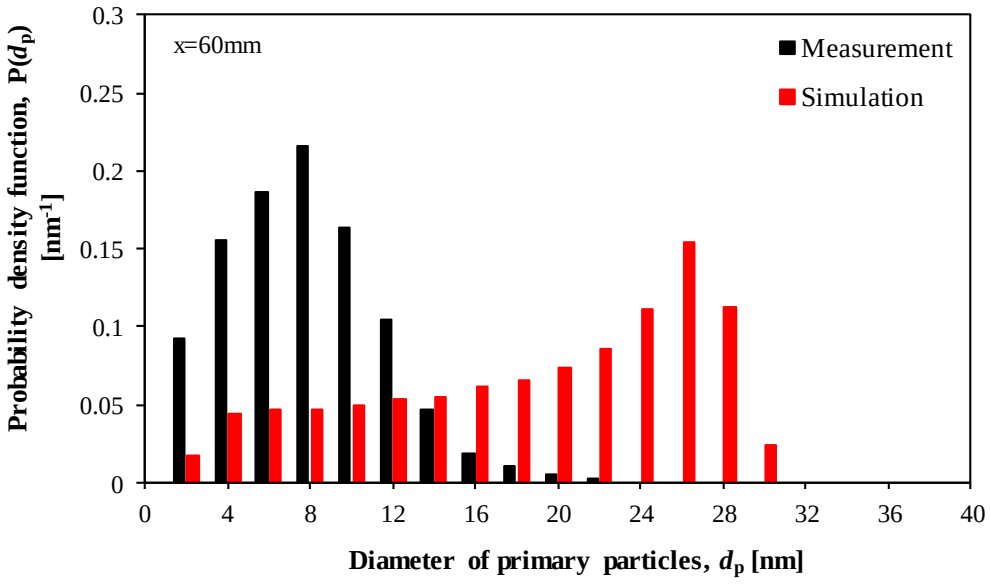

Figure 6- 11: Soot size distribution at x = 60 mm from injector for Sandia *n*-dodecane test case at an ambient density of 22.8 kg/m^3, temperature of 900 K and oxygen content of 15%.

The same soot sampling procedure is carried out for the 21% O_2 Sandia *n*-dodecane case. The experimental sampling locations are fixed at *x*=36 mm, 45 mm and 60 mm from the injector location. The experimental and simulated soot size distributions are displayed in Figure 6-12. At upstream of the flame jet i.e. *x*=36 mm from the injector, the experimental soot size measurement predicts a Gaussian distribution, where the peak soot size is approximately 14 nm. The soot size distribution remains as a bell shape but becomes narrower as it goes downstream from 36 mm to 60 mm from injector. Based on the measurement, the largest soot size at *x*=36 mm is 42 nm while that at *x*=60 mm is 22 nm. The simulated soot size distribution shows an opposite trend. At upstream where *x*=36 mm, the soot size distribution corresponds reasonably well with the experimental measurement. However, a wider soot size distribution is predicted as it goes downstream as compared to the experimental distribution. The largest predicted primary soot sizes are 44 nm and 80 nm at *x*=45 mm and *x*=60 mm, respectively.

This section shows that the predicted soot concentration distributions using the LST model correspond reasonably well with the results predicted by its Eulerian counterpart. The soot size distribution in the Doshisha *n*-heptane test case simulated by the LST model also qualitatively agrees with the experimental measurement and the MOM results. However, when the performance of the model is quantitatively evaluated using the Sandia *n*-dodecane data, the Lagrangian predicted soot size appears to be larger than the measured soot size. This can be attributed to the underestimation of soot oxidation rates and/or the absence of surface ageing factor. The effects of these parameters on the soot concentration distribution and primary soot size are investigated in Chapter 7.

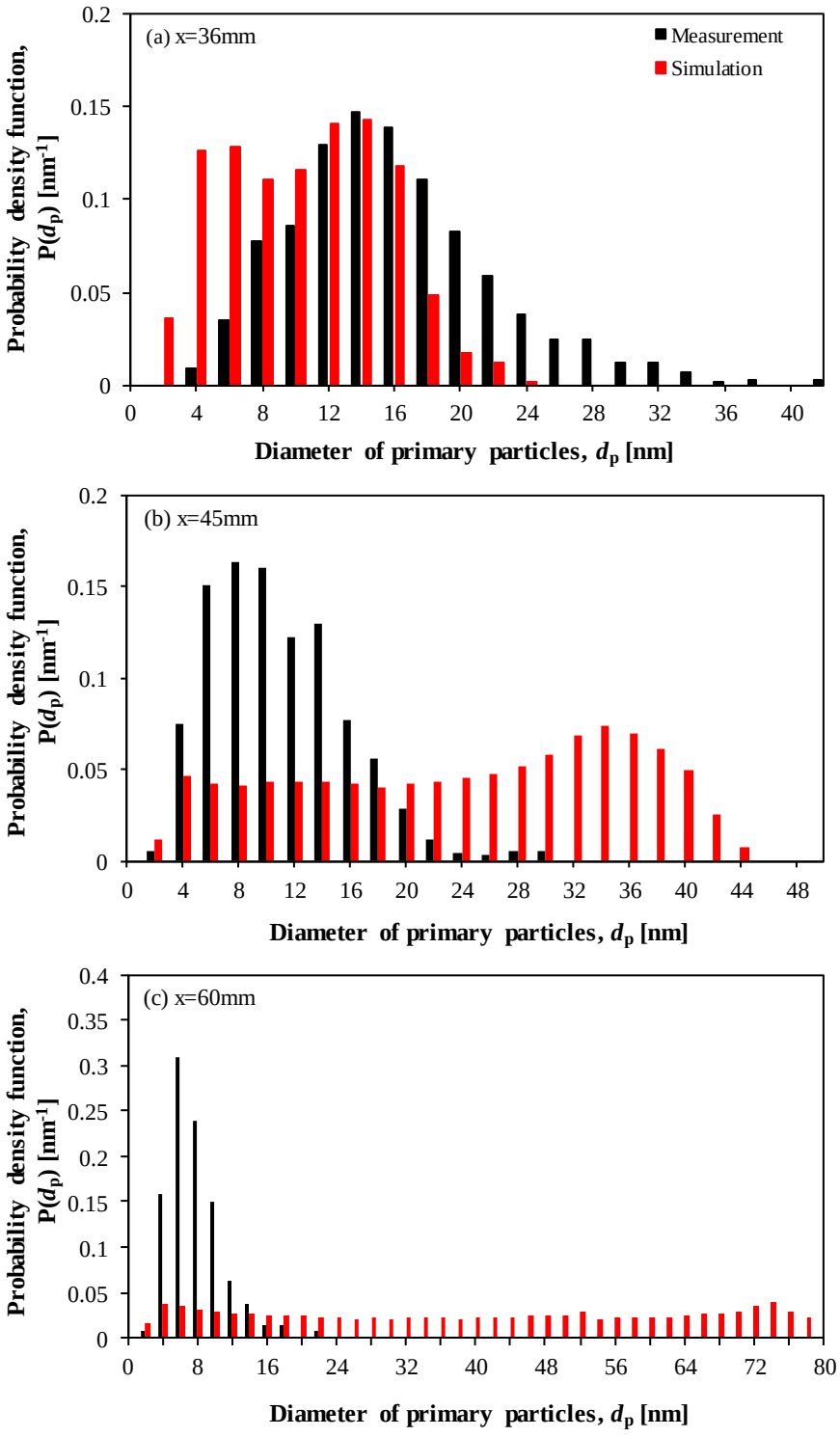

Figure 6- 12: Soot size distribution at (a) x = 36 mm, (b) x = 45 mm and (c) x = 60 mm from injector for Sandia *n*-dodecane test case at ambient density of 22.8 kg/m^3, temperature of 900 K and oxygen content of 21%.

6.5 Concluding Remarks

The validation of LST is carried out here by comparing the transient and steady-state SVF and soot sizing distribution with measurement data. The predicted SVF by the LST model matches qualitatively with the Eulerian and measured data at different O_2 levels and ambient densities. However, the LST model overpredicts the peak soot location by 30 mm relative to the experimental peak soot location. On the other hand, the mean primary soot diameter distributions predicted via the LST model matches qualitatively with the MOM results from literature. However, this is not the case for the Eulerian method which implies that the LST model outperforms the Eulerian method in predicting soot size.

Besides this, quantitative validation is carried out by comparing individual primary soot size distribution between LST model and measured data from literature. The validation is performed only for Sandia *n*-dodecane case, at 15% and 21% O_2 levels. Overall, the primary soot size distribution is predicted to be the same order as the measured primary soot size distribution despite predicting larger soot size than the ones measured. The overprediction in soot size and peak soot location may be attributed to the underestimation of soot oxidation rates and/or the absence of surface ageing factor. Therefore, parametric studies of these factors are carried out in Chapter 7 to understand its effect on SVF and primary soot size distribution.

CHAPTER 7
SENSITIVITY STUDY OF LAGRANGIAN SOOT MODEL

7.1 Introduction

In the previous chapter, the soot clouds predicted by LST model are further downstream relative to the experimental soot cloud. This overprediction of peak soot location is hypothesised to be attributed to larger predicted soot size by the LST model. The larger soot particles computed take a longer time to be fully oxidised, thus propagating further downstream from the injector location and leading to the observed overprediction of peak soot location. This hypothesis is supported by the findings in Figure 6-11 and Figure 6-12 of Chapter 6 which showed larger computed primary soot size than the measured soot size. Therefore, two approaches are suggested in order to reduce the predicted soot sizing, namely (i) increase the oxidation rates (O_2 and OH factors) and (ii) include surface ageing factor in the surface growth model. The higher oxidation rates are expected to decrease the time for full soot oxidation thus preventing the soot particles from propagating further downstream. The incorporation of surface ageing is expected to decrease the surface growth rates thus leading to smaller soot particles. The smaller soot particles take shorter time to be fully oxidised, hence causing a more upstream soot cloud prediction.

This chapter is structured such that the selection of suitable surface ageing function is first carried out in Section 7.2, followed by sensitivity study on the primary soot size prediction from Section 7.3 to 7.6. The sensitivity test is carried out to study the effect of increasing oxidation rates and the presence of surface ageing factor on primary soot size distribution prediction. Finally, key findings are reported in Section 7.7.

7.2 Choice of Surface Ageing Factor Function

There have been various studies suggesting that the surface ageing factor, α varies with different flame properties. Much attention has been given to investigate the correlation between α and flame temperature, particle residence time, and particle size [31,38,39,62,284–287]. The various forms of α proposed in the literature are listed in Table 7-1.

Table 7- 1: Proposed surface ageing functions from various literatures.

Proposed by	Surface ageing function
Frenklach and Wang [68]	0.1
Dworkin et al. [63]	0.078
Singh et al. [31]	$\begin{cases} 1 \; for \; A_p \leq \theta \\ 0.2 \; for \; A_p > \theta \end{cases}$ (a)
Singh et al. [31]	$0.2 + 0.8\, exp(-CA_p)$ (b)
Kazakov et al. [287]	$\frac{1}{2}\left(\tanh\left(\frac{8168}{T} - 4.57\right) + 1\right)$ (c)

(a) This is a step-correlated surface ageing factor. A_p is the particle residence time, while θ is defined as the critical age defining the boundary between the two step values. θ is set as 12 ms for the flame studies in [31].

(b) This is an exponential-correlated surface ageing factor. Different values for *C* have been used for different flame studies in [31].

(c) This is a temperature-correlated surface ageing factor, where *T* refers to the temperature.

A constant α is found to be inadequate in predicting accurate SVF in flame configurations [39]. Therefore, the remaining three surface ageing functions, which are the two surface ageing functions that correlate with particle residence time and the temperature-correlated surface ageing, are evaluated by comparing their primary soot size distribution prediction. The two surface ageing functions suggested by Singh et al. [31] are based on their premixed laminar flame experiment and stochastic simulation. Their numerical results showed that the particle residence time could reach up to 100 ms [31], however preliminary numerical studies for Sandia *n*-dodecane spray case show that the particle residence time is less than 3 ms. Therefore, the constants, *C* and θ are altered arbitrary to fit the shorter particle residence time for the diesel spray studies carried out in this thesis. The constants associated to each surface ageing functions and the surface ageing functions tested

are shown in Table 7-2. The critical age constant, θ in the step-correlation case is set to 0.2 ms and 0.8 ms for case Age1 and Age2, respectively. As for the exponential-correlation case, the constant C is calibrated such that α reaches steady-state at 0.2 ms and 0.8 ms for case Age3 and Age4, respectively. The surface ageing factor profiles for the particle residence time correlation surface ageing function are presented in Figure 7-1. A temperature correlated surface ageing factor is tested for case Age5. This correlation was proposed by Kazakov et al. [287] and obtained through experimental correlation in laminar premixed ethylene flames at a pressure of 10 bar. This surface ageing factor was successfully implemented in diesel spray flame numerical studies [286,288].

Table 7- 2: Test cases for different surface ageing functions with their respective constants.

Test case	Surface ageing function used	Constants set
Age1	$1\ for\ A_p \leq \theta$ $0.2\ for\ A_p > \theta$	$\theta = 0.2\ ms$
Age2	$1\ for\ A_p \leq \theta$ $0.2\ for\ A_p > \theta$	$\theta = 0.8\ ms$
Age3	$0.2 + 0.8\exp(-CA_p)$	$C = 35$
Age4	$0.2 + 0.8\exp(-CA_p)$	$C = 10$
Age 5	$\frac{1}{2}\left(\tanh\left(\frac{8168}{T} - 4.57\right) + 1\right)$	-

The comparison of surface ageing functions is carried out for Sandia *n*-dodecane case, at 21% O_2 condition. Figure 7-2 and 7-3 show the performance of the step-correlated and exponential-correlated surface ageing functions, respectively, in predicting soot size distribution at different axial locations along the spray axis. Age2 predicts soot size distribution that does not correlate well with the experimental size distributions at downstream axial locations despite having comparable predictions at *x*=36 mm from injector location. The results predicted by Age1 correlate well with the measured distribution at all axial locations where the

predicted maximum soot size is closer to the measured size. However, at downstream region of x=60 mm from injector location, the predicted soot distribution shows higher number of large soot particles. This finding contradicts with the measured distribution which shows higher number of small soot particles.

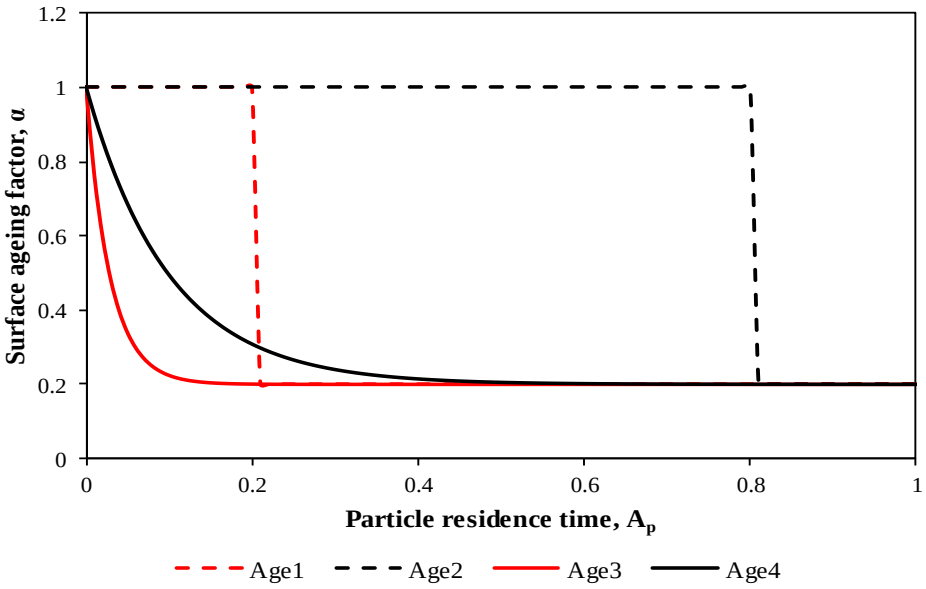

Figure 7- 1: Surface ageing profiles of different surface ageing functions.

On the other hand, the exponential-correlation surface ageing functions work better relative to the step-correlation surface ageing functions in predicting soot size distribution. Both Age3 and Age4 functions predicts soot size distribution that correspond well with measured distribution at all axial locations despite Age3 predicting smaller soot size than Age4. However, at x=60 mm from injector location, both Age3 and Age4 functions predict higher number of large soot particle which contradicts the experimental finding shown in Figure 7-3(c). The findings from Figure 7-2 and 7-3, which show that both step- and exponential-correlation functions predicted higher number of large soot particles, imply their inability to capture accurate soot size distribution.

As for the temperature-correlation function (case Age5), the predicted soot size distributions are comparable at x=36 mm and x=45 mm from injector location, but overpredicted at downstream region of x=60 mm. Despite this overprediction, there

is no distinct high soot number of large soot size predicted as in those predicted by the step- and exponential-correlation surface ageing functions. The soot particles predicted have almost equally distributed soot sizes. Furthermore, it is later highlighted in Section 7.6 that the soot distributions predicted matches quite well with the experimental profiles. Therefore, the surface ageing function which correlates with temperature [287] is chosen as the suitable surface ageing function without calibrations for the sensitivity case study in Section 7.3.

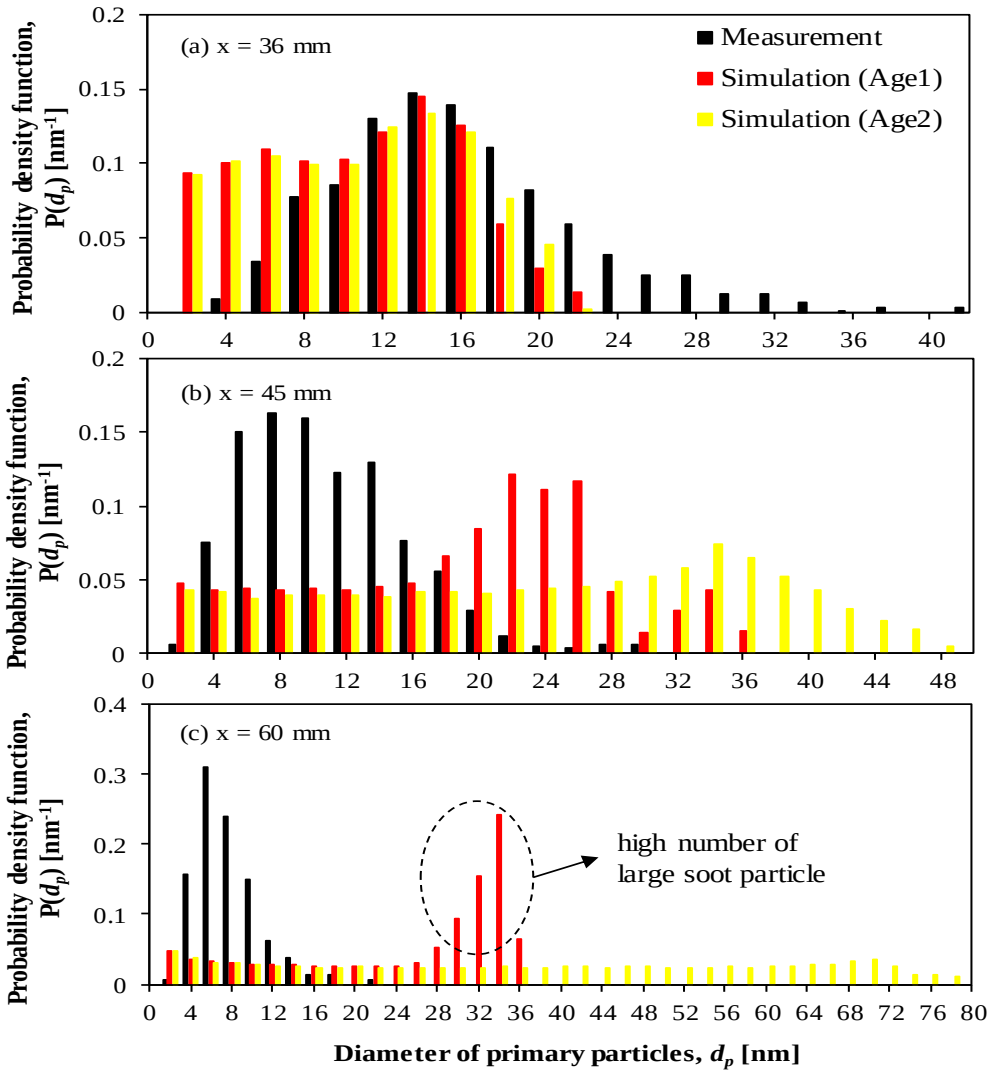

Figure 7- 2: Comparing the Lagrangian predicted soot size distribution using step-correlated surface ageing function at different axial location of (a) *x*=36 mm, (b) *x*=45 mm and (c) *x*=60 mm from injector location along the spray axis.

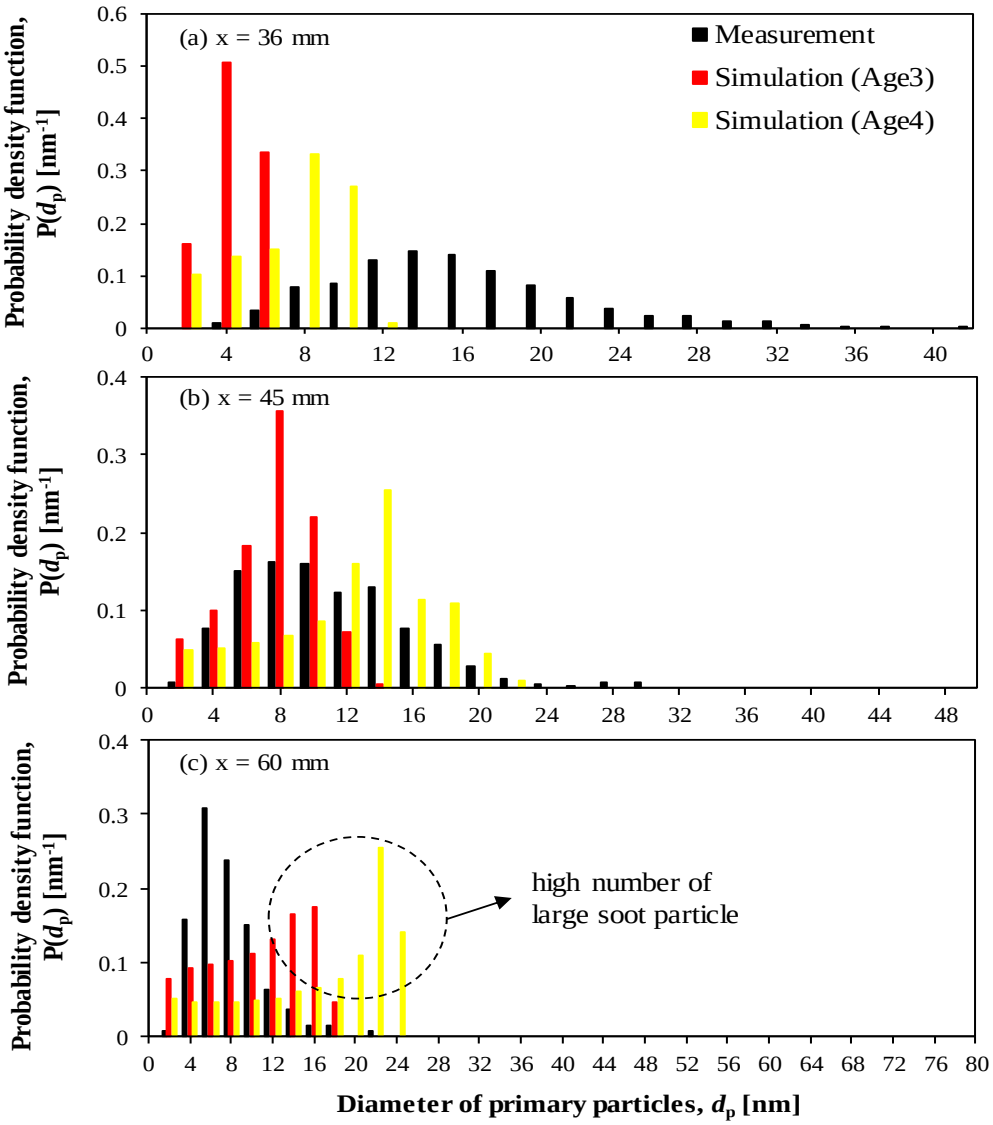

Figure 7- 3: Comparing the Lagrangian predicted soot size distribution using exponential-correlated surface ageing function at different axial location of (a) *x*=36 mm, (b) *x*=45 mm and (c) *x*=60 mm from injector location along the spray axis.

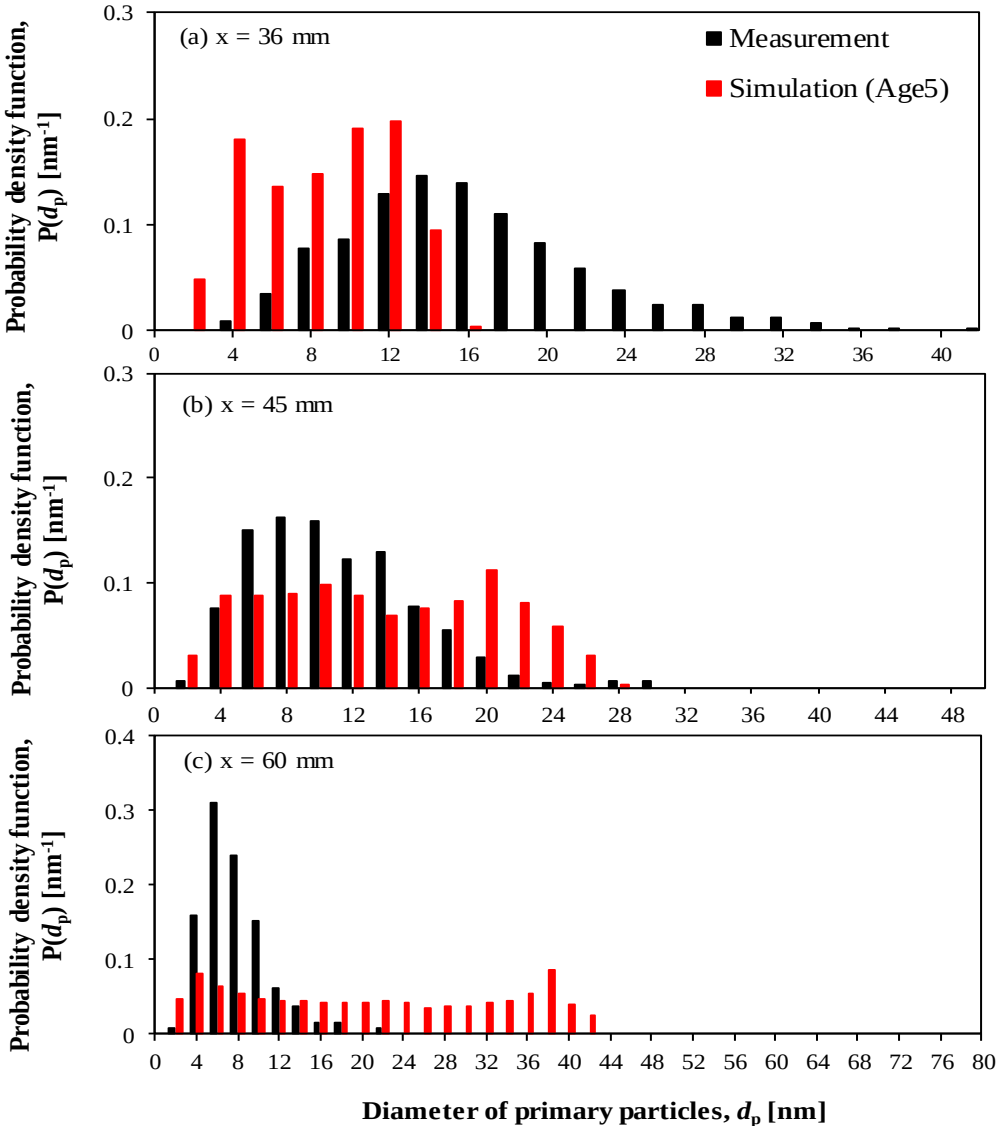

Figure 7- 4: Comparing the Lagrangian predicted soot size distribution using temperature-correlated surface ageing function at different axial location of (a) *x*=36 mm, (b) *x*=45 mm and (c) *x*=60 mm from injector location along the spray axis.

7.3 Sensitivity Analysis Case Setup

A test matrix as shown in Table 7-3 is constructed to investigate the effects of rates of O_2 and *OH* oxidation as well as the soot surface ageing effect on the LST model prediction. Sensitivities of the soot oxidation rates and surface ageing are examined using the 21% O_2 Sandia *n*-dodecane test case. The sensitivity of O_2 oxidation model constant, C_{O_2}, is tested by increasing it by a factor 2 while the *OH* collision coefficient, η_{coll}, is increased from the default value of 0.04 [169] to 0.13 [220]. The surface ageing function used here is the temperature-correlated surface ageing function by Kazakov et al. [286,287], as shown in Table 7-1. Their performances are compared based on their predictions of the ensemble SVF profiles and soot size distribution at different axial locations along the spray axis. The ensemble SVFs are averaged from 4.0 ms to 6.0 ms ASOI, where the soot production has reached quasi-steady state. The SVF values are normalised with the peak SVF value in their respective simulations.

Table 7- 3: Test matrix to study the effect of increasing the oxidation factor and considering surface ageing.

		Descriptions		
Configuration	**Test case name**	**O_2 model constant x 2**	***OH* collision coefficient = 0.13**	**Presence of surface ageing**
-	Baseline	-	-	-
1	O_2	√	-	-
2	*OH*	-	√	-
3	O_2 + *OH*	-	√	-
4	Ageing	-	-	√
5	Ageing + O_2	√	-	√
6	Ageing + *OH*	-	√	√
7	Ageing + O_2 +*OH*	√	√	√

7.4 Effects of Oxidation Rates on Soot Prediction

Figure 7-5 shows the ensemble-averaged normalised SVF profiles along the spray axis without surface ageing. It should be highlighted that the soot particle size distribution using configurations 1 to 3 are identical. Hence, only the results of configuration 3 are presented. As seen in Figure 7-5, without the presence of surface ageing, the soot distribution does not show significant differences when the oxidation rates are varied. The current result implies that an increase in the soot oxidation rate has no impact on the soot distribution. Figure 7-6 depicts the soot size distribution without surface ageing at various axial locations. It is observed that the size distributions predicted using configuration 3 are close to that of the baseline setup. This, again, implies that the soot size prediction is also not sensitive to the oxidation rates.

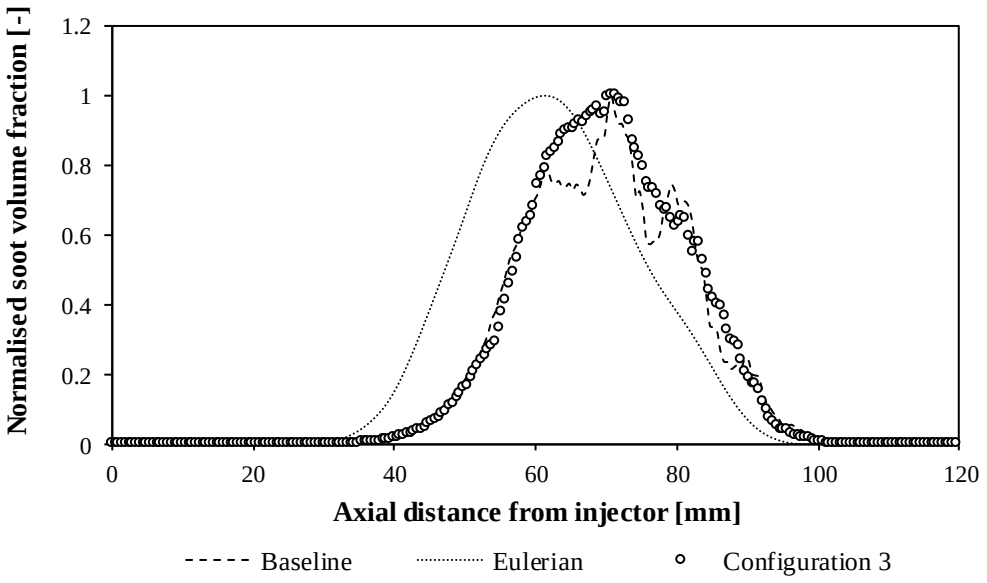

Figure 7- 5: Comparison of predicted normalised SVF along spray axis when changing oxidation rates with measurement, Eulerian and Baseline SVF profiles.

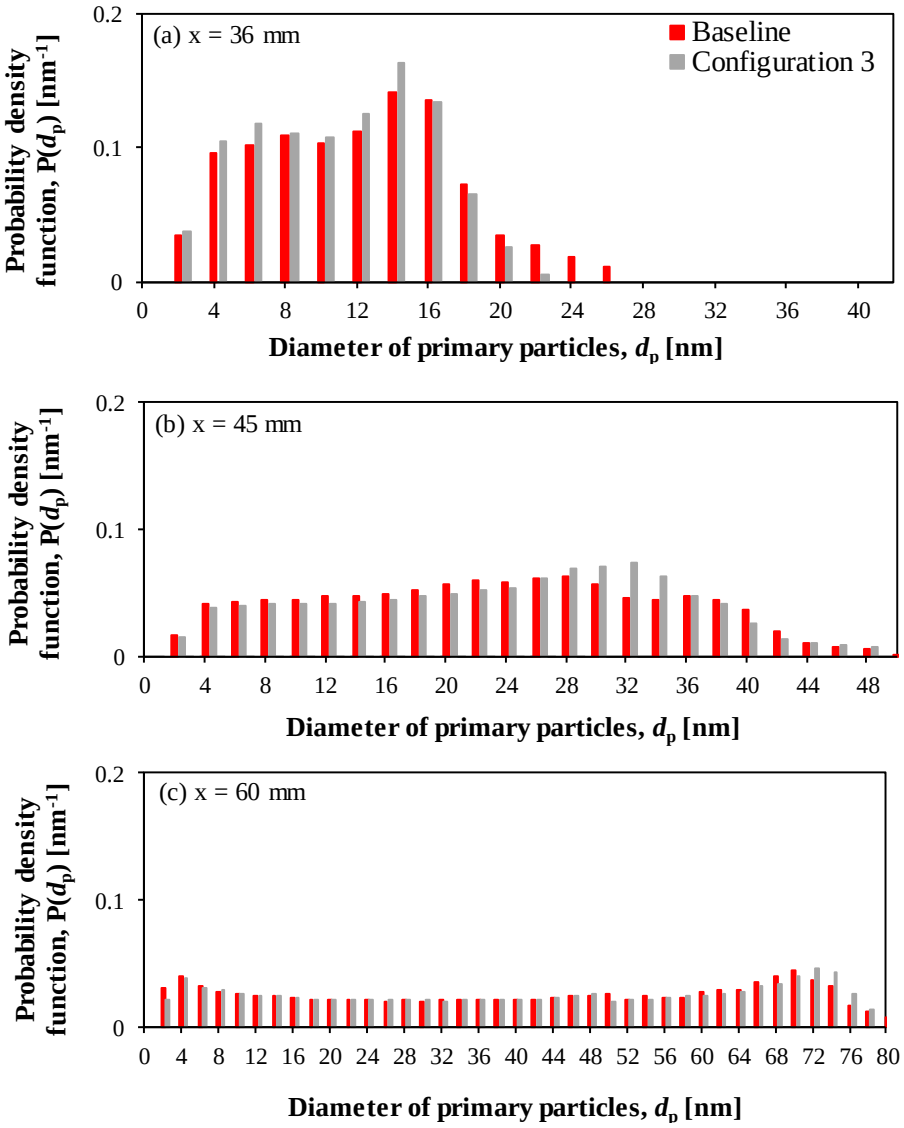

Figure 7- 6: Comparison of predicted soot size distribution at (a) *x*=36 mm, (b) *x*=45 mm and (c) *x*=60 mm when changing oxidation rates with measured soot size distribution.

7.5 Effects of Surface Ageing on Soot Prediction

Figure 7-7 shows the ensemble-averaged normalised SVF profiles along the spray axis when surface ageing is included. By incorporating surface ageing into the simulation, it is shown in Figure 7-7 that there is slight improvement in the soot profile along the spray axial. The peak soot location is predicted to be more upstream relative to the default case. The default case peaks at around 70 mm from injector while the cases with surface ageing have an average peak location at 65 mm from injector. Moreover, the whole profile of the surface ageing profiles is shifted upstream by 5.0 mm and better correspond with the Eulerian predicted soot profile. There are differences between predicted normalised SVF for configuration 4 and 7. It is observed that for configuration 7, the SVF profile coincides relative better with the Eulerian prediction during the oxidation stage, at axial location $x >$ 70 mm.

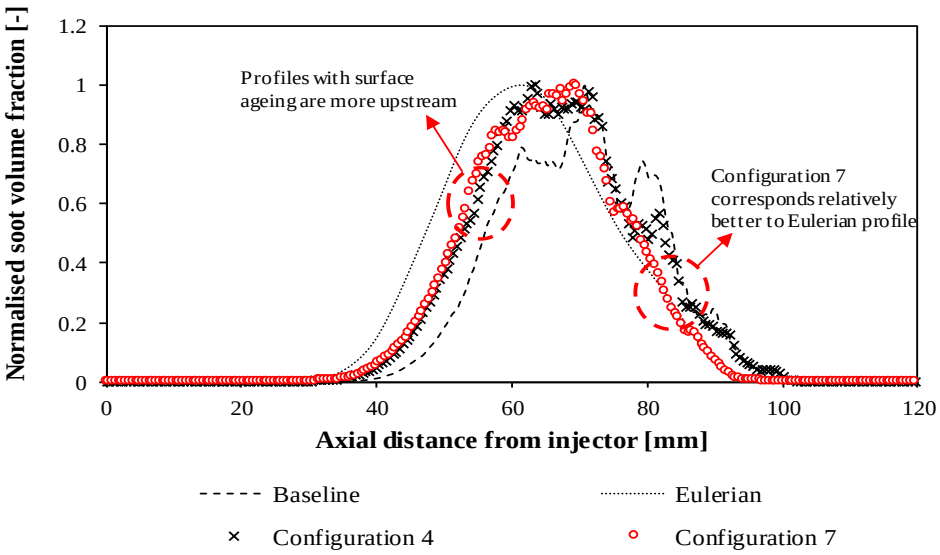

Figure 7- 7: Comparison of predicted normalised SVF along spray axis when changing oxidation rates with measurement, Eulerian and Baseline SVF profiles.

Figure 7-8 depicts the soot size distribution with surface ageing at various axial locations. With the presence of surface ageing, the predicted maximum soot particle sizes decrease for all three locations. A maximum soot size reduction of 48% is

achieved at x=60 mm, whereas a soot size reduction of 30% is obtained for the other two upstream locations. These results suggest that the prediction of soot size distribution is sensitive to the surface ageing process. Furthermore, there is no distinct difference between soot size distribution predicted by configuration 4 and 7. Thus, further reinforcing that increasing oxidation rates have little effect on the soot size predictions. However, as the SVF profile computed by configuration 7 corresponds better than the one by configuration 4, configuration 7 is concluded to be the better case and is used in all numerical studies from here on.

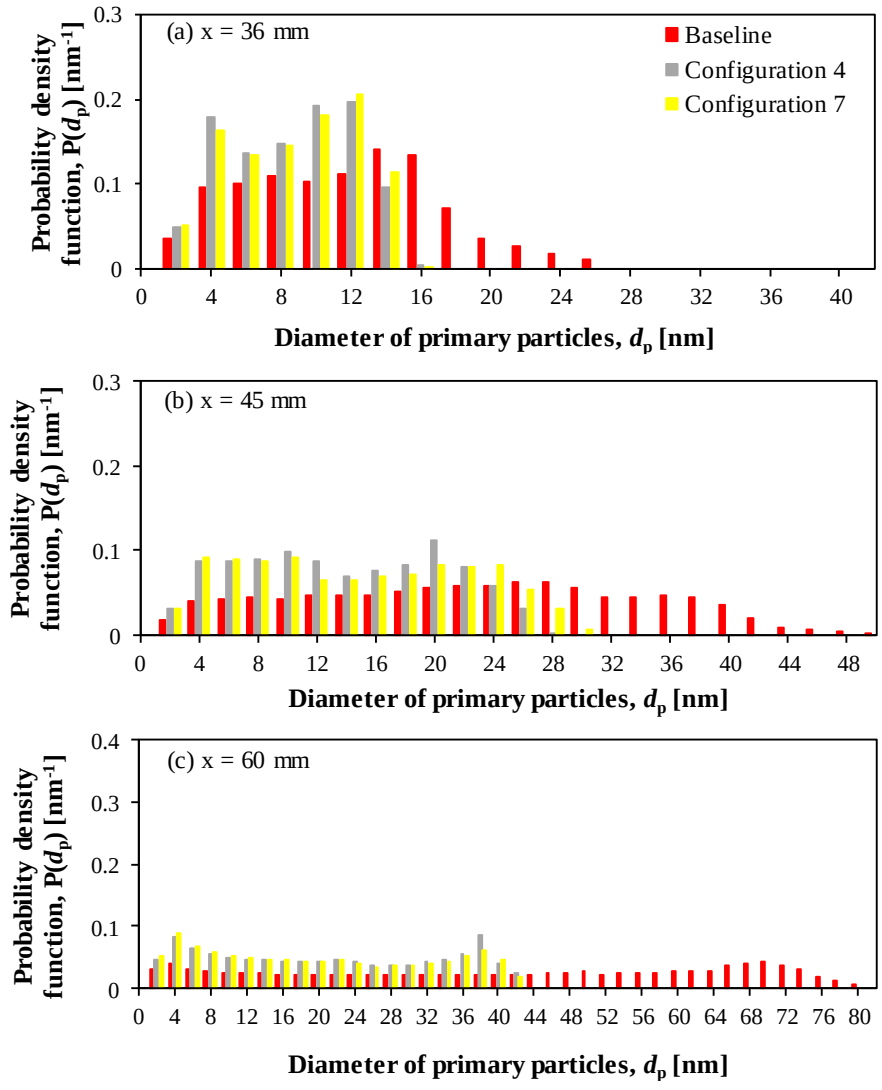

Figure 7- 8: Comparison of predicted soot size distribution at (a) *x*=36 mm, (b) *x*=45 mm and (c) *x*=60 mm when changing oxidation rates with measured soot size distribution.

7.6 Effects of SVF position on Soot Prediction

As depicted in Figure 7-8, the maximum soot sizes predicted by the LST model still increase from x=36 mm to x=60 mm, even when surface ageing is taken into consideration. This contradicts the experimental data which shows otherwise. The decrease in soot size is attributed to the soot oxidation process. The reason for this observation may be due to the further downstream soot cloud predicted by the LST model as shown in Figure 6-9. As such, locations where soot formation or soot oxidation dominates are expected to be different.

This can be better illustrated using Figure 7-9 which provides comparisons of the experimental and numerical ensemble SVF along the spray axis for O_2 levels 21%. For instance, for the 21% O_2 case, Cenker et al. [282] defined the first and the last sampling points (x=36 mm and 60 mm) as the "peak soot" and "soot oxidation", respectively. The sampling point of x=45 mm is defined as an intermediate zone between peak soot formation and soot oxidation [282]. This location is henceforth addressed as the "transition zone" for brevity. For the LST results, the associated "peak soot", "transition zone" and "soot oxidation" are located at x=65 mm, 72 mm and 89 mm, respectively.

Figure 7-10 depicts the predicted soot size distribution at new measuring locations based on the predicted soot cloud position using LST model. The predicted maximum soot sizes by the LST model at the new "peak soot", "transition zone" and "soot oxidation" locations decrease as it goes downstream from injector location. This now agrees with the variation shown by the experimental data. In addition to this, it is noted that the Gaussian distribution curve is captured at both the "transition zone" and "soot oxidation" locations, but not for the "peak soot" location. The largest difference between the experimental and simulated maximum soot particle size is recorded to be 14 nm.

The overestimated soot particle size shown in Figure 7-10 can be partially attributed to the usage of only the temperature-correlated surface ageing function. It is possible to incorporate a surface ageing function that takes into account the temperature and particle residence time together as performed in [39] but for laminar flame configuration. As the main objective of this work is to develop and validate the LST solver, calibration or development of surface ageing function is therefore not carried out here to match the experimental soot size.

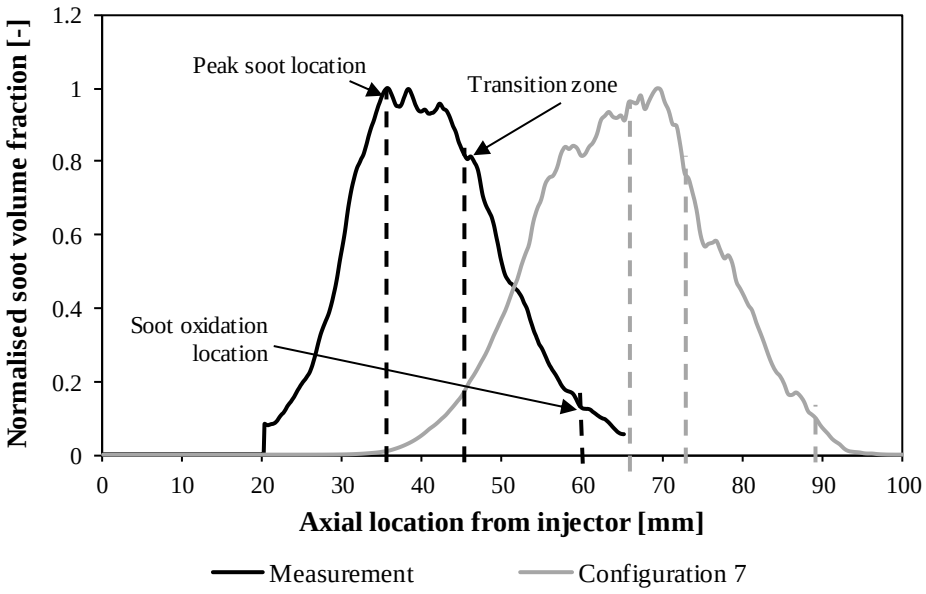

Figure 7- 9: Normalised SVF profiles along the axial direction for experimental and configuration 7 showing the peak soot, transition and soot oxidation locations.

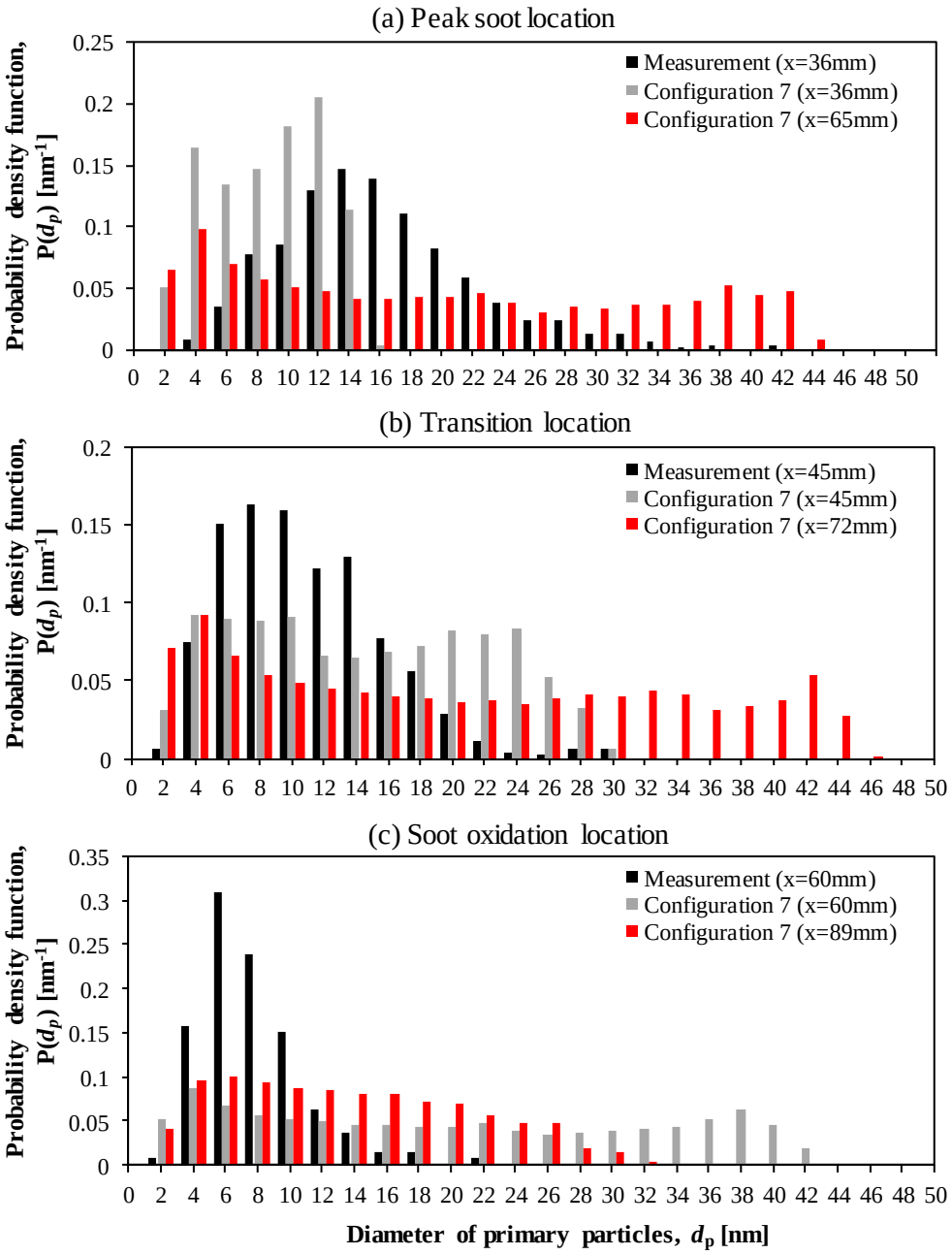

Figure 7- 10: Comparing soot size distribution at LST and experimental (a) peak soot, (b) transition and (c) oxidation locations for configuration 7 with experimental measured soot size distribution.

7.7 Concluding Remarks

Sensitivities of the surface ageing and oxidation rates on the predictions of both SVF and primary soot particle size distributions are investigated here. Higher oxidation rates alone do not affect the SVF distribution and primary soot size distribution. The presence of surface ageing factor causes the predicted SVF to be more upstream and yield a smaller primary soot size distribution. The incorporation of both surface ageing factor and higher oxidation rates for OH and O_2 yield relatively better results in terms of SVF and size distribution. A 5.0 mm upstream shift in the SVF profile and a maximum soot size reduction of 48% can be obtained when incorporating surface ageing effect. Furthermore, comparison of the computed and measured primary soot size distribution based on their corresponding soot cloud locations show better correlation between them. The largest difference between the experimental and simulated maximum primary soot particle size is retained approximately two-fold. Also, the Gaussian distribution curves at certain locations are reproduced.

CHAPTER 8

SOOT MORPHOLOGY STUDY USING LAGRANGIAN SOOT TRACKING

8.1 Background

Recent researchers have found that implementing EGR [40,122] or changing the ambient density [121] have significant effect on the soot distribution and concentration levels in the spray plume. Besides investigating soot concentration levels, the effects of EGR and ambient density on soot sizing have also gain the attention from researchers. Experimental techniques using LII and LS have been implemented to gain more insights into the evolution of soot size [33,40,282,283,289,290]. In addition to optical imaging techniques, intrusive techniques such as thermophoretic sampling [22–24,40,150,205,282,283,291] has been carried out to obtain in-flame soot particles. Recently, the effect of ambient oxygen on primary soot size was conducted by Kuribayashi et al. [40] via TEM analysis of soot sampled thermophoretically from spray flame, in a constant volume combustion chamber. Only two ambient oxygen levels were investigated, 21% and 15%. It was observed that the mean primary soot size for 21% case and 15% case were similar [40]. However, no clear explanations of this observation were presented in the literature. Furthermore, the major limitation of this sampling and analysing method is the time resolution. Since the TEM grid is constantly exposed to diesel flame, the sampled soot is considered to be a time-integrated mixture of soot particles throughout the injection and combustion duration.

Setting against this background, a numerical study is carried out using the developed LST model to investigate the effect of ambient oxygen and density on soot sizing in *n*-heptane spray flame. The aim is to investigate the effects of ambient oxygen on primary soot size and gain deeper insights during the transient period of soot formation. Furthermore, this study also aims to provide explanation to the experimental observation carried out by Kuribayashi and co-workers. Besides

ambient oxygen, the effect of ambient density is also investigated here due to the lack of literature studies regarding its effect on primary soot size.

The numerical investigation carried out in this chapter is based on numerical setup and model settings as the Sandia *n*-heptane case, presented in Chapter 5. The operating conditions and injector parameters are those similarly presented in Table 5-1, Chapter 5. Moreover, the LST model which includes surface ageing (as presented in Chapter 7) is implemented in this numerical case for the computation of soot particles. The chapter starts by discussing the effect of ambient oxygen and density on the steady-state SVF profile at the spray axis in Section 8.2. This is followed by the study of soot size distribution for soot particles formed at the core of the jet during transient and steady-state period. The investigation of the effect of ambient oxygen and density on the soot size distribution in the whole soot cloud is later carried out in Section 8.4. Lastly, the results obtained in this phase of work are summarised in Section 8.5.

8.2 Effect of Ambient Oxygen and Density on Soot Volume Fraction Profile

The predicted SVF results using Eulerian and improved Lagrangian method are compared against experimental SVF from [265] for different oxygen concentrations and ambient densities. The normalised SVF profiles along spray axis are shown in Figure 8-1 and Figure 8-2 for low density (14.8 kg/m^3) and high density (30.0 kg/m^3) Sandia *n*-heptane case, respectively.

At low density, the spatial predictions of SVF by both methods coincide qualitatively with the experimental SVF at all oxygen levels as shown in Figure 8-1. Both the Lagrangian and Eulerian predicted soot cloud are shown to move downstream from the injector location as oxygen level decreases, which correspond to the experimental observation. However, all the predicted soot clouds by both simulation methods are further downstream relative to the measured soot cloud, as shown in Figure 8-1. Using the improved Lagrangian method (presence of surface ageing), soot profiles predicted by Lagrangian method coincides well with the ones

predicted by the Eulerian method for all oxygen levels. This implies that the improved Lagrangian method has comparable performance as the Eulerian method in predicting SVF profile. All these phenomena and observations are similarly captured for the high density cases in Figure 8-2.

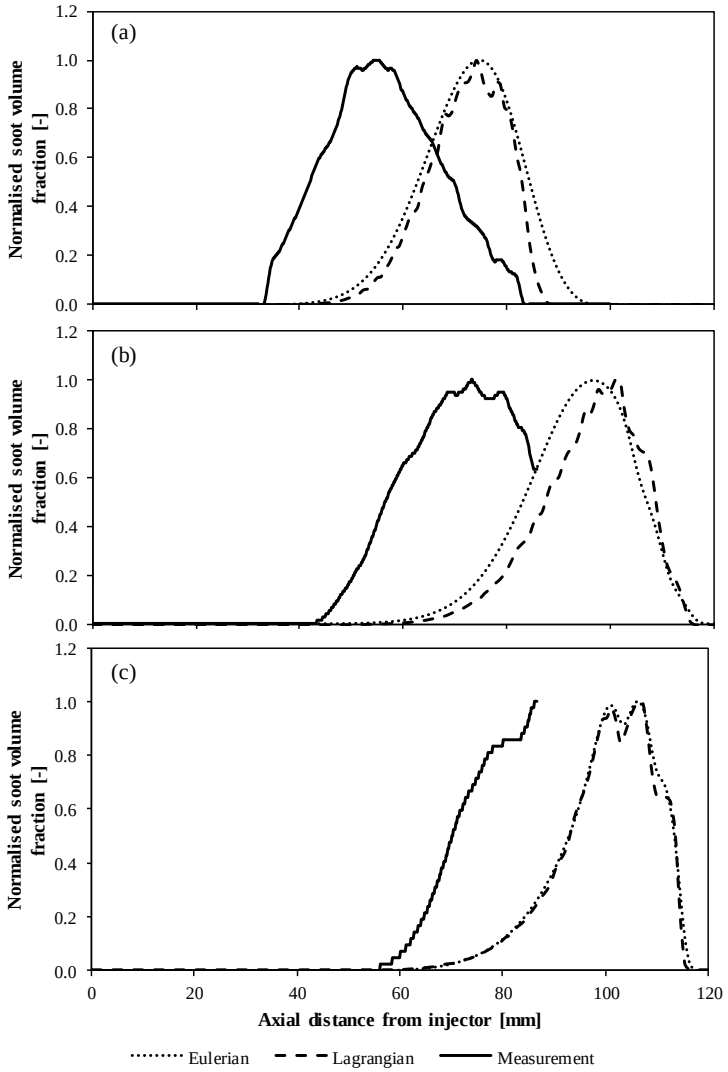

Figure 8- 1: Normalised SVF against axial distance from injector for (a) 21%, (b) 15% and (c) 12% oxygen levels at low density (14.8 kg/m^3) and ambient temperature of 1000 K.

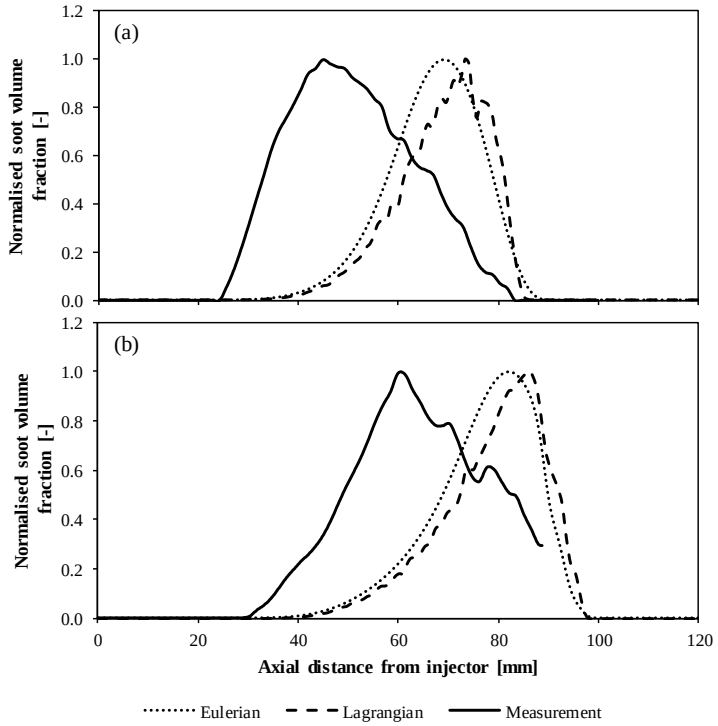

Figure 8- 2: Normalised SVF against axial distance from injector for (a) 15% and (b) 12% oxygen levels at high density (30.0 kg/m^3) and ambient temperature of 1000 K.

8.3 Effect of Ambient Oxygen and Density on Soot Sizing in Core Jet

Besides showing the prediction of SVF profiles, the effects of ambient oxygen and densities on soot size distribution at the core of spray jet for low density and high density Sandia *n*-heptane cases are studied. The improved Lagrangian method is implemented here to predict the soot size distribution at various axial locations along the spray axis for different ambient oxygen and density cases. The analysis of Lagrangian soot particles here follows the same methodology as stated in Section 6.4.3.

The soot size distribution for various ambient oxygen and density cases are shown in Figure 8-3. The prediction is carried out along the spray axis from x=40 mm to x=120 mm. At low density, significant soot particles are present at x=40 mm for the

21% O_2 case whereas they are present further downstream at x=50 mm and x=60 mm for the 15% and 12% O_2 cases, respectively. The observation that location of soot onset moves downstream as oxygen level decreases coincides with experimental observation in [122,282]. It is shown for all ambient oxygen levels and densities cases in Figure 8-3 that as soot particles migrate downstream, the soot particle diameters increase. This observation shows that soot particles are undergoing surface growth process as they are being convected downstream due to the momentum of the spray. From Figure 8-3, the predicted soot size is shown to increase as ambient density increases [121]. For oxygen level 15%, the maximum predicted soot size is approximately 8-10 nm at low density and 12-14 nm at high density. Similarly, the maximum predicted soot size for the 12% case is approximately 4-6 nm and 10-12 nm at low and high density, respectively. Furthermore, the predicted soot particles at higher density are shown to form nearer to the injector location than the ones predicted by the low density condition [265]. This is likely due to the shorter ignition delay and lift-off length when density increases.

The mean primary soot diameter along the core of spray jet is presented in Figure 8-4 for various ambient oxygen levels and ambient densities. Similarly, the mean diameter is shown to increase as ambient density increases [121]. However, the effect of ambient oxygen levels on the predicted mean diameter shows non-monotonic trend at ambient density of 14.8 kg/m^3. It is shown here that the mean diameter at peak soot cloud location for 21% and 15% are approximately the same, whereas the mean diameter for 12% is the lowest. The mean diameter for 21% O_2 level attains its highest at x=70 mm from injector location whereas for the 15% O_2 case, similar mean diameter is attained further downstream at x=100 mm. This result agrees with the experimental measured mean soot size obtained in [40] which also shows similar mean soot size for both 21% and 15% oxygen level cases. However, the reason for this observation was not clearly stated in [40]. Hence, further analysis using LST model is carried out in hope to shed light on this matter.

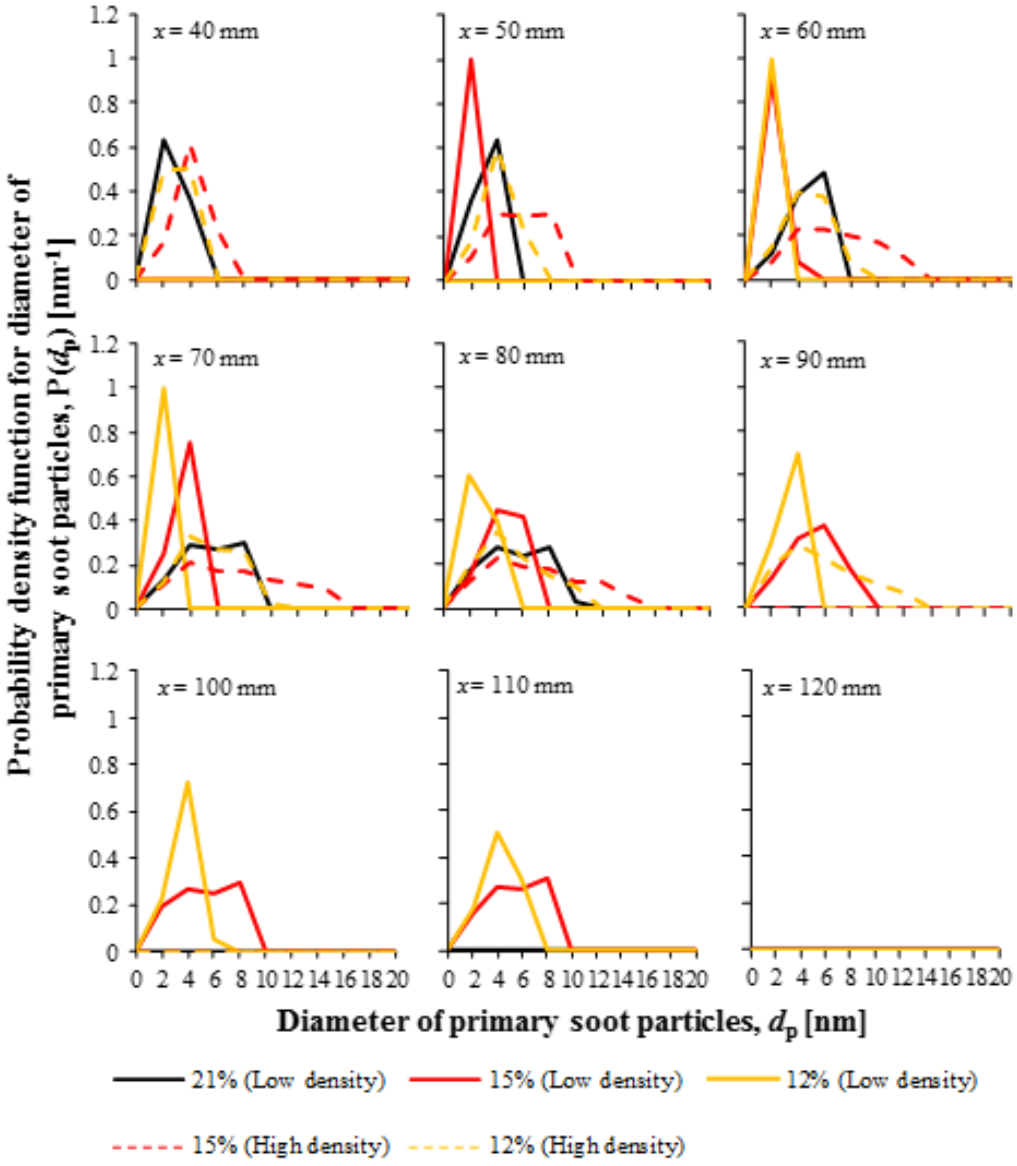

Figure 8- 3: Soot sizing distribution predicted using LST model for different ambient oxygens and densities along various axial locations from injector location.

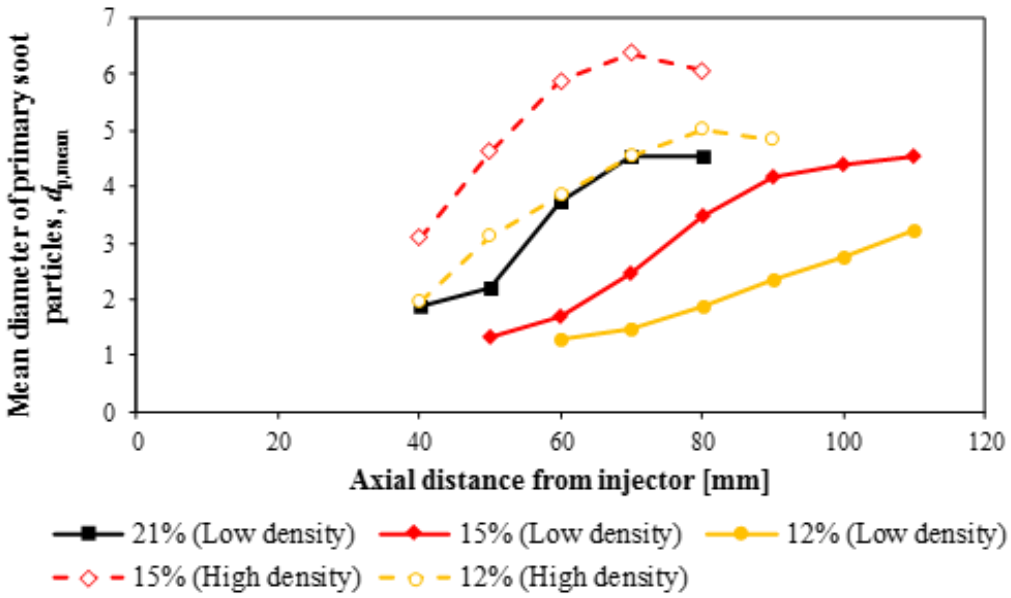

Figure 8- 4: Mean soot sizing predicted using LST model for different ambient oxygens and densities along various axial locations from injector location. [The filled symbols refer to low density cases; hollow symbols refer to high density cases]

The steady-state distribution of primary soot diameter in the core of spray jet for different oxygen levels and ambient densities are presented in Figure 8-5. Similar to the results in Figure 8-4, identical maximum soot diameter is predicted for the 21% and 15% case at ambient density of 14.8 kg/m^3. Meanwhile, the maximum soot diameter for the 12% case is the lowest. The maximum soot diameters are 8.3 nm and 8.0 nm for the 21% and 15% case, respectively. The soot cloud span for both 15% and 12% is approximately 60 mm which is longer than the 21% case by 10 mm. As for the high density case, the maximum primary soot diameter for the 15% case is approximately 13 nm, while the 12% case predicts a maximum soot diameter of around 10 nm. Despite predicting smaller soot size, the soot cloud span for the 12% case is longer than the 15% case.

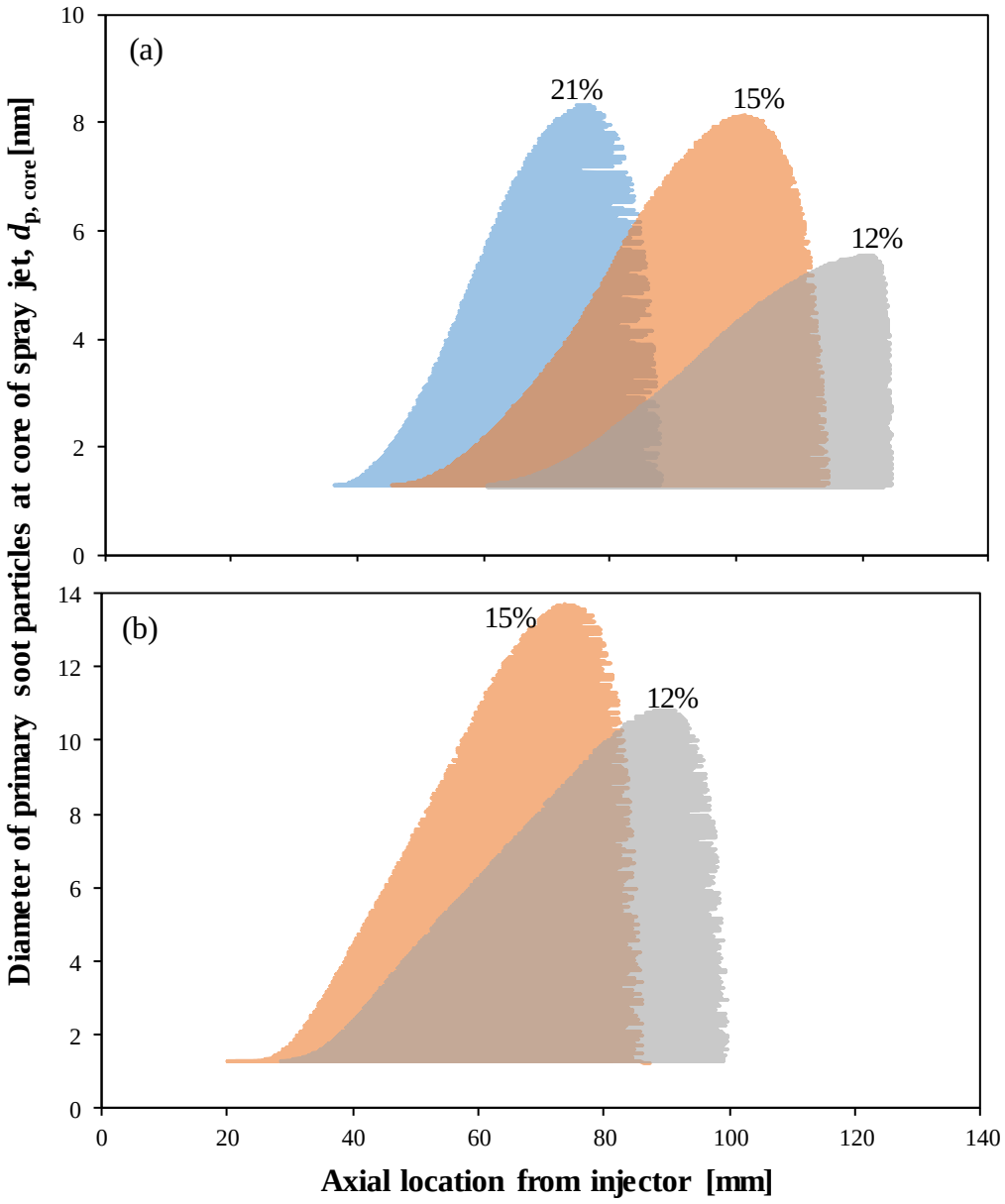

Figure 8- 5: Steady-state soot size distribution at core of spray jet for (a) low density case (14.8 kg/m^3) and (b) high density case (30.0 kg/m^3). [The oxygen levels are inserted in the figure]

The effects of ambient oxygen and ambient density on the soot size are further analysed by comparing their steady-state net growth rates along spray axis, as shown in Figure 8-6. The observation that higher density results in higher soot size can be attributed to the higher net growth rate experienced by the soot particles. As shown in Figure 8-6, the net growth rate for both 15% and 12% oxygen cases at density of 30.0 kg/m^3 are higher than their low density counterparts. The soot size predicted in the 12% case is the lowest as it has the lowest net growth rates among all other cases. As it is shown in Figure 8-4 and 8-5 that the peak soot size predicted for 21% and 15% is similar, thus the net growth rates for both cases are expected to have equal magnitude. On the contrary, the net growth profiles in Figure 8-6 show that the net growth rate for 21% case is very much higher than the 15% case, by a factor of approximately 2.4. The observation of higher net growth at 21% oxygen level than 15% is similarly reported in [122,292].

It is hypothesised that the net growth rates for 21% may be lower than the 15% case or vice versa during the transient period of soot evolution, which lead to the same predicted soot size for both 21% and 15% cases. Furthermore, the results presented in Figure 8-3 to 8-6 are the time-integrated results based on all the Lagrangian particles recorded and analysed from start of ignition to 6.0 ms ASOI. Therefore, in order to gain better insight on the effect of ambient oxygen and density on soot sizing, deeper analysis during the transient period is carried out. The transient net growth rates for low and high density cases are presented in Figure 8-7. In addition, the transient spatial soot size distributions are presented in Figure 8-8 and 8-9 for low and high density cases, respectively. As the ignition delay is different at different ambient oxygen level and ambient density, it is more useful to carry out the transient analysis after soot onset (ASO). The soot onset timings for each operating conditions are tabulated in Table 8-1.

Table 8- 1: Soot onset timing for different ambient oxygen and density case of Sandia *n*-heptane spray.

Ambient density [kg/m^3]	Ambient oxygen [%]	Soot onset timing [ms]
14.8	21	0.55
	15	0.94
	12	1.38
30	15	0.41
	12	0.57

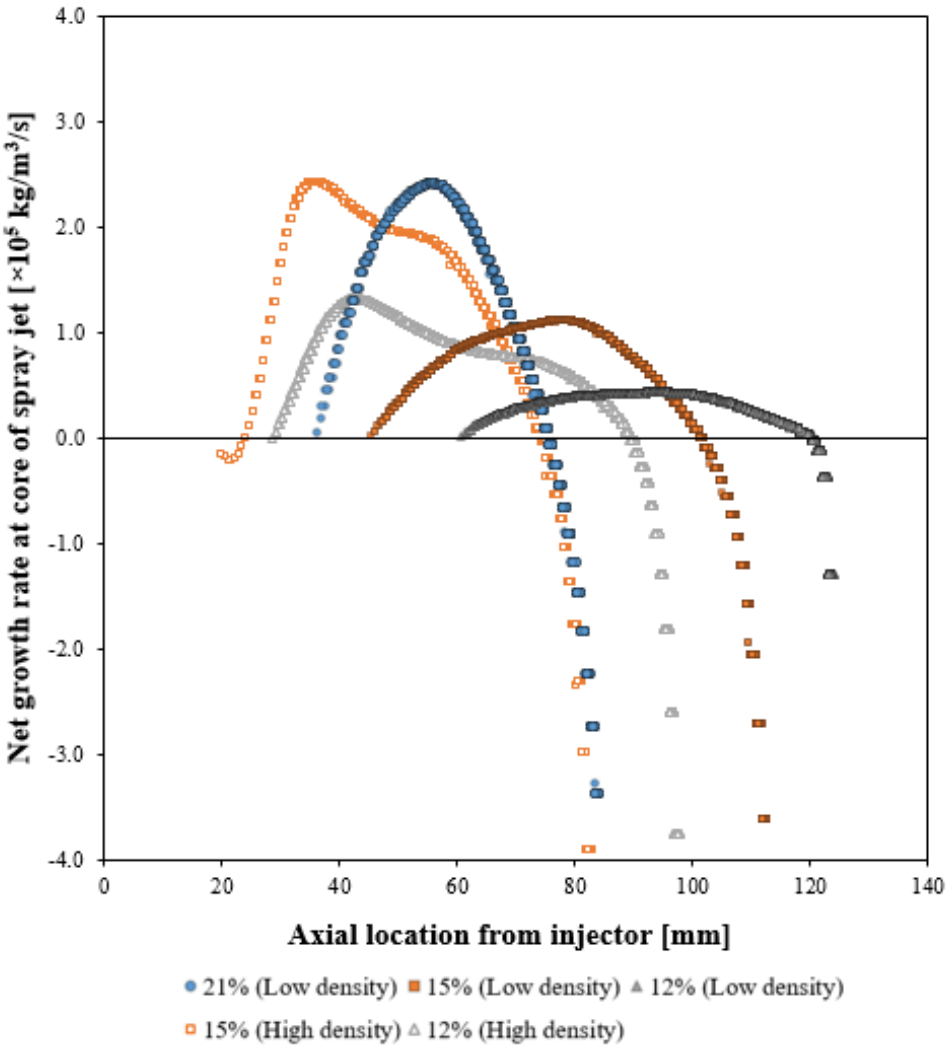

Figure 8- 6: The steady-state net growth rates at core of spray jets for different ambient oxygen and density cases. [The filled symbols refer to low density cases; hollow symbols refer to high density cases]

Contrary to hypothesis above, the peak net growth rates for the 21% are shown to be higher than the 15% case throughout the injection duration as seen in Figure 8-7. The peak net growth rates for 21% is approximately 2.4×10^5 kg/m^3/s while the peak net growth rates for 15% is approximately halved of it. In Figure 8-8, it is a shown that the peak diameter is reached at a shorter time for the 21% case than the 15% case. The peak diameter for the 21% case is attained at 3.0 ASO, whereas the peak diameter is reached at later time of 4.0 ASO for the 15% case. Therefore, it is postulated that the soot diameter is not just affected by the absolute value of the net growth rates but may also be affected by the residence time of soot in the soot cloud and soot cloud span. The duration of soot experiencing surface growth process gets shorter when the cloud span is short. Despite having a lower net growth rate, the longer span in the 15% case implies that soot undergoes surface growth for a longer duration thus enabling soot particles to reach much larger sizes. This hypothesis is supported by analysing the soot age distribution for the low density cases as shown in Figure 8-10.

Soot age refers to the duration from the moment it is formed till the moment it is fully oxidised [31]. The soot age distribution for all low and high density cases are similar at 1.0 ASO and 2.0 ASO. However, at 3.0 ASO, the maximum soot age for the 21% case is lower than all other cases as seen in Figure 8-10. This trend persists to 4.0 ASO. The lower maximum soot age for the 21% case indicates that the lifespan of the soot particles inside the soot cloud is relatively shorter than the lifespan of soot particles in other cases. This implies that the soot particles in the 21% case undergo shorter surface growth processes whereas the soot particles in the 15% case undergo longer surface growth processes. At oxygen level of 15%, the longer surface growth process experienced by the soot particles has compensated for the lower net growth rates. Hence, leading to similar soot size as the 21% case.

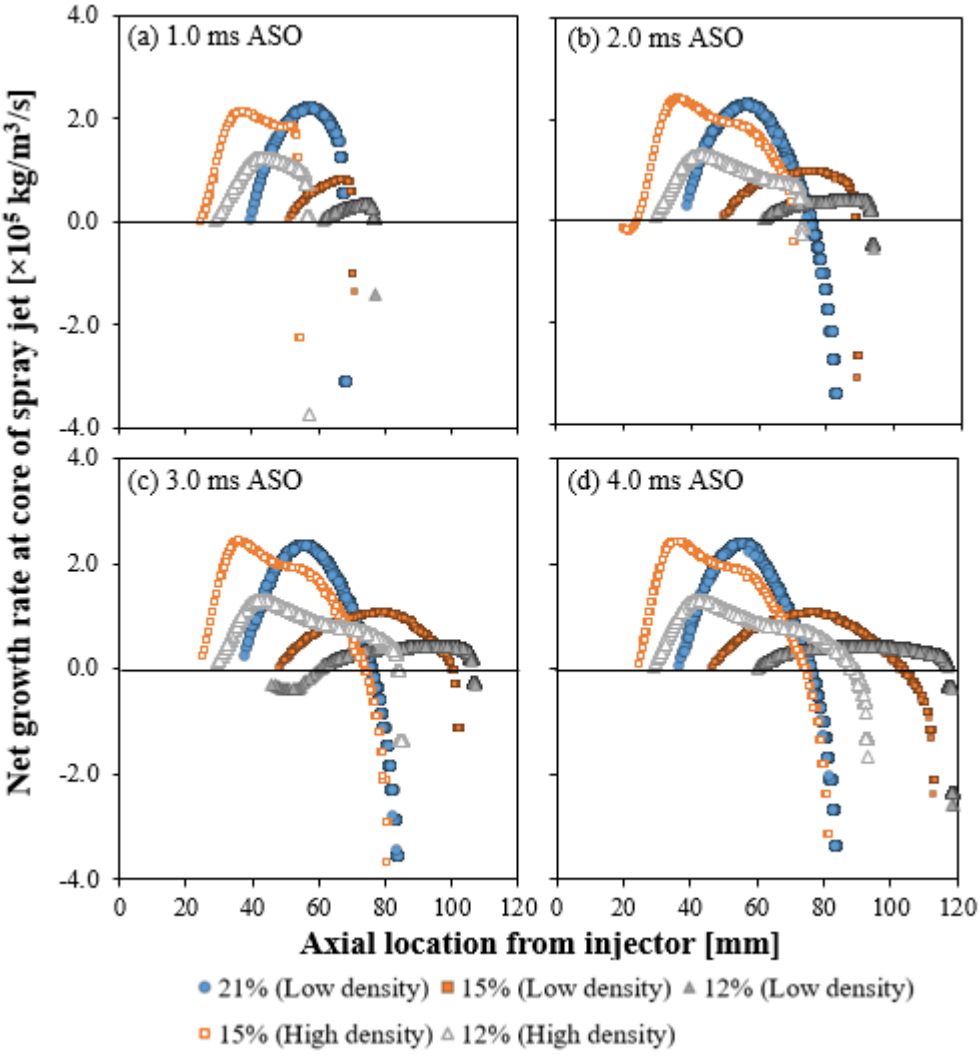

Figure 8- 7: Transient net growth rates at core of spray jet for different ambient oxygen and density cases at different timings ASO. [The filled symbols refer to low density cases; hollow symbols refer to high density cases]

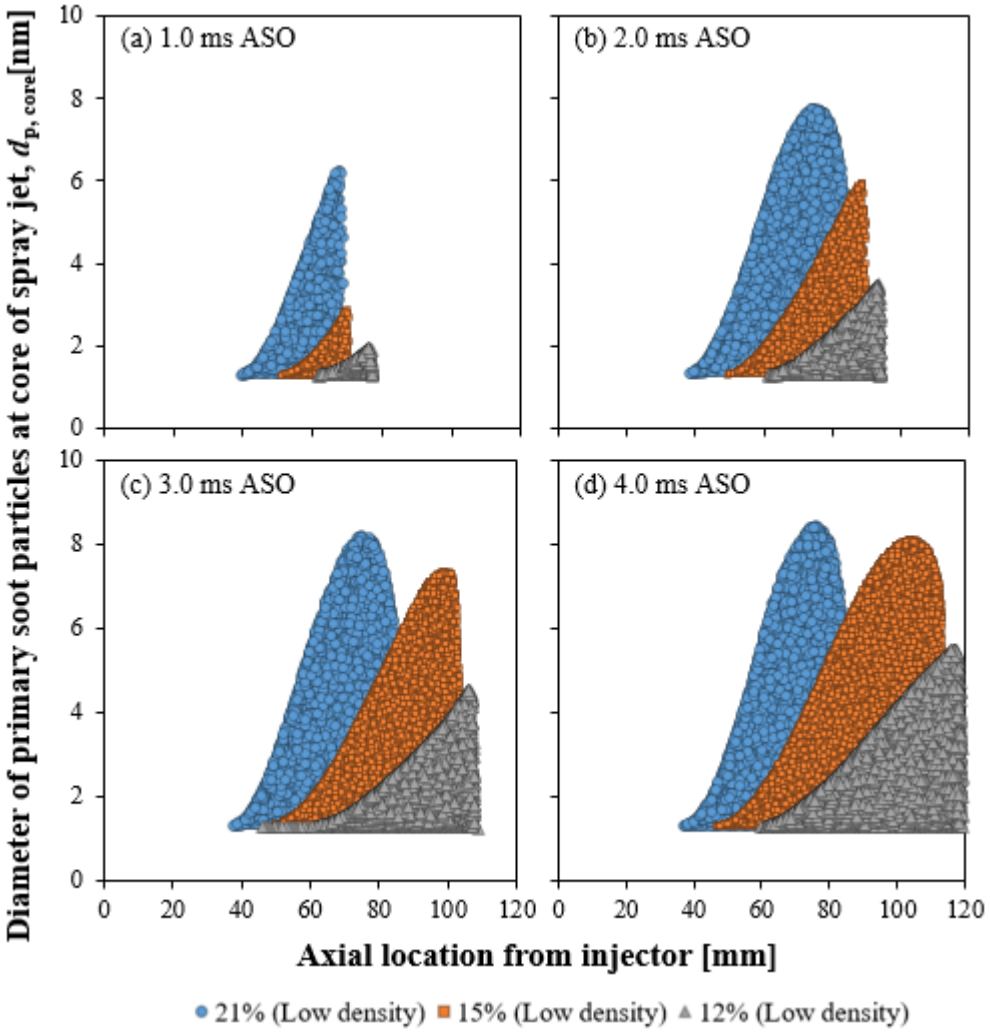

Figure 8- 8: Transient soot sizing distribution of soot particles at the core of the spray jet for low density cases (14.8 kg/m^3).

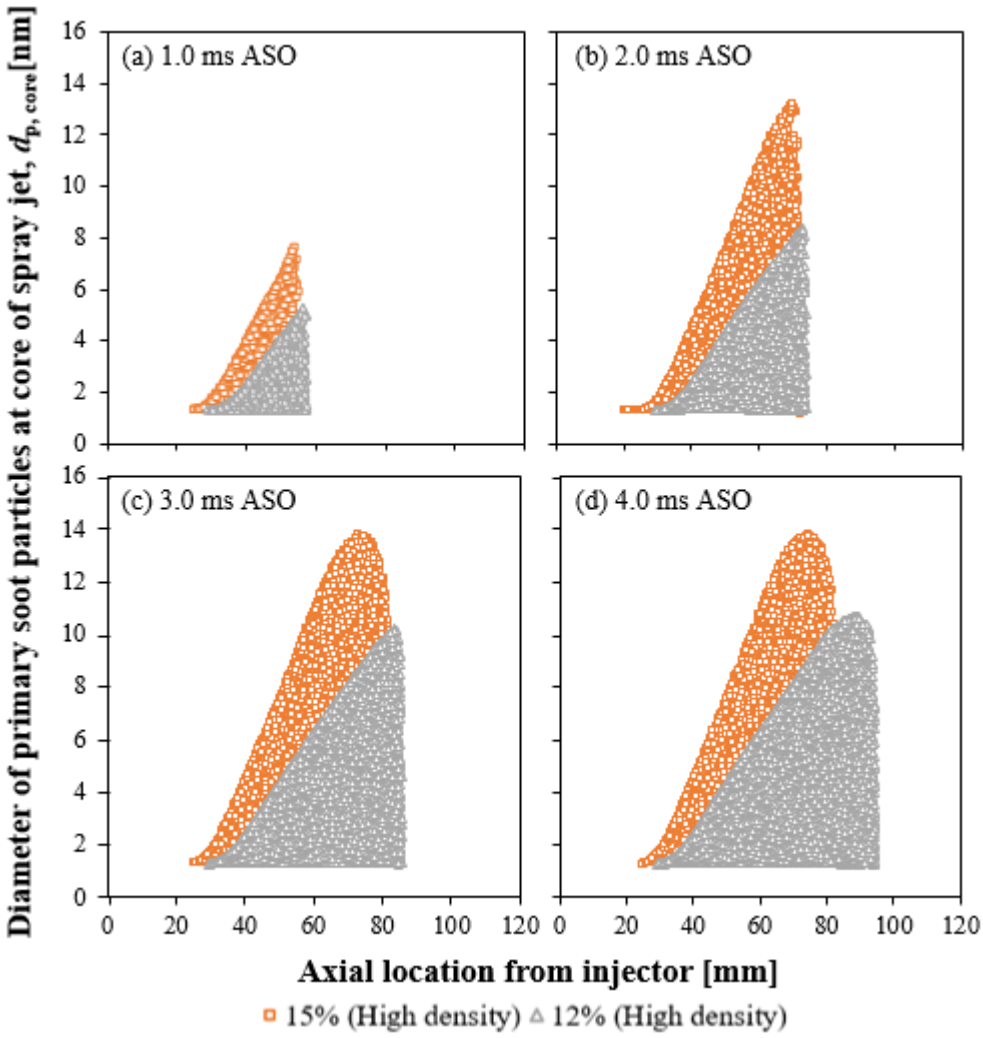

Figure 8- 9: Transient soot sizing distribution of soot particles at the core of the spray jet for high density cases (30.0 kg/m^3).

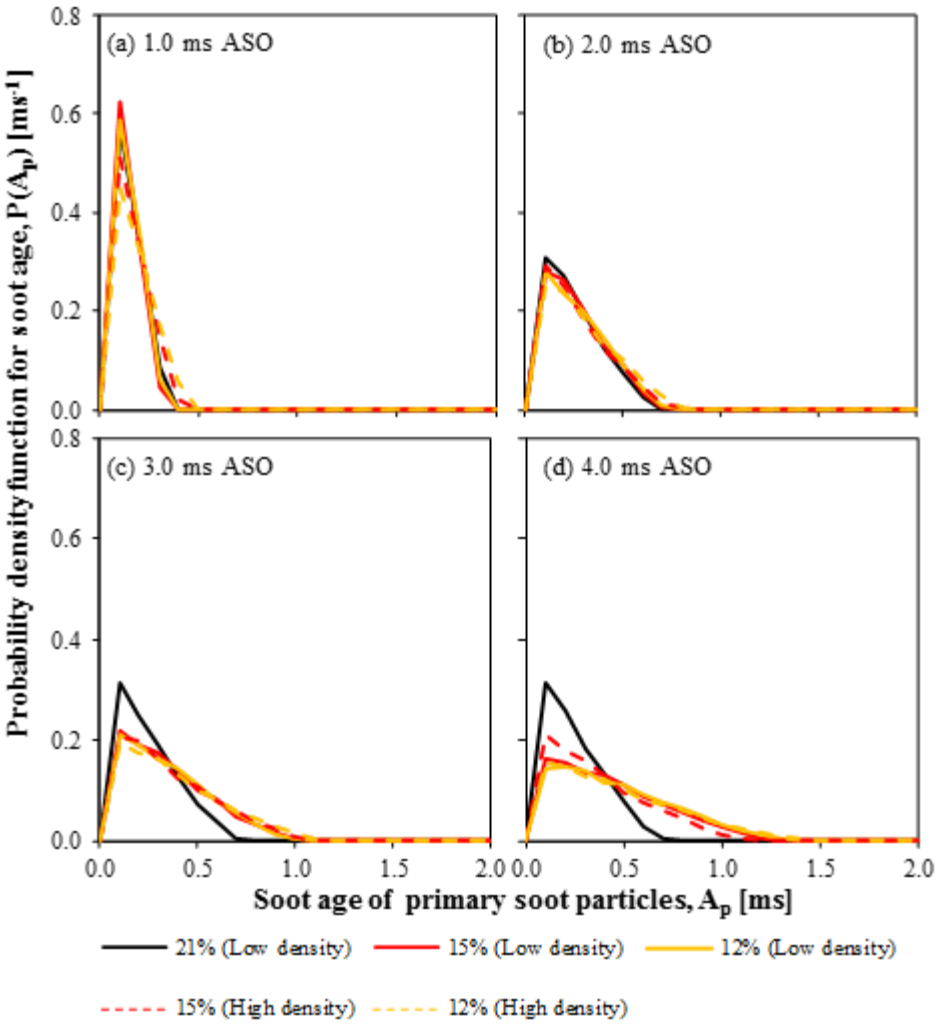

Figure 8- 10: Transient soot age distribution of soot particles at the core of spray jet predicted using LST model for different ambient oxygens and densities at different timing ASO. [Solid lines refer to low density cases; dashed lines refer to high density cases]

At high density, the net growth rates for the 15% case is higher than the 12% case as seen in Figure 8-6 and 8-7. However, the cloud span for the 15% case is shorter than the latter case as observed in Figure 8-5. Despite having longer cloud span than the 15% case, the peak soot diameter attained for the 12% case is still smaller than the 15% case as presented in Figure 8-5 and 8-9. This is because the soot age for both 15% and 12% case is similar at all timings ASO, as shown in Figure 8-10. This finding implies that lower surface growth rate does not guarantee small soot size,

the soot cloud span and the age of soot particles also play a crucial role in dictating the soot size. A similar explanation was made by Idicheria et al. [122] on the effect of EGR on the soot mass. They explained that the sudden increase in soot mass when oxygen level decreases from 21% to 15% is due to the competition between soot formation rates and residence time [122].

8.4 Effect of Ambient Oxygen and Density on Soot Sizing in Soot Cloud

Besides studying the soot sizing at the core of the spray jet, the effect of ambient oxygen and density on soot size distribution in the whole soot cloud is also investigated. This study is carried out from soot onset timing for different ambient oxygen levels and densities. Figure 8-11 to 8-13 show the transient soot size distribution for low density cases; Figure 8-14 and 8-15 show the transient soot size distribution for the high density cases.

The first-soot location is seen to move downstream as oxygen level and ambient density decrease [122] as seen from Figure 8-11 to 8-15. Furthermore, the rate of increase in soot size as soot particles propagate downstream is shown to decrease with decreasing oxygen levels and ambient density which is probably due to the lower combustion temperature as seen from Figure 8-11 to 8-15. A lower combustion temperature leads to lower soot formation rates [122], thus slowing down the formation and growth of soot particles. It is observed that during the early phases, soot is mainly formed at the periphery of the flame, which is in the vicinity of the diffusion flame zone where the temperature is expected to be higher than the reactions in the spray core. There is almost no traceable soot in the central region of the jet due to lower temperature and richer mixture. Based on the observations, a general trend is followed, where many small young soot particles formed in the upstream grow into larger particles in the downstream due to surface growth in the spray flame [283]. The growth rate is shown to be higher near the periphery of the flame as compared to other regions at the spray head. This higher growth rate is likely due to the soot particles undergoing higher surface growth rates at high temperature zone [177].

All the test cases are shown to follow the soot formation processes suggested by Kosaka et al. [290]. The soot formation, surface growth and oxidation processes are explained as follows according to Figure 8-11:

In the early soot formation process, the soot precursors are formed in the whole leading portion of the spray flame immediately after ignition. The soot precursor located at the periphery of spray flame is converted to soot particles first as shown during the soot onset in Figure 8-12 to 8-16. As combustion process continues, larger fuel-rich region is present at the centre of the spray jet. This slowly leads to more soot particles being converted from soot precursors at the central fuel-rich region as shown at 0.2 ms ASO to 0.8 ms ASO in Figure 8-12 to 8-16. The young soot particles, which are formed throughout the fuel-rich region, grow by surface growth during convection to the spray head. At the spray tip, the soot particles are pushed aside to the spray periphery by the motion of head vortices. Eventually, the soot particles are oxidised around the periphery of the luminous flame-plume when they flow outward to regions with high *OH* concentration.

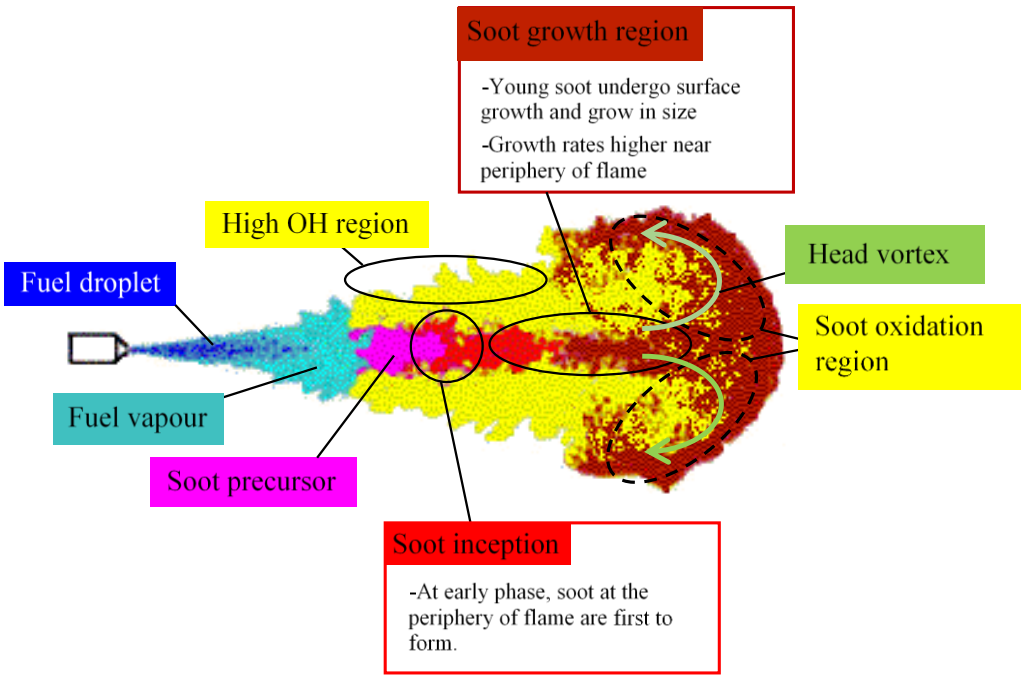

Figure 8- 11: Conceptual model for the soot formation, surface growth and oxidation processes in reacting spray, adopted from [290]**.**

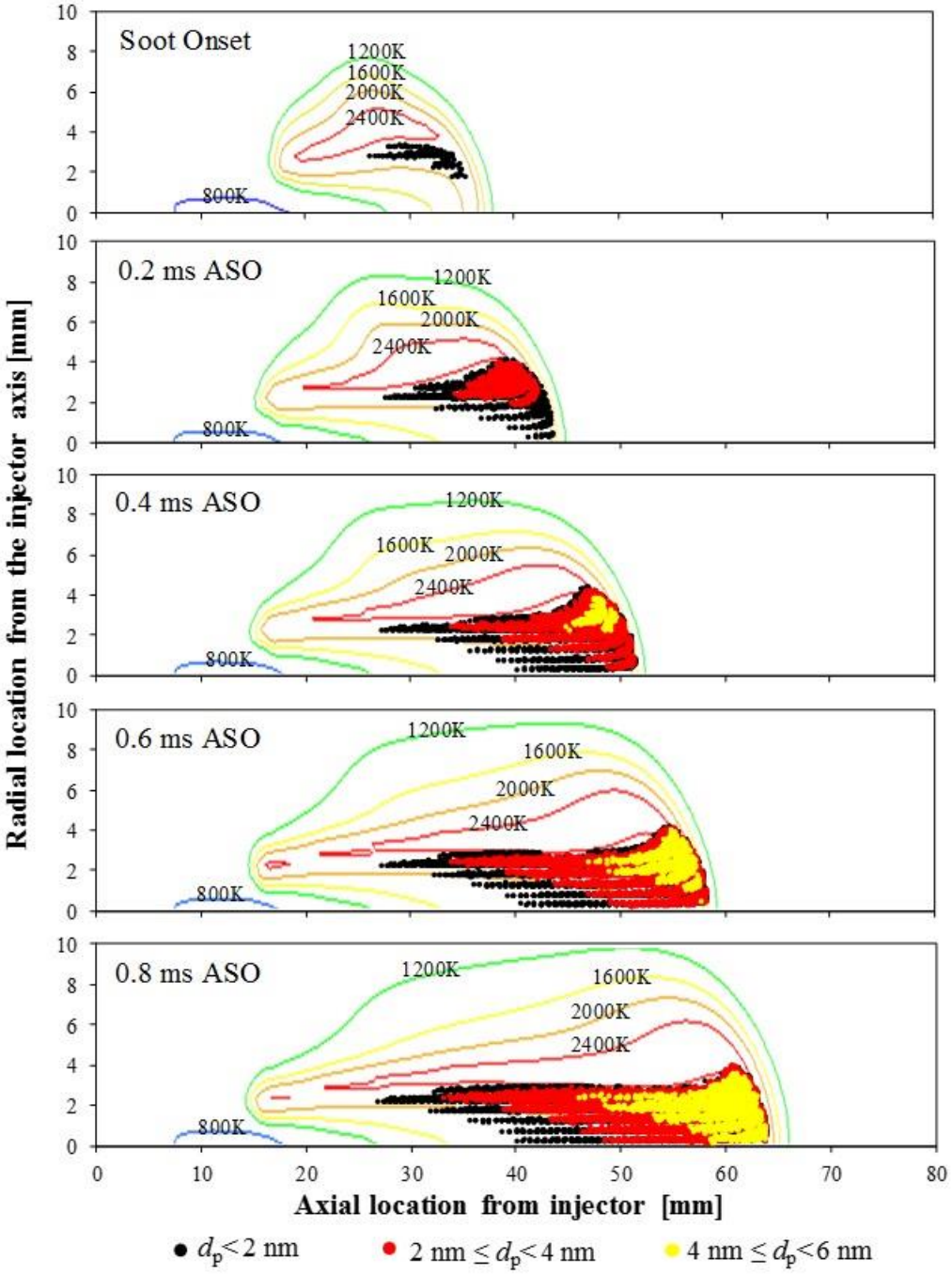

Figure 8- 12: Transient soot sizing distribution in the whole spray jet superimposed on the temperature profile for the 21%, low density case (14.8 kg/m^3) at different timings ASO.

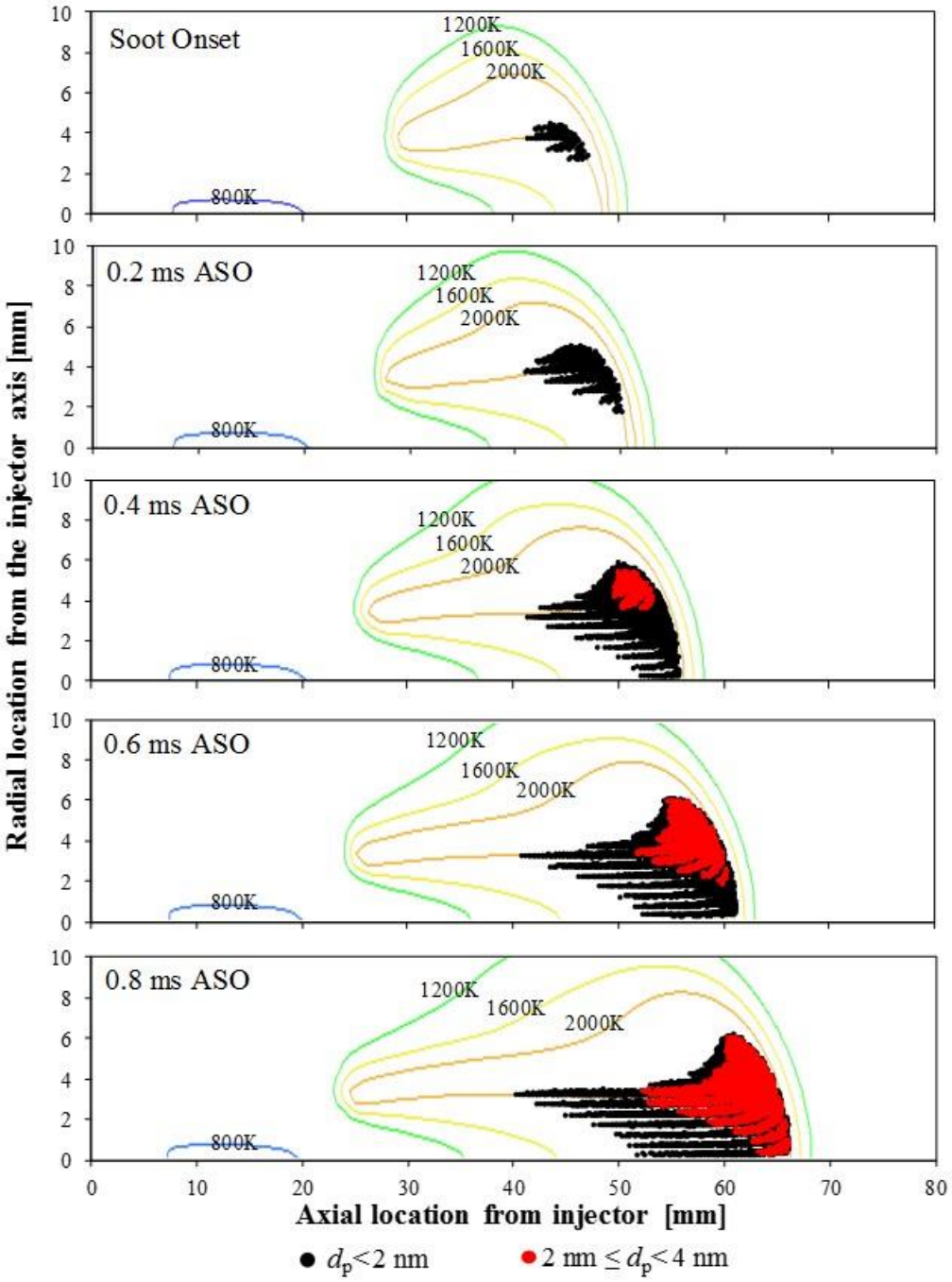

Figure 8- 13: Transient soot sizing distribution in the whole spray jet superimposed on the temperature profile for the 15%, low density case (14.8 kg/m^3) at different timings ASO.

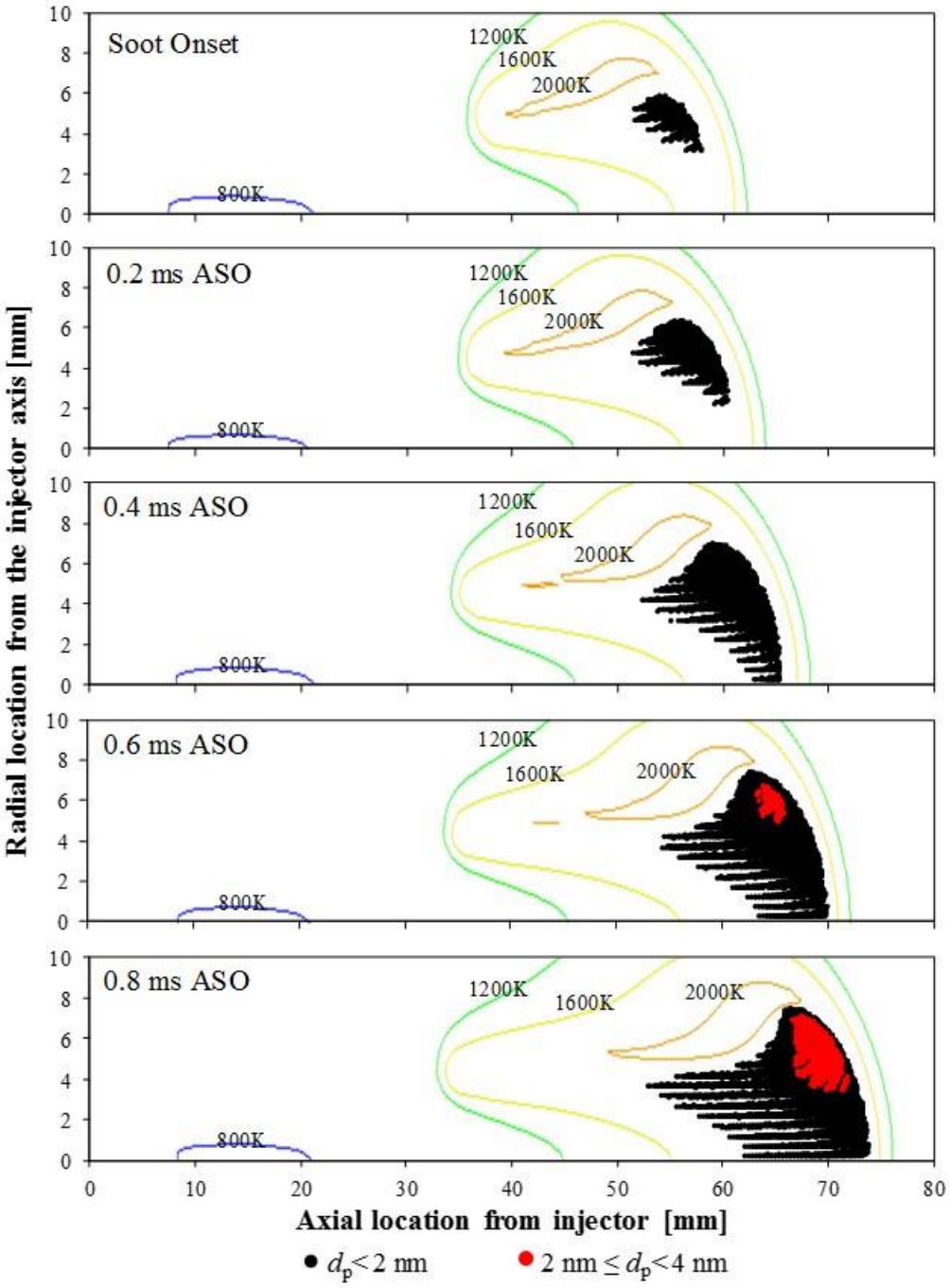

Figure 8- 14: Transient soot sizing distribution in the whole spray jet superimposed on the temperature profile for the 12%, low density case (14.8 kg/m^3) at different timings ASO.

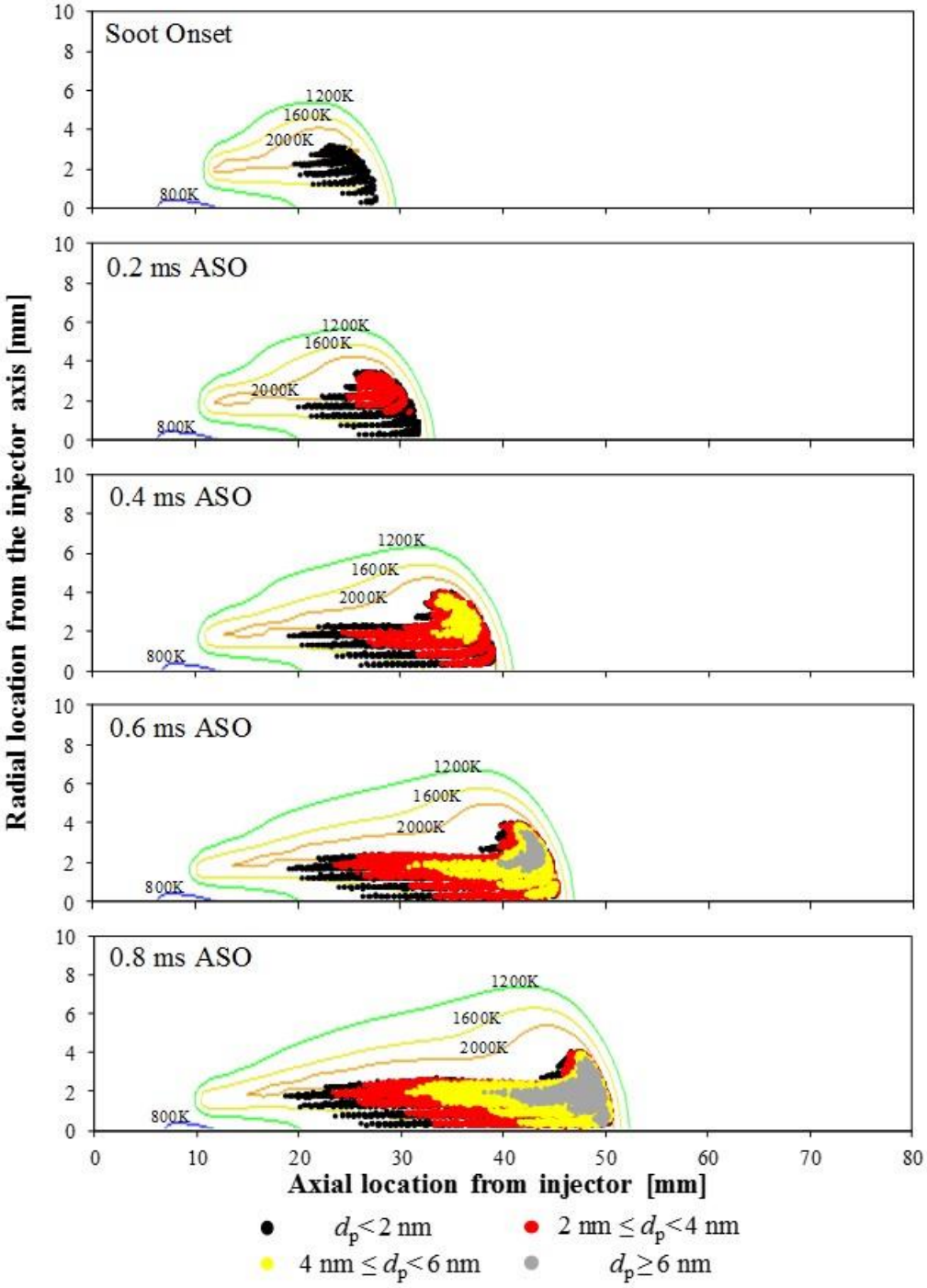

Figure 8- 15: Transient soot sizing distribution in the whole spray jet superimposed on the temperature profile for the 15%, high density case (30.0 kg/m^3) at different timings ASO.

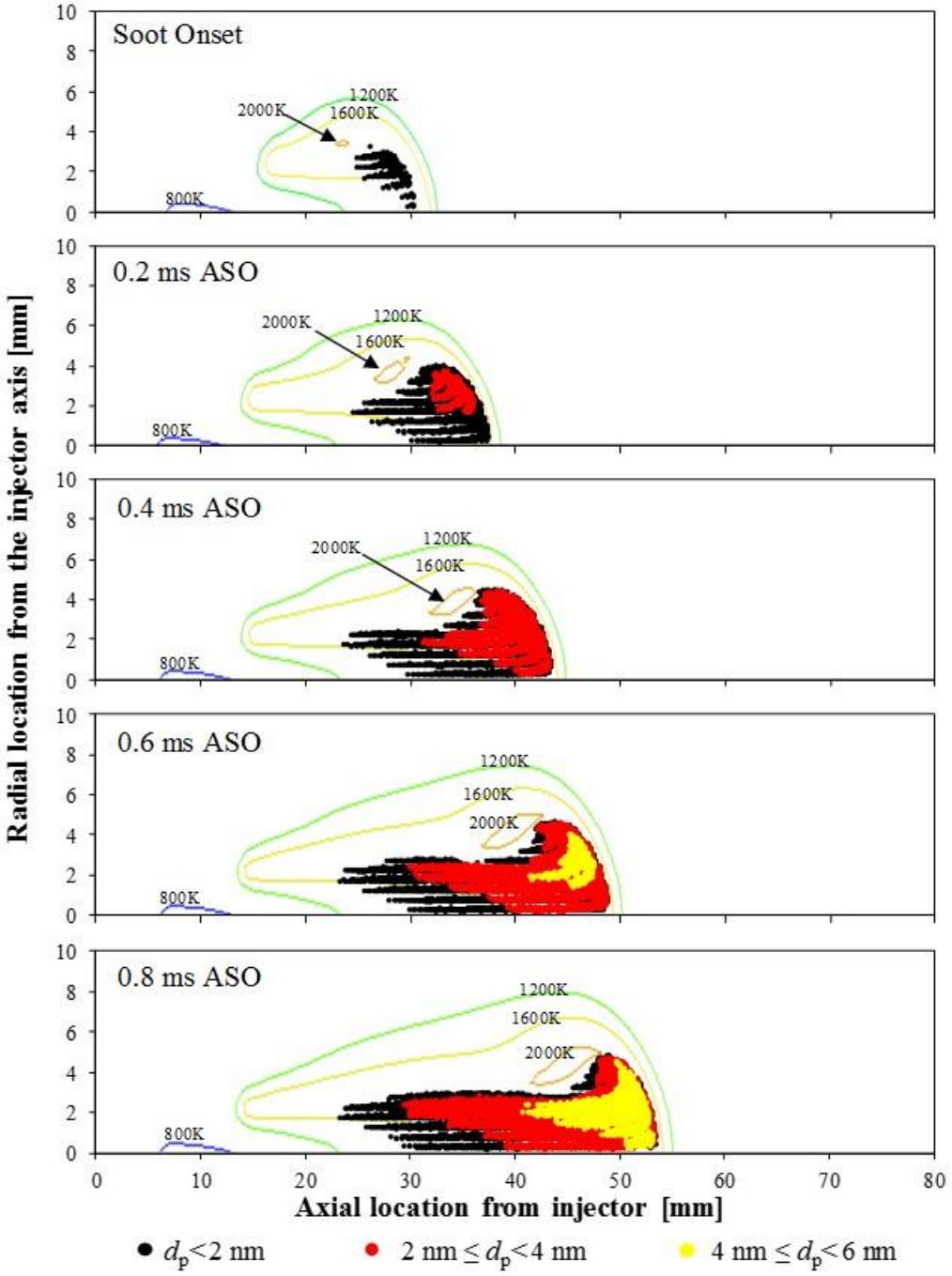

Figure 8- 16: Transient soot sizing distribution in the whole spray jet superimposed on the temperature profile for the 12%, high density case (30.0 kg/m^3) at different timings ASO.

The experiments and numerical studies carried out by other researchers [150,201,279,282,289,291,293] have been focusing solely on the sizing and concentration of the soot formed. Based on the author's knowledge, there has been only a few studies on soot age [31,38,39], in which most are related to surface reactivity of soot. By studying the soot age of individual soot particles formed, one would be able to identify whether the soot cloud is dominant by old or young soot particles. There is a possibility that the majority of large particles are old particles formed earlier in the combustion process. It is shown that young and old particles have significantly different properties, appearances and internal nanostructure [294–299]. Knowing the maturity of the soot particles may lead to a better understanding and formulation of soot formation process. Furthermore, it is previously shown in Section 8.3 that soot age plays a crucial role in affecting soot sizing. Therefore, the soot diameter with respect to its corresponding soot age is plotted and shown in Figure 8-17 to 8-21. Figure 8-17 to 8-19 refer to the low density cases; Figure 8-20 and 8-21 refer to the high density cases.

From Figure 8-17, it is seen that primary soot particles formed before 0.2 ms ASO are almost entirely oxidised by 0.6 ms ASO. This implies that the large particles present at 0.6 ms ASO are entirely made out of soot particles which are formed between 0.2 ms to 0.4 ms ASO. Similar observation is seen for the 15% low and high density cases in Figure 8-18 and 8-21, respectively. Based on the soot diameter-age distribution, for 21% and 15% cases, the maximum soot age achieved is around 0.4 ms at both high and low densities. This means that ambient density has no effect on the lifespan of the soot particles in the spray jet during this transient period despite having a larger growth rate when ambient density increases. For 12% low and high density cases, the soot age can reach up to 0.58 ms as shown in Figure 8-19 and 8-21. This is likely due to the lower combustion temperature at lower oxygen level.

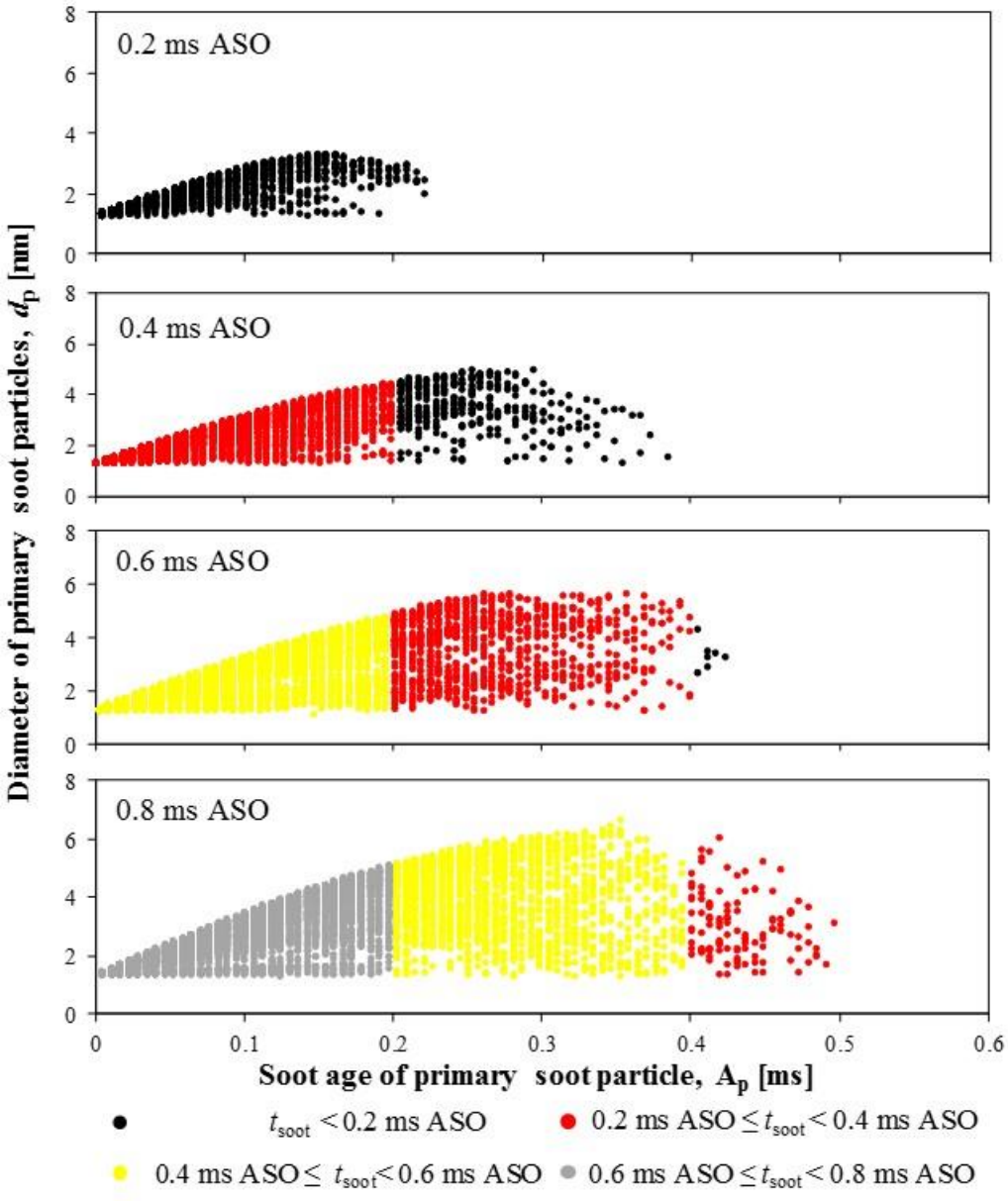

Figure 8- 17: Transient soot sizing distribution against corresponding soot age in the whole spray jet for the 21%, low density case (14.8 kg/m^3). [t_{soot} refers to the time of formation for the primary soot particle]

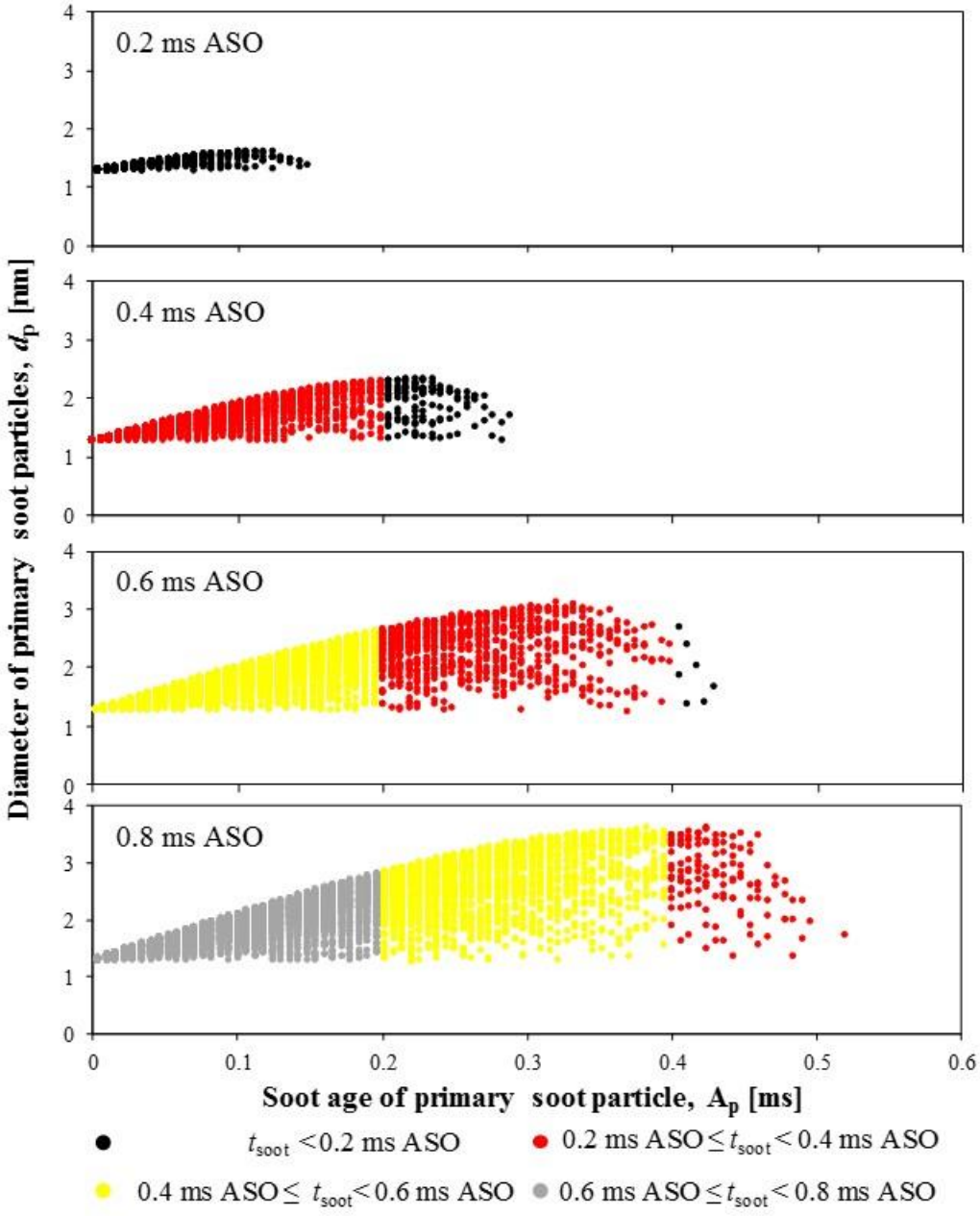

Figure 8- 18: Transient soot sizing distribution against corresponding soot age in the whole spray jet for the 15%, low density case (14.8 kg/m^3). [t_{soot} refers to the time of formation for the primary soot particle]

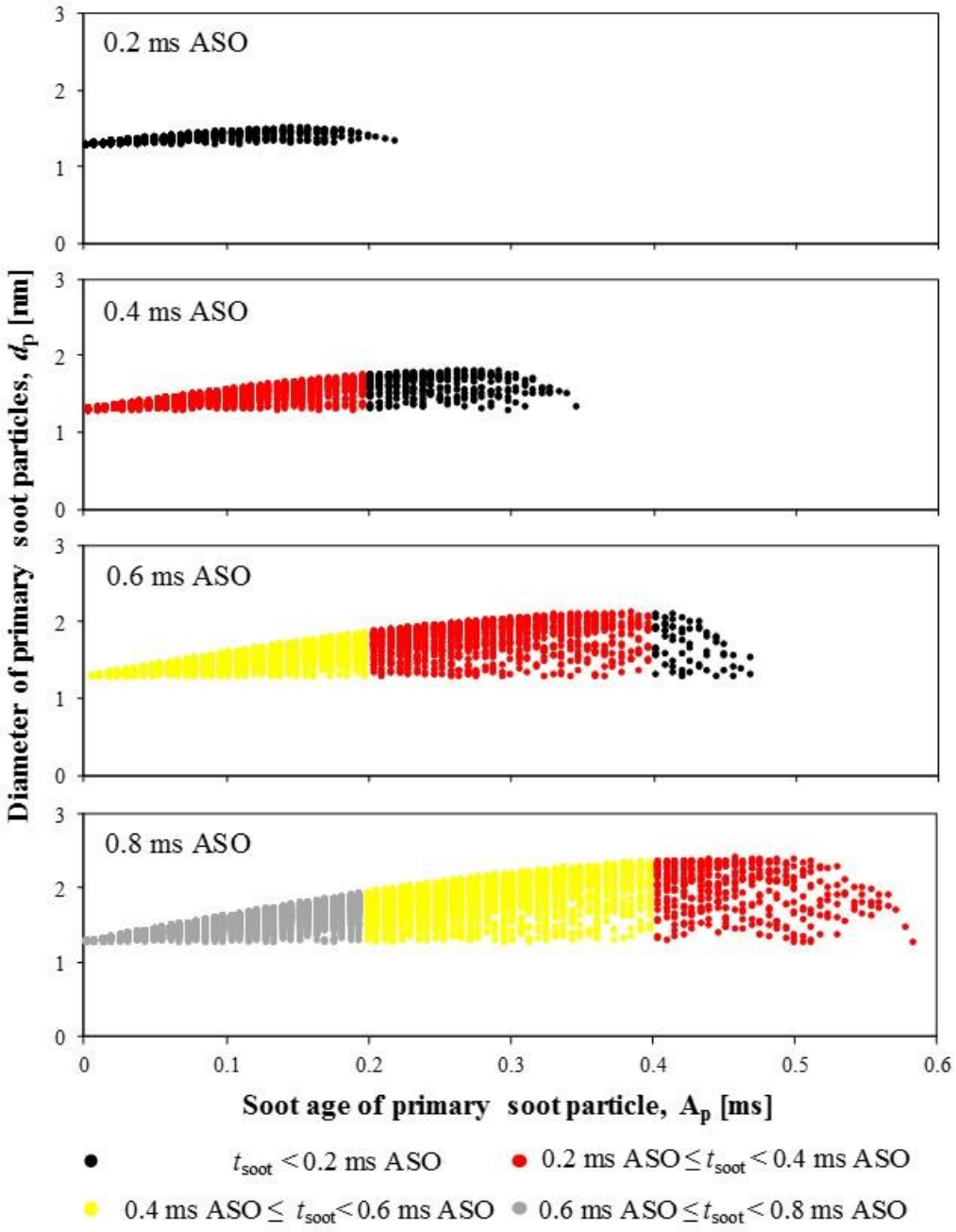

Figure 8- 19: Transient soot sizing distribution against corresponding soot age in the whole spray jet for the 12%, low density case (14.8 kg/m^3). [t_{soot} refers to the time of formation for the primary soot particle]

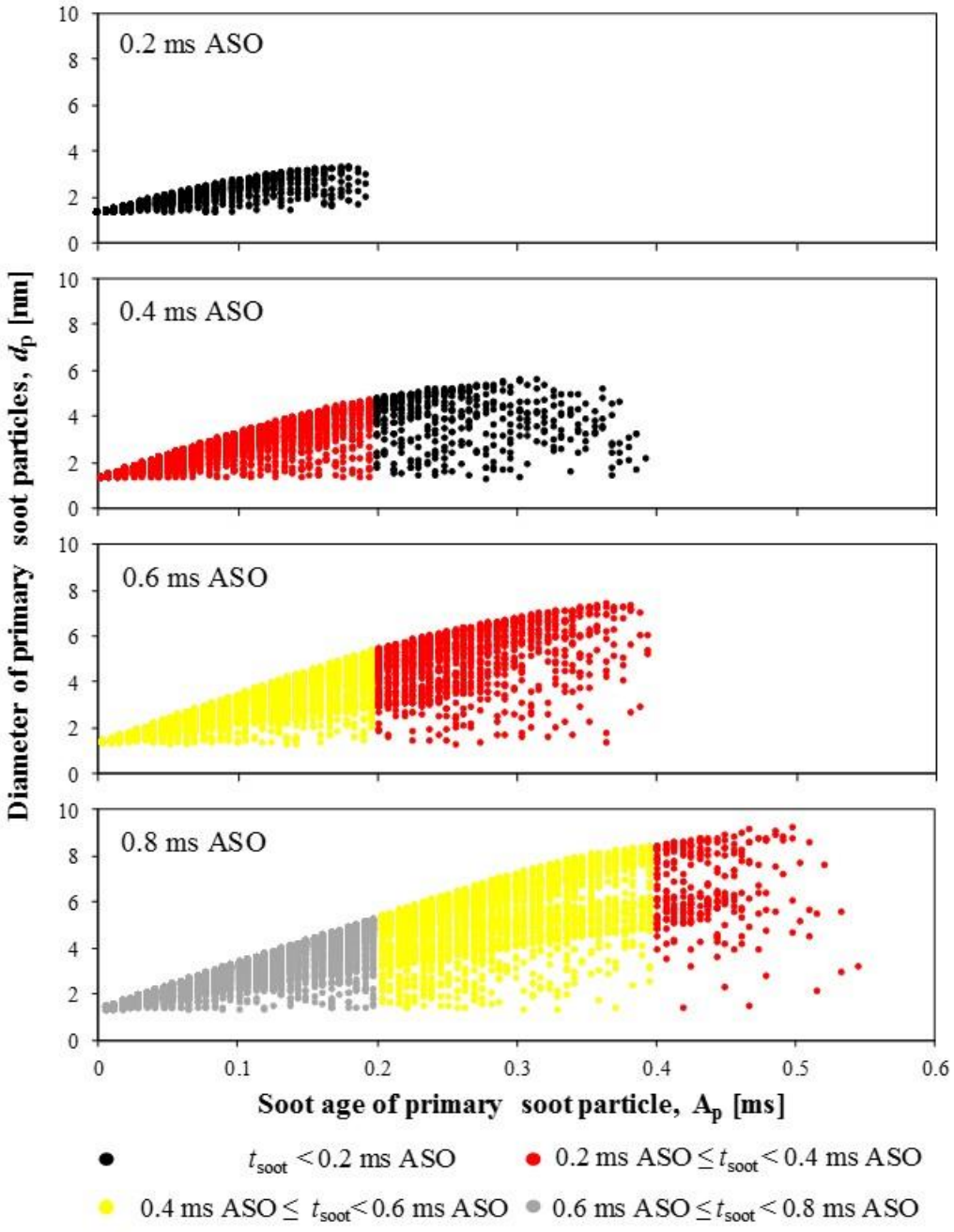

Figure 8- 20: Transient soot sizing distribution against corresponding soot age in the whole spray jet for the 15%, high density case (30.0 kg/m^3). [t_{soot} refers to the time of formation for the primary soot particle]

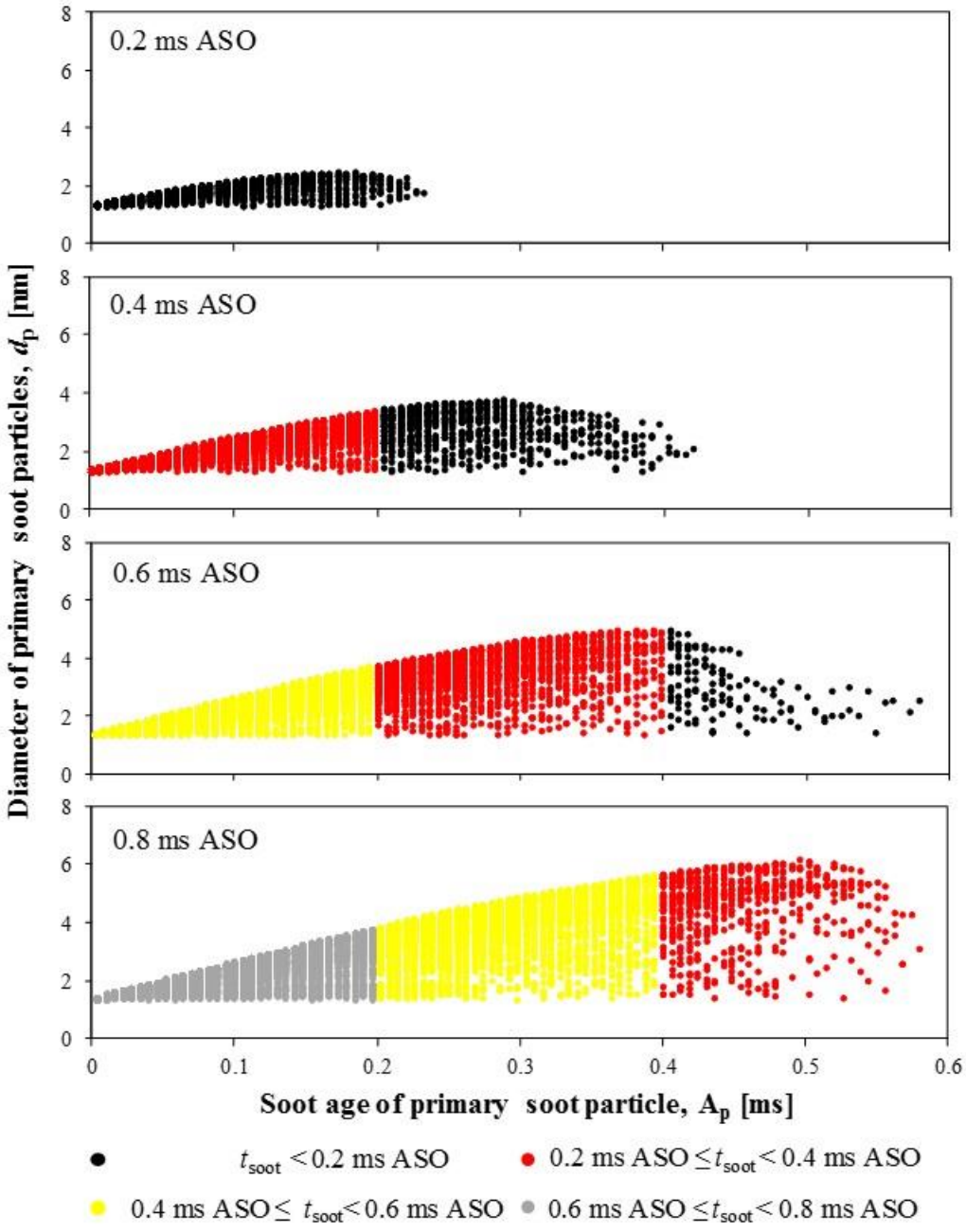

Figure 8- 21: Transient soot sizing distribution against corresponding soot age in the whole spray jet for the 12%, high density case (30.0 kg/m^3). [t_{soot} refers to the time of formation for the primary soot particle]

8.5 Concluding Remarks

The effect of ambient oxygen level and density on SVF prediction and primary soot size distribution is carried out using the LST model. The model implemented have incorporated surface ageing effect. The numerical studies are performed based on Sandia *n*-heptane case setup and operating conditions.

An increase in ambient density results in a larger predicted peak and mean primary soot size along the core of spray jet. Non-monotonic trend in both peak and mean primary soot size is observed when oxygen level decreases from 21% to 12%. Smaller primary soot size is only observed when oxygen level decreases from 15% to 12%. However, no change in primary soot size is observed between the 21% and 15% O_2 level cases despite the latter having relatively lower net growth rates. This observation can be attributed to the longer soot cloud span and soot age for the 15% case than the 21% case. The finding implies that primary soot size is not solely dependent on the growth rates, but also on the soot cloud span and soot age. The study on the effect of soot size distribution for soot particles in the whole soot cloud is also carried out. An increase in ambient density and ambient oxygen result in a more upstream first-soot location. The maximum soot age predicted is approximately 0.4 ms for both 21% and 15% O_2 cases at both ambient densities. A lower oxygen level leads to a higher maximum soot age of 0.58 ms due to lower combustion temperature.

This study of soot age is still relatively new as experimental data is scarcely available. However, the advent of this soot age study shows the potential of this parameter to answer various fundamental questions in soot processes and be used in the study of soot microstructure.

CHAPTER 9

CONCLUSIONS AND FUTURE WORK

9.1 Conclusions

This chapter concludes the key findings obtained in this research study. A Lagrangian soot tracking (LST) model is developed and validated in both *n*-heptane and *n*-dodecane spray flame, under diesel-like conditions. The validation is done by comparing the predicted SVF, mean soot diameter and soot size distribution to the experimental data. A sensitivity study is carried out to shed light on the observed overprediction of peak SVF location and soot size distribution. The sensitivity study is done by studying the effect of surface ageing factor and oxidation rates (O_2 and OH) on soot size distribution. Lastly, the soot morphology in *n*-heptane spray flame are elucidated with respect to the variation of ambient oxygen level and ambient density in constant volume combustion chamber, under diesel-like condition. These main findings are further elaborated in the following sections.

9.1.1 Development of LST Model

The LST model is developed by treating the soot particles in the spray flame as Lagrangian particles. Their motion in the fluid field is computed using the particle momentum equation. The soot sub-models adopted from MB soot model allow the LST model to capture the inception, surface growth and oxidation phenomenon during diesel spray combustion. In addition, treating soot particles as Lagrangian particles has allowed accessibility to individual soot information, such as instantaneous position, velocity, size, and environmental parameters. These additional data would give a different perspective to the understand of soot formation processes. Furthermore, the LST model is also demonstrated to be easily integrated with reduced mechanisms to predict both SVF and soot sizing distribution in spray flame.

9.1.2 Verification and Validation of LST Model in Constant Volume Spray Flame

The LST model is shown to have comparable performance to its Eulerian counterpart in predicting SVF at different O_2 levels and ambient densities for *n*-heptane and *n*-dodecane spray flame. When it comes to predicting soot sizing distribution, the LST model is shown to perform better than the Eulerian model. Furthermore, the LST model allows access and storage to additional soot information, including individual soot location and diameter. All these imply that the LST model is a better alternative than the Eulerian model as it can capture both the soot concentration and primary soot size distribution with reasonable accuracy, while having accessibility to additional soot information. Despite better performance, the LST model is shown to overpredict the peak soot location and primary soot size distribution as compared to experimental data. The overprediction can be attributed to the lack of surface ageing effect.

9.1.3 Sensitivity Study by Incorporating Surface Ageing Effect and Higher Oxidation Rates

The overprediction of peak SVF location and primary soot size distribution are hypothesised to be caused by the lack of surface ageing effect and lower oxidation rates. Parametric studies have found that surface ageing factor affects both SVF and size distribution. The presence of surface ageing effect causes the SVF profile to be slightly more upstream and the smaller primary soot size predicted. The higher oxidation rates do not show significant effect on both SVF profiles and primary soot size distribution. However, it is shown that the combined incorporation of surface ageing factor and higher oxidation rates lead to the better predictions for both SVF and size distribution. Moreover, by comparing the computed and measured primary soot size distribution based on their corresponding soot cloud locations yield the best correlation between simulated and experimental results. The largest difference between the experimental and simulated maximum primary soot particle size is approximately two-fold. These results indicate the significant role of surface ageing effect in a Lagrangian soot model. In addition, the better correlation of results between LST model and measurements further supports the LST model being a

good alternative to study soot concentration and sizing in diesel spray flame applications.

9.1.4 Effect of Ambient Oxygen and Density on Soot Morphology in Constant Volume Spray Flame

The SVF profiles along the spray axis predicted by the improved LST are shown to coincide with the results by Eulerian model at different oxygen levels and ambient densities. An increase in ambient density from 14.8 to 30.0 kg/m^3 is shown to increase the primary soot size at the core of spray jet. The primary soot size remains constant when oxygen level decreases from 21% to 15%, but later decreases when oxygen level is reduced further to 12%. This observation is attributed to the longer soot cloud span and soot age for the 15% case. These findings imply the importance of soot cloud span and soot age in determining the primary soot size, instead of it being solely dependent on net growth rates. The effect of ambient density on soot age was not significant, whereas, a lower oxygen level resulted in a longer soot age. The new parameter, soot age, is demonstrated to be a useful parameter in soot analysis as it gives a different perspective to the soot formation process.

9.2 Limitations and Suggestions for Future Work

As of now, the LST model is limited to study only the evolution of primary soot size formed in diesel spray flame. As coagulation effect is omitted, information such as overall soot aggregate size and fractal dimension is unavailable. However, as soot aggregate is made of primary soot particles, accurate modelling of primary soot size by the LST model can provide a good foundation to move towards incorporating aggregate modelling in the future.

For better modelling results, larger chemical mechanisms that predict better soot precursors and surface growth species concentrations can be integrated with the LST model to better capture the soot processes. Besides using acetylene as soot precursor species, other alternatives such as benzene or pyrene can be used in the LST model. Furthermore, the LST model can be improved and modified from a phenomenological soot model which considers far more soot formation processes than the semi-empirical models. The surface ageing factor incorporated in the LST

model can be extended to consider soot age and diameter, in addition to only temperature.

The modelling of soot formation and oxidation in constant volume spray flame can be extended to study the effect of temperature and injector parameters on the soot size distribution. Soot age should be considered from here on to be an important parameter and be computed in all numerical studies to give better insight on the soot formation and oxidation processes.

BIBLIOGRAPHY

[1] Megaridis CM, Dobbins RA. Soot aerosol dynamics in a laminar ethylene diffusion flame. Symp. Combust., vol. 22, Elsevier; 1989, p. 353–62.

[2] YAZICIOGLU AG, Megaridis CM, Campbell A, Lee K-O, Choi MY. Measurement of fractal properties of soot agglomerates in laminar coflow diffusion flames using thermophoretic sampling in conjunction with transmission electron microscopy and image processing. Combust Sci Technol 2001;171:71–87.

[3] Bockhorn H. Combustion Generated Fine Carbonaceous Particles: Proceedings of an International Workshop Held in Villa Orlandi, Anacapri, May 13-16, 2007. KIT Scientific Publishing; 2009.

[4] Schwartz J. Air pollution and daily mortality: a review and meta analysis. Environ Res 1994;64:36–52.

[5] Brown LM, Collings N, Harrison RM, Maynard AD, Maynard RL. Ultrafine particles in the atmosphere. World Scientific; 2003.

[6] Pueschel RF, Boering KA, Verma S, Howard SD, Ferry G V, Goodman J, et al. Soot aerosol in the lower stratosphere: Pole-to-pole variability and contributions by aircraft. J Geophys Res Atmos 1997;102:13113–8.

[7] Jacobson MZ. Strong radiative heating due to the mixing state of black carbon in atmospheric aerosols. Nature 2001;409:695–7.

[8] Bond TC, Doherty SJ, Fahey DW, Forster PM, Berntsen T, DeAngelo BJ, et al. Bounding the role of black carbon in the climate system: A scientific assessment. J Geophys Res Atmos 2013;118:5380–552.

[9] Highwood EJ, Kinnersley RP. When smoke gets in our eyes: The multiple impacts of atmospheric black carbon on climate, air quality and health. Environ Int 2006;32:560–6.

[10] Daido S, Kodama Y, Inohara T, Ohyama N, Sugiyama T. Analysis of soot accumulation

inside diesel engines. JSAE Rev 2000;21:303–8.

[11] Suhre BR, Foster DE. In-cylinder soot deposition rates due to thermophoresis in a direct injection diesel engine. SAE Technical Paper; 1992.

[12] Kittelson DB, Ambs JL, Hadjkacem H. Particulate emissions from diesel engines: influence of in-cylinder surface. SAE Technical Paper; 1990.

[13] Dennis AJ, Garner CP, Taylor DHC. The effect of EGR on diesel engine wear. SAE Technical Paper; 1999.

[14] Esangbedo C, Boehman AL, Perez JM. Characteristics of diesel engine soot that lead to excessive oil thickening. Tribol Int 2012;47:194–203.

[15] Colacicco P, Mazuyer D. The role of soot aggregation on the lubrication of diesel engines. Tribol Trans 1995;38:959–65.

[16] Yoshida K, Sakurai T. Mechanism of valve train wear caused by diesel soot. J JSLE, Int Ed 1989:99–104.

[17] Kittelson DB. Engines and nanoparticles: a review. J Aerosol Sci 1998;29:575–88.

[18] European Parliament, Council of the European Union. REGULATION (EC) No 715/2007 OF THE EUROPEAN PARLIAMENT AND OF THE COUNCIL of 20 June 2007 on type approval of motor vehicles with respect to emissions from light passenger and commercial vehicles (Euro 5 and Euro 6) and on access to vehicle repair and mai. Off J Eur Union 2007;L171:1–16. doi:OJEU 29.6.2007 L171.

[19] Le Coq L. Élimination Des Particules. Tech l'Ingénieur 2006;33:20.

[20] Tree DR, Svensson KI. Soot processes in compression ignition engines. Prog Energy Combust Sci 2007;33:272–309.

[21] Zhang R, Zhang Y, Kook S. Comparison between In-Flame and Exhaust Soot Particles in a Single-Cylinder, Light-Duty Diesel Engine 2014.

[22] Kook S, Zhang R, Szeto K, Pickett LM, Aizawa T. In-Flame Soot Sampling and Particle Analysis in a Diesel Engine. SAE Int J Fuels Lubr 2013;6:80–97. doi:10.4271/2013-01-

0912.

[23] Yamaguchi T, Kondo K, Nishigai H, Takano S, Aizawa T. Direct Sampling, TEM analysis and optical measurement of soot particles at different axial locations in a transient spray flame. SAE Int J Fuels Lubr 2011;5:316–28.

[24] Aizawa T, Nishigai H, Kondo K, Yamaguchi T, Nerva J-G, Genzale C, et al. Transmission Electron Microscopy of Soot Particles Directly Sampled in Diesel Spray Flame - A Comparison between US#2 and Biodiesel Soot. SAE Int J Fuels Lubr 2012;5:665–73. doi:10.4271/2012-01-0695.

[25] Kong S-C, Patel A, Yin Q, Klingbeil A, Reitz RD. Numerical modeling of diesel engine combustion and emissions under HCCI-like conditions with high EGR levels. SAE Trans 2003;112:1500–10.

[26] Richards KJ, Subramaniam MN, Reitz RD, Lai M-C, Henein NA, Miles PC. Modeling the effects of EGR and injection pressure on emissions in a high-speed direct-injection diesel engine. SAE Technical Paper; 2001.

[27] Roy SP, Mehta RS, Haworth DC. SOOT MODELING IN LAMINAR FLAMES USING A DISCRETE SECTIONAL METHOD n.d.

[28] Roy SP, Arias PG, Lecoustre VR, Haworth DC, Im HG, Trouvé A. Development of high fidelity soot aerosol dynamics models using method of moments with interpolative closure. Aerosol Sci Technol 2014;48:379–91.

[29] Frenklach M. Method of moments with interpolative closure. Chem Eng Sci 2002;57:2229–39.

[30] Balthasar M, Kraft M. A stochastic approach to calculate the particle size distribution function of soot particles in laminar premixed flames. Combust Flame 2003;133:289–98.

[31] Singh J, Balthasar M, Kraft M, Wagner W. Stochastic modeling of soot particle size and age distributions in laminar premixed flames. Proc Combust Inst 2005;30:1457–65.

[32] Zhang Q, Guo H, Liu F, Smallwood GJ, Thomson MJ. Modeling of soot aggregate

formation and size distribution in a laminar ethylene/air coflow diffusion flame with detailed PAH chemistry and an advanced sectional aerosol dynamics model. Proc Combust Inst 2009;32:761–8.

[33] Ito T, Hosaka T, Ueda M, Senda J, Fujimoto H. Detailed kinetic modeling and laser diagnostics of soot formation process in diesel jet flame. SAE Technical Paper; 2004.

[34] Gelbard F, Seinfeld JH. Simulation of multicomponent aerosol dynamics. J Colloid Interface Sci 1980;78:485–501.

[35] Gelbard F, Tambour Y, Seinfeld JH. Sectional representations for simulating aerosol dynamics. J Colloid Interface Sci 1980;76:541–56.

[36] Pope CJ, Howard JB. Simultaneous particle and molecule modeling (SPAMM): An approach for combining sectional aerosol equations and elementary gas-phase reactions. Aerosol Sci Technol 1997;27:73–94.

[37] Zhao B, Yang Z, Johnston M V, Wang H, Wexler AS, Balthasar M, et al. Measurement and numerical simulation of soot particle size distribution functions in a laminar premixed ethylene-oxygen-argon flame. Combust Flame 2003;133:173–88.

[38] Veshkini A, Dworkin SB, Thomson MJ. A soot particle surface reactivity model applied to a wide range of laminar ethylene/air flames. Combust Flame 2014;161:3191–200.

[39] Khosousi A, Dworkin SB. Soot surface reactivity during surface growth and oxidation in laminar diffusion flames. Combust Flame 2015;162:4523–32.

[40] Kuribayashi M, Mizutani Y, Ishizuka Y, Taki N, Aizawa T. Effects of ambient oxygen concentration on soot processes in diesel spray flame-A qualitative comparison between TEM analysis and LII/Scattering laser measurements. SAE Int J Fuels Lubr 2014;7:693–703.

[41] Xi J, Zhong B. Soot in diesel combustion systems. Chem Eng Technol 2006;29:665–73.

[42] Donnet J-B. Fifty years of research and progress on carbon black. Carbon N Y 1994;32:1305–10.

[43] Dobbins RA, Subramaniasivam H. Soot precursor particles in flames. Soot Form. Combust., Springer; 1994, p. 290–301.

[44] Dubinin MM, Walker Jr PL. Chemistry and physics of carbon. Vol 2Marcel Dekker, New York 1966:51.

[45] Violi A, Voth GA, Sarofim AF. A time-scale problem for the formation of soot precursors in premixed flames. Prepr Pap-Am Chem Soc, Div Fuel Chem 2003;48:545.

[46] Karataş AE, Gülder ÖL. Soot formation in high pressure laminar diffusion flames. Prog Energy Combust Sci 2012;38:818–45. doi:http://dx.doi.org/10.1016/j.pecs.2012.04.003.

[47] Mitchell P, Frenklach M. Monte Carlo simulation of soot aggregation with simultaneous surface growth-why primary particles appear spherical. Symp Combust 1998;27:1507–14.

[48] Glassman I, Yetter RA, Glumac NG. Combustion. Academic press; 1996.

[49] Baquet TG, Grotheer H, Aigner M. Simultaneous detection of two types of soot precursor particles using photoionization mass spectrometry. Rapid Commun Mass Spectrom 2007;21:4060–4.

[50] Ishiguro T, Takatori Y, Akihama K. Microstructure of diesel soot particles probed by electron microscopy: first observation of inner core and outer shell. Combust Flame 1997;108:231–4.

[51] Grotheer H-H, Wolf K, Hoffmann K. Photoionization mass spectrometry for the investigation ofácombustion generated nascent nanoparticles and their relation toálaser induced incandescence. Appl Phys B 2011;104:367–83.

[52] D'Anna A, D'Alessio A, Minutolo P, Bockhorn H. Mechanisms and Models. Soot Form. Combust., Springer; 1994, p. 83–103.

[53] Chen HX, Dobbins RA. Crystallogenesis of particles formed in hydrocarbon combustion. Combust Sci Technol 2000;159:109–28.

[54] Vander Wal RL, Tomasek AJ, Pamphlet MI, Taylor CD, Thompson WK. Analysis of HRTEM images for carbon nanostructure quantification. J Nanoparticle Res 2004;6:555–68.

[55] Sakai M, Iguma H, Kondo K, Aizawa T. Nanostructure Analysis of Primary Soot Particles Directly Sampled in Diesel Spray Flame via HRTEM. SAE Technical Paper; 2012.

[56] Smith OI. Fundamentals of soot formation in flames with application to diesel engine particulate emissions. Prog Energy Combust Sci 1981;7:275–91.

[57] Haynes BS, Wagner HG. Soot formation. Prog Energy Combust Sci 1981;7:229–73.

[58] Palmer HB, Cullis CF. The formation of carbon from gases. Chem Phys Carbon 1965;1:265–325.

[59] Glassman I. Soot formation in combustion processes. Symp. Combust., vol. 22, Elsevier; 1989, p. 295–311.

[60] Bockhorn H. Soot formation in combustion: mechanisms and models. vol. 59. Springer Science & Business Media; 2013.

[61] Richter H, Howard JB. Formation of polycyclic aromatic hydrocarbons and their growth to soot—a review of chemical reaction pathways. Prog Energy Combust Sci 2000;26:565–608.

[62] Appel J, Bockhorn H, Frenklach M. Kinetic modeling of soot formation with detailed chemistry and physics: laminar premixed flames of C 2 hydrocarbons. Combust Flame 2000;121:122–36.

[63] Dworkin SB, Zhang Q, Thomson MJ, Slavinskaya NA, Riedel U. Application of an enhanced PAH growth model to soot formation in a laminar coflow ethylene/air diffusion flame. Combust Flame 2011;158:1682–95.

[64] CS M, DM C, LD P. Experimental study of fuel decomposition and hydrocarbon growth processes for practical fuel components: heptanes. Combust Flame 2003;134:339–53. doi:10.1016/S0010-2180(03)00113-5.

[65] Echavarria CA, Sarofim AF, Lighty JS, D'Anna A. Evolution of soot size distribution in premixed ethylene/air and ethylene/benzene/air flames: Experimental and modeling study. Combust Flame 2011;158:98–104.

[66] McEnally CS, Schaffer AM, Long MB, Pfefferle LD, Smooke MD, Colket MB, et al. Computational and experimental study of soot formation in a coflow, laminar ethylene diffusion flame. Symp. Combust., vol. 27, Elsevier; 1998, p. 1497–505.

[67] Frenklach M, Wang H. Detailed mechanism and modeling of soot particle formation. In: Bockhorn H, editor. Soot Form. Combust., Springer-Verlag Berlin Heidelberg; 1994, p. 165–92.

[68] Frenklach M, Wang H. Detailed modeling of soot particle nucleation and growth. Symp Combust 1991;23:1559–66.

[69] Frenklach M. Reaction mechanism of soot formation in flames. Phys Chem Chem Phys 2002;4:2028–37.

[70] Naydenova I. Soot formation modeling during hydrocarbon pyrolysis and oxidation behind shock waves. Doktorarbeit, Ruprecht-Karls-Universität Heidelb 2007.

[71] Frenklach M, Clary DW, Gardiner WC, Stein SE. Detailed kinetic modeling of soot formation in shock-tube pyrolysis of acetylene. Symp. Combust., vol. 20, Elsevier; 1985, p. 887–901.

[72] Frenklach M, Gardiner WC, Stein SE, Clary DW, Yuan T. Mechanism of soot formation in acetylene-oxygen mixtures. Combust Sci Technol 1986;50:79–115.

[73] Leusden CP, Peters N. Experimental and numerical analysis of the influence of oxygen on soot formation in laminar counterflow flames of acetylene. Proc Combust Inst 2000;28:2619–25.

[74] Frenklach M, Ebert LB. Comment on the proposed role of spheroidal carbon clusters in soot formation. J Phys Chem 1988;92:561–3.

[75] Amann CA, Siegla DC. Diesel particulates—what they are and why. Aerosol Sci Technol 1981;1:73–101.

[76] Tao F. Numerical modeling of soot and NO x formation in non-stationary diesel flames with complex chemistry. Chalmers University of Technology; 2003.

[77] Smith GW. Kinetic aspects of diesel soot coagulation. SAE Technical Paper; 1982.

[78] Howard JB. Carbon addition and oxidation reactions in heterogeneous combustion and soot formation. Symp. Combust., vol. 23, Elsevier; 1991, p. 1107–27.

[79] D'anna A, Violi A, D'alessio A, Sarofim AF. A reaction pathway for nanoparticle formation in rich premixed flames. Combust Flame 2001;127:1995–2003.

[80] Krestinin A V, Kislov MB, Raevskii A V, Kolesova OI, Stesik LN. On the mechanism of soot particle formation. Kinet Catal 2000;41:90–8.

[81] Krestinin A V. Polyyne model of soot formation process. Symp. Combust., vol. 27, Elsevier; 1998, p. 1557–63.

[82] Krestinin A V. Formation of soot particles as a process involving chemical condensation of polyines. Chem Phys REPORTS C/C KHIMICHESKAIA Fiz 1998;17:1441–62.

[83] Krestinin A V. Detailed modeling of soot formation in hydrocarbon pyrolysis. Combust Flame 2000;121:513–24.

[84] Warnatz J, Maas U, Dibble RW. Combustion: physical and chemical fundamentals, modeling and simulation, experiments, pollutant formation. 2006 n.d.

[85] Harris SJ, Weiner AM. Surface growth of soot particles in premixed ethylene/air flames. Combust Sci Technol 1983;31:155–67.

[86] Macadam S, Beér JM, Safofim AF, Hoffmann AB. Soot surface growth by polycyclic aromatic hydrocarbon and acetylene addition. Symp. Combust., vol. 26, Elsevier; 1996, p. 2295–302.

[87] Haynes DS, Bartok W, Sarofim AF. Fossil Fuel Combustion 1991.

[88] Harris SJ, Weiner AM. Chemical kinetics of soot particle growth. Annu Rev Phys Chem 1985;36:31–52.

[89] Haynes BS, Wagner HG. The surface growth phenomenon in soot formation. Zeitschrift Für Phys Chemie 1982;133:201–13.

[90] HARRIS SJ, WEINER AM. Determination of the rate constant for soot surface growth. Combust Sci Technol 1983;32:267–75.

[91] Dasch CJ. The decay of soot surface growth reactivity and its importance in total soot formation. Combust Flame 1985;61:219–25. doi:http://dx.doi.org/10.1016/0010-2180(85)90103-8.

[92] Woods IT, Haynes BS. Soot surface growth at active sites. Combust Flame 1991;85:523–5. doi:http://dx.doi.org/10.1016/0010-2180(91)90156-6.

[93] Dobbins RA, Fletcher RA, Lu W. Laser microprobe analysis of soot precursor particles and carbonaceous soot. Combust Flame 1995;100:301–9.

[94] Mitchell P, Frenklach M. Particle aggregation with simultaneous surface growth. Phys Rev E 2003;67:61407.

[95] Kellerer H, Koch R, Wittig S. Measurements of the growth and coagulation of soot particles in a high-pressure shock tube. Combust Flame 2000;120:188–99.

[96] D'Alessio A, Barone AC, Cau R, D'Anna A, Minutolo P. Surface deposition and coagulation efficiency of combustion generated nanoparticles in the size range from 1 to 10nm. Proc Combust Inst 2005;30:2595–603.

[97] Lahaye J. Soot in combustion systems and its toxic properties. vol. 7. Springer Science & Business Media; 2013.

[98] Siegla D. Particulate carbon: formation during combustion. Springer Science & Business Media; 2013.

[99] Jander H. Soot formation in combustion: an international round table discussion. Vandenhoeck & Ruprecht; 1990.

[100] Nagle J, Strickland-Constable RF. Oxidation of Carbon between 1000-2000 C. Proc Fifth Carbon Conf 1962;1:154.

[101] Lee KB, Thring MW, Beer JM. On the rate of combustion of soot in a laminar soot flame. Combust Flame 1962;6:137–45.

[102] Liu F, Guo H, Smallwood GJ, Gülder ÖL. Numerical modelling of soot formation and oxidation in laminar coflow non-smoking and smoking ethylene diffusion flames. Combust Theory Model 2003;7:301–15.

[103] Fenimore CP, Jones GW. Oxidation of soot by hydroxyl radicals. J Phys Chem 1967;71:593–7.

[104] Stanmore BR, Brilhac J-F, Gilot P. The oxidation of soot: a review of experiments, mechanisms and models. Carbon N Y 2001;39:2247–68.

[105] Neoh KG, Howard JB, Sarofim AF. Effect of oxidation on the physical structure of soot. Symp Combust 1985;20:951–7.

[106] Xu F, El-Leathy AM, Kim CH, Faeth GM. Soot surface oxidation in hydrocarbon/air diffusion flames at atmospheric pressure. Combust Flame 2003;132:43–57.

[107] Santoro RJ, Semerjian HG, Dobbins RA. Soot particle measurements in diffusion flames. Combust Flame 1983;51:203–18.

[108] Dobbins RA, Megaridis CM. Morphology of flame-generated soot as determined by thermophoretic sampling. Langmuir 1987;3:254–9. doi:10.1021/la00074a019.

[109] Wiartalla A, Bäcker H, Dürnholz M. Influence of injection system parameters on spray development combustion and soot formation by optical measurement techniques in a model combustion chamber. SAE Technical Paper; 1995.

[110] Corcione FE, Merola SS, Vaglieco BM. Nanometric Particle Formation in Optically Accessible Engine Diesel. SAE Technical Paper; 2001.

[111] Zhang Q, Rubini PA. Modelling of light extinction by soot particles. Fire Saf J 2011;46:96–103.

[112] Nakakita K, Nagaoka M, Fujikawa T, Ohsawa K, Yamaguchi S. Photographic and three dimensional numerical studies of Diesel soot formation process. SAE Technical Paper;

1990.

[113] Hadef R, Geigle KP, Meier W, Aigner M. Soot characterization with laser-induced incandescence applied to a laminar premixed ethylene–air flame. Int J Therm Sci 2010;49:1457–67.

[114] Singh S, Reitz RD, Musculus MPB. 2-colorthermometry experiments and high-speed imaging of multi-mode diesel engine combustion. SAE Trans 2005;114:1605–21.

[115] Ma H, Stevens R, Stone R. In-cylinder temperature estimation from an optical spray-guided DISI engine with color-ratio pyrometry (CRP). SAE Technical Paper; 2006.

[116] Azetsu A, Ito H. Effects of ambient air composition on flame temperature and soot formation in intermittent spray combustion. SAE Technical Paper; 2009.

[117] Azetsu A, Hiroaki ITO. Effects of CO2 and N2 mixing into ambient air on flame temperature and soot formation in intermittent spray combustion. SAE Technical Paper; 2007.

[118] Wang X, Kuti OA, Zhang W, Nishida K, Huang Z. Effect of injection pressure on flame and soot characteristics of the biodiesel fuel spray. Combust Sci Technol 2010;182:1369–90.

[119] Zhang J, Jing W, Roberts WL, Fang T. Soot temperature and KL factor for biodiesel and diesel spray combustion in a constant volume combustion chamber. Appl Energy 2013;107:52–65.

[120] Musculus MPB, Singh S, Reitz RD. Gradient effects on two-color soot optical pyrometry in a heavy-duty DI diesel engine. Combust Flame 2008;153:216–27.

[121] Pickett LM, Siebers DL. Soot in diesel fuel jets: effects of ambient temperature, ambient density, and injection pressure. Combust Flame 2004;138:114–35. doi:http://dx.doi.org/10.1016/j.combustflame.2004.04.006.

[122] Idicheria CA, Pickett LM. Soot formation in diesel combustion under high-EGR conditions. SAE Technical Paper; 2005.

[123] Yamamoto K, Takemoto M. Measurement of PAH and soot of diffusion flames in a triple port burner. Fuel Process Technol 2013;107:99–106.

[124] Schulz C, Kock BF, Hofmann M, Michelsen H, Will S, Bougie B, et al. Laser-induced incandescence: recent trends and current questions. Appl Phys B 2006;83:333–54.

[125] Narayanaswamy V, Clemens NT. Simultaneous LII and PIV measurements in the soot formation region of turbulent non-premixed jet flames. Proc Combust Inst 2013;34:1455–63.

[126] Kock BF, Tribalet B, Schulz C, Roth P. Two-color time-resolved LII applied to soot particle sizing in the cylinder of a Diesel engine. Combust Flame 2006;147:79–92.

[127] Bobba MK, Musculus MPB. Laser diagnostics of soot precursors in a heavy-duty diesel engine at low-temperature combustion conditions. Combust Flame 2012;159:832–43.

[128] Bougie B, Ganippa LC, van Vliet AP, Meerts WL, Dam NJ, ter Meulen JJ. Laser-induced incandescence particle size measurements in a heavy-duty diesel engine. Combust Flame 2006;145:635–7. doi:http://dx.doi.org/10.1016/j.combustflame.2006.03.002.

[129] Ryser R, Gerber T, Dreier T. Soot particle sizing during high-pressure Diesel spray combustion via time-resolved laser-induced incandescence. Combust Flame 2009;156:120–9. doi:http://dx.doi.org/10.1016/j.combustflame.2008.08.005.

[130] Menkiel B, Donkerbroek A, Uitz R, Cracknell R, Ganippa L. Measurement of in-cylinder soot particles and their distribution in an optical HSDI diesel engine using time resolved laser induced incandescence (TR-LII). Combust Flame 2012;159:2985–98. doi:http://dx.doi.org/10.1016/j.combustflame.2012.03.008.

[131] Menkiel B, Donkerbroek A, Uitz R, Cracknell R, Ganippa L. Combustion and soot processes of diesel and rapeseed methyl ester in an optical diesel engine. Fuel 2014;118:406–15. doi:http://dx.doi.org/10.1016/j.fuel.2013.10.074.

[132] Cenker E, Kondo K, Bruneaux G, Dreier T, Aizawa T, Schulz C. Assessment of soot particle-size imaging with LII at Diesel engine conditions. Appl Phys B 2015;119:765–

76. doi:10.1007/s00340-015-6106-0.

[133] Pinson JA, Mitchell DL, Santoro RJ, Litzinger TA. Quantitative, planar soot measurements in a DI diesel engine using laser-induced incandescence and light scattering. SAE Technical Paper; 1993.

[134] Dec JE, Zur Loye AO, Siebers DL. Soot distribution in a DI diesel engine using 2-D laser-induced incandescence imaging. SAE Technical Paper; 1991.

[135] Dec JE. Soot distribution in a DI diesel engine using 2-D imaging of laser-induced incandescence, elastic scattering, and flame luminosity. SAE Technical Paper; 1992.

[136] Vander Wal RL. Soot precursor carbonization: Visualization using LIF and LII and comparison using bright and dark field TEM. Combust Flame 1998;112:607–16.

[137] Dobbins RA, Fletcher RA, Chang H-C. The evolution of soot precursor particles in a diffusion flame. Combust Flame 1998;115:285–98.

[138] Abid AD, Heinz N, Tolmachoff ED, Phares DJ, Campbell CS, Wang H. On evolution of particle size distribution functions of incipient soot in premixed ethylene–oxygen–argon flames. Combust Flame 2008;154:775–88.

[139] Vander Wal RL, Tomasek AJ. Soot oxidation: dependence upon initial nanostructure. Combust Flame 2003;134:1–9.

[140] Jung H, Kittelson DB, Zachariah MR. Kinetics and visualization of soot oxidation using transmission electron microscopy. Combust Flame 2004;136:445–56.

[141] Williams TC, Shaddix CR, Jensen KA, Suo-Anttila JM. Measurement of the dimensionless extinction coefficient of soot within laminar diffusion flames. Int J Heat Mass Transf 2007;50:1616–30.

[142] Vander Wal RL, Ticich TM, Stephens AB. Can soot primary particle size be determined using laser-induced incandescence? Combust Flame 1999;116:291–6.

[143] Vander Wal RL, Jensen KA. Laser-induced incandescence: excitation intensity. Appl Opt 1998;37:1607–16.

[144] Vander Wal RL. Laser-induced incandescence: excitation and detection conditions, material transformations and calibration. Appl Phys B 2009;96:601–11.

[145] Bladh H, Johnsson J, Rissler J, Abdulhamid H, Olofsson N-E, Sanati M, et al. Influence of soot particle aggregation on time-resolved laser-induced incandescence signals. Appl Phys B 2011;104:331–41.

[146] Bambha RP, Dansson MA, Schrader PE, Michelsen HA. Effects of volatile coatings on the laser-induced incandescence of soot. Appl Phys B 2013;112:343–58.

[147] Tian K, Liu F, Thomson KA, Snelling DR, Smallwood GJ, Wang D. Distribution of the number of primary particles of soot aggregates in a nonpremixed laminar flame. Combust Flame 2004;138:195–8.

[148] Tian K, Liu F, Yang M, Thomson KA, Snelling DR, Smallwood GJ. Numerical simulation aided relative optical density analysis of TEM images for soot morphology determination. Proc Combust Inst 2007;31:861–8.

[149] Kook S, Pickett LM. Soot volume fraction and morphology of conventional and surrogate jet fuel sprays at 1000-K and 6.7-MPa ambient conditions. Proc Combust Inst 2011;33:2911–8.

[150] Kondo K, Yamaguchi T, Nishigai H, Takano S, Aizawa T. High-Resolution Transmission Electron Microscopy of Soot Directly Sampled at Different Axial Locations in Diesel Spray Flame 2011. doi:10.4271/2011-24-0068.

[151] Aizawa T, Takahata N, Okabe K, Mizutani Y. Effect of Fuel Aromatics on In-Flame Diesel Soot Nanostructure via HRTEM. SAE Technical Paper; 2015.

[152] Zhang R, Kook S. Structural evolution of soot particles during diesel combustion in a single-cylinder light-duty engine. Combust Flame 2015;162:2720–8. doi:http://dx.doi.org/10.1016/j.combustflame.2015.04.008.

[153] Kazakov A, Foster DE. Modeling of soot formation during DI diesel combustion using a multi-step phenomenological model. SAE Technical Paper; 1998.

[154] Khan IM, Greeves G, Probert DM. Air pollution control in transport engines. Inst Mech

Eng 1971:205.

[155] Micklow GJ, Gong W. A multistage combustion model and soot formation model for direct-injection diesel engines. Proc Inst Mech Eng Part D J Automob Eng 2002;216:495–504.

[156] Tesner PA, Smegiriova TD, Knorre VG. Kinetics of dispersed carbon formation. Combust Flame 1971;17:253–60.

[157] Hiroyasu H, Kadota T. Models for combustion and formation of nitric oxide and soot in direct injection diesel engines. SAE Technical Paper; 1976.

[158] Kennedy IM. Models of soot formation and oxidation. Prog Energy Combust Sci 1997;23:95–132.

[159] Hiroyasu H, Kadota T, Arai M. Development and use of a spray combustion modeling to predict diesel engine efficiency and pollutant emissions: Part 1 combustion modeling. Bull JSME 1983;26:569–75.

[160] Cheng X, Chen L, Hong G, Yan F, Dong S. Modeling study of soot formation and oxidation in DI diesel engine using an improved soot model. Appl Therm Eng 2014;62:303–12.

[161] Tao F, Srinivas S, Reitz RD, Foster DE. Comparison of three soot models applied to multi-dimensional diesel combustion simulations. JSME Int J Ser B Fluids Therm Eng 2005;48:671–8.

[162] Golovitchev VI, Tao F, Chomiak J. Numerical evaluation of soot formation control at diesel-like conditions by reducing fuel injection timing. SAE Technical Paper; 1999.

[163] Patterson MA, Kong S-C, Hampson GJ, Reitz RD. Modeling the effects of fuel injection characteristics on diesel engine soot and NOx emissions. SAE Technical Paper; 1994.

[164] Komninos NP, Rakopoulos CD. Modeling HCCI combustion of biofuels: A review. Renew Sustain Energy Rev 2012;16:1588–610.

[165] Rakopoulos CD, Rakopoulos DC, Giakoumis EG, Kyritsis DC. Validation and

sensitivity analysis of a two zone Diesel engine model for combustion and emissions prediction. Energy Convers Manag 2004;45:1471–95.

[166] Fairweather M, Jones WP, Lindstedt RP. Predictions of radiative transfer from a turbulent reacting jet in a cross-wind. Combust Flame 1992;89:45–63.

[167] Woolley RM, Fairweather M. Conditional moment closure modelling of soot formation in turbulent, non-premixed methane and propane flames. Fuel 2009;88:393–407.

[168] Moss JB, Stewart CD, Young KJ. Modeling soot formation and burnout in a high temperature laminar diffusion flame burning under oxygen-enriched conditions. Combust Flame 1995;101:491–500.

[169] Brookes SJ, Moss JB. Predictions of soot and thermal radiation properties in confined turbulent jet diffusion flames. Combust Flame 1999;116:486–503.

[170] Pang KM, Ng HK, Gan S. Simulation of temporal and spatial soot evolution in an automotive diesel engine using the Moss–Brookes soot model. Energy Convers Manag 2012;58:171–84.

[171] Chernov V, Zhang Q, Thomson MJ, Dworkin SB. Numerical investigation of soot formation mechanisms in partially-premixed ethylene–air co-flow flames. Combust Flame 2012;159:2789–98.

[172] Lindstedt PR. Simplified soot nucleation and surface growth steps for non-premixed flames. Soot Form. Combust., Springer; 1994, p. 417–41.

[173] Fusco A, Knox-Kelecy AL, Foster DE. Application of a phenomenological soot model to diesel engine combustion. Proc. Int. Symp. COMODIA, vol. 94, 1994.

[174] Liu Y, Tao F, Foster DE, Reitz RD. Application of a multiple-step phenomenological soot model to HSDI diesel multiple injection modeling. SAE Technical Paper; 2005.

[175] Tao F, Reitz RD, Foster DE, Liu Y. Nine-step phenomenological diesel soot model validated over a wide range of engine conditions. Int J Therm Sci 2009;48:1223–34.

[176] Jia M, Peng ZJ, Xie MZ. Numerical investigation of soot reduction potentials with diesel

homogeneous charge compression ignition combustion by an improved phenomenological soot model. Proc Inst Mech Eng Part D J Automob Eng 2009;223:395–412.

[177] Tao F, Foster DE, Reitz RD. Soot Structure in a Conventional Non-Premixed Diesel Flame 2006. doi:10.4271/2006-01-0196.

[178] Pang B, Xie M-Z, Jia M, Liu Y-D. Development of a phenomenological soot model coupled with a skeletal PAH mechanism for practical engine simulation. Energy & Fuels 2013;27:1699–711.

[179] Mehta RS, Haworth DC, Modest MF. An assessment of gas-phase reaction mechanisms and soot models for laminar atmospheric-pressure ethylene–air flames. Proc Combust Inst 2009;32:1327–34.

[180] Shum JJ. The Development and Validation of a Simplified Soot Model for use in Soot Emissions Prediction in Natural Gas Fuelled Engine Simulations 2012.

[181] Mueller ME, Blanquart G, Pitsch H. A joint volume-surface model of soot aggregation with the method of moments. Proc Combust Inst 2009;32:785–92.

[182] Karlsson A, Magnusson I, Balthasar M, Mauss F. Simulation of soot formation under diesel engine conditions using a detailed kinetic soot model. SAE Technical Paper; 1998.

[183] Song Y-N, Zhong B-J. Modeling of soot and polycyclic aromatic hydrocarbons in diesel diffusion combustion. Chem Eng Technol 2008;31:1418.

[184] Naik C V, Puduppakkam K V, Meeks E. Simulation of Soot Volume Fraction and Size in High-Pressure Lifted Flames Using Detailed Reaction Mechanisms. ASME Turbo Expo 2014 Turbine Tech Conf Expo 2014:V04BT04A025.

[185] Priesching P, Tatschl R, Mauß F, Saric F, Netzell K, Bauer W, et al. Soot Particle Size Distribution- A Joint Work for Kinetic Modelling and Experimental Investigations. SAE Technical Paper; 2005.

[186] Salenbauch S, Cuoci A, Frassoldati A, Saggese C, Faravelli T, Hasse C. Modeling soot

formation in premixed flames using an Extended Conditional Quadrature Method of Moments. Combust Flame 2015;162:2529–43.

[187] Aubagnac-Karkar D, Michel J-B, Colin O, Noël L, Darabiha N. A Sectional Soot Model for RANS Simulation of Diesel Engines. SAE Technical Paper; 2014.

[188] Aubagnac-Karkar D, Michel J-B, Colin O, Vervisch-Kljakic PE, Darabiha N. Sectional soot model coupled to tabulated chemistry for Diesel RANS simulations. Combust Flame 2015;162:3081–99. doi:http://dx.doi.org/10.1016/j.combustflame.2015.03.005.

[189] Moniruzzaman CG, Yu F. Modeling Soot Size Distribution Evolution and Pollutant Formation Inside Diesel Engine Using a 0D Multi-zone Gas Parcel Model with Detailed Chemistry and Soot Microphysics. SAE Int J Engines 2014;7:1336–69.

[190] Eibeck A, Wagner W. An efficient stochastic algorithm for studying coagulation dynamics and gelation phenomena. SIAM J Sci Comput 2000;22:802–21.

[191] Violi A. Modeling of soot particle inception in aromatic and aliphatic premixed flames. Combust Flame 2004;139:279–87.

[192] Violi A, Voth GA, Sarofim AF. The relative roles of acetylene and aromatic precursors during soot particle inception. Proc Combust Inst 2005;30:1343–51.

[193] Tunér M, Pasternak M, Mauß F, Bensler H. A PDF-Based Model for Full Cycle Simulation of Direct Injected Engines. SAE Technical Paper; 2008.

[194] Pasternak M, Mauss F, Bensler H. Diesel Engine Cycle Simulation with a Reduced Set of Modeling Parameters Based on Detailed Kinetics. SAE Technical Paper; 2009.

[195] Franken T, Mauss F. Development of Methodology for Predictive Diesel Combustion Simulation Using 0D Stochastic Reactor Model. SAE Technical Paper; 2016.

[196] Celnik M, Patterson R, Kraft M, Wagner W. Coupling a stochastic soot population balance to gas-phase chemistry using operator splitting. Combust Flame 2007;148:158–76.

[197] Raj A, Celnik M, Shirley R, Sander M, Patterson R, West R, et al. A statistical approach

to develop a detailed soot growth model using PAH characteristics. Combust Flame 2009;156:896–913.

[198] Merchan-Merchan W, Sanmiguel SG, McCollam S. Analysis of soot particles derived from biodiesels and diesel fuel air-flames. Fuel 2012;102:525–35.

[199] Song J, Lee KO. Fuel property impacts on diesel particulate morphology, nanostructures, and NOx emissions. SAE Technical Paper; 2007.

[200] Savic N, Rahman MM, Miljevic B, Saathoff H, Naumann KH, Leisner T, et al. Influence of biodiesel fuel composition on the morphology and microstructure of particles emitted from diesel engines. Carbon N Y 2016;104:179–89.

[201] Vishwanathan G, Reitz RD. Application of a semi-detailed soot modeling approach for conventional and low temperature diesel combustion–Part I: Model performance. Fuel 2015;139:757–70.

[202] Zhu J, Lee KO, Yozgatligil A, Choi MY. Effects of engine operating conditions on morphology, microstructure, and fractal geometry of light-duty diesel engine particulates. Proc Combust Inst 2005;30:2781–9.

[203] Lapuerta M, Ballesteros R, Martos FJ. The effect of diesel engine conditions on the size and morphology of soot particles. Int J Veh Des 2009;50:91–106.

[204] Lu T, Cheung CS, Huang Z. Effects of engine operating conditions on the size and nanostructure of diesel particles. J Aerosol Sci 2012;47:27–38.

[205] Zhang R, Kook S. Influence of Fuel Injection Timing and Pressure on In-Flame Soot Particles in an Automotive-Size Diesel Engine. Environ Sci Technol 2014;48:8243–50.

[206] Hadavi SA, Li H, Biller P, Lea-Langton A, Andrews G, Przybyla G. Rape seed oil B100 diesel engine particulate emissions: The influence of intake oxygen on particle size distribution. SAE Technical Paper; 2012.

[207] Mahmood WMFW, LaRocca A, Shayler PJ, Bonatesta F, Pegg I. Predicted Paths of Soot Particles in the Cylinders of a Direct Injection Diesel Engine. SAE Technical Paper; 2012.

[208] Zuber MA, Mahmood WMFW, Harun Z, Abidin ZZ, La Rocca A, Shayler P, et al. Modeling of In-Cylinder Soot Particle Size Evolution and Distribution in a Direct Injection Diesel Engine. SAE Technical Paper; 2015.

[209] Katta VR, Blevins LG, Roquemore WM. Dynamics of an inverse diffusion flame and its role in polycyclic-aromatic-hydrocarbon and soot formation. Combust Flame 2005;142:33–51.

[210] Fuentes A, Rouvreau S, Joulain P, Vantelon J-P, Legros G, Torero JL, et al. Sooting behavior dynamics of a non-buoyant laminar diffusion flame. Combust Sci Technol 2007;179:3–19.

[211] Piscaglia F, Onorati A, Rutland CJ, Foster DE. Multi-dimensional modeling of the soot deposition mechanism in diesel particulate filters. SAE Int J Fuels Lubr 2009;1:210–30.

[212] Piscaglia F, Rutland CJ, Foster DE. Development of a CFD model to study the hydrodynamic characteristics and the soot deposition mechanism on the porous wall of a diesel particulate filter. SAE Technical Paper; 2005.

[213] Zhang P, Roberts RM, Benard A. Computational guidelines and an empirical model for particle deposition in curved pipes using an Eulerian-Lagrangian approach. J Aerosol Sci 2012;53:1–20.

[214] Katta VR, Forlines RA, Roquemore WM, Anderson WS, Zelina J, Gord JR, et al. Experimental and computational study on partially premixed flames in a centerbody burner. Combust Flame 2011;158:511–24. doi:http://dx.doi.org/10.1016/j.combustflame.2010.09.022.

[215] Roquemore WM, Katta V, Stouffer S, Belovich V, Pawlik R, Arstingstall M, et al. Soot studies of laminar diffusion flames with recirculation zones. Proc Combust Inst 2009;32:729–36. doi:http://dx.doi.org/10.1016/j.proci.2008.06.104.

[216] Farrell JT, Cernansky NP, Dryer FL, Friend DG, Hergart CA, Law CK, et al. Development of an experimental database and kinetic models for surrogate diesel fuels. SAE Pap 2007:01–0201. doi:10.4271/2007-01-0201.

[217] Curran HJ, Gaffuri P, Pitz WJ, Westbrook CK. A comprehensive modeling study of n-heptane oxidation. Combust Flame 1998;114:149–77.

[218] Pei Y, Hawkes ER, Kook S. A comprehensive study of effects of mixing and chemical kinetic models on predictions of n-heptane jet ignitions with the PDF method. Flow, Turbul Combust 2013;91:249–80.

[219] Bhattacharjee S, Haworth DC. Simulations of transient n-heptane and n-dodecane spray flames under engine-relevant conditions using a transported PDF method. Combust Flame 2013;160:2083–102. doi:http://dx.doi.org/10.1016/j.combustflame.2013.05.003.

[220] Leung KM, Lindstedt RP, Jones WP. A simplified reaction mechanism for soot formation in nonpremixed flames. Combust Flame 1991;87:289–305.

[221] Sukumaran S, Van Huynh C, Kong S-C. Numerical modeling of soot emissions in diesel sprays based on detailed fuel and PAH chemistry. Combust Sci Technol 2013;185:1696–714.

[222] Vishwanathan G, Reitz RD. Development of a practical soot modeling approach and its application to low-temperature diesel combustion. Combust Sci Technol 2010;182:1050–82.

[223] Liu S, Hewson JC, Chen JH, Pitsch H. Effects of strain rate on high-pressure nonpremixed n-heptane autoignition in counterflow. Combust Flame 2004;137:320–39.

[224] Patel A, Kong S-C, Reitz RD. Development and validation of a reduced reaction mechanism for HCCI engine simulations. SAE Technical Paper; 2004.

[225] Fu X, Aggarwal SK. Fuel unsaturation effects on NOx and PAH formation in spray flames. Fuel 2015;160:1–15.

[226] Lu T, Law CK. Strategies for mechanism reduction for large hydrocarbons: n-heptane. Combust Flame 2008;154:153–63.

[227] Lu T, Law CK, Yoo CS, Chen JH. Dynamic stiffness removal for direct numerical simulations. Combust Flame 2009;156:1542–51.

[228] Vishwanathan G, Reitz RD. Modeling Soot Formation Using Reduced PAH Chemistry in n-Heptane Lifted Flames With Application to Low Temperature Combustion. ASME 2008 Intern. Combust. Engine Div. Spring Tech. Conf., American Society of Mechanical Engineers; 2008, p. 29–36.

[229] Wang H, Reitz RD, Yao M, Yang B, Jiao Q, Qiu L. Development of an n-heptane-n-butanol-PAH mechanism and its application for combustion and soot prediction. Combust Flame 2013;160:504–19.

[230] Bolla M, Farrace D, Wright YM, Boulouchos K, Mastorakos E. Influence of turbulence–chemistry interaction for n-heptane spray combustion under diesel engine conditions with emphasis on soot formation and oxidation. Combust Theory Model 2014;18:330–60.

[231] Bolla M, Wright YM, Boulouchos K, Borghesi G, Mastorakos E. Soot formation modeling of n-heptane sprays under diesel engine conditions using the conditional moment closure approach. Combust Sci Technol 2013;185:766–93.

[232] d'Errico G, Ettorre D, Lucchini T. Simplified and detailed chemistry modeling of constant-volume diesel combustion experiments. SAE Int J Fuels Lubr 2008;1:452–65.

[233] Pang KM, Jangi M, Bai X-S, Schramm J. Evaluation and optimisation of phenomenological multi-step soot model for spray combustion under diesel engine-like operating conditions. Combust Theory Model 2015;19:279–308.

[234] Pang KM, Jangi M, Bai X-S, Schramm J. Investigation of chemical kinetics on soot formation event of n-heptane spray combustion. SAE Technical Paper; 2014.

[235] Som S, Senecal PK, Pomraning E. Comparison of RANS and LES turbulence models against constant volume diesel experiments. 24th Annu Conf Liq At Spray Syst ILASS Am San Antonio, TX 2012;Di:1–11.

[236] Kong S-C, Sun Y, Rietz RD. Modeling Diesel Spray Flame Liftoff, Sooting Tendency, and NOx Emissions Using Detailed Chemistry With Phenomenological Soot Model. J Eng Gas Turbines Power 2007;129:245. doi:10.1115/1.2181596.

[237] Luo Z, Som S, Sarathy SM, Plomer M, Pitz WJ, Longman DE, et al. Development and validation of an n-dodecane skeletal mechanism for spray combustion applications. Combust Theory Model 2014;18:187–203.

[238] Wang H, Ra Y, Jia M, Reitz RD. Development of a reduced n-dodecane-PAH mechanism and its application for n-dodecane soot predictions. Fuel 2014;136:25–36. doi:http://dx.doi.org/10.1016/j.fuel.2014.07.028.

[239] Gong C, Jangi M, Bai X-S. Large eddy simulation of n-Dodecane spray combustion in a high pressure combustion vessel. Appl Energy 2014;136:373–81.

[240] Pandurangi SS, Bolla M, Wright YM, Boulouchos K, Skeen SA, Manin J, et al. Onset and Progression of Soot in high-pressure n-Dodecane Sprays under Diesel-Engine Conditions. Int J Engine Res Under Rev 2016. doi:10.1177/1468087416661041.

[241] Pei Y, Hu B, Som S. Large-Eddy Simulation of an n-Dodecane Spray Flame Under Different Ambient Oxygen Conditions. J Energy Resour Technol 2016;138:32205. doi:10.1115/1.4032771.

[242] Anderson DA, Tannehill JC, Pletcher RH. Computational fluid mechanics and heat transfer 1984.

[243] Peters N. Turbulent combustion. Cambridge university press; 2000.

[244] Hallaji M, Mazaheri K. Comparison of LES and RANS in Numerical Simulation of Turbulent Non-Premixed Flame under MILD Combustion Condition. 7th Mediterr. Combust. Symp. Chia Laguna, Cagliari, Sardinia, Italy, Sept. 11, vol. 15, 2011.

[245] Sutherland W. LII. The viscosity of gases and molecular force. London, Edinburgh, Dublin Philos Mag J Sci 1893;36:507–31.

[246] Kee RJ, Coltrin ME, Glarborg P. Chemically reacting flow: theory and practice. John Wiley & Sons; 2005.

[247] Hirschfelder JO, Curtiss CF, Bird RB, Mayer MG. Molecular theory of gases and liquids. vol. 26. Wiley New York; 1954.

[248] Poinsot T, Veynante D. Theoretical and numerical combustion. RT Edwards, Inc.; 2005.

[249] Reynolds O. On the dynamical theory of incompressible viscous fluids and the determination of the criterion. Proc R Soc London 1894;56:40–5.

[250] Favre A. EQUATIONS DES GAZ TURBULENTS COMPRESSIBLES. 2. METHODE DES VITESSES MOYENNES METHODE DES VITESSES MACROSCOPIQUES PONDEREES PAR LA MASSE VOLUMIQUE. J Mec 1965;4:391.

[251] Versteeg HK, Malalasekera W. An introduction to computational fluid dynamics: the finite volume method. Pearson Education; 2007.

[252] Jones WP, Launder Be. The prediction of laminarization with a two-equation model of turbulence. Int J Heat Mass Transf 1972;15:301–14.

[253] Nordin PA. Complex chemistry modeling of diesel spray combustion. Chalmers University of Technology; 2001.

[254] Basset AB. A treatise on hydrodynamics: with numerous examples. vol. 2. Deighton, Bell and Company; 1888.

[255] Boussinesq J. Théorie analytique de la chaleur: mise en harmonie avec la thermodynamique et avec la théorie mécanique de la lumière. vol. 2. Gauthier-Villars; 1903.

[256] Oseen CW. Hydrodynamik Akademische Verlagsgesellschaft 1927.

[257] Reitz RD, Diwakar R. Effect of drop breakup on fuel sprays. SAE Technical Paper; 1986.

[258] Crowe CT, Sharma MP, Stock DE. The particle-source-in cell (PSI-CELL) model for gas-droplet flows. J Fluids Eng 1977;99:325–32.

[259] Hall RJ, Smooke MD, Colket MB. Physical and chemical aspects of combustion. Gordon and Breach 1997.

[260] Zhang Z, Chen Q. Comparison of the Eulerian and Lagrangian methods for predicting particle transport in enclosed spaces. Atmos Environ 2007;41:5236–48.

[261] Schiller L, Naumann Z. A drag coefficient correlation. Vdi Zeitung 1935;77:51.

[262] Kitanidis PK. Particle-tracking equations for the solution of the advection-dispersion equation with variable coefficients. Water Resour Res 1994;30:3225–7.

[263] Saffaripour M, Veshkini A, Kholghy M, Thomson MJ. Experimental investigation and detailed modeling of soot aggregate formation and size distribution in laminar coflow diffusion flames of Jet A-1, a synthetic kerosene, and n-decane. Combust Flame 2014;161:848–63.

[264] Mahgerefteh H, Rykov Y, Denton G. Courant, Friedrichs and Lewy (CFL) impact on numerical convergence of highly transient flows. Chem Eng Sci 2009;64:4969–75.

[265] ECN. Engine Combustion Network 2010. www.sandia.gov/ecn/.

[266] Weller HG, Tabor G, Jasak H, Fureby C. A tensorial approach to computational continuum mechanics using object-oriented techniques. Comput Phys 1998;12:620–31.

[267] Mondal HN, Roy S. Numerical Analysis of Droplet Combustion in a Cylindrical Furnace. J Chem Eng 2010:14.

[268] Pang KM, Ng HK, Gan S. Development of an integrated reduced fuel oxidation and soot precursor formation mechanism for CFD simulations of diesel combustion. Fuel 2011;90:2902–14.

[269] Tan SM, Ng HK, Gan S. CFD modelling of soot entrainment via thermophoretic deposition and crevice flow in a diesel engine. J Aerosol Sci 2013;66:83–95. doi:10.1016/j.jaerosci.2013.08.007.

[270] Tan SM, Ng HK, Gan S. Computational study of crevice soot entrainment in a diesel engine. Appl Energy 2013;102:898–907. doi:10.1016/j.apenergy.2012.09.029.

[271] Chevalier C. P. louessard, UC Muller and J. Warn. A“ Detail. Low-Temperature React. Mech. n-Heptane Auto-Ignition” Int. Symp. COMODIA, vol. 90, 1990, p. 93–7.

[272] Hong SJ, Wooldridge MS, Im HG, Assanis DN, Pitsch H. Development and application of a comprehensive soot model for 3D CFD reacting flow studies in a diesel engine.

Combust Flame 2005;143:11–26. doi:DOI 10.1016/j.combustflame.2005.04.007.

[273] Lucchini T, D'Errico G, Ettorre D, Ferrari G. Numerical Investigation of Non-Reacting and Reacting Diesel Sprays in Constant-Volume Vessels. SAE Int J Fuels Lubr 2009;2:966–75. doi:10.4271/2009-01-1971.

[274] Bolla M, Farrace D, Wright YM, Boulouchos K. Modelling of soot formation in a heavy-duty diesel engine with conditional moment closure. Fuel 2014;117, Part:309–25. doi:http://dx.doi.org/10.1016/j.fuel.2013.09.041.

[275] Bajaj C, Ameen M, Abraham J. Evaluation of an unsteady flamelet progress variable model for autoignition and flame lift-off in diesel jets. Combust Sci Technol 2013;185:454–72.

[276] Farrace D, Bolla M, Wright YM, Boulouchos K. Predicting In-Cylinder Soot in a Heavy-Duty Diesel Engine for Variations in SOI and TDC Temperature Using the Conditional Moment Closure Model. SAE Int J Engines 2013;6:1580–93. doi:10.4271/2013-24-0016.

[277] D'Errico G, Lucchini T, Contino F, Jangi M, Bai X-S. Comparison of well-mixed and multiple representative interactive flamelet approaches for diesel spray combustion modelling. Combust Theory Model 2014;18:65–88.

[278] Yao T, Pei Y, Zhong B-J, Som S, Lu T. A Hybrid Mechanism for n-Dodecane Combustion with Optimized Low-Temperature Chemistry. 9th U. S. Natl. Combust. Meet., 2015, p. 1–10.

[279] Chishty MA, Bolla M, Pei Y, Hawkes ER, Kook S, Lu T. Soot Formation Modelling of Spray-A Using a Transported PDF Approach 2015. doi:10.4271/2015-01-1849.

[280] Pei Y, Hawkes ER, Kook S. Transported probability density function modelling of the vapour phase of an n-heptane jet at diesel engine conditions. Proc Combust Inst 2013;34:3039–47.

[281] Pang KM, Poon HM, Ng HK, Gan S, Schramm J. Soot Formation Modeling of n-dodecane and Diesel Sprays under Engine-Like Conditions. SAE Technical Paper; 2015.

[282] Cenker E, Gilles B, Christof S. Imaging measurements of soot particle size and soot volume fraction with laser-induced incandescence at Diesel engine conditions. Ph.D. diss., Ecole Centrale Paris, 2014.

[283] Kuribayashi M, Ishizuka Y, Aizawa T. Sizing of Soot Particles in Diesel Spray Flame-A Qualitative Comparison between TEM Analysis and LII/Scattering Laser Measurements. SAE Technical Paper; 2013.

[284] El-Leathy AM, Kim CH, Faeth GM, Xu F. Soot surface reactions in high-temperature laminar diffusion flames. AIAA J 2004;42:988–96.

[285] Guo H, Liu F, Smallwood GJ, Gülder ÖL. Numerical study on the influence of hydrogen addition on soot formation in a laminar ethylene–air diffusion flame. Combust Flame 2006;145:324–38.

[286] Tao F, Golovitchev VI, Chomiak J. A phenomenological model for the prediction of soot formation in diesel spray combustion. Combust Flame 2004;136:270–82.

[287] Kazakov A, Wang H, Frenklach M. Detailed modeling of soot formation in laminar premixed ethylene flames at a pressure of 10 bar. Combust Flame 1995;100:111–20.

[288] Kaminaga T, Kusaka J, Ishii Y. A three-dimensional numerical study on exhaust gas emissions from a medium-duty diesel engine using a phenomenological soot particle formation model combined with detailed chemistry. Int J Engine Res 2008;9:283–96.

[289] Tree DR, Foster DE. Optical Measurements of Soot Particle Size, Number Density, and Temperature in a Direct Injection Diesel Engine as a Function of Speed and Load 1994. doi:10.4271/940270.

[290] Kosaka H, Aizawa T, Kamimoto T. Two-dimensional imaging of ignition and soot formation processes in a diesel flame. Int J Engine Res 2005;6:21–42. doi:10.1243/146808705X7347.

[291] Nerva J-G, Yamaguchi T, Iguma H, Nishigai H, Kondo K, Takano S, et al. Transmission Electron Microscopy of Soot Particles sampled directly from a Biodiesel Spray Flame. SAE Int J Fuels Lubr 2011;5:2011-01–2046. doi:10.4271/2011-01-2046.

[292] Shen M, Gallo Y, Waldheim BBO, Nilsson P, Eriksson A, Pagels J, et al. Analysis of Soot Particles in the Cylinder of a Heavy Duty Diesel Engine with High EGR. SAE Tech Pap 2015. doi:10.4271/2015-24-2448.Copyright.

[293] Kook S, Pickett LM. Soot volume fraction and morphology of conventional, fischer-tropsch, coal-derived, and surrogate fuel at diesel conditions. SAE Int J Fuels Lubr 2012;5:647–64.

[294] Camacho J, Tao Y, Wang H. Kinetics of nascent soot oxidation by molecular oxygen in a flow reactor. Proc Combust Inst 2015;35:1887–94. doi:10.1016/j.proci.2014.05.095.

[295] Kholghy M, Saffaripour M, Yip C, Thomson MJ. The evolution of soot morphology in a laminar coflow diffusion flame of a surrogate for Jet A-1. Combust Flame 2013;160:2119–30. doi:10.1016/j.combustflame.2013.04.008.

[296] Kholghy MR, Veshkini A, Thomson MJ. The core-shell internal nanostructure of soot - A criterion to model soot maturity. Carbon N Y 2016;100:508–36. doi:10.1016/j.carbon.2016.01.022.

[297] D'Anna A. Combustion-formed nanoparticles. Proc Combust Inst 2009;32 I:593–613. doi:10.1016/j.proci.2008.09.005.

[298] D'Anna A, Rolando A, Allouis C, Minutolo P, D'Alessio A. Nano-organic carbon and soot particle measurements in a laminar ethylene diffusion flame. Proc Combust Inst 2005;30:1449–55. doi:10.1016/j.proci.2004.08.276.

[299] Hurt RH, Crawford GP, Shim H-S. Equilibrium nanostructure of primary soot particles. Proc Combust Inst 2000;28:2539–46. doi:10.1016/S0082-0784(00)80670-0.